The Performance of Pulsating Heat Pipes as Thermal Switches in Redundant Cryocooler Systems

by

Bryant W. Mueller

A dissertation submitted in partial fulfillment of

the requirements for the degree of

Doctor of Philosophy

(Mechanical Engineering)

at the

UNIVERSITY OF WISCONSIN – MADISON

2021

Date of final oral examination: 12/03/2021

The dissertation is approved by the following members of the final oral committee:

Franklin K. Miller, Associate Professor, Mechanical Engineering
John M. Pfotenhauer, Professor, Mechanical Engineering
Gregory F. Nellis, Professor, Mechanical Engineering
Frank E. Pfefferkorn, Professor, Mechanical Engineering
Jennifer A. Franck, Assistant Professor, Engineering Physics

APPROVED

Franklin Miller
Associate Professor
Department of Mechanical Engineering

John Pfotenhauer
Professor
Department of Mechanical Engineering

Acknowledgments

There are a great many people to thank who, without their support and encouragement, this work (and my pursuit of a PhD in general) would not have been possible. Undoubtedly the most important of these is my wife Crystal, who has personally sacrificed sleep, time, and patience while solo parenting on many occasions so that I could address issues with my research at the lab or furiously work through physics homework problems. I 'love you more', Crystal! My sons Theodore and Elliot, both born during my time working on this project, have had a dearth of dad time during my studies, and I'm excited to repay my debt to them post graduation.

Next are my parents, Wayne and Nancy Mueller, who have consistently encouraged both my older sister Heidi and me to pursue advanced degrees and career goals. My desire to best my sister in honor roll appearances and GPA in high school certainly helped lay the foundation for study habits that help me through college. Mom, dad, and Heidi: thank you.

My immediate family is only surpassed in their promotion of education by my late Grandma Joyce, who, after being raised on a farm during the Great Depression in Michigan's Upper Peninsula (the 'U.P.') and limited in her own formal education to a high school diploma, furiously instilled the value of higher education into each of her children and grandchildren. Among her three children and ten grandchildren, all have Bachelor's degrees, at least five have Master's degrees, and two have doctorates. I have no doubt that this tally would be far lower and I would not be writing this if not for her efforts. With all these diplomas, there is frequent jesting in the extended group about who is 'the smartest one in the family'; although everyone truly knows this is

Grandma Joyce. Grandma: I wish we could celebrate *my* promotion to 'the smartest one in the family' over coffee, donuts, and sheepshead. My other grandparents also must be mentioned and thanked for their endless support and encouragement: my late Grandpa Wally, and my Grandma Bernice, and my late Grandpa Roger, the latter a car mechanic and woodworker who instilled in me a 'do it right the first time' approach to all things mechanical and whose patience in teaching his skills to others is surpassed by no one.

Many people in the Solar Engineering Lab and Cryogenic Engineering Lab at UW-Madison deserve mentions here. First and foremost is my advisor, Associate Professor Franklin Miller. Without his persuasive efforts, I likely would not have returned to begin a doctorate program after six years in the workforce post Master of Science graduation. Furthermore, my co-advisor Professor John Pfotenhauer has been a great resource for troubleshooting all things cryogenic which has undoubtedly saved numerous hours of tinkering and testing in the laboratory. Thank you both, and also to the remainder of my PhD committee: Professor Frank Pfefferkorn, Professor Greg Nellis, and Assistant Professor Jennifer Franck.

My graduate colleagues Uzoma Mmeje, Jennifer Detlor, Zhiyi Jiang, Chloe Gunderson, James Barkas, Logan Kossel, and Kacie Salmon have all offered a combination of thought-provoking conversation (engineering related and otherwise) and commiseration regarding experiments, coursework, and teaching which have made my time as a graduate student far more entertaining and less stressful than it would have been without their presence. Amir Jahromi and Diego Fonseca, graduate student colleagues during my prior stint at UW-Madison while pursing my Mas-

ter's, earn special mentions here for encouragement to purse a doctorate (Amir) and work prior work on cryogenic PHPs (Diego), both which have immensely aided in my experimental efforts as PhD student. Other mentions go to Gabe Bernhardt and Al Yingling – both from the liquid helium facility – who have lent their expertise on numerous tool finding and equipment rigging missions during my time working near their office, and undergraduate assistant Lucy Fitzgerald – who contributed many professional quality machined parts to my project. Thanks to everyone mentioned here!

Finally, I must thank the Office of Naval Research for funding the research contained within this dissertation and the Department of Mechanical Engineering at UW-Madison for several semesters of teaching assistant opportunities.

Table of Contents

List of Figures

List of Tables

1 Introduction

Mechanical cryogenic cooling systems – typically Gifford-McMahon, pulse tube, Brayton, and Stirling designs – are frequently deployed to provide low temperature cooling in extremely challenging environments. Space science programs, for instance, rely on cryocoolers to chill photon detectors for detection of a variety of wavelengths and mission objectives over a wide range of operating temperatures [1]. Some noteworthy examples include

- the Gamma-Ray and Neutron Spectrometer (GRNS) instrument on the Mercury MESSENGER mission for mapping the elemental composition of the planet's crust, cooled to 90K by a 0.5 W Ricor K508 Stirling cryocooler [2],
- the Atmospheric Infrared Sounder (AIRS) instrument on NASA's Earth Observing System Aqua platform, for precision temperature measurements as a function of atmosphere depth, with a focal plane array cooled to 58 K by two redundant pulse tube cryocoolers [3],
- and the Compact Reconnaissance Imaging Spectrometer for Mars (CRISM) instrument on the Mars Reconnaissance Orbiter for identifying water-related mineral formations on the planet, with a focal plane array cooled to 100 K by three redundant Ricor K508 (each 0.5 W at 80 K) Stirling cryocoolers [4].

Low temperature cooling is also a requirement for a number of defense applications, with mechanical cryocoolers necessary for cooling infrared focal plane arrays for thermal imaging systems onboard the Apache helicopter and M1A2 Abrams battle tank [5], and for cooling superconducting communication system electronics [6][7].

Although the temperature and cooling capacity requirements vary quite significantly across these applications, all demand some combination of high reliability, minimal downtime, small package volume, low mass, and portability within remote locations (where maintenance is costly, high risk, or impossible). Designing cryogenic cooling systems to meet such criteria is limited by the typical operating lifetimes of mechanical cryocoolers, which vary between technologies but are typically on the order of several operating years. Table 1.1 lists typical expected operating lifetimes for various mechanical cryocooler technologies.

Table 1.1. Typical operating lifetimes for mechanical cryocoolers

Cryocooler technology	Typical time to failure (hours)	Source
Gifford-McMahon	14400	[8]
Stirling	14200-20000	[9][10]
Pulse tube	44700-50000+	[11][8] [12]
Brayton	85000+	[12]

Extending mission timescales beyond these cryocooler lifetime limits is a highly valuable proposition, allowing instruments additional time to collect data and possibly avoiding the need to launch followup spacecraft to replace depreciated equipment. Although the reliability of mechanical cryocoolers has increased markedly over the past few decades [9][13], cooling systems implementing some number of redundant cryocoolers remain the preferred route to extend the useful lifetime of instruments beyond the lifetime of a single cryocooler [1].

Cryocooler redundancy increases overall system reliability by a simple mechanism: the connection of multiple coolers in parallel to a common cold plate (where the cooling load is applied) via conductive metal buses. The set of parallel cryocoolers can be duty cycled – each can cool the load independently – essentially multiplying the time to total system failure by the number of re-

dundant cryocoolers. Such a scheme is not without engineering penalty, however. Rather obviously, additional coolers will add volume and mass to the system, which is typically expensive for both spacecraft and terrestrial defense applications. Furthermore, these penalties scale at a greater rate than the cryocooler count - each inactive cryocooler introduces a parasitic load to the common cold plate which in turn increases the capacity requirements (and therefore volume and mass) of each cryocooler over the requirement for the non-redundancy design case. To overcome the latter issue, thermal switches can be placed between each cryocooler and the cooling load, limiting the parasitic load into the common cold plate [14]. Figure 1.1 illustrates the arrangement of components and relevant heat flows for an example redundant cryocooler system with and without thermal switches.

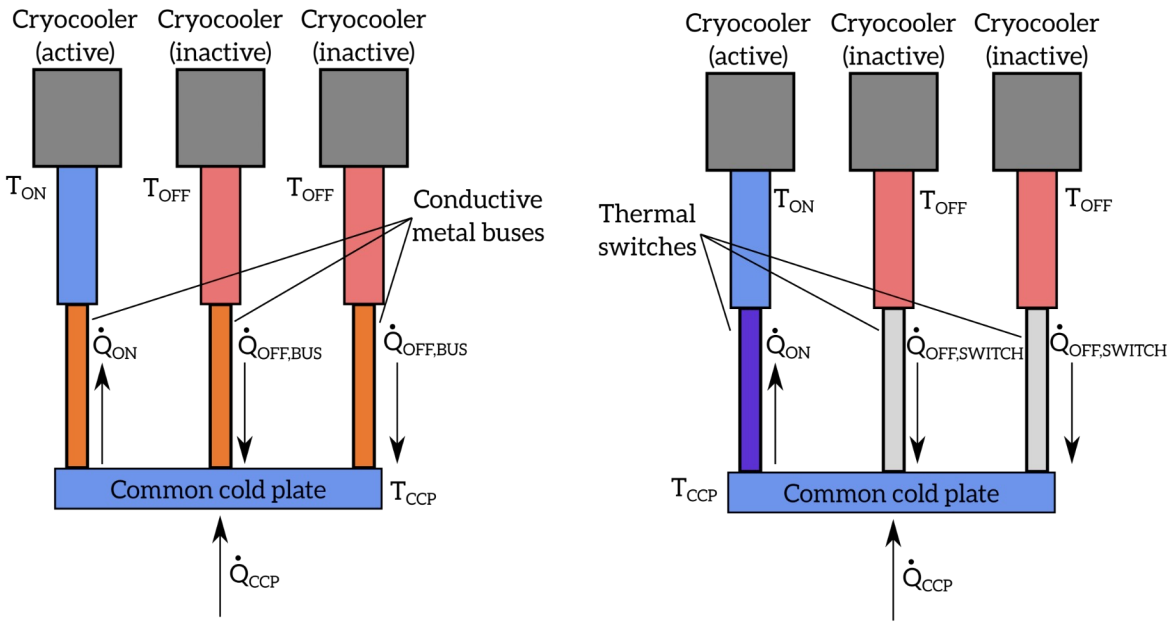

Figure 1.1. Schematic of redundant cryocooler concepts using direct thermal buses without heat switches (left) and with thermal switches (right).

In Figure 1.1, T_{ON} is the temperature of an active cryocooler cold head, T_{OFF} is the temperature of an inactive cryocooler cold head, T_{CCP} is the temperature of the common cold plate, and $\dot{Q}_{CCP}$ is the cooling load applied to the common cold plate. Typically $T_{OFF} \gg T_{ON}$ and $T_{ON} \simeq T_{CCP}$. $\dot{Q}_{ON}$ is the cooling power of the active cryocooler through an active thermal switch or a conductive metal bus, $\dot{Q}_{OFF,BUS}$ is the parasitic load through the conductive metal bus, and $\dot{Q}_{OFF,SWITCH}$ is the parasitic load through the thermal switch. The goal of the thermal switch is to achieve $\dot{Q}_{OFF,SWITCH} \ll \dot{Q}_{ON}$ such that the capacity of the remaining active cryocooler is not overwhelmed with the OFF state parasitic loads from the inactive cryocoolers, leaving T_{CCP} unchanged as long as a single cryocooler remains active. This is possible by actuating the conductance of the link, which can only be achieved with a switch and not the direct metal bus (which has an essentially fixed conductance). To avoid degrading the reliability of the overall redundant cryocooler system, the thermal switches introduced must have greater reliability than the cryocoolers they are isolating. This essentially limits suitable switch designs to simple assemblies which implement a thermal break mechanism without the need for active mechanical actuation. Furthermore, the switching mechanisms must be small in both in volume and mass to meet any restrictions on those quantities imposed by the application.

Redundant cryocooler systems with thermal switches have an additional benefit which may be exploited in terrestrial environments where system maintenance *is* feasible: the ability to keep an instrument cold (and functional) while a single cryocooler is removed from the system. This could allow, for instance, a failed cryocooler to be removed and repaired while an instrument remains operational. Another similar application, using an evaporating bath of a liquid cryogen as

the ‘redundant’ cooling mechanism would allow temporary portability of a cryostat. For instance, a mechanical cryocooler connected to an instrument via a thermal switch in its ON state could simultaneously cool down the instrument and surround it in a bath of liquid cryogen. After a sufficient fill is achieved, the cryocooler could be disconnected from its (large) compressor and the thermal switch actuated to the OFF state. Untethered from its compressor, the system can be made quite portable in terms of size and mass, with the charge of liquid cryogen acting as a temporary cooling source for both the instrument and parasitic loads. Such a system may be able to remain cold for timescales on the order of hours or days, depending on the design requirements.

A fairly wide variety of thermal switch technology exits that can be (in some cases already has been) implemented to limit parasitic heat loads into redundant cryocooler systems – a sampling of which are reviewed in Section 1.1.2. However, each of these existing technologies has limitations with respect to the demanding space and defense design requirements highlighted previously. In an effort to overcome these limitations, this present work investigates the novel use of nitrogen and helium pulsating heat pipes (PHPs) as thermal switches in redundant cryocooler applications. Prior to introducing PHPs and their usefulness as thermal switches, however, it is worthwhile to review the state-of-the art for thermal switches in general.

1.1 Thermal switch background

Thermal switches are, quite simply, devices which either restrict or allow the transport of thermal energy between thermal reservoirs at different temperatures via a conduction, convective, or radiative actuation mechanism. A simple schematic of a thermal switch, showing the heat flows between two constant temperature thermal reservoirs is shown in Figure 1.2.

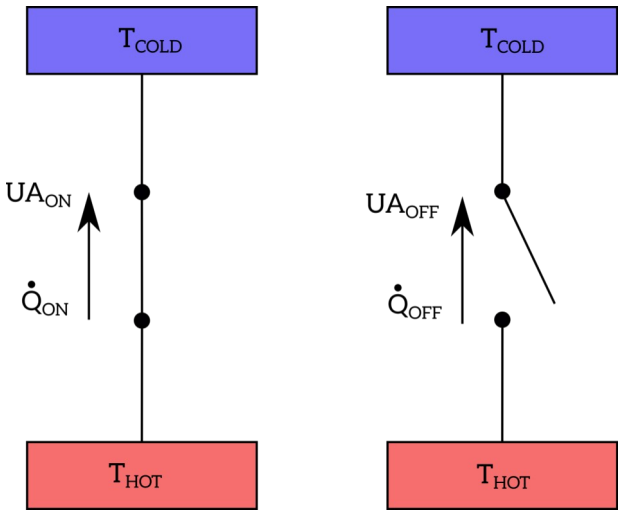

Figure 1.2. Schematic of a thermal switch in an ON (left) and OFF (right) state showing associated heat flows and switch conductance between two thermal reservoirs at maintained at different temperatures

Here $\dot{Q}_{ON}$ is the heat transfer through the switch in the ON state, $\dot{Q}_{OFF}$ is the heat transfer through the switch in the OFF state, UA_{ON} is the switch conductance in the ON state, and UA_{OFF} is the switch conductance in the OFF state. Note that conductances are defined as

$$UA_{ON} = \frac{|\dot{Q}_{ON}|}{T_{HOT} - T_{COLD}} \tag{1.1}$$

and

$$UA_{OFF} = \frac{|\dot{Q}_{OFF}|}{T_{HOT} - T_{COLD}} \tag{1.2}$$

, where T_{HOT} and T_{COLD} are the temperatures of the hot and cold reservoirs, respectively. A related variation, where the switch acts as a diode, is shown in Figure 1.3. In this case, the switch is constructed to allow thermal energy transport in only one direction (from the 'lower' reservoir to the 'upper' reservoir). A diode switch must be capable of switching states when the reservoir temperatures invert.

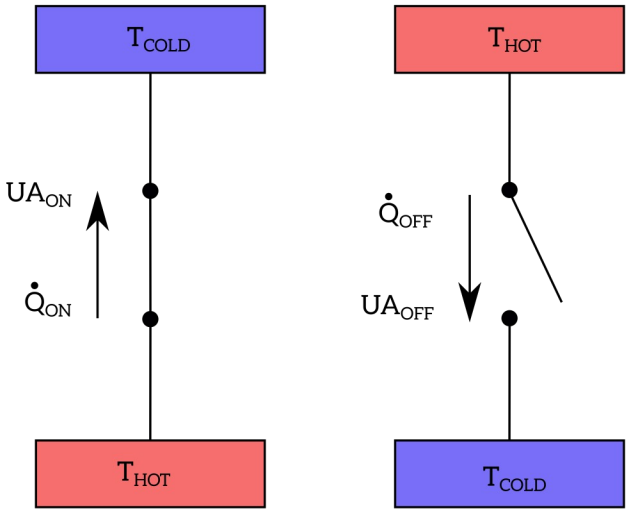

Figure 1.3. Schematic of a thermal diode switch showing heat flows and switch conductance between two thermal reservoirs in the ON state (left) and the OFF state with inverted reservoir temperatures (right)

Ideally, thermal switches are binary devices – the switch is either in the high conductance ON or the low conductance OFF state. This implies an instantaneous switching time. In practice, the actuation will take a finite amount of time during which the conductance will vary continuously between the ON and OFF state values. This non-ideal behavior is governed by the device physics and is dependent on the switch technology.

A thermal switch can be either actively or passively actuated, depending on the design and operating physics of the switch. Active actuation means that the transition between the switch states is controlled by a powered mechanism and can therefore be programmed to open or close based on conditions external to the thermal switch itself. A simple example of active actuation is an electromagnetic-driven mechanical contact switch, in which the thermal contact surfaces are brought into or out of contact with the force from a solenoid. The solenoid can be actuated by essentially any condition feasible by computer programming. Passive actuation, meanwhile, means that a property of the switch itself results in actuation between the states. For instance, the ther-

mal contact surfaces of a thermal expansion switch are brought into or out of contact by the temperature-dependent expansion or contraction of a material integrated into the switch. Although the temperature of the switch can be changed by an external conditions (say, applying a heat load), the switch activation is entirely passive and requires no externally applied force. Passive switches typically offer reduced flexibility over active switches in terms of control, but maybe desirable from a design simplicity or reliability perspective due to their lack of control system and possibly reduced count of components susceptible to mechanical wear.

Both active and passive switches can conceivably be *mechanically* passive, in the sense that the actuation mechanism requires no mechanical contact. For instance, an actively actuated but mechanically passive switch may use an externally magnetic field from a solenoid to draw highly conductive liquid metal into and out of a region between a set of static thermal contacts. A passively activated *and* mechanically passive switch may depend on the temperature of the switch to influence if high conductivity liquid or low conductivity vapor exists in a region between a set of static thermal contacts. Mechanically passive devices – either actively or passively actuated – are important for applications requiring low failure rates and high reliability.

1.1.1 Characterization, design criteria, and figure of merit

Thermal switches are typically characterized by several key parameters. Perhaps most obviously, the switch must be sized to accommodate a design ON state heat load $\dot{Q}_{ON}$ at specified switch reservoir temperatures $T_{HOT,ON}$ and $T_{COLD,ON}$. These temperatures are ideally identical and define both the maximum allowable associated temperature gradient over the ON state switch and the nominal ON state temperature. In addition, the maximum allowable OFF state parasitic

load $\dot{Q}_{OFF}$ associated with specified OFF state reservoir temperatures $T_{HOT,OFF}$ and $T_{COLD,OFF}$ must be defined. This also defines the maximum parasitic load associated with the expected temperature gradient. Note that the reservoir temperatures can in general be different for both the ON and OFF switch states. Overall this is equivalent to specifying the ON state heat load $\dot{Q}_{ON}$, the ON state conductance UA_{ON}, the OFF state heat load $\dot{Q}_{OFF}$, the OFF state conductance UA_{OFF}, and the reservoir temperature on one side of the switch in both the ON and OFF states (the temperature on the other side of the switch is implicitly defined through the conductance). Alternatively, the design OFF state conductance may be specified in terms of the ON state conductance and the switching ratio

$$SR = \frac{UA_{ON}}{UA_{OFF}} \tag{1.3}$$

, a figure of merit which directly compares the ON state conductance to the OFF state conductance. These required thermal switch specifications are summarized in Table 1.2.

Table 1.2. Required specifications for a thermal switch

Switch Parameter	Description
$\dot{Q}_{ON}$	Heat transfer in the ON state
$\dot{Q}_{OFF}$	Heat transfer in the OFF state
UA_{ON}	Conductance in the ON state
UA_{OFF} or SR	Conductance in the OFF state or switching ratio
$T_{HOT,ON}$ or $T_{COLD,ON}$	Hot or cold reservoir temperatures in the ON state
$T_{HOT,OFF}$ or $T_{COLD,OFF}$	Hot or cold reservoir temperatures in the OFF state

In addition to the thermal specifications mentioned above, some applications may impose additional constraints on the design of a thermal switch. For example, micrometer or millimeter scale thermal switches, using movable liquid mercury droplets [15] or carbon nanotube contractors

[16] as the switching mechanism, are designed for integration into specialized microprocessing chips which require both active control and fast switching times. Other applications more pertinent to this work – such as cryocooler redundancy in spacecraft cooling systems – place a high value on mechanically passive operation and reliability [17]. Additional design criteria such as the ability of the switch to accommodate tortuous heat flow paths, ease of fabrication, compactness in terms of both volume and mass, and cost may be important factors in the design.

1.1.2 Review of existing thermal switch technologies

A wide variety of thermal switch designs exist and are available for use today at cryogenic temperatures. A brief introduction to these existing switch designs, their switching mechanisms, and their primary use cases is necessary to build a case why PHPs may offer superior performance. In particular, the benefits and deficiencies of each existing cryogenic thermal switch type are presented here in order to highlight the reasons for their niche applications and why their performance may constrained in other systems. To the knowledge of the author, the review in this section offers a fairly comprehensive overview of the currently available cryogenic thermal switch technologies; they are discussed in no particular order.

1.1.2.1 Piezoelectric mechanical contact switches

Forced mechanical contacts are perhaps the simplest conceivable switch design (thermal or otherwise). Indeed, magnetically actuated *electrical* relay switches are ubiquitous in engineering applications. A mechanical contact *thermal* switch is conceptually quite similar to an electrical relay: apply a clamping force to a pair of thermally conductive surfaces to mate them together with minimum thermal contact resistance (the ON state), and apply a restoring force in the opposite direction to separate the contacts (the OFF state). The forces can be supplied with a variety of

mechanisms – springs and electromagnets may be used for a simple thermal analog of an electrical relay switch. Another way to apply the clamping and restoring forces is with a piezoelectric actuator. A proof-of-principle piezoelectric thermal switch has been built, tested, and proposed for use at temperatures less than 10 K in adiabatic demagnetization refrigerators (ADRs) for space applications [18]. Figure 1.4 shows an annotated schematic describing the structure of the switch and an image of the prototype switch assembly.

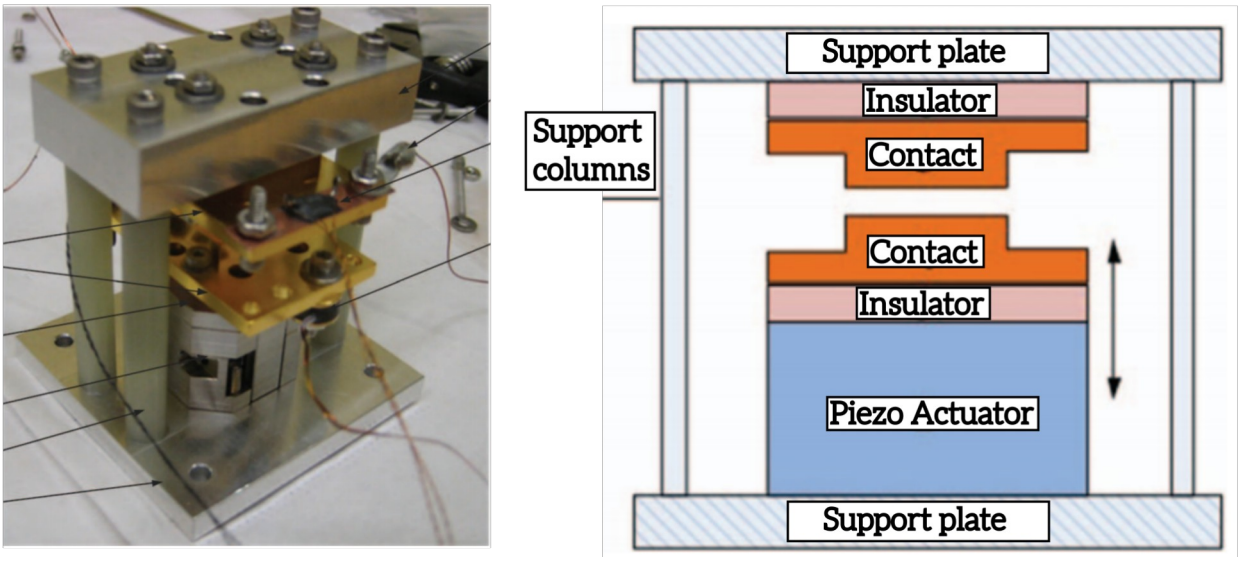

Figure 1.4. Image and schematic of a proof-of-principle piezoelectric mechanical contact switch for use at temperatures less than 10 K. Adapted from [18].

The main benefit of a mechanical piezeoelectric switch, as described in [18], is that the actuation is active and therefore independent of temperature (any condition may be used to flip the switch state). Furthermore, the switch requires no pressurized gas to operate and therefore requires no hermetic seals. These points are enticing with regards to an ADR, for which the current state-of-the art switch technology is a gas gap switch (see Section 1.1.2.3 below for more information on these). However, there is a price to pay for these conveniences: the switch is volumetrically bulky, has a large mass, and has a low heat transfer capacity; issues which stem from the fact that

the necessary large clamping forces require a stiff and high density support structure. Moving mechanical components and clamped mating contact surfaces result in long term reliability concerns due to the wear surfaces in the actuator and possible cold welding of the clamped thermal joint, respectively. Most importantly from a thermal performance perspective, the switching ratio is quite low. Also, because the heat transfer capacity is essentially limited by the contact area, scaling this switch type for use at ON state heat loads above those typical for the reject heat of a sub-10 K ADR would require the switch to become much larger and heaver than the example analyzed here, possibility prohibiting use in high heat load applications. Table 1.3 summarizes the important thermal switch performance metrics for the pizeoelectric switch in addition to the other switch technologies explored in this review.

1.1.2.2 Thermal expansion mechanical contact switches

Another type of mechanical contact switch uses the thermal expansion and contraction of a solid state material to apply the clamping and restorative forces to the mechanical contacts. These are often referred to in the literature as CTE (coefficient of thermal expansion) switches. Several example devices designed for use in space-based redundant cryocooler applications have been demonstrated [17][19]; obviously such a use case is especially relevant for the present work. A schematic of the CTE switch from [19] is shown in Figure 1.5. The schematic shows a cross section view of a cylindrical assembly, with aluminum alloy contact surfaces (‘Conductor A’ and ‘Conductor B’) separated at room temperature by a gap. A concentric cylinder made from a material with a high CTE – ultra high molecular weight polyethylene in this case – surrounds the ‘Conductor B’ flanges. When the assembly cools, the polymer cylinder contracts, pulling the outer contact flanges (‘Conductor B’) together with the inner contact cylinder (‘Conductor A’)

and actuating the switch to the ON state. On warming, the reverse process occurs, separating the contacts and actuating the switch to the OFF state.

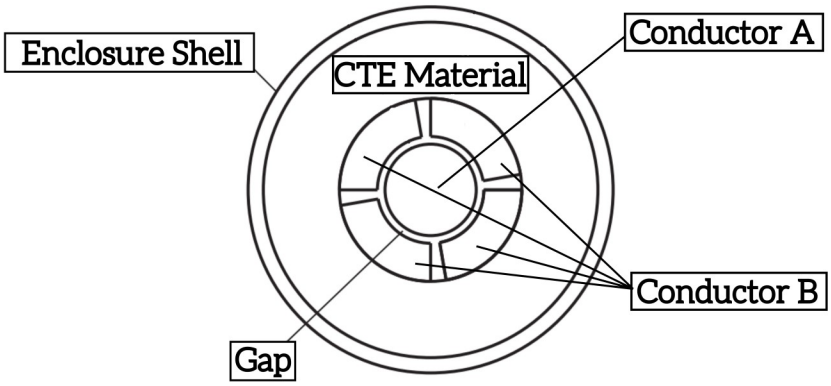

Figure 1.5. Cylindrical cross section view schematic of a proof-of-principle thermal expansion mechanical contact switch for use at temperatures around 100 K. Adapted from [19].

This technology has attractive advantages from a reliability perspective – actuation is passive and temperature dependent based on material physical properties – no active mechanical actuators are present which may wear over time. However, both creep of the polymer and cold welding of the thermal contact surfaces may be an issue in the long term. From a performance metric standpoint, the switch offers a moderately high switching ratio and ON state heat transfer capacity while having a fairly small mass and volume. However, applying this technology to different switching temperature ranges (especially near 4 K temperatures) may be difficult, as a high CTE material is required to generate sufficient clamping and restorative forces. Like the piezoelectric switch discussed previously, the heat transfer capacity will scale with the thermal contact area. This again means scaling this switch type for use at larger ON state heat loads (over the 1 W design in [19]) would require the switch to become much larger and heaver than the example analyzed here, possibility prohibiting use in high heat load applications.

1.1.2.3 Gas gap switches

Gas gap heat switches are the standard switch technology used in sub-Kelvin ADRs for space applications [20][21][22][23][24]. The devices feature two conductive heat transfer surfaces separated by a small gap. In the ON state, a conductive gas (typically helium, nitrogen, or neon) is introduced to the gap, allowing heat transfer between the surfaces via conduction through the gas. In the OFF state, the gas is removed via a cryopump (typically by cooling a getter material such as charcoal or zeolite in a connected chamber), which in turn insulates the surfaces from each other due to the resulting vacuum in the gap. Figure 1.6 depicts the cross section of typical gas gap switch.

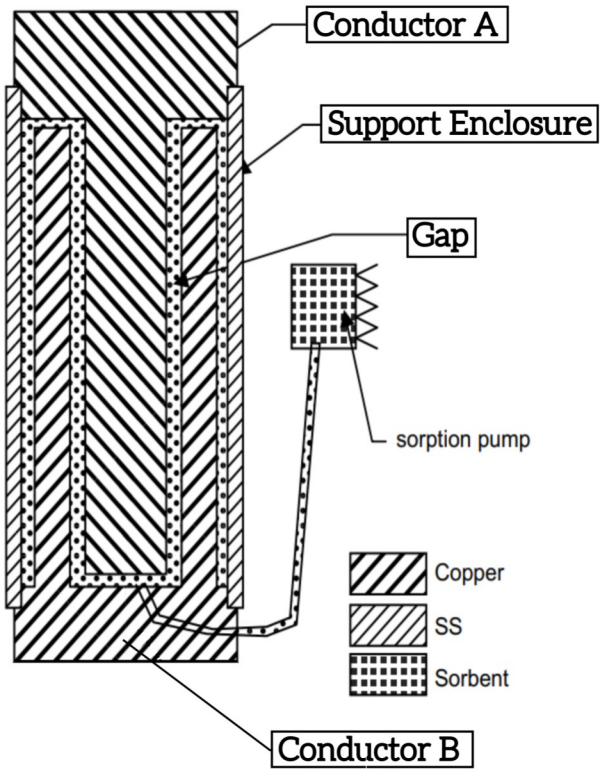

Figure 1.6. Cross section view schematic of a gas gap switch from an ADR. Adapted from [24]

A primary benefit of gas gap switches is an inherently high reliability – the devices contain neither moving mechanical components or mating metal surfaces and are therefore mechanically passive. This owes to the use of a conductive gas as the switching mechanism. Furthermore, moderately high switching ratios are attainable. However, there are several key drawbacks to these switches. Precision manufacturing methods are required to construct the small gap dimensions required to keep the gas conductance high, and radiative coupling between the high view factor conductive surfaces limits the OFF state temperature differential over which a gas gap switch can operate. The ON state heat transfer capacity – as with the mechanical contact switches – is again limited by the surface area of the conductive surfaces, which effectively limits the heat transfer through the gas gap. As with the piezoelectric switch, scaling a gas gap switch for use at ON state heat loads above those typical for the reject heat of a sub-10 K ADR would require the switch to become much larger and heaver than the example analyzed here, possibility prohibiting use in high heat load applications.

1.1.2.4 Traditional heat pipe diode switches

Traditional heat pipes can be used as diode thermal switches with addition of a liquid trap on the cold end to prevent reverse operation. Figure 1.7 is a schematic of such a device, which consists of a single tube containing a wick structure connecting the evaporator and condenser plates [25] [26]. Here the ON switch state occurs when heat is applied to the evaporator, slightly raising the evaporator temperature above the condenser temperature which in turns evaporates the liquid and raises the pressure at that location. This provides a pressure differential to move vapor towards the condenser, while liquid is returned to the evaporator via the wick. In the OFF state, the condenser temperature is raised above the evaporator temperature, creating an opportunity for re-

verse operation (and therefore an opportunity for a large parasitic load on the evaporator). The cold liquid trap placed between the thermal load and the evaporator, however, collects the condensate in this scenario and starves the 'condenser' (now the evaporator) of liquid before the parasitic load can significantly warm the 'evaporator'.

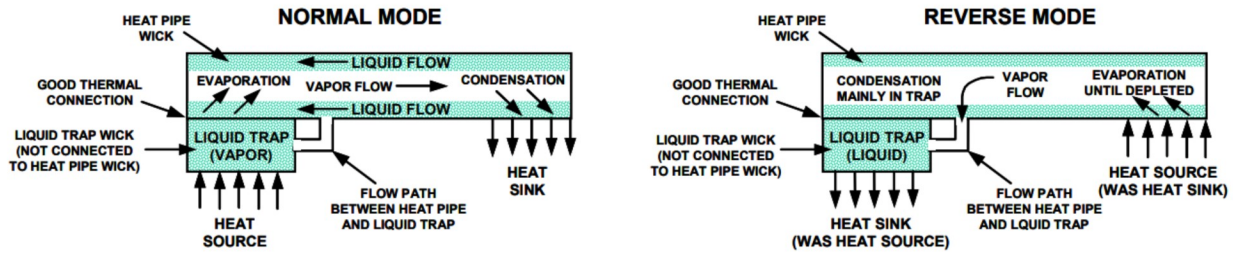

Figure 1.7. Cross section view schematic of a traditional heat pipe diode thermal switch. Adapted from [25]

As with gas gap switches, traditional heat pipe diode switches benefit from high reliability due to their mechanically passive, temperature dependent actuation and their lack of mechanical moving parts. Very high switching ratios are possible due to the excellent ON state conductance of a heat pipe associated with its liquid circulation, and a wide variety of switching temperatures are possible through the use of different fluids. However, external fill tanks are used to keep the initial room temperature charge pressures of the cryogen (methane or ethane, in the papers discussed here) reasonable. This is likely due in part to the large hoop stresses which develop at high pressures in the large (approximate 5 mm) diameter tubes used for these heat pipes. A smaller diameter heat pipe would be able to withstand larger internal pressures, but manufacturing the wick structure and retaining the same ON state performance characteristics in this case may be difficult.

1.1.2.5 Magnetoresistive switches

For applications at temperatures less than about 10 K, magnetoresistive thermal switches are possible. These devices consist of a small single crystal of gallium, cadmium, or zinc whose thermal conductivity is inversely dependent on the applied magnetic field [27]. With this type of switch, very high switching ratios are possible using magnetic field changes from 0.0 T to 1.5 T. However, such high fields may prohibit the switch from being located near sensitive electronics, depending on the application. Furthermore, manufacturing single crystals is rather complicated and expensive, especially if large switches are necessary to accommodate heat loads at scales larger than those for which the prototypes in [27] are developed.

1.1.3 Performance summary of existing thermal switch technologies

A summary of performance metrics for each of the heat switch technologies reviewed in this section is provided in Table 1.3. Information directly available from the references is transferred verbatim into the table. Quantities which are not directly provided in the papers are calculated or estimated from information given in the source material; some of the estimates are very approximate due to the lack of detailed design and test information supplied by the authors. It is therefore prudent to view the parameters listed in Table 1.3 as rough estimates of the capabilities of the switching technologies rather than a detailed study of the their limitations.

Table 1.3. Example performance of existing cryogenic thermal switch technologies. Parameters are approximate and represent devices in the listed references. The examples listed may not represent the full capability of the technologies.

Thermal switch type	**Switch mass [g]**	**Approximate switching temperature [K]**	**ON state conductance UA_{ON}, [mW/K]**	**OFF state conductance UA_{OFF}, [mW/K]**	**Switching ratio SR**	**Enclosure volume V_{switch}, [mm^3]**	**ON state load capacity $\dot{Q}_{switch,ON}$, [mW]**	**Source**
Piezoelectric - driven mechanical contact[1]	400	4.0 to 10	2.6 to 5.5	0.0280	93 to 196	1500	50	[18] [28]
Thermal expansion - driven mechanical contact	25	100	890	1.6000	556	21	500	[17] [19]
Gas gap[2]	215	1.2	30	0.1000	300	0.05	50	[21] [22] [23]
Traditional heat pipe diode[3]	49	100	1	0.4125	2100	18	500	[25] [26]
Magneto-resistive[4]	1.4	< 10	20	0.2000 to 0.0025	100 to 8000	0.25	100	[27]

1.2 Pulsating heat pipes (PHPs) background

PHPs are an established category of mechanically passive heat transfer devices, typically comprised of two plates – one hot (the evaporator) and one cold (the condenser) – linked thermally and structurally by a multi-pass serpentine tube filled with a two-phase fluid [29][30][31][32]. The serpentine fluid tube can be constructed as an open-loop or closed-loop circuit; the open-loop version caps each end of the tube, while the closed-loop design connects the tube ends to form a continuous fluid path. A schematic depicting the closed-loop type is shown in Figure 1.8.

1 Roughly estimated using a typical ADR heat rejection power of 50 mW from the listed sources

2 Roughly estimated using a typical ADR heat rejection power of 50 mW from the listed sources

3 Estimated (very roughly) using volumes in the reference and an aluminum density of 2700 kg/m^3

4 Estimated (very roughly) using volumes in the reference and a gallium density of 5900 kg/m$^{3.}$. Switch mass and volume do not include a necessary 1.5 T electromagnetic field source.

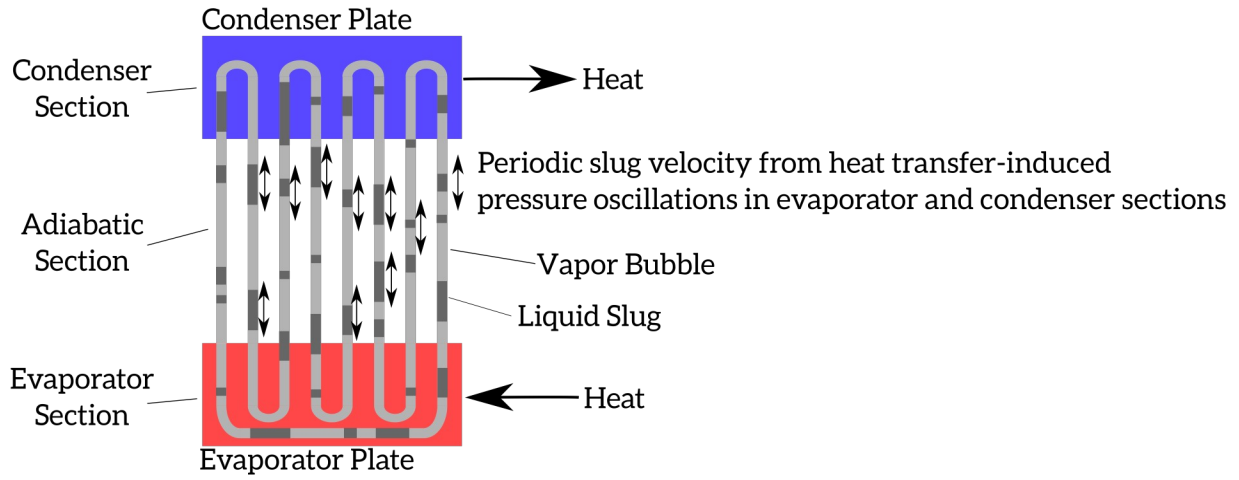

Figure 1.8. Schematic of a closed loop pulsating heat pipe depicting fluid oscillations and flow of heat. Adapted from [31] and [32].

To operate, a small temperature gradient between the two plates is imposed by applying a heat load to the evaporator section and simultaneously removing heat from the condenser section. The section of tubes connecting the condenser and evaporator are typically assumed to be adiabatic (this region of the PHP is aptly named the adiabatic section). With a temperature gradient imposed over the plates, energy transport from from the hot evaporator to the cold condenser can, in general, occur via several modes: thermally-driven advective flow of the two-phase fluid within the tube, conduction through the tube walls, and net radiation exchange between the surfaces at different temperatures.

In most designs and operating scenarios, the advective flow of the fluid is by far the dominant energy transport mechanism. For such a thermally-driven two phase flow to develop, the PHP tubing must be designed to allow axial pressure gradients to develop within the tube in order to provide a fluid pumping mechanism. This is achieved by ensuring that surface tension forces are dominant within the fluid. In such a case the liquid slugs always span the cross section of the

tube, preventing stratified mixing of the vapor and liquid phases and allowing axial pressure gradients to develop, guaranteeing a liquid slug / vapor plug flow regime for the two-phase flow [33]. Additionally, in terrestrial applications, locating the evaporator at lower gravitational potentials than the condenser allows buoyancy forces to aid in pumping. With two-phase liquid slug / vapor plug flow ensured by the PHP tube sizing, the high temperature of the evaporator and low temperature of the condenser cause local evaporation and condensation of the working fluid at these locations. The corresponding localized pressure spikes and depressions of the fluid in turn provide the pumping mechanism to drive the flow. These pressure gradients force the hot vapor from the evaporator to the condenser (where it contracts as it cools) and the cool liquid from the condenser to the evaporator (where it expands as it warms), creating a non-equilibrium, periodic reversing advective flow of fluid plugs and vapor bubbles within the tube. In closed-loop PHPs, a net overall circulation can develop [34][30] in addition to the oscillating flow, allowing superior energy transport rates relative to the open-loop design. For this reason, closed-loop PHPs are usually preferred over the open-loop type.

Energy transport in a PHP experiencing thermally-driven advective flow occurs at substantial rates relative to the driving temperature difference. The ability of PHP to transport energy, relative to the imposed temperature gradient, is commonly reported in the literature by the effective thermal conductivity

$$k_{EFF} = \frac{\dot{Q}_{PHP}}{T_{EVAP} - T_{COND}} \frac{L_{ADIA}}{A} \tag{1.4}$$

and effective conductance

$$UA_{EFF} = \frac{\dot{Q}_{PHP}}{T_{EVAP} - T_{COND}} \tag{1.5}$$

, where $\dot{Q}_{PHP}$ is the PHP heat load, L_{ADIA} is the adiabatic section length, A is the total cross sectional area of all the adiabatic section tubes based on the external tube diameter, T_{EVAP} is the evaporator temperature, and T_{COND} is the condenser temperature. The idea of the effective thermal conductivity is to allow comparison of the thermal transport ability of the PHPs to that of solid materials with equivalent lengths and cross section areas. Table 1.4 contains examples of PHP effective thermal conductivity and maximum heat transfer capacity reported in the literature, along with the values for copper (generally the best *affordable* solid metal conductor) at the equivalent temperature.

PHP thermal design is typically governed by two key constraints. First, as previously mentioned, surface tension forces must always dominate the fluid dynamics for two-phase slug / plug flow to occur. This imposes constraints on the tube diameter given the properties of the working fluid. Consider a vapor bubble moving through a liquid in a terrestrial vertical tube: three forces (viscous, buoyant, and surface tension) and the inertia govern the motion of the bubble [35]. Empirical data [36] suggest that a critical ratio of buoyant to surface tension forces exists such that a gas bubble with *any* viscosity will *always* be completely decelerated by the surface tension. It is convenient here to define a dimensionless ratio of buoyant to surface tension forces, the Eötvös number

Table 1.4. Effective conductance and maximum heat load reported for relevant PHPs in the literature.

Reference	Working fluid	Approximate operating temperature [K]	Adiabatic section length, L_{ADIA} [mm]	Condenser section length, L_{COND} [mm]	Evaporator section length, L_{EVAP} [mm]	Effective thermal conductivity[5], k_{EFF} [W/m-K]	Copper RRR 100 thermal conductivity[37] [38] at equivalent operating temperature [W/m-K]
Jiao 2009 [39]	nitrogen	77	100	60	40	3148 – 7154	553
Fonseca 2018 [40]			80	70	70	17500 – 62500	
Mito 2010 [41]			100	30	30	5000 – 18000	
Mito 2010 [41]	neon	25	100	30	30	1000 – 8000	2388
Liang 2018 [42]			480	110	110	3466 – 30854	
Fonseca 2014 [43]	helium	4	90	125	117	2100 – 2800	642
Xu 2016 [44]			100	50	50	4800 – 13000	
Fonseca 2018 [45]			300	90	60	10000 – 55400	
Fonseca 2018 [35]			1000	90	60	150000	
Mito 2010 [41]	hydrogen	21	100	30	30	500 – 3000	2416
Patel 2016 [46]	water	315	100	50	40	384 – 1474	396
Okazaki 2014 [47]	r410A	225	2000	200	200	155000 – 373000	404

5 Ranges are quite large due to dependence on heat load, liquid fill ratio, and operating temperature. Measurement uncertainty can also be quite large since small temperature differences must be resolved. See Section 2.5 for further discussion regarding uncertainties.

$$Eo = \frac{(\rho_L - \rho_V) g d_i^2}{\sigma} \tag{1.6}$$

and a dimensionless ratio of the inertial to buoyant forces, the Froude number

$$Fr = \frac{\rho_L u^2}{(\rho_L - \rho_V) g d_i^2} \tag{1.7}$$

, where ρ_L is the liquid density, ρ_V is the vapor density, g is the gravitational acceleration, d_i is the internal diameter of the tube, σ is the surface tension, and u is the bubble velocity. The critical Eötvös number Eo_c for which surface tension dominates is shown by the convergence of empirical data for fluids with a wide range of viscosities in Figure 1.9, and is generally accepted to occur at

$$Eo_c = 4 \tag{1.8}$$

. By Equations 1.6 and 1.8, a critical (minimum) inner tube diameter can be defined as

$$d_{i,c} = \sqrt{\frac{Eo_c \sigma}{(\rho_L - \rho_V) g}} = 2\sqrt{\frac{\sigma}{(\rho_L - \rho_V) g}} \tag{1.9}$$

. The critical diameter depends rather strongly on the fluid type and quite weakly on the fluid saturation temperature.

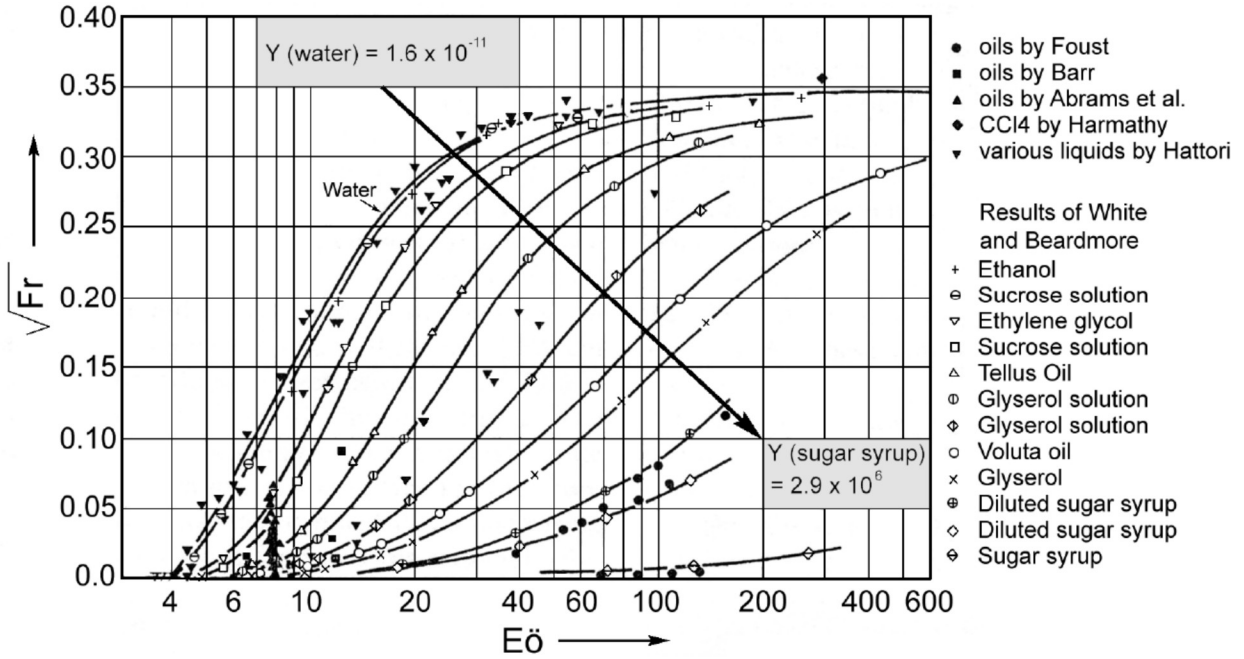

Figure 1.9. Emperical data showing the Froude number as a function of the Eötvös, with convergence to Fr=0 at the critical Eötvös number [36].

Figure 1.10 shows these dependencies for various fluids while also surveying the available fluids available for PHPs at different operating temperatures. The important message here is that at values below the critical Eötvös number (or critical diameter), the gas-liquid interface spans the entire tube cross-section – exactly the condition needed to maintain slug-plug flow in a PHP. Note that, in a microgravity environment, the gravity-induced buoyancy force becomes irrelevant and the critical diameter must be determined by alternative means [48][49]. In this case, one possible criteria to block a transition out of slug-plug flow is to ensure the energy stored by the surface tension of a vapor bubble exceeds the kinetic energy of a liquid slug [50]. This essentially replaces the Eötvös number with the Weber number

$$\mathrm{We}=\frac{\rho_L d_i u^2}{\sigma} \tag{1.10}$$

and the critical Eötvös number with the critical Weber number

$$We_c = 4 \tag{1.11}$$

. By Equations 1.10 and 1.11, a critical (minimum) inner tube diameter then can be defined as

$$d_{i,c} = \frac{We_c \sigma}{\rho_L u^2} = \frac{4\sigma}{\rho_L u^2} \tag{1.12}$$

. A second alternative to determining a critical diameter in microgravity is a semi-empirical approach which includes the effects of both inertia and viscosity [51]

$$d_{i,c} = \sqrt{\frac{160\,\mu_L}{\rho_L u^2}\sqrt{\frac{\sigma}{(\rho_L - \rho_V)g}}} \tag{1.13}$$

. These alternative critical diameters for microgravity should be viewed as an order-of-magnitude approximation, as the fluid velocity is not constant within a PHP.

A second thermal design constraint for PHPs somewhat opposes that of the critical diameter – the total tube cross sectional area of all parallel tubes in the adiabatic section must be sufficiently large to accommodate the maximum design heat load applied to the PHP evaporator at the design temperature. Heat loads in excess of this critical design load raise the overall temperature of the PHP and cause dryout – near total evaporation of the fluid in the PHP – thereby starving the PHP of liquid and preventing the formation of liquid slugs in the tubes. This inhibits buildup of the driving pressure gradients and blocks the dominant mechanism for energy transport between the evaporator and condenser plates. Advective flow is halted at this dryout condition, leaving conduction through the tube walls and stagnant working fluid vapor as the only remaining thermal connection between the evaporator and condenser plates (assuming radiative loads are negligi-

ble). To accommodate the design heat load on the evaporator while simultaneously satisfying the critical diameter constraint necessary to maintain slug / plug flow, a minimum number of parallel tubes must be present in the adiabatic section of the PHP.

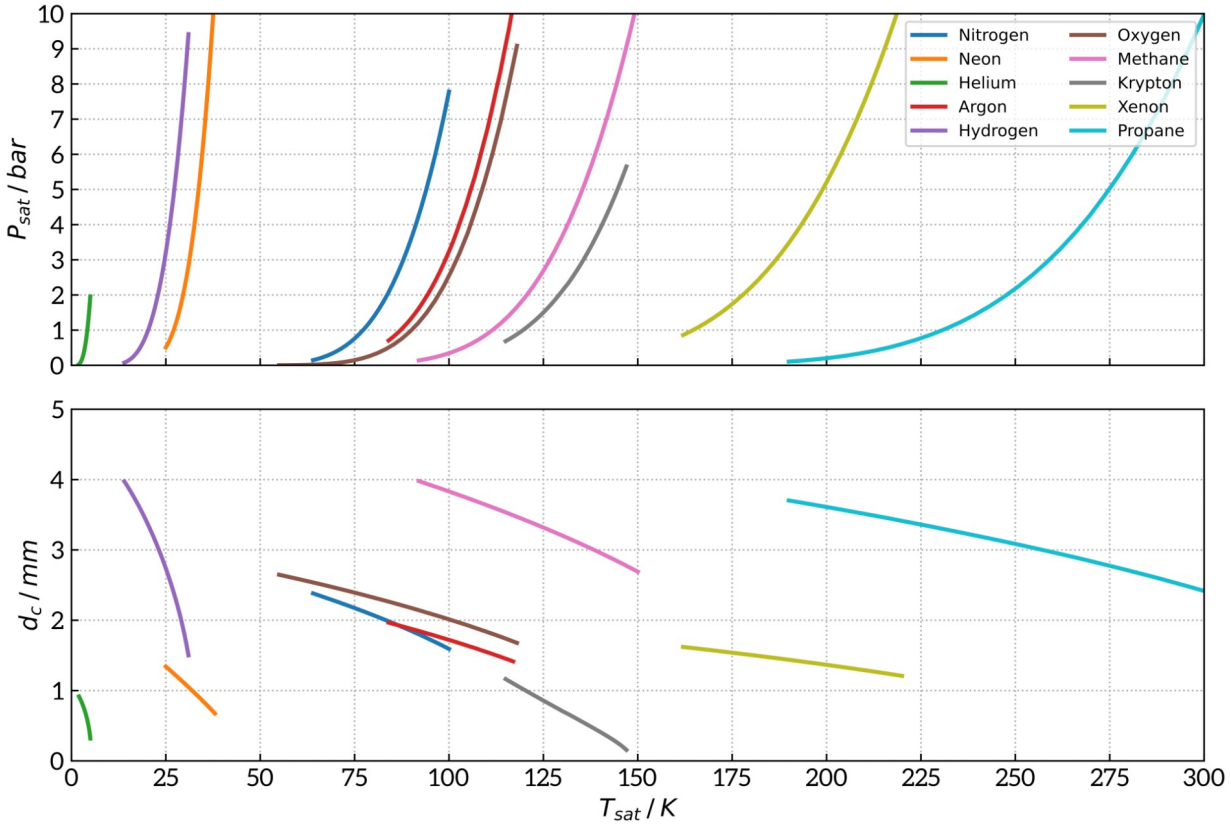

Figure 1.10. Critical diameter and saturation pressure as a function of saturation temperature for various fluids.

PHPs have several other noteworthy characteristics in addition to their excellent thermal transport properties. As mechanically passive devices with no moving parts, PHPs are inherently highly reliable. In addition, PHPs can also transfer heat over fairly large distances – successful operation with adiabatic section lengths of 480 mm, 1000 mm, and 2000 mm have been demonstrated [42][52][47]. Some work using PHPs with non-linear tube paths for the adiabatic section have been tested [42], allowing further flexibility in the placement of the evaporator and con-

denser sections. There is likely a limit to the adiabatic section tube length allowable 'minor' losses associated with tube bends in the adiabatic section, but they perhaps depend on the working fluid and are currently unknown; additional investigation is needed to determine these limits. Furthermore, with the use of thin-walled stainless steel tubing and thin metal plates for the condenser and evaporator, PHPs can be constructed with very low mass. Lastly, PHPs are proven to function with a wide variety of working fluids (including cryogens) at various operating temperatures, as shown by the literature highlights in Table 1.4.

1.3 PHPs as thermal switches

PHPs possess several characteristics making them well suited for use as thermal switches. First, and most importantly, PHPs are capable of impressive effective thermal conductance when operating in the advective flow regime (see Table 1.4). If the PHP is functioning as a thermal switch, this means a very high ON state conductance can be achieved when advective flow thermally links the evaporator and condenser plates. In turn, this allows a large numerator in the switching ratio of Equation 1.3. Furthermore, a low OFF state conductance for a PHP thermal switch can be attained by using the dryout regime to severely limit energy transport between the evaporator and condenser plates. In the dryout state, a PHP thermal switch provides a very small denominator in the thermal switching ratio equation due to the poor thermal conductivity of stagnant vapor in the tubes, given that conduction through the tube walls and radiative coupling of the evaporator and condenser plates are negligible. Table 1.5 compares the advective flow effective thermal conductivity of PHPs reported in the literature (first shown in Table 1.4) with the theoretical effective thermal conductivity of those same PHPs filled instead with stagnant gases. A theoretical switching ratio based on these conductivities is also provided. The analysis ignores conduction

through the tube walls and radiative coupling between the evaporator and condenser – the former of which turns out to be the dominate heat transfer mechanism in the OFF state for the switches tested in this work (see Section 4.2 and Section 4.3), yet nicely illustrates the potential performance of PHP thermal switches.

A PHP thermal switch, then, leverages the onset of dryout (evaporation of a critical amount of liquid) to actuate from the ON to the OFF state, and the onset of advective flow (condensation of a critical amount of vapor) to actuate from the OFF state to ON state. This actuation (either from ON to OFF or OFF to ON) occurs completely passively at a temperature determined by the saturation properties of the working fluid and the overall specific volume of the fluid in the PHP. The latter is typically characterized by the liquid fill ratio

$$FR = \frac{V_{L,PHP}(T_{sat})}{V_{PHP}} \tag{1.14}$$

, where $V_{L,PHP}(T_{sat})$ is the liquid volume in the PHP at a design saturation temperature and V_{PHP} is the total PHP volume. No mechanical actuation is necessary to change switching states – dryout is completely determined by the fill ratio and the mean PHP temperature (with the latter determined by the applied evaporator heat load) – meaning that a PHP thermal switch is mechanically passive. Finally, the switch from the ON state to the OFF state for a PHP thermal switch occurs quickly – the effective conductance abruptly changes at the onset of dryout or advective flow, allowing for a nearly instantaneous thermal isolation or linkage upon actuation of the switch.

Table 1.5. Effective thermal conductivity of PHPs from literature featured in Table 1.4 for both advective flow (as reported by the sources) and stagnant vapor (with thermal conductivity calculated at the temperatures indicated). Conduction through the tube walls and radiation are neglected.

Paper	**Working fluid**	**Approximate operating temperature (ON state) [K]**	**Effective thermal conductivity with advective flow (ON state), k_{EFF} [W/m-K]**	**Effective thermal conductivity with stagnant vapor, k_{EFF} [W/m-K]**		**Theoretical switching ratio[6], SR**	
				Saturated vapor at ON state temperature	**At 1 bar and 300 K**	**Saturated vapor at ON state temperature**	**At 1 bar and 300 K**
Jiao 2009 [39]	nitrogen	77	3148 – 7154	0.007	0.026	449714 – 1022000	121076 – 275154
Fonseca 2018 [40]			17500 – 62500			2500000 – 8928571	673077 – 2403846
Mito 2010 [41]			5000 – 18000			714286 – 2571430	192308 – 692308
Mito 2010 [41]	neon	25	1000 – 8000	0.008	0.050	125000 – 1000000	20000 – 160000
Liang 2018 [42]			3466 – 30854			433250 – 3856750	69320 – 617080
Fonseca 2014 [43]	helium	4	2100 – 2800	0.008	0.156	262500 – 350000	13462 – 17949
Xu 2016 [44]			4800 – 13000			600000 – 1625000	30770 – 83333
Fonseca 2018 [45]			10000 – 55400			1250000 – 6925000	64102 – 355128
Fonseca 2018 [35]			150000			18750000	961538
Mito 2010 [41]	hydrogen	21 K	500 – 3000	0.019	0.187	26316 – 157895	2674 - 16043
Patel 2016 [34]	water	315 K	384 – 1474	0.020	0.610	17400 – 73700	630 – 2416
Okazaki 2014 [47]	r410A	225 K	155000 – 373000	0.018	0.013	8611110 – 20722200	11923100 – 28692300

6 Again, ranges are quite large due to dependence on heat load, liquid fill ratio, and operating temperature. Measurement uncertainty can also be quite large since small temperature differences must be resolved. See Section 2.5 for more details.

1.4 PHPs as thermal switches in high reliability redundant cryocooler applications

The actuation process of a PHP thermal switch is nuanced and necessitates a more detailed description than that provided in the prior section. For this, consider the application of PHP thermal switches to a cryogenic cooling system with two redundant cryocoolers. A schematic of such a system is shown in Figure 1.11. Each cryocooler in this system is connected to a common cold plate with a PHP – Cryocooler-I connects with PHP-I and Crycooler-II connects with PHP-II. Consider now two possible operating scenarios for the pair of cryocoolers: one with both Cryocooler-I and Cryocooler-II active, and the other with Cryocooler-I active but Cryocooler-II inactive. The former scenario is depicted on the left side of Figure 1.11 and the latter on the right. Both scenarios feature an applied heat load on the common cold plate. With both cryocoolers active, PHP-I and PHP-II are each in a state of advective flow (the ON state for the PHP thermal switch), delivering a portion of the common cold plate heat load to their associated cryocooler. In this state the common cold plate, PHP-I condenser, and PHP-II condenser are all at nearly the same temperature (say, within a range of a few Kelvin). Now consider now an event that causes Cryocooler-II to cease operation, in turn allowing the temperature of the PHP-II condenser to rise significantly above the temperature of the PHP-II evaporator and common cold plate as it warms from its thermal interface with the ambient environment. As the PHP-II condenser warms, heat is conducted into the PHP-II working fluid, quickly causing complete evaporation (dryout) in PHP-II condenser and adiabatic sections. Some liquid may remain in the evaporator section, as it remains below the critical temperature. With the condenser and adiabatic sections completely dry, the PHP insulates the common cold plate from a potential parasitic heat load incoming from the warm, inactive Cryocooler-II because the advective flow within is seized. The PHP-II evaporator

remains cold, as it is connected to the common cold plate which continues to be cooled by PHP-I and Cryocooler-I. The rapid warming of a PHP condenser therefore automatically and passively actuates a PHP thermal switch in the ON state into the OFF state.

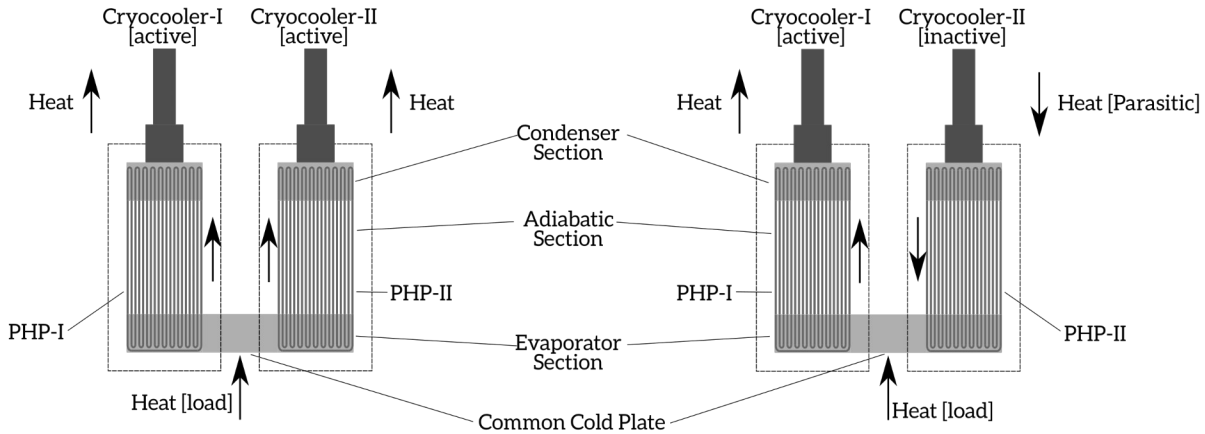

Figure 1.11. Schematic of a redundant cryocooler system with PHP thermal switches installed between the cryocooler cold heads and common cold plate. Energy flows shown for scenarois with both Cryocooler-I and Cryocooler-II operating (left) and for Cryocooler-I operating and Cryocooler-II non-operating (right).

The reverse actuation is also passive and automatic. Consider now the re-activation of Cryocooler-II after it has been inactive for an extended period. In this case, Cryocooler-II and the PHP-II condenser are initially substantially hotter than the continually operating Cryocooler-I, PHP-I, the common cold plate, and the evaporator of PHP-II. The PHP-II condenser and adiabatic sections are initially dry. After reactivation, Cryocooler-II cools the PHP-II condenser along with the vaporized working fluid. Eventually, the PHP-II condenser is brought below the critical temperature and condensation of the vapor occurs, rewetting the condenser and soon thereafter initiating the slug-plug advective flow. This constitutes an automatic passive actuation of the PHP thermal switch from the OFF state to the ON state.

A few final notes regarding this redundant cryocooler system with PHP thermal switches are worth highlighting. First, *either* of the redundant cryocoolers could experience a deactivation and the common cold plate would remain continuously cooled by the remaining functioning cryocooler. The aforementioned effects on the PHP operation simply occur in PHP associated with whichever cryocooler is deactivated. Additionally, the actuation temperature of the switch is governed by the choice of working fluid (and somewhat weakly by the fill ratio); recall that Figure 1.10 shows possible cryogenic fluids depending on the actuation temperature required. Lastly, as previously discussed, PHPs in advective slug-plug flow are known to retain high thermal conductance even with large adiabatic section lengths [52]. This is a powerful characteristic for PHP thermal switch, as thermal conductance in the OFF state can be reduced by increasing the adiabatic section length per Equation 1.4 without detriment to the ON state conductance. In concept this allows the switching ratio to be increased simply by increasing the length of the adiabatic section, assuming again that radiative exchange is negligible.

1.5 Benefits of PHPs relative to existing thermal switch technologies

Several uses are presented in Section 1.1 for redundant cryocooler systems featuring thermal switches as a mechanism to limit parasitic heat loads from a failed cryocooler. Switches with large switching ratios are a basic requirement for this type of redundancy, and in concept, any of the switching technologies presented in Section 1.1.2 may be used to meet this requirement. For some specific use cases, however, using PHPs as the thermal switch in a redundant cryocooler system is particularly alluring due to the unique combination of characteristics unrelated to the switching ratio possessed by PHPs.

Spacecraft cooling systems for photon detectors, either for near-Earth satellites or for more distant interplanetary missions, are one such application. Reliability of thermal systems here is mission critical, as maintenance is impractical or impossible due to the inaccessibility of the spacecraft. The appeal of cryocooler redundancy is fairly obvious in this situation. Using PHPs as the thermal switching mechanism in these systems offers several advantages over other technologies. First and foremost, PHPs are completely mechanically passive. Lacking typical wear items such as bearings and seals associated with rotating or sliding machinery, the risk of failure of a PHP switch lies in the fatigue strength of the tube joints (brazed, welded, or soldered) which are responsible for containing the pressurized working fluid in the system. As common engineering alloys can be used for the tube, the failure risk of a properly engineered and fabricated PHP tube joint should be quite low. The introduction of PHPs into a spacecraft cooling system should therefore add little risk of failure to the overall cooling system. This contrasts with the long-term polymer creep and contact cold welding concerns [17] of thermal expansion mechanical contact switches that are also proposed for use in this application. Piezoelectric mechanical contact switches must also contend with the long-term cold welding of the contacts and mechanical wear of surfaces in the piezoelectric mechanism.

Minimization of launch mass is also critical for spacecraft applications. With tubes typically fabricated from thin-walled stainless steel, total PHP mass is dominated by the evaporator and condenser plates. In laboratory designs, these plates are typically constructed from copper for its high thermal conductance and fabrication convenience; however, in a spacecraft cooling system, these plates may be integrated into other components or made from a lower density conductive

metal. For instance, the PHP evaporator tubes may be brazed directly to the exterior of an instrument being cooled, eliminating the need for a separate PHP evaporator plate entirely. If the evaporator or condenser plates must be physically separate from other components, thin plates of aluminum could be substituted for copper (although joining the stainless steel tubing to an aluminum rather than copper alloy adds complexity to the assembly process). The small volume and mass of PHPs makes them highly competitive relative to the bulky support structure required by a piezoelectric switch. Related to this, the extremely simple PHP construction compares well to a traditional diode heat pipe, the latter of which is constrained to larger tube cross section areas (and therefore higher OFF state parasitic conduction and smaller charge pressure limitations due to greater hoop stresses in the tube walls) in order to accommodate an internal wick structure.

Furthermore, PHPs have been shown to nominally function in microgravity[7] [48][49] and can be designed to accommodate a wide range of heat loads by scaling the count of parallel tubes connecting the evaporator and condenser plates. PHPs also offer flexibility in the placement of the cooling load relative to the system cooling radiator. As already mentioned, PHPs allow the cooling load to be physically distanced from the radiator since the adiabatic section lengths can be quite large [52]. The adiabatic section tubes can, in concept, also take shapes other than than straight tube runs typically seen in published laboratory PHP devices, which can be a powerful feature in intricate volume-constrained spacecraft designs. Such design flexibility is not possible with gas gap switches or the mechanical contact -based switches.

7 Although more microgravity characterization is likely required before their use in actual spacecraft instrumentation

Terrestrial systems requiring fast initial cool down periods (when the system is cooled from ambient temperature with a mechanical cryocooler) and physical compactness for temporary post-cool down portability (when parasitic loads are removed by a boiling cryogen) present a second application where PHP thermal switches may be highly competitive against other switch technologies. Many of the attributes of PHP thermal switches listed previously for the spacecraft applications are also valued here, especially their low mass, small total system volume, and high reliability due to lack of moving parts. Terrestrial applications likely require larger ON state heat transfer capacities through the switch compared with the spacecraft applications, however. PHPs can outperform all of the other switching categories in this aspect due to the extremely high conductance offered by the slug-plug advective flow in the ON state. This allows PHPs to scale to meet increased heat transfer capacity requirements with little spatial or mass penalty, which is simply not possible with the conduction-based switches (mechanical contact, gas gap, and magnetoresistive) which must scale in cross section area to transfer additional load.

1.6 Project objectives

The ultimate goal of this work is to prove that cryogenic PHPs can be used effectively as thermal switches in redundant cryocooler applications. Two experimental facilities are designed and fabricated in sequence to achieve this: a facility to test *nitrogen* PHP thermal switches (operating near 80 K) and a facility to test helium PHP thermal switches (operating near 4 K). Developing the nitrogen PHP thermal switch test facility prior to that for the helium PHPs allows the concept to be first tested in a facility without the additional engineering challenges added when working at liquid helium temperatures.

To prove that nitrogen and helium PHPs can function as thermal switches, specific objectives are set for the project:

- Design, fabricate, and assemble a proof-of-principle redundant cryocooler test facility with *nitrogen* PHP thermal switches
- Design, fabricate, and assemble a proof-of-principle redundant cryocooler test facility with *helium* PHP thermal switches
- Experimentally confirm that both nitrogen and helium PHP thermal switches offer high switching ratios and successfully allow redundant cryocooler operation, by
    - Measuring ON and OFF state heat flows, effective thermal conductivies, and switching ratios for both the nitrogen and helium PHP thermal switches over a range of fill ratios, condenser temperatures, and applied common cold plate heat loads
    - Modeling the nitrogen and helium PHP thermal switch ON and OFF state heat flows and effective thermal conductivity
    - Comparing the modeled ON and OFF state thermal switch heat flows and effective thermal conductivity to the experimental results.
    - Comparing the measured nitrogen and helium PHP thermal switch performance to existing thermal switch technologies.

The following sections address these project objectives in detail – Section 2 describes the nitrogen PHP thermal switch testing and facility construction, and Section 3 describes the helium PHP thermal switch testing and facility construction. Section 6 provides a comparison of the PHP performance testing results to the existing cryogenic thermal switch technologies reviewed earlier in this section.

2 Nitrogen PHP thermal switch performance characterization in a redundant cryocooler system

The first portion of this work involves the design, fabrication, and performance characterization of *nitrogen* PHP thermal switches (with switching temperatures near 77 K). This switching temperature is in a range useful for various types of existing space detectors [2][3][4], providing some direct motivation for testing a PHP thermal switch with nitrogen as the working fluid. Ultimately, however, the characterization of helium PHPs with switching temperatures near 4 K are a better test of the technology, as the lower switching temperature allows use in a wider range of possible applications [6][7]. A secondary motivation, then, for testing a nitrogen PHP thermal switch is to provide a (relatively) simple proof-of-concept demonstration for the cryogenic PHP thermal switch concept without the need to immediately address the additional engineering tasks associated with working with liquid helium.

2.1 Test facility overview

To properly examine the performance of nitrogen PHP thermal switches in a redundant cryocooler system, a specialized experimental facility is required. The facility developed for this task is shown via several isometric solid model assembly views in Figure 2.1, images of the actual assembly in Figure 2.2, and profiles views of the assembly in Figure 2.3 (solid model) and Figure 2.4 (image). Each figure is annotated with locations of important components.

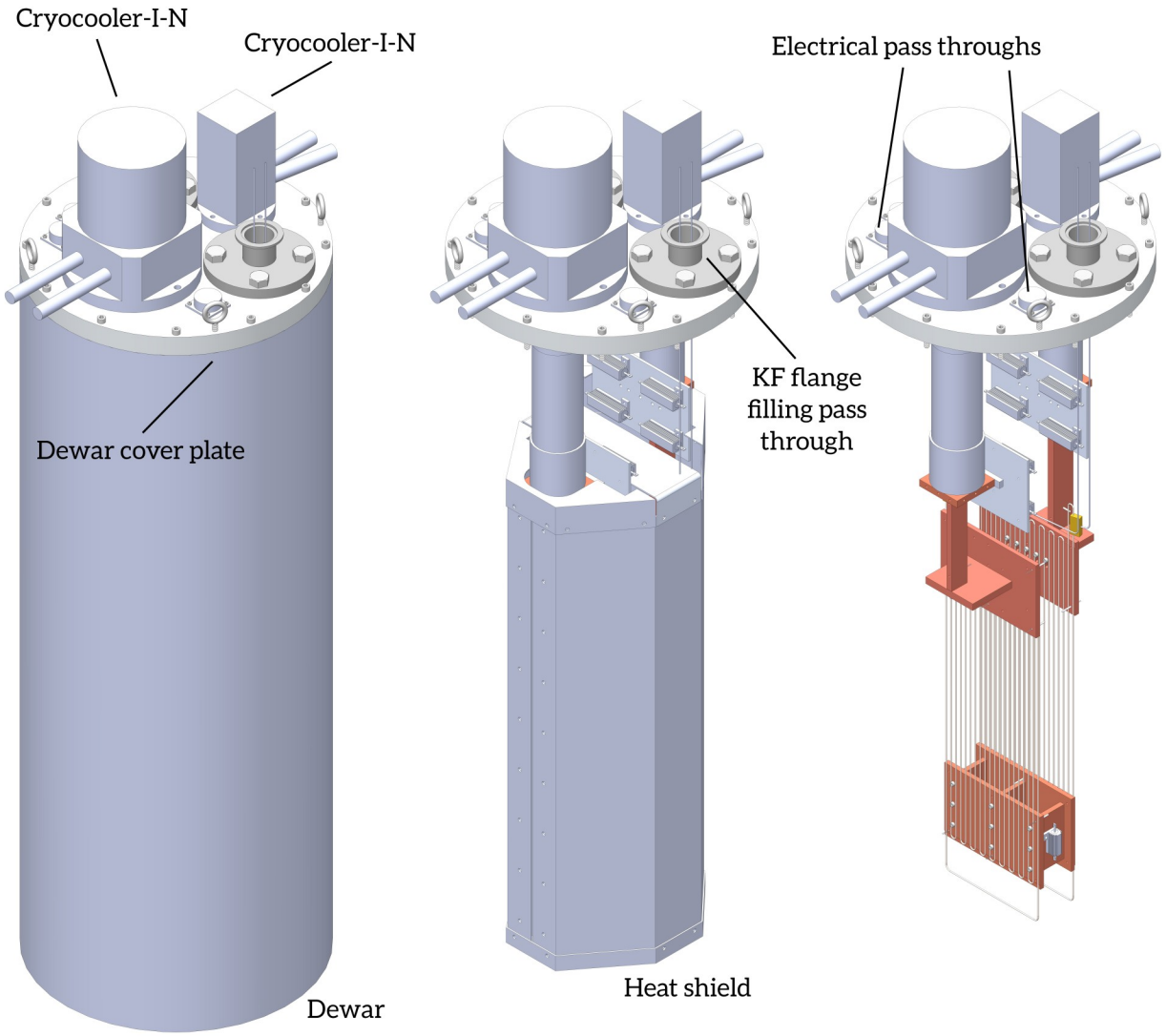

Figure 2.1. Solid model view of the nitrogen PHP thermal switch experiment facility with dewar visible (left), dewar hidden (middle), and both dewar and heat shield hidden (right).

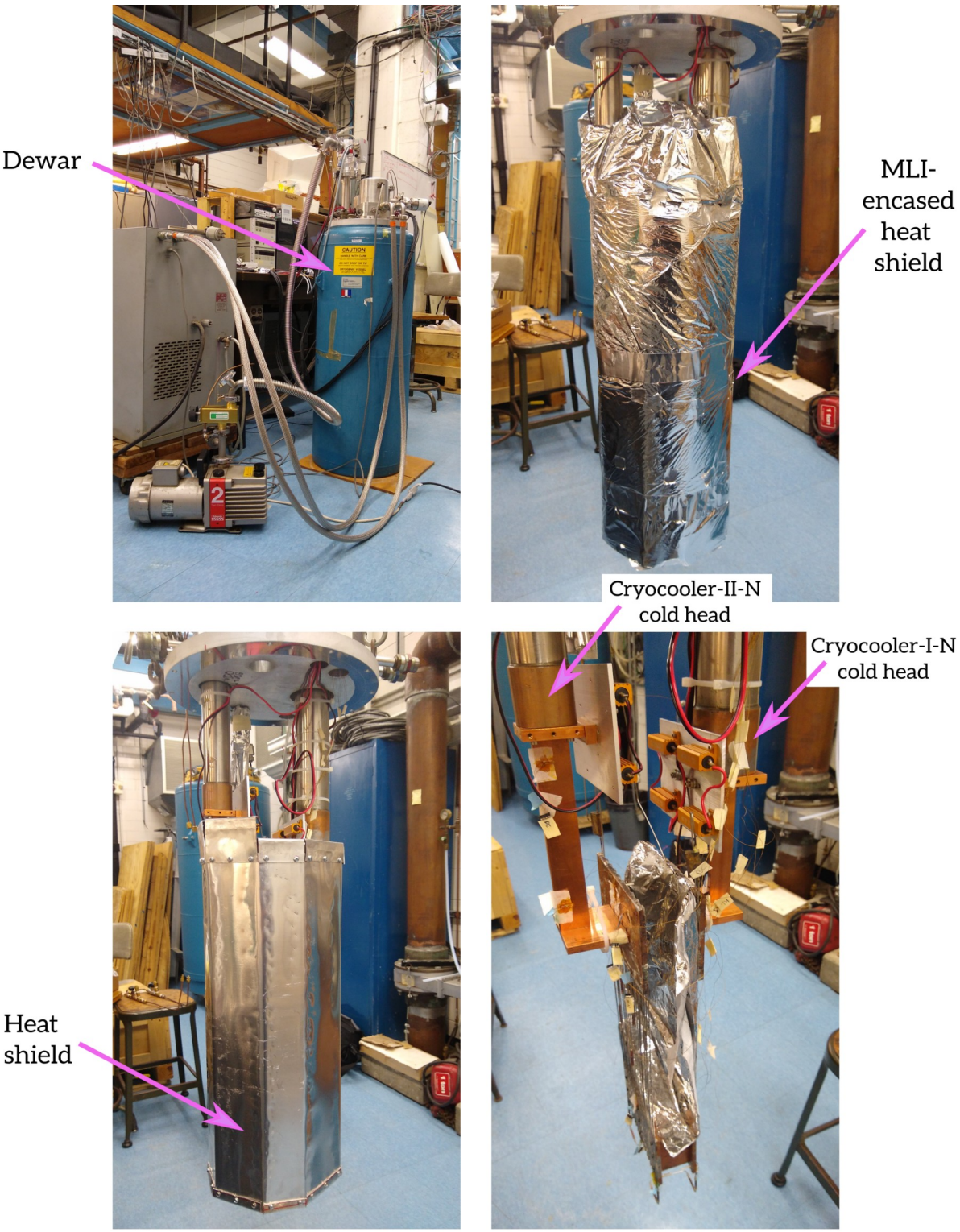

Figure 2.2. Images showing the nitrogen PHP thermal switch experiment facility – dewar exterior (upper left), MLI wrapped heat shield (upper right), heat shield without MLI (lower left), and heat shield removed (lower right).

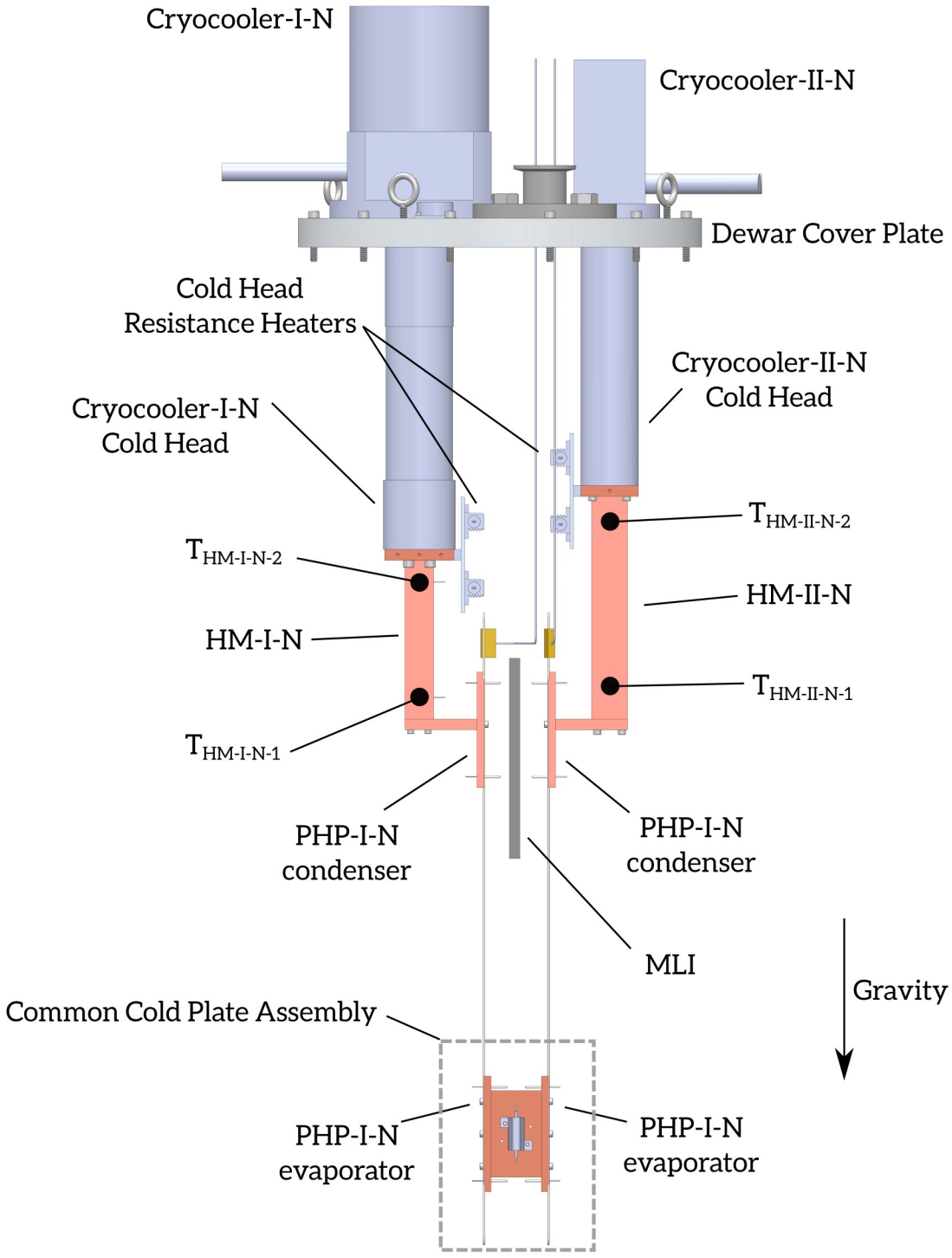

Figure 2.3. Solid model profile view of the nitrogen PHP switch experiment facility with the dewar and heat shield excluded. Temperature sensor locations indicated with black circles.

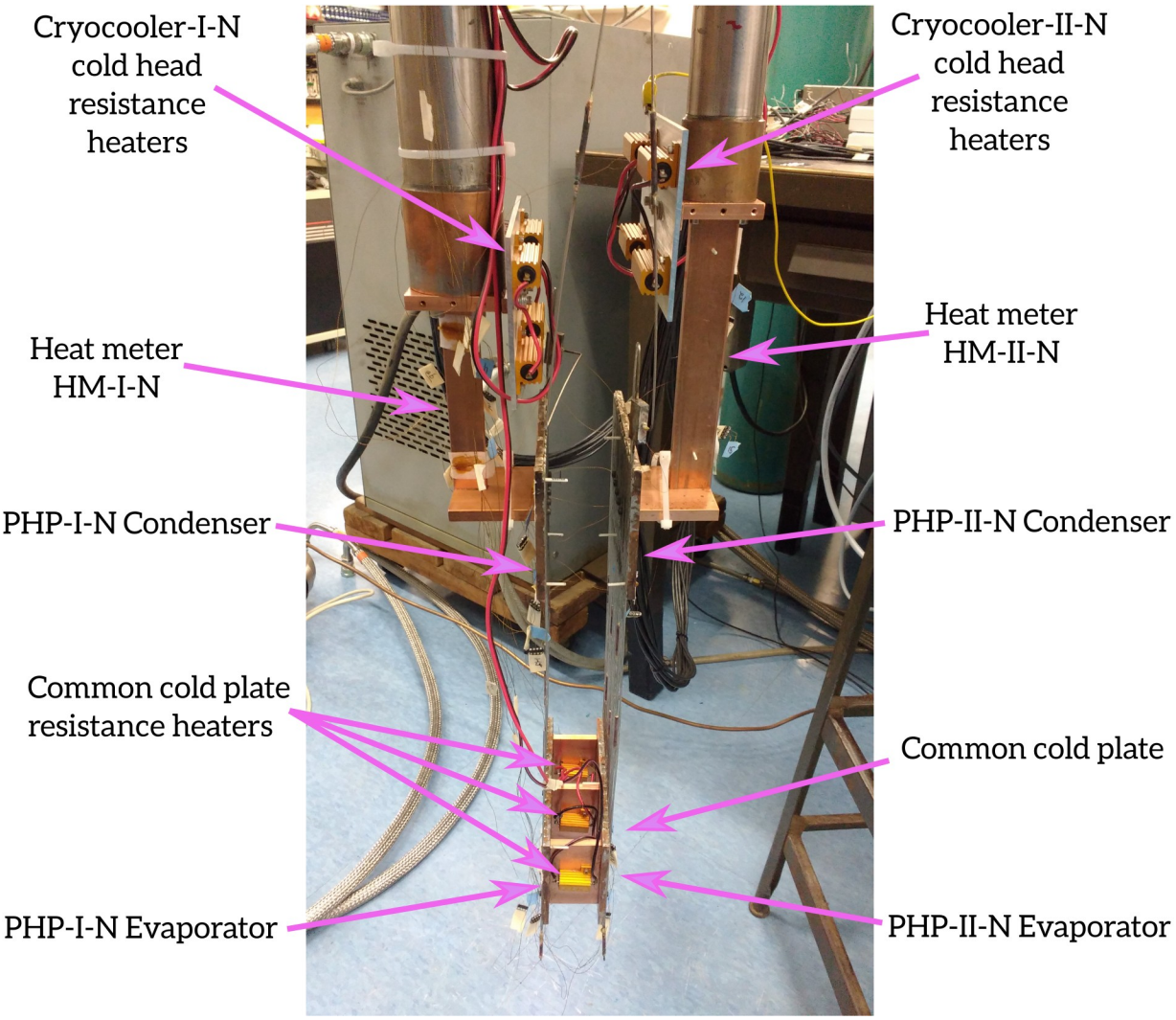

Figure 2.4. Profile view image of the nitrogen PHP thermal switch experiment facility with the dewar, heat shield, and MLI excluded excluded.

The setup features two redundant Gifford-McMahon cryocoolers – labeled Cryocooler-I-N[8] (a Cryomech AL125 rated for 120W at 80K) and Cryocooler-II-N (a Cryomech AL60 rated at 60W at 80K) – each mounted vertically (their displacer axes parallel to the gravity field) in a single dewar. The cryocoolers are secured to the dewar on a single custom designed 6061 aluminum dewar cover plate. Included on the cover plate are two KF-40 ASA flange adapters (Kurt J. Lesker

8 The 'N' suffix refers to the nitrogen PHP thermal switch test facility and is used with various symbols in this work

models QF40XASA5G) for the connection of the dewar vacuum pump hoses and nitrogen PHP filling lines, along with three electrical passthrough connectors (one Deteronics DT02H-16-8PN and two DT02H-20-41PN) for thermometer and heater leads. The external vacuum and PHP filling plumbing is described in the appendix Section 8.1. Facility dimensions are shown in Table 2.1.

Table 2.1. Nitrogen PHP thermal switch test facility dimensions

Dimension	**Value**
Dewar internal diameter	30 cm
Dewar internal height	120 cm

Two custom designed and fabricated PHPs[9] are installed in the facility – labeled PHP-I-N and PHP-II-N – and are associated with Cryocooler-I-N and Cryocooler-II-N, respectively. Each PHP condenser plate is structurally and thermally linked to its respective cryocooler cold head via custom designed conduction heat meters labeled HM-I-N and HM-II-N. The heat meters are rectangular copper bars of known length and cross sectional area with thermometers installed near each end of the bar[10]. A suite of four electrical resistance heaters (TE Connectivity model HSA50R75J) mounted to each cryocooler cold head, powered by LabVIEW PID controlled programmable direct current power supplies, allow active control of the PHP condenser temperatures. The two PHP evaporators are joined via a set of three copper connector plates, collectively comprising the common cold plate assembly, as shown in Figure 2.5 and Figure 2.6. Three electrical resistance heaters (TE Connectivity model HSA255R6J) are attached to this assembly and are driven with a direct current power supply to provide the common cold plate heat load to the

9 See section 2.2 for a full description of the PHP design

10 See section 2.3 for details of heat meter construction and calibration.

PHPs. Calibrated current shunts and potential dividers are used to measure the delivered electrical power.

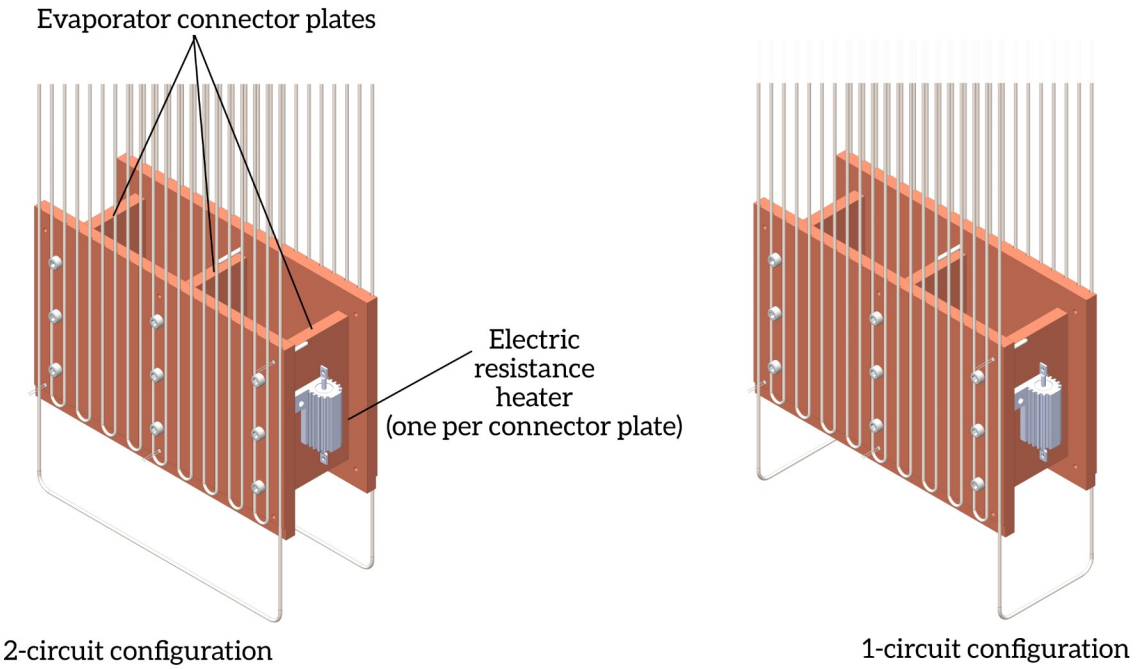

Figure 2.5. Solid model detail views of the nitrogen PHP thermal switch facility common cold plate assembly with the 2-circuit and 1-circuit configurations highlighted.

The PHPs, common cold plate assembly, and heat meters are surrounded by a 1.6mm thick 1100 aluminum heat shield maintained at all times at approximately 80 K. The heat shield is cooled directly by the Cryocooler-I-N cold head, bypassing entirely the Cryocooler-I-N heat meter. This design[11] requires Cryocooler-I-N to be operating at all times, as the shield must always be active to limit parasitic radiative loads from the warm internal surface of the dewar on the PHPs, common cold plate, and heat meters. A testing constraint is therefore imposed that only Cryocooler-

11 Such a direct-to-cold head heat shield connection is not practical for an actual redundant cryocooler application, as it is not known which crycocooler will fail in the field (and the shield must stay active after the failure). It is used here to simplify the proof-of-concept facility design. The shielding design in the helium PHP thermal switch test facility more closely mimics a practical design for an actual redundant crycooler system and is discussed fully in Section 3.1.

II-N can be used to simulate a cryocooler failure, as Cryocooler-I-N can not be deactivated without the shield warming to ambient temperature.

Multilayer insulation (MLI) fully encapsulates the active 70 K heat shield in an effort to reduce the radiation load which much be removed by Cryocooler-I-N. Additionally, sheets of MLI are placed between the PHP-I-N and PHP-II-N condenser plates, which experience a large radiation view factor (illustrated in Figure 2.3). This provides radiation insulation when a large temperature difference (approximately 210 K) develops between the PHP-I-N and PHP-II-N condenser plates after Cryocooler-II-N is deactivated.

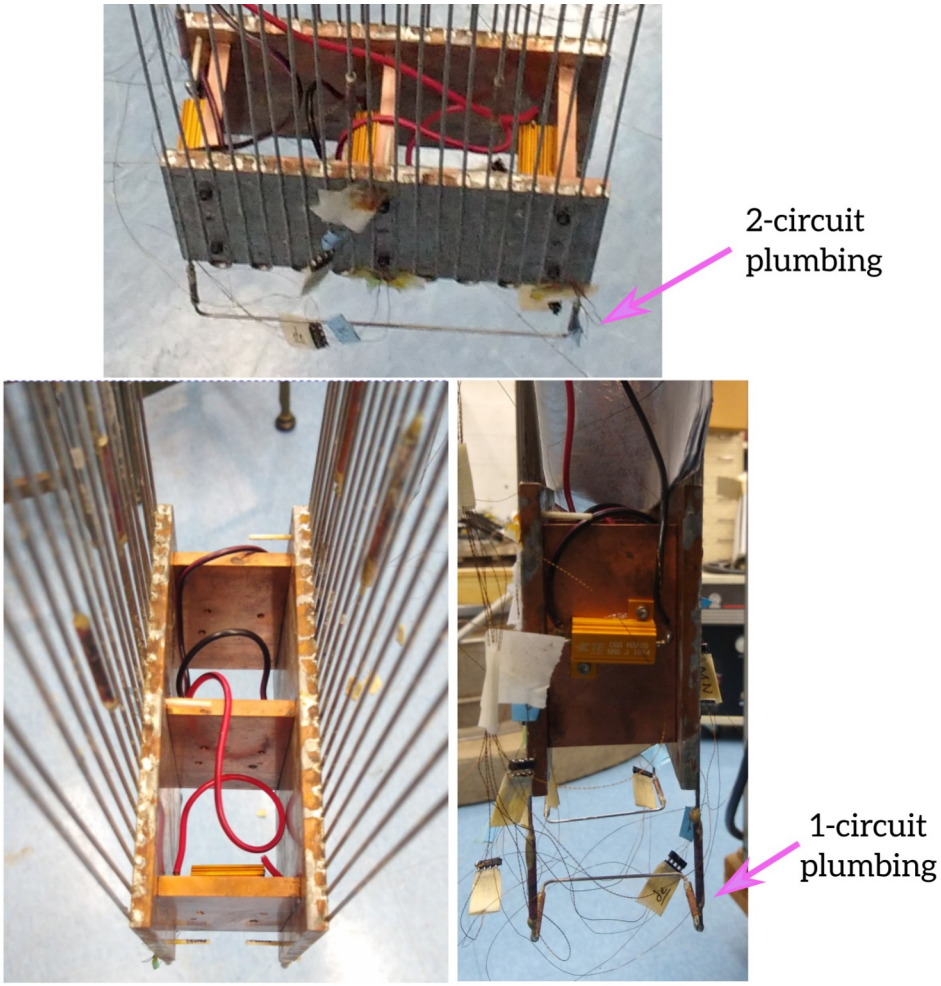

Figure 2.6. Photo of the nitrogen thermal switch test facility common cold plate assembly with 2-circuit plumbing (top and lower left) and 1-circuit plumbing (lower right).

2.2 Nitrogen PHP design and construction

The nitrogen PHP thermal switch experiment features two custom designed PHPs, labeled PHP-I-N and PHP-II-N, connected to Cryocooler-I-N and Cryocooler-II-N respectively. Images of these PHP assemblies are shown in Figure 2.7, solid model CAD assemblies are shown in Figure 2.8, and design details are listed in Table 2.2. The PHPs are identical – except for the routing of the filling tubes – with the number of parallel tubes crudely chosen by scaling the total maximum PHP heat transfer per internal cross sectional area reported by other nitrogen PHP studies [39]

[40][41]. This is intended to *roughly* allow about 10W of heat transfer capacity per PHP before dryout for the PHPs built in the present work. Each PHP evaporator and condenser plate is fabricated from 110 copper, while the tubing is assembled with 304 stainless steel (Microgroup model 304H17S). Both PHPs operate in bottom heated mode, as they are vertically oriented with the evaporators at lower gravitational potentials than the condensers. Note that the inner tube diameter is safely less than the critical diameter of about 2 mm required for slug-vapor flow calculated with Equation 1.9 and Figure 1.10, considering the saturated nitrogen working fluid.

Table 2.2. Nitrogen PHP design information. X in a symbol subscript can be I or II depending on the PHP name column.

PHP Name → / **Parameter ↓**	**PHP-I-N**	**PHP-II-N**
Associated cryocooler	Cryocooler-I-N	Cryocooler-II-N
Number of Parallel Tubes, $N_{PHP-X-N,TUBES}$	20	
Inner Tube Diameter, $d_{PHP-X-N,i}$ [mm]	1.08	
Outer Tube Diameter, $d_{PHP-X-N,o}$ [mm]	1.47	
Adiabatic Section Length, $L_{PHP-X-N,ADIA}$ [mm]	254.00	
Condenser Section Length, $L_{PHP-X-N,COND}$ [mm]	102.00	
Evaporator Section Length, $L_{PHP-X-N,EVAP}$ [mm]	102.00	
Tube Spacing (center axis), $L_{PHP-X-N,TS}$ [mm]	7.14	
Condenser Section Width, $W_{PHP-X-N,COND}$ [mm]	155.00	
Evaporator Section Width, $W_{PHP-X-N,EVAP}$ [mm]	155.00	
Condenser Section Thickness, $TH_{PHP-X-N,COND}$ [mm]	6.50	
Evaporator Section Thickness, $TH_{PHP-X-N,EVAP}$ [mm]	6.50	
PHP Volume, $V_{PHP-X-N}$ [mm^3]	8550	

The PHP tubing assemblies are custom bent and joined with a copper sleeve tube (shown only in Figure 2.7) and silver braze. A brass tee connector fits a filling line to each PHP fluid loop, also with silver braze. Zinc chloride flux (Harris Stay-Clean Liquid Flux) and soft solder join the stainless steel PHP tubing to the copper evaporator and condenser plates. Each nitrogen PHP

condenser and evaporator plate has three attached platinum resistance temperature sensors[12] (Lakeshore Cryotronics model PT-102) installed in through holes with thermal vacuum grease (Apiezon N Cryogenic High Vacuum) and secured with varnish (VGE-7031). Temperature sensor locations are shown in Figure 2.8.

Two PHP plumbing configurations are investigated with the nitrogen PHP thermal switch facility, each illustrated in Figure 2.9. In the 2-circuit configuration, the PHP-I-N and PHP-II-N fluid circuits are completely independent; the working fluid volumes are filled separately and completely isolated from each other. In the 1-circuit configuration, the PHP-I-N and PHP-II-N fluid circuits are combined in series, share a fluid volume, and are filled simultaneously.

12 See the Appendix, Section 8.4 for calibration details.

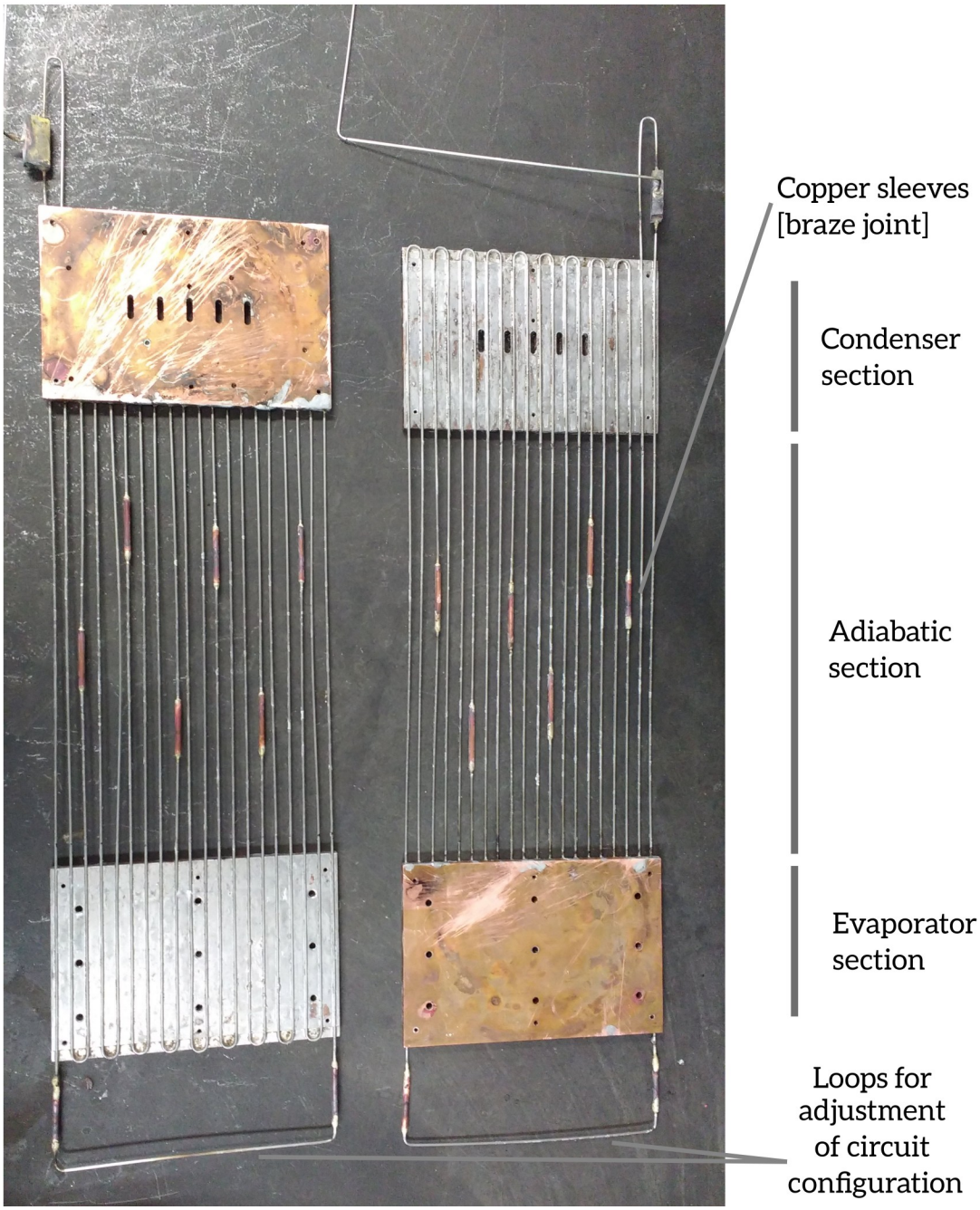

Figure 2.7. Image of the assembled PHP-I-N (right) and PHP-II-N (left).

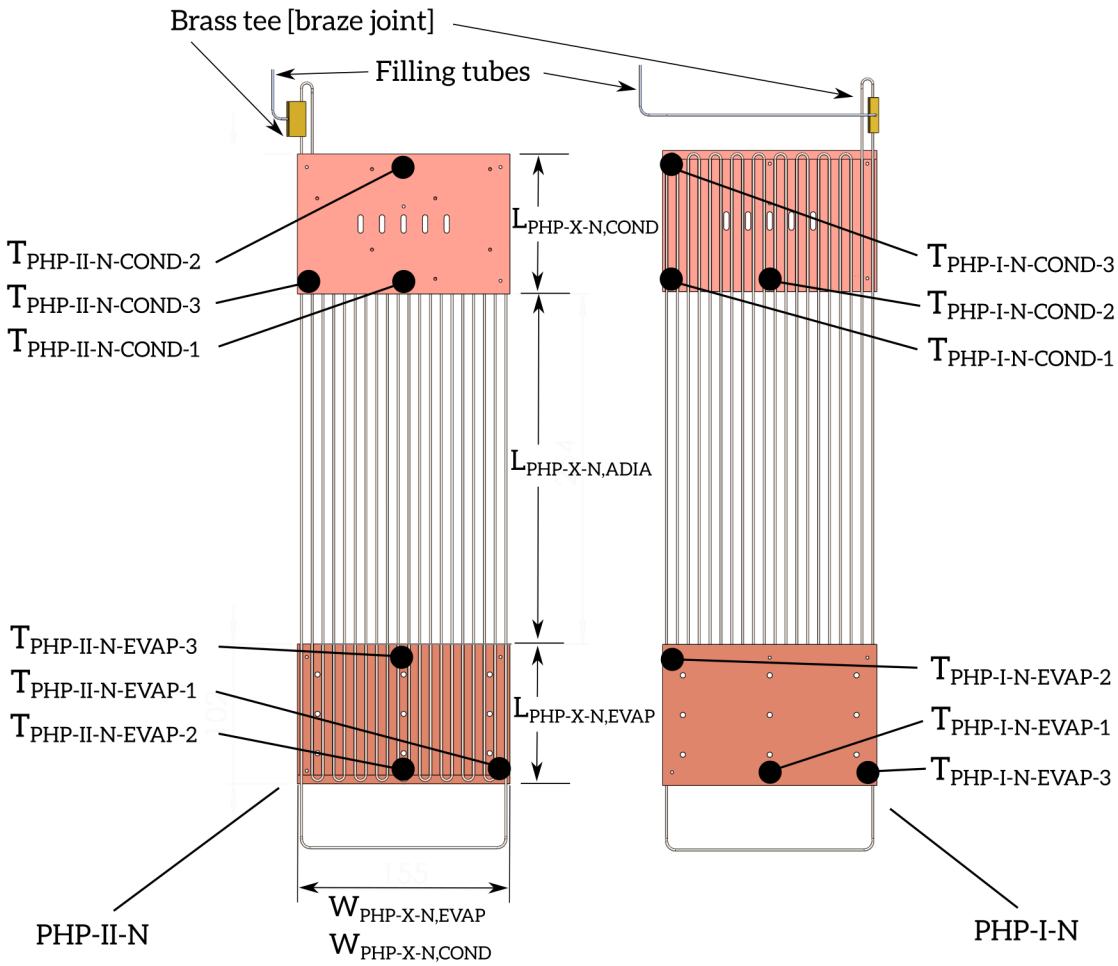

Figure 2.8. Solid model of the assembled PHP-I-N (right) and PHP-II-N (left). Shown in the 2-circuit configuration. Temperature sensor locations indicated by black circles.

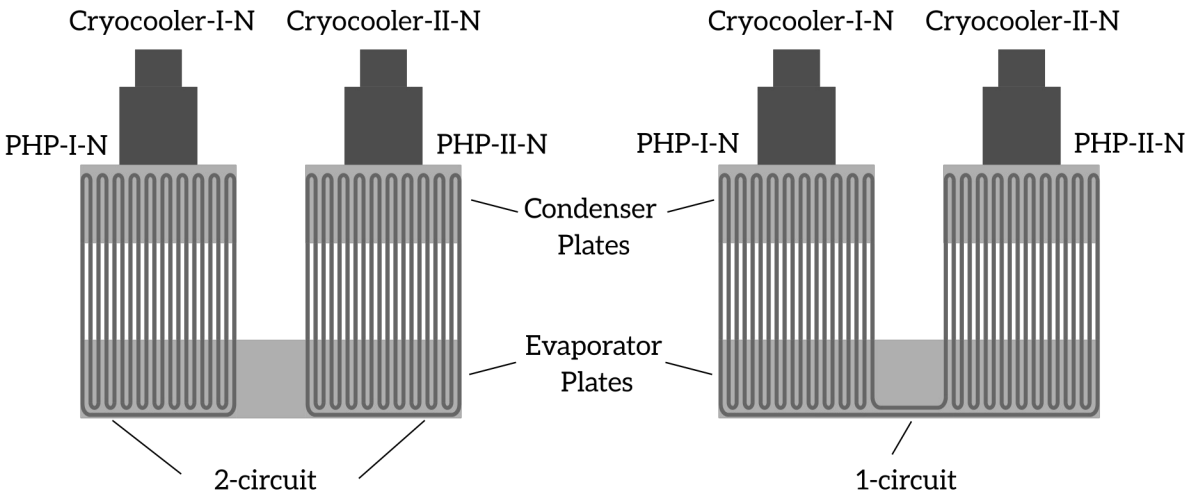

Figure 2.9. Schematic of the PHP-I-N and PHP-II-N in the 2-circuit configuration and 1-circuit configuration.

2.3 Heat meter design, fabrication, and calibration

Independent measurement of the heat loads through PHP-I-N and PHP-II-N is accomplished with the associated heat meters, PHP-I-N and PHP-II-N. These instruments are rectangular 110 copper bars of known length and cross sectional area, with platinum resistance temperature sensors (Lakeshore Cryotronics model PT-102[13]) installed in through holes near each end of the bar with thermal vacuum grease (Apiezon N Cryogenic High Vacuum) and varnish (VGE-7031). Machine screws and thermal vacuum grease are used for the thermal-mechanical connection at both ends of the heat meters to minimize contact resistance. Figure 2.10 shows a solid model profile view and image of the actual heat meter assemblies, while Table 2.3 lists heat meter design details.

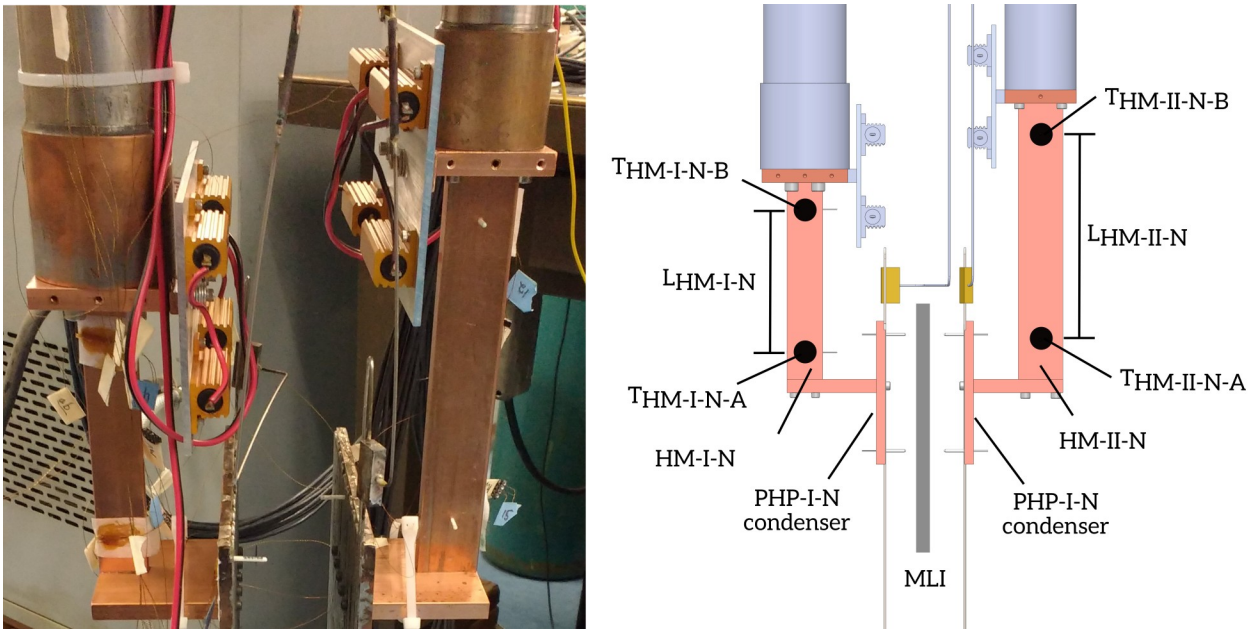

Figure 2.10. Image (left) and solid model (right) of the nitrogen PHP switch test facility's heat meter assemblies. HM-I-N and HM-II-N measure the heat loads through PHP-I-N and PHP-II-N, respectively. Platinum resistance temperature sensor locations indicated on solid model.

13 See the Appendix, Section 8.4 for calibration details.

The heat meters for the nitrogen thermal switch test facility are designed to balance competing requirements regarding the temperature gradient over the meter: a large temperature gradient is required to attain accurate heat transfer measurements in consideration of the temperature sensor uncertainty (±0.25 K), yet the gradient must be limited because the cryocooler capacity declines with decreasing cold head temperatures. Too large of temperature gradient over the heat meter will reduce $T_{HM-I-N,B}$ or $T_{HM-II-N,B}$ in Figure 2.10 such that the corresponding cryocooler capacity is reduced far enough that it can no longer remove the heat transferred through the connected PHP. Figure 2.11 shows expected temperature gradients and relative uncertainty in the heat load measurement as a function of the heat load for a copper heat meter with different possible cross section area-to-length (A/L) ratios and the uncertainty of the PT-102 temperature sensors. Based on the cryocooler capacity maps and the estimated nitrogen PHP heat transfer capacity, the heat meters are budgeted a maximum 10 K temperature gradient between the temperature sensors with an applied load of 10 W. An A/L = 0.002 [m] is chosen to accommodate this, although the uncertainty (in relative terms) of the heat transfer measurement suffers below about 2 W.

Table 2.3. Nitrogen PHP thermal switch test facility heat meter design information. X in a symbol subscript can be I or II depending on the column.

Heat Meter Name → / **Parameter ↓**	**HM-I-N**	**HM-II-N**
Associated Cryocooler Name	Cryocooler-I-N	Cryocooler-II-N
Material	110 Copper	
Length between temperature sensors, L_{HM-X-N} [m]	0.101600	0.144653
Area cross section, A_{HM-X-N} [m^2]	0.000202	0.000303
Area to length ratio, $\frac{A_{HM-X-N}}{L_{HM-X-N}}$ [m]	0.001984	0.002090
Calibration Regime	60K–90K	60K–90K 285K–300K

The heat meter conductance, which is strongly temperature dependent and weakly impurity dependent[14] at the temperatures of interest for the nitrogen PHP thermal switch experiments, is calibrated for each meter in the range of temperatures where measurements are necessary. HM-I-N requires calibration from approximately 60 K to 90 K (as Cryocooler-I-N is always active), while HM-II-N requires calibration from approximately 60 K to 90 K and approximately 285 K to 300 K (as Cryocooler-II-N can either be active or inactive). This dual range calibration allows HM-II-N to measure the PHP-II-N heat load with the thermal switch in either the ON or OFF state.

The heat meter calibration setup varies slightly from the facility setup described in Section 2.1, with the PHPs physically removed from the facility and the suite of cold head resistance heaters moved to the former location of the PHP condensers (the cold head resistance heaters and PHP condensers are shown in their typical positions in Figure 2.10). In this arrangement, the resistance heaters can supply a known, well characterized heat load to the heat meters for calibration. In both calibration regimes, a series of measurements are obtained with sweeps of both the supplied electric heat load and the heat meter temperature furthest from the cryocoolers ($T_{HM-I-N,A}$ and $T_{HM-II-N,A}$). Table 2.4 indicates the range of sampled heat loads and temperature ranges for each heat meter and calibration regime. A linear fit of the sample data is performed to obtain the mean heat meter thermal conductivity[15] associated with the mean heat meter

14 The compositional impurities of the copper stock used for the meters is neither manufacturer certified nor accurately known prior to calibration.

15 Actually, the conductance is fit and the conductivity is obtained by $k_{HM-X-N} = \frac{L_{HM-X-N}}{A_{HM-X-N}} UA_{HM-X-N}$.

temperature and heat load offset for each calibration regime. These values are tabulated in Table 2.4 for each heat meter.

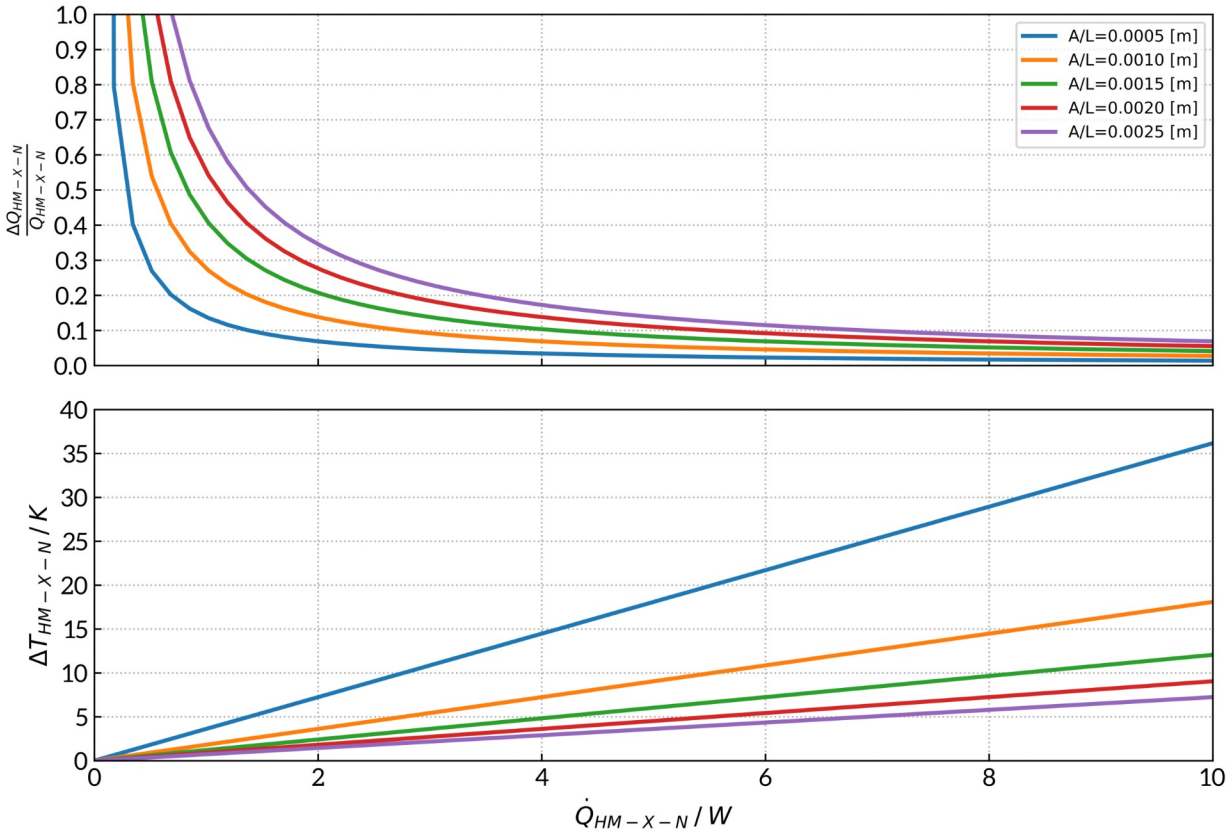

Figure 2.11. Modeled nitrogen PHP thermal switch heat meter relative accuracy (top) and temperature drop (bottom) as a function of heat load for different area-to-length ratios. Assumes constant thermal conductivity of RRR100 copper at 77.0 K. Uncertainties reflect manufacturer long-term repeatability for the PT102 platinum resistance sensors sensors (+- 0.25 K).

Table 2.4. Nitrogen PHP thermal switch test facility heat meter calibration details. X in a symbol subscript can be I or II depending on the column.

Heat meter name→	HM-I-N	HM-II -N	
Parameter ↓ Calibration regime→	60K–90K	60K–90K	285K–300K
Number of calibration samples in data set	19	17	4
Range of supplied electric heat loads [W]	0.00 to 12.24	0.00 to 11.96	0.00 to 9.20
Range of temperatures in $T_{HM-X-N,A}$ and $T_{HM-X-N,B}$ from all calibration data, $T_{HM-X-N,MIN}$ to $T_{HM-X-N,MAX}$ [K]	67.10 to 80.32	67.56 to 79.20	288.48 to 295.85
Mean temperature in $T_{HM-X-N,A}$ and $T_{HM-X-N,B}$ from all calibration data, $T_{HM-X-N,MEAN}$, [K]	73.48	73.26	291.42
Thermal conductivity at mean heat meter temperature, $k_{HM-X-N,MEAN}$ [W/m-K]	604.47	570.67	506.49
Heat Load Offset, $\dot{Q}_{OFFSET,HM-X-N}$ [W]	0.09	-0.04	4.00
Effective copper RRR, RRR_{HM-X-N} [16]	105.30	65.40	

For the 60 K – 90 K regime, the heat meter calibrations are determined by first interpolating[17] the residual resistance ratios (RRRs) of the copper bars at the mean heat meter temperature and mean conductivity reported in Table 2.4. The temperature dependent conductivity property data [37][38] for the interpolated RRR of each heat meter is then used in a numerical solution to the conduction problem to determine the heat load input (the applied heat load during calibration, or the PHP heat load during actual operation) as a function of the end temperature measurements

$$\dot{Q}_{PHP-I-N} = -\int_{T_{HM-I-N,A}}^{T_{HM-I-N,B}} k_{HM-I-N}(T)\frac{A_{HM-I-N}}{L_{HM-I-N}}dT + \dot{Q}_{OFFSET,HM-I-N} \tag{2.1}$$

16 HM-I-N and HM-II-N have somewhat different estimated RRR values, which at first glance is concerning since the stock material is from the same supplier. This is explained by unaccounted bias in the temperature measurements, error in the position of the temperature sensors, error in the cross sectional area measurement, and conductivity being only weakly dependent on RRR at the mean calibration temperature.

17 See the Appendix, Section 8.5, for details.

$$\dot{Q}_{PHP-II-N} = -\int_{T_{HM-II-N,A}}^{T_{HM-II-N,B}} k_{HM-II-N}(T)\frac{A_{HM-II-N}}{L_{HM-II-N}}dT + \dot{Q}_{OFFSET,HM-II-N} \quad (2.2)$$

. The offsets in these calibrations are fairly small and likely arise from bias voltages in the temperature measurements caused by electrical noise emanating from facility equipment (the cryocoolers, turbo pump, rotary vane pump, and resistance heater power supplies) which is not accounted for in the temperature sensor calibrations.

For the 285K – 300K regime, the thermal conductivity is assumed constant at the measured value as it is a very weak function of temperature and the measurement temperature range is small

$$\dot{Q}_{PHP-II-N} = -k_{HM-II-N,MEAN}\int_{T_{HM-II-N,A}}^{T_{HM-II-N,B}} \frac{A_{HM-II-N}}{L_{HM-II-N}}dT + \dot{Q}_{OFFSET,HM-II-N} \quad (2.3)$$

. The heat load offset in this regime is substantial compared to that in the 60 K – 90 K regime and is not simply due to bias voltages in the temperature sensor signals. Here Cryocooler-I-N remains active as Cryocooler-II-N is inactive, hence the radiation shield and HM-I-N remain at approximately 80 K. The offset heat load therefore stems from the effect of radiation cooling the lower portion of HM-II-N (which is at about 290 K) via the view to the radiation shield (at about 80 K).

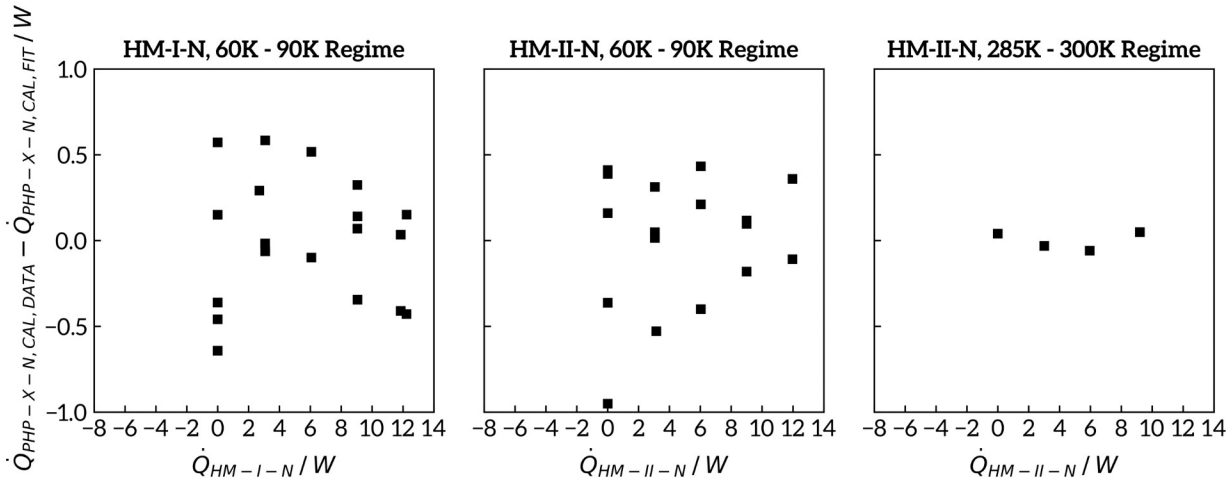

Figure 2.12. Difference between measured calibration heat load and the calibration fit predicted heat load as a function of the nominal measured calibration heat load for the heat meters in the nitrogen PHP thermal switch test facility. Multiple data points at a single measured heat load correspond to different heat meter end temperatures $T_{HM\text{-}X\text{-}N\text{-}A}$. HM-I-N calibrated in the 60 K – 90 K regime and HM-II-N calibrated in the 60 K – 90 K and 285 K – 300 K regimes.

Errors between the calibration measurements and the fit functions for $\dot{Q}_{PHP-I-N}=f(T_{HM-I-N-A}, T_{HM-I-N-B})$ and $\dot{Q}_{PHP-II-N}=f(T_{HM-II-N-A}, T_{HM-II-N-B})$ are shown in Figure 2.12 as a function of the nominal measured calibration heat load. For the 60 K to 90 K regimes of both HM-I-N and HM-II-N, resolution is about ±0.5 W. The 285 K to 300 K regime for HM-II-N has a somewhat better resolution of about ±0.1 W, but there are fewer samples in the calibration data set.

2.4 Measurements and performance characteristics

The nitrogen PHP thermal switch test facility's raison d'etre is to test the performance of its nitrogen PHPs as thermal switches. To do so, the facility must perform measurements of several key quantities related to PHP operation. Table 2.5 lists and describes these quantities and the relevant measurement equipment.

Table 2.5. Measurements provided by the nitrogen PHP thermal switch test facility

Quantity	Measurement Devices(s)	Comments
$T_{HM-I-N-A}$	Lakeshore Cryotronics PT-102 sensor	See Figure 2.10 for locations See Appendix 8.4 for calibration details
$T_{HM-I-N-B}$	Lakeshore Cryotronics PT-102 sensor	
$T_{HM-II-N-A}$	Lakeshore Cryotronics PT-102 sensor	
$T_{HM-II-N-B}$	Lakeshore Cryotronics PT-102 sensor	
$T_{PHP-I-N,COND}$	• Lakeshore Cryotronics PT-102 sensor, $T_{PHP-I-N,COND-1}$ • Lakeshore Cryotronics PT-102 sensor, $T_{PHP-I-N,COND-2}$ • Lakeshore Cryotronics PT-102 sensor, $T_{PHP-I-N,COND-3}$	See Figure 2.8 for locations See Appendix 8.4 for calibration details
$T_{PHP-II-N,COND}$	• Lakeshore Cryotronics PT-102 sensor $T_{PHP-II-N,COND-1}$ • Lakeshore Cryotronics PT-102 sensor, $T_{PHP-II-N,COND-2}$ • Lakeshore Cryotronics PT-102 sensor, $T_{PHP-II-N,COND-3}$	
$T_{PHP-I-N,EVAP}$	• Lakeshore Cryotronics PT-102 sensor $T_{PHP-I-N,EVAP-1}$ • Lakeshore Cryotronics PT-102 sensor, $T_{PHP-I-N,EVAP-2}$ • Lakeshore Cryotronics PT-102 sensor, $T_{PHP-I-N,EVAP-3}$	
$T_{PHP-II-N,EVAP}$	• Lakeshore Cryotronics PT-102 sensor, $T_{PHP-II-N,EVAP-1}$ • Lakeshore Cryotronics PT-102 sensor, $T_{PHP-II-N,EVAP-2}$ • Lakeshore Cryotronics PT-102 sensor, $T_{PHP-II-N,EVAP-3}$	
$\dot{Q}_{CCP-N}$	Not applicable – calculated quantity	See Equation 2.4
$\dot{Q}_{PHP-I-N}$		See Equation 2.1 [+] indicates heat flow from common cold plate to the Cryocooler-I-N cold head.
$\dot{Q}_{PHP-II-N}$		See Equations 2.2 and 2.3 [+] indicates heat flow from common cold plate to the Cryocooler-II-N cold head [-] indicates heat flow direction from Cryocooler-II-N cold head to common cold plate (parasitic)
$k_{PHP-I-N,EFF}$		See Equation 2.7
$k_{PHP-II-N,EFF}$		See Equation 2.8
$UA_{PHP-I-N,EFF}$		See Equation 2.9
$UA_{PHP-II-N,EFF}$		See Equation 2.10
$SR_{PHP-II-N}$		See Equation 2.15
$FR_{PHP-I-N}$		See Equation 1.14 with $T_{SAT}=77.36K$ and Appendix 8.3
$FR_{PHP-II-N}$		

Quantities in Table 2.5 are which indirectly measured require some additional description beyond the listed information. These include the electric heat power applied to the CCP

$$\dot{Q}_{CCP-N} = V_{CCP-N} I_{CCP-N} \tag{2.4}$$

, defined in terms of the electric potential and direct current applied to the heaters

$$I_{CCP-N} = \frac{V_{CCP-N,I}}{R_{CCP-N,C}} \tag{2.5}$$

$$V_{CCP-N} = V_{CCP-N,V} \frac{R_{CCP-N,A} + R_{CCP-N,B}}{R_{CCP-N,B}} \tag{2.6}$$

, which are measured by the current shut and voltage divider setup shown in Figure 2.13. Here $V_{CCP-N,I}$ and $V_{CCP-N,V}$ are measured and resistance values in the circuits are $R_{CCP-N,A} = 120616\Omega$, $R_{CCP-N,B} = 997.430\Omega$, and $R_{CCP-N,C} = 0.0250\Omega$.

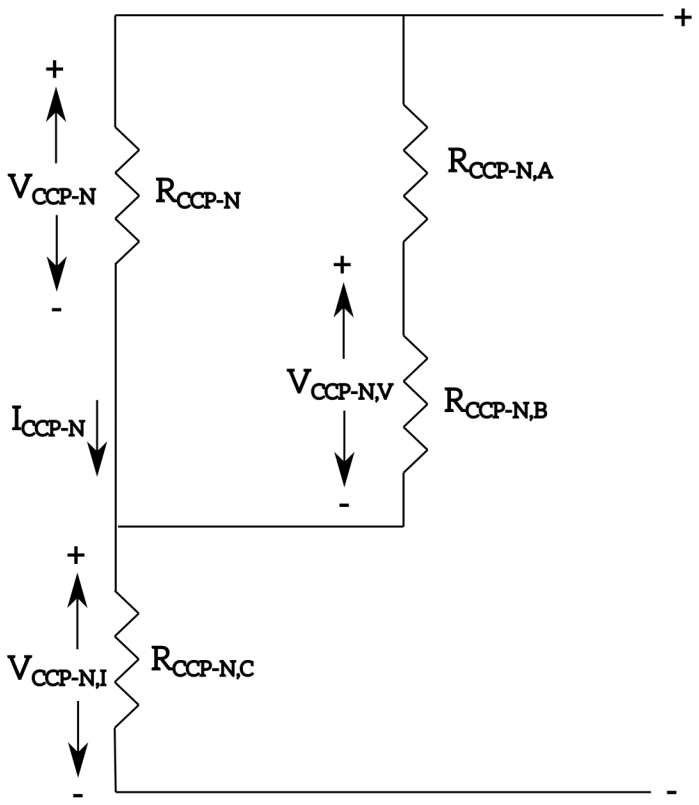

Figure 2.13. Direct current potential divider and current shunt for measurement of the common cold plate heat load.

The effective thermal conductivity for each of the nitrogen PHPs are defined as

$$k_{PHP-I-N,EFF} = \frac{|\dot{Q}_{PHP-I-N}|}{|T_{PHP-I-N,COND} - T_{PHP-I-N,EVAP}|} \frac{L_{PHP-I-N,ADIA}}{N_{PHP-I-N,TUBES}\pi\left(\frac{d_{PHP-I-N,o}}{2}\right)^2} \tag{2.7}$$

$$k_{PHP-II-N,EFF} = \frac{|\dot{Q}_{PHP-II-N}|}{|T_{PHP-II-N,COND} - T_{PHP-II-N,EVAP}|} \frac{L_{PHP-II-N,ADIA}}{N_{PHP-I-N,TUBES}\pi\left(\frac{d_{PHP-II-N,o}}{2}\right)^2} \tag{2.8}$$

, the associated conductances are

$$UA_{PHP-I-N,EFF} = \frac{|\dot{Q}_{PHP-I-N}|}{|T_{PHP-I-N,COND} - T_{PHP-I-N,EVAP}|} \tag{2.9}$$

$$UA_{PHP-II-N,EFF} = \frac{|\dot{Q}_{PHP-II-N}|}{|T_{PHP-II-N,COND} - T_{PHP-II-N,EVAP}|} \tag{2.10}$$

, and the temperatures of the evaporator and condenser plates are taken as the average values from the local temperature sensors

$$T_{PHP-I-N,COND} = \frac{T_{PHP-I-N,COND-1} + T_{PHP-I-N,COND-2} + T_{PHP-I-N,COND-3}}{3} \tag{2.11}$$

$$T_{PHP-I-N,EVAP} = \frac{T_{PHP-I-N,EVAP-1} + T_{PHP-I-N,EVAP-2} + T_{PHP-I-N,EVAP-3}}{3} \tag{2.12}$$

$$T_{PHP-II-N,COND} = \frac{T_{PHP-II-N,COND-1} + T_{PHP-II-N,COND-2} + T_{PHP-II-N,COND-3}}{3} \tag{2.13}$$

$$T_{PHP-II-N,EVAP} = \frac{T_{PHP-II-N,EVAP-1} + T_{PHP-II-N,EVAP-2} + T_{PHP-II-N,EVAP-3}}{3} \tag{2.14}$$

. These simply apply the nitrogen PHP geometry and temperature measurements to the effective thermal conductivity and effective conductance for general PHPs defined in Equation 1.4 and Equation 1.5. Note that, while the PHP heat flow measurements $\dot{Q}_{PHP-I-N}$ and $\dot{Q}_{PHP-II-N}$ have signs indicating the heat flow direction, the effective thermal conductivity and effective conductances are defined as positive quantities no matter the direction of heat transfer. The ultimate performance measure for a thermal switch is the switching ratio, defined for a general switch by Equation 1.3, and for PHP-II-N as

$$SR_{PHP-II-N} = \frac{UA_{PHP-II-N,EFF,ON}}{UA_{PHP-II-N,EFF,OFF}} \tag{2.15}$$

. A switching ratio for PHP-I-N is not measured because, as previously discussed, Cryocooler-I-N is always operating to cool the facility radiation shielding. Due to this limitation of the facility, the PHP-I-N OFF state cannot be accessed during testing and therefore the PHP-I-N switching ratio cannot be measured. Note that, in general, both the numerator and denominator of Equation

2.15 can vary with the PHP condenser and evaporator temperatures, heat load, and fill ratio. However, since the OFF state condenser and evaporator temperature difference of PHP-II-N is very large relative to that in the ON state, $UA_{PHP-II-N,EFF,OFF}$ is several orders of magnitude smaller than $UA_{PHP-II-N,EFF,ON}$ and remains relatively constant with changes in $\dot{Q}_{CCP-N}$. Therefore, in the calculation of the switching ratio via Equation 2.15, $UA_{PHP-II-N,EFF,OFF}$ is considered a constant which is calculated as the mean of all experiment measurements over all evaporator loads, fill ratios, and PHP plumbing configurations.

A worst case uncertainty analysis, presented in Table 2.6, is applied to all calculated quantities relating to the nitrogen PHP thermal switch performance. This approach accounts for possible bias in the measurement variables that would not contribute to the error in a sum of squares method and results in asymmetric uncertainty bands. Superscripts (+) and (-) denote the upper and lower uncertainty limits. Uncertainties due to digital-to-analog conversion in the data acquisition hardware are negligible relative to the measured variable uncertainty and are therefore not treated here. Table 2.7 lists uncertainties for measured variables.

Table 2.6. Uncertainty definitions for calculated quantities in the nitrogen PHP thermal switch test facility. 'max' and 'min' uncertainties refer to the maximum or minimum function value obtained from the four possible combinations of input temperatures

Quantity	Upper(+) and lower(-) uncertainty limits
I_{CCP-N}	$I^{+}_{CCP-N} = \frac{V_{CCP-N,I}}{R_{CCP-N,C} - \Delta R_{CCP-N,C}}$
	$I^{-}_{CCP-N} = \frac{V_{CCP-N,I}}{R_{CCP-N,C} + \Delta R_{CCP-N,C}}$
V_{CCP-N}	$V^{+}_{CCP-N} = V_{CCP-N,V} \frac{R_{CCP-N,A} + \Delta R_{CCP,A} + R_{CCP-N,B} + \Delta R_{CCP,B}}{R_{CCP-N,B} - \Delta R_{CCP,B}}$
	$V^{-}_{CCP-N} = V_{CCP-N,V} \frac{R_{CCP-N,A} - \Delta R_{CCP,A} + R_{CCP-N,B} - \Delta R_{CCP,B}}{R_{CCP-N,B} + \Delta R_{CCP,B}}$
$\dot{Q}_{CCP-N}$	$\dot{Q}^{+}_{CCP-N} = V^{+}_{CCP-N} I^{+}_{CCP-N}$
	$\dot{Q}^{-}_{CCP-N} = V^{-}_{CCP-N} I^{-}_{CCP-N}$
$\dot{Q}_{PHP-I-N}$	$\dot{Q}^{+}_{PHP-I-N} = \max\left[f\left(T_{HM-I-N,A} \pm \Delta T_N, T_{HM-I-N,B} \pm \Delta T_N\right) - f\left(T_{HM-I-N,A}, T_{HM-I-N,B}\right)\right]$
	$\dot{Q}^{-}_{PHP-I-N} = \min\left[f\left(T_{HM-I-N,A} \pm \Delta T_N, T_{HM-I-N,B} \pm \Delta T_N\right) - f\left(T_{HM-I-N,A}, T_{HM-I-N,B}\right)\right]$
$\dot{Q}_{PHP-II-N}$	$\dot{Q}^{+}_{PHP-II-N} = \max\left[f\left(T_{HM-II-N,A} \pm \Delta T_N, T_{HM-II-N,B} \pm \Delta T_N\right) - f\left(T_{HM-II-N,A}, T_{HM-II-N,B}\right)\right]$
	$\dot{Q}^{-}_{PHP-II-N} = \min\left[f\left(T_{HM-II-N,A} \pm \Delta T_N, T_{HM-II-N,B} \pm \Delta T_N\right) - f\left(T_{HM-II-N,A}, T_{HM-II-N,B}\right)\right]$
$k_{PHP-I-N,EFF}$	$k^{+}_{PHP-I-N,EFF} = \frac{\lvert\dot{Q}^{+}_{PHP-I-N}\rvert}{\lvert(T_{PHP-I-N,COND} - \Delta T_N) - (T_{PHP-I-N,EVAP} + \Delta T_N)\rvert} \frac{(L_{PHP-I-N,ADIA} + \Delta L_{ADIA-N})}{N_{PHP-I-N,TUBES}\,\pi\left(\frac{(d_{PHP-I-N,o} - \Delta d_{o-N})}{2}\right)^2}$
	$k^{-}_{PHP-I-N,EFF} = \frac{\lvert\dot{Q}^{-}_{PHP-I-N}\rvert}{\lvert(T_{PHP-I-N,COND} + \Delta T_N) - (T_{PHP-I-N,EVAP} - \Delta T_N)\rvert} \frac{(L_{PHP-I-N,ADIA} - \Delta L_{ADIA-N})}{N_{PHP-I-N,TUBES}\,\pi\left(\frac{(d_{PHP-I-N,o} + \Delta d_{o-N})}{2}\right)^2}$
$k_{PHP-II-N,EFF}$	$k^{+}_{PHP-II-N,EFF} = \frac{\lvert\dot{Q}^{+}_{PHP-II-N}\rvert}{\lvert(T_{PHP-II-N,COND} - \Delta T_N) - (T_{PHP-II-N,EVAP} + \Delta T_N)\rvert} \frac{(L_{PHP-II-N,ADIA} + \Delta L_{ADIA-N})}{N_{PHP-II-N,TUBES}\,\pi\left(\frac{(d_{PHP-II-N,o} - \Delta d_{o-N})}{2}\right)^2}$
	$k^{-}_{PHP-II-N,EFF} = \frac{\lvert\dot{Q}^{-}_{PHP-II-N}\rvert}{\lvert(T_{PHP-II-N,COND} + \Delta T_N) - (T_{PHP-II-N,EVAP} - \Delta T_N)\rvert} \frac{(L_{PHP-II-N,ADIA} - \Delta L_{ADIA-N})}{N_{PHP-II-N,TUBES}\,\pi\left(\frac{(d_{PHP-II-N,o} + \Delta d_{o-N})}{2}\right)^2}$
$UA_{PHP-I-N,EFF}$	$UA^{+}_{PHP-I-N,EFF} = \frac{\lvert\dot{Q}^{+}_{PHP-I-N}\rvert}{\lvert(T_{PHP-I-N,COND} - \Delta T_N) - (T_{PHP-I-N,EVAP} + \Delta T_N)\rvert}$
	$UA^{-}_{PHP-I-N,EFF} = \frac{\lvert\dot{Q}^{-}_{PHP-I-N}\rvert}{\lvert(T_{PHP-I-N,COND} + \Delta T_N) - (T_{PHP-I-N,EVAP} - \Delta T_N)\rvert}$
$UA_{PHP-II-N,EFF}$	$UA^{+}_{PHP-II-N,EFF} = \frac{\lvert\dot{Q}^{+}_{PHP-II-N}\rvert}{\lvert(T_{PHP-II-N,COND} - \Delta T_N) - (T_{PHP-II-N,EVAP} + \Delta T_N)\rvert}$
	$UA^{-}_{PHP-II-N,EFF} = \frac{\lvert\dot{Q}^{-}_{PHP-II-N}\rvert}{\lvert(T_{PHP-II-N,COND} + \Delta T_N) - (T_{PHP-II-N,EVAP} - \Delta T_N)\rvert}$
$SR_{PHP-II-N}$	$SR^{+}_{PHP-II-N} = \frac{UA^{+}_{PHP-II-N,EFF,ON}}{UA^{-}_{PHP-II-N,EFF,OFF}}$
	$SR^{-}_{PHP-II-N} = \frac{UA^{-}_{PHP-II-N,EFF,ON}}{UA^{+}_{PHP-II-N,EFF,OFF}}$
$FR_{PHP-I-N}$	See Appendix 8.3
$FR_{PHP-II-N}$	See Appendix 8.3

Table 2.7. Uncertainty definitions for measured quantities in the nitrogen PHP thermal switch test facility

Quantity	Uncertainty limits
$R_{CCP-N,A}$	$\pm\Delta R_{CCP-N,A}=\pm 2\Omega$
$R_{CCP-N,B}$	$\pm\Delta R_{CCP-N,B}=\pm 0.005\Omega$
$R_{CCP-N,C}$	$\pm\Delta R_{CCP-N,C}=\pm 0.00125\Omega$
$d_{PHP-I-N,o}$	$\pm\Delta d_{o-N}=\pm 0.020\,mm$
$d_{PHP-II-N,o}$	
$L_{PHP-I-N,ADIA}$	$\pm\Delta L_{ADIA-N}=\pm 0.2\,mm$
$L_{PHP-II-N,ADIA}$	
$T_{HM-I-N-A}$, $T_{HM-I-N-B}$, $T_{HM-II-N-A}$, $T_{HM-II-N-B}$, $T_{PHP-I-N,COND}$, $T_{PHP-II-N,COND}$, $T_{PHP-I-N,EVAP}$, $T_{PHP-II-N,EVAP}$	$\pm\Delta T_N=\pm 0.25\,K$

2.5 Experimental results

Measurements of $\dot{Q}_{PHP-I-N}$, $\dot{Q}_{PHP-II-N}$, $k_{PHP-I-N,EFF}$, $k_{PHP-II-N,EFF}$, $UA_{PHP-I-N,EFF}$, $UA_{PHP-II-N,EFF}$, $T_{PHP-I-N,COND}$, $T_{PHP-I-N,EVAP}$, $T_{PHP-II-N,COND}$, $T_{PHP-II-N,EVAP}$, and $SR_{PHP-II-N}$ are presented here for a range of $\dot{Q}_{CCP-N}$, $FR_{PHP-I-N}$, $FR_{PHP-II-N}$, PHP circuit configurations, and cryocooler operating statuses. Table 2.8 summarizes the testing parameters while the corresponding fill ratio uncertainties are listed in Table 2.9. Experiment measurements are plotted in Figure 2.14 and Figure 2.15 as functions of the applied common cold plate heat load $\dot{Q}_{CCP-N}$ and Cryocooler-II-N status for the 2-circuit and 1-circuit PHP configuration, respectively.

All data are obtained at steady PHP operating conditions, meaning that the PHP condenser and evaporator temperatures are time independent over the approximately 20 minute data collection

interval (obviously ignoring the smaller scale, high frequency pulsing associated with PHP operating). Furthermore, the measurements are obtained with no regard to the ramping (up or down) application of $\dot{Q}_{CCP-N}$, as the PHP performance changes are found to be negligible whether the prior $\dot{Q}_{CCP-N}$ in a measurement sequence is a higher or lower value. Measurements at different $FR_{PHP-I-N}$ and $FR_{PHP-II-N}$ are obtained by deactivating both cryocoolers, warming the entire system to ambient temperature, fully evacuating the nitrogen charge from the PHPs, and refilling to the new fill ratio. Note that the PHP-II-N shutoff valve (see Figure 8.1) is opened when Cryocooler-II-N is deactivated for $FR_{PHP-II-N}>0.30$ in order to keep pressures in the PHP lines below about 6 bar and limit stress on the soft solder joints in the PHP filling lines.

Table 2.8. Nitrogen PHP thermal switch test system operating parameters

PHP circuit configuration	Cryocooler-I-N status	Cryocooler-II-N status	$FR_{PHP-I-N}, FR_{PHP-II-N}$	$m_{PHP-I-N}, m_{PHP-II-N}$ [kg]	$\dot{Q}_{CCP-N}$ [W]
2-circuit	Active	Active	0.520, 0.207	0.00360, 0.00142	0 to 20
		Inactive	0.260, 0.259 0.302, 0.303 0.415, 0.415 0.520, 0.520	0.00182, 0.00181 0.00211, 0.00212 0.00289, 0.00288 0.00360, 0.00360	0 to 16
1-circuit		Active	0.507	0.00702	0 to 20
		Inactive	0.547 0.596 0.705	0.00757 0.00825 0.00974	0 to 9

Table 2.9. Nitrogen PHP thermal switch test system fill ratio uncertainties (see Appendix 8.3 for definitions)

Configuration	$FR_{PHP-I-N}$	$FR^{+}_{PHP-I-N}$	$FR^{-}_{PHP-I-N}$	$FR_{PHP-II-N}$	$FR^{+}_{PHP-II-N}$	$FR^{-}_{PHP-II-N}$
2-circuit	0.520	0.570	0.476	0.207	0.286	0.236
	0.260	0.288	0.237	0.259	0.334	0.277
	0.302	0.333	0.275	0.303	0.456	0.380
	0.415	0.457	0.380	0.415	0.570	0.476
	0.520	0.570	0.476	0.520	0.230	0.188
1-circuit	0.507	0.554	0.466			
	0.547	0.598	0.503			
	0.596	0.652	0.548			
	0.705	0.770	0.649			

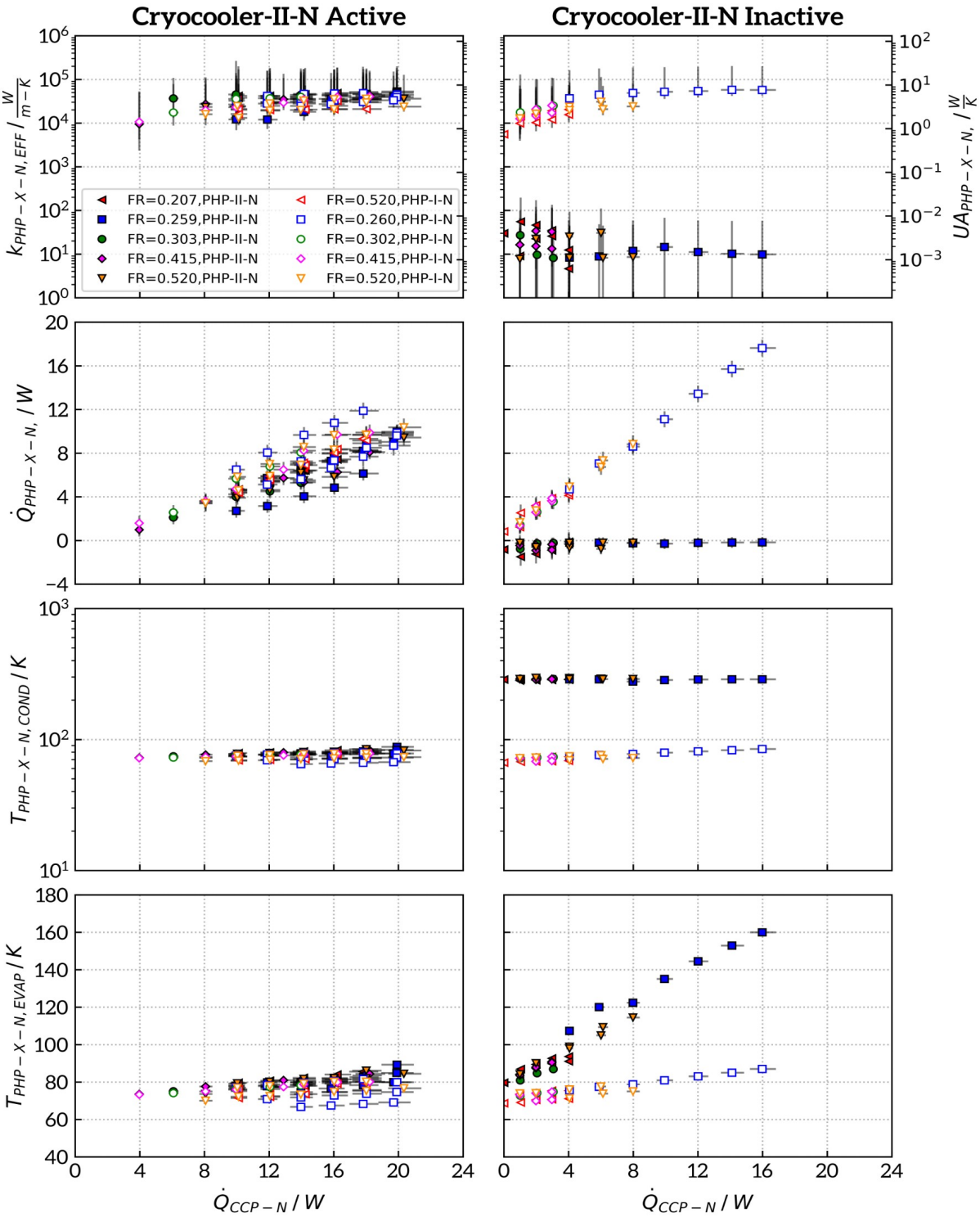

Figure 2.14. Effective conductivity, conductance, heat transfer, condenser temperature, and evaporator temperature over a range of common cold plate heat loads for PHP-I-N and PHP-II-N in the 2-circuit configuration.

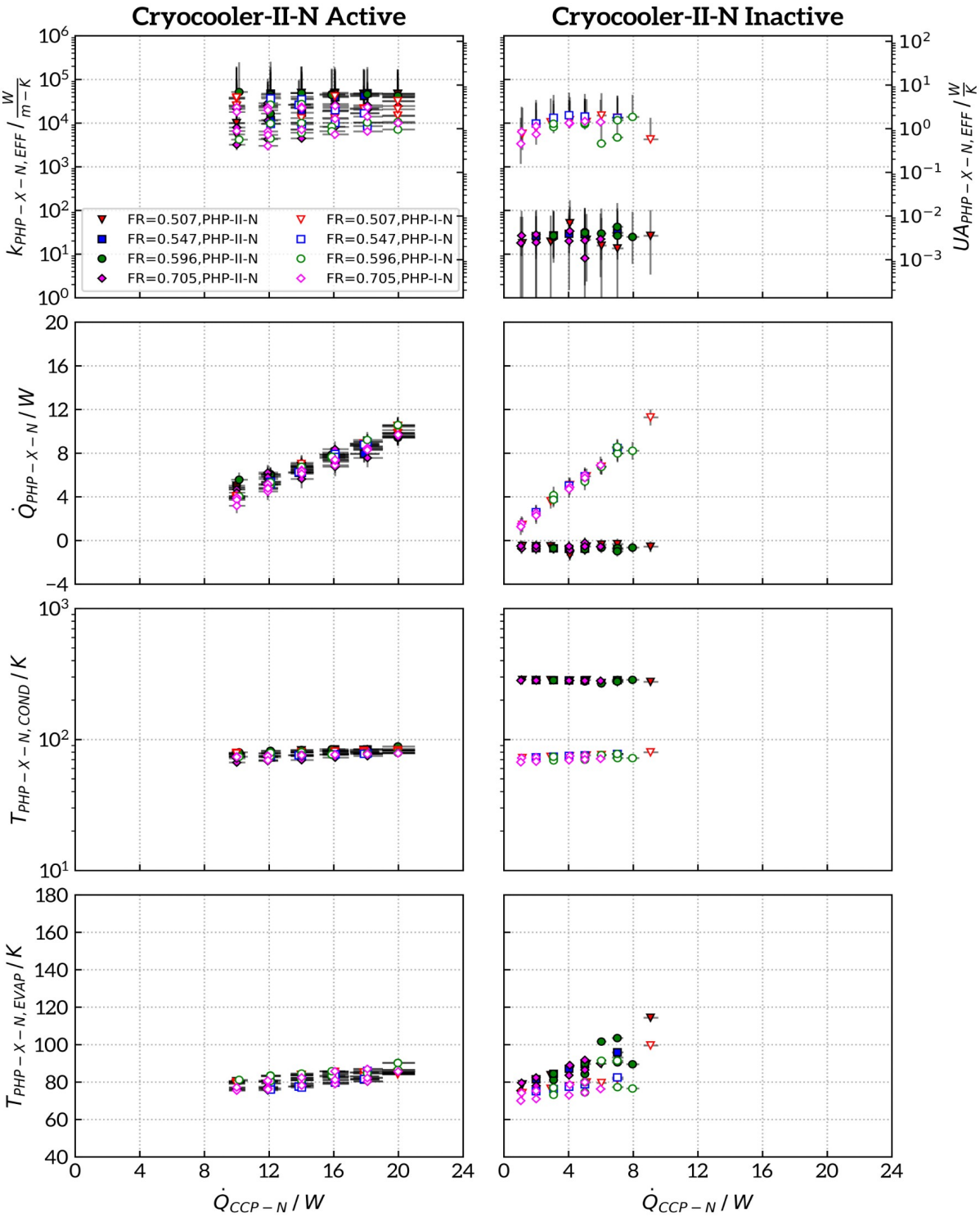

Figure 2.15. Effective conductivity, conductance, heat transfer, condenser temperature, and evaporator temperature over a range of common cold plate heat loads for PHP-I-N and PHP-II-N in the 1-circuit configuration.

2.5.1 Validation of heat meter calibrations

The measurement data sets presented in Figure 2.14 and Figure 2.15 contain data with simultaneous measurements from HM-I-N, HM-II-N and the applied electric heat power on the common cold plate. These simultaneous measurements, along with a system energy balance, can be used to help verify the accuracy of the heat meter calibrations. With Cryocooler-IU-N and Cryocooler-II-N either active or inactive, an energy balance on a system consisting of PHP-I-N, PHP-II-N, HM-I-N, HM-II-N, and the common cold plate

$$\dot{Q}_{CCP-N} = \dot{Q}_{PHP-I-N} + \dot{Q}_{PHP-II-N} \tag{2.16}$$

, depicted in Figure 2.16, holds nearly within the uncertainty bands for each measurement point.

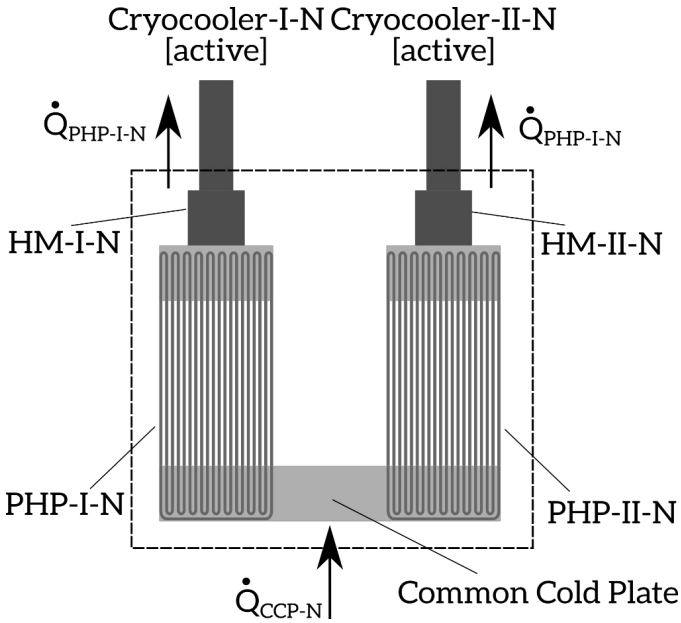

Figure 2.16. Schematic showing energy balance (neglecting radiation) on a system consisting of PHP-I-N, PHP-II-N, HM-I-N, HM-II-N, and the common cold plate.

This is shown in Figure 2.17, which plots the sum of $\dot{Q}_{PHP-I-N}$ and $\dot{Q}_{PHP-II-N}$ as a function of $\dot{Q}_{CCP-N}$ for all nitrogen PHP thermal switch operation data along with the expected perfect

energy balance for comparison. The excellent agreement over all $\dot{Q}_{CCP-N}$ provides an independent confirmation of the accuracy of the heat meter calibrations. Note that the four points above $\dot{Q}_{CCP-N}=10\,W$ in the right panel of Figure 2.17 are extrapolated well outside of the calibrated region for HM-I-N, which may account for the slightly high readings from the heat meter for these data.

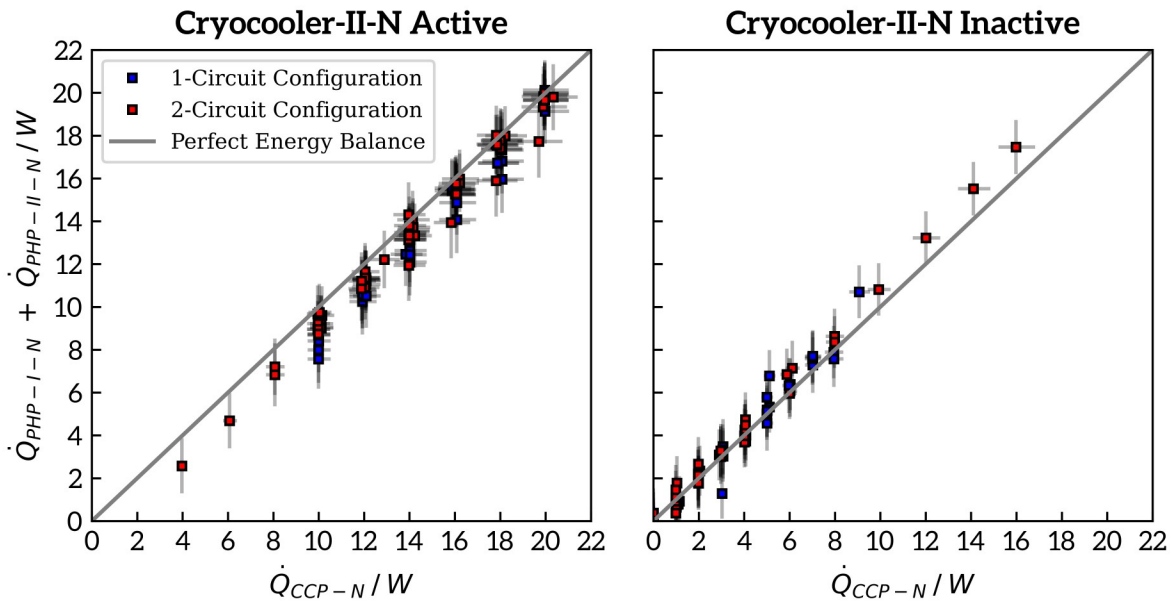

Figure 2.17. Sum of heat meter measurements as a function of the applied common cold plate heat load.

2.5.2 PHP heat transfer, effective conductivity, and evaporator/condenser temperature difference in the ON and OFF switch states

An initial observation from Figure 2.14 and Figure 2.15 shows that when Cryocooler-I-N and Cryocooler-II-N are active – for either plumbing configuration – the majority of effective thermal conductivity measurements fall between 10000 W/m-K and 70000 W/m-K. The correspond-

ing effective conductance values are between about 1 W/K and 7 W/K. These ON state performance values are approximately consistent with those for other nitrogen PHPs of similar size reported in the literature [39][40][41].

Again for either PHP plumbing configuration, when Cryocooler-II-N is inactive, the parasitic heat leak through the OFF state PHP-II-N, $\dot{Q}_{PHP-II-N}$, is nearly constant for all measurements with a mean of -0.54 W while $\dot{Q}_{CCP-N}$ is varied between 0 W and 16 W. As discussed in Section 2.4, this is because with Cryocooler-II-N inactive the temperature difference between the PHP-II-N evaporator and condenser is large (for all measurements $T_{PHP-II-N-EVAP}$ is near 80 K and $T_{PHP-II-N-COND}$ is approximately 290 K) and varies little while the effective conductivity of the contained static vapor is very low. Note that because the PHP geometry is also fixed, this implies that $k_{PHP-II-N,EFF}$ and $UA_{PHP-II-N,EFF}$ also do not change much per Equation 2.8 and Equation 2.10. Figure 2.18 shows the distributions of $\dot{Q}_{PHP-II-N}$ and $k_{PHP-II-N,EFF}$ for all measurements with Cryocooler-II-N inactive (PHP-II-N in the OFF state). The distributions are nearly normal and notably not multi modal, suggesting that there is no unforeseen dependence of the OFF state heat leak on the fill ratio over the range tested here. In Section 4.2 the measurements of parasitic heat load through PHP-II-N discussed here are compared to a simple model which considers conduction through the parallel paths of the stagnant gas and tube wall for each of the parallel tubes comprising PHP-II-N.

Finally, note that the parasitic load $\dot{Q}_{PHP-II-N}$, which must be removed from the common cold plate entirely through the ON state PHP-I-N and Cryocooler-I-N, is about 8 percent of the maxi-

mum demonstrated capacity of PHP-I-N in the 2-circuit configuration[18], 10 percent of the maximum capacity demonstrated in the 1-circuit configuration, and 3 percent of the available capacity of Cryocooler-I-N after accounting for the heat shield load. PHP-II-N is therefore functioning quite effectively as a thermal switch, providing insulation to protect the common evaporator plate from the hot PHP-II-N condenser plate while allowing Cryocooler-I-N to continue cooling the evaporator load.

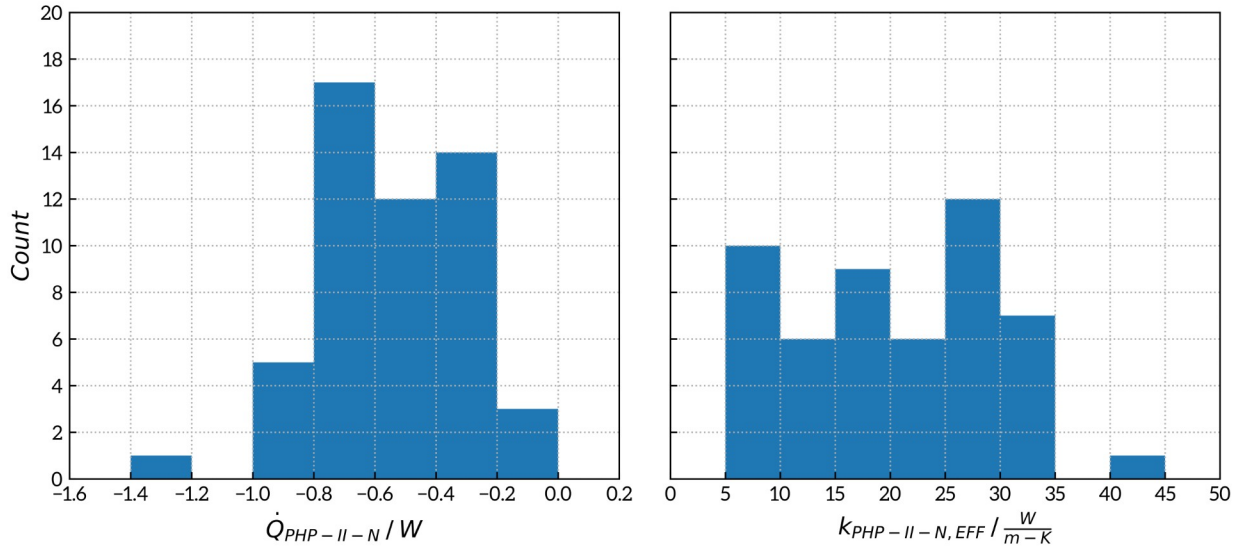

Figure 2.18. Distribution of parasitic heat leak through the OFF state PHP-II-N, $\dot{Q}_{PHP-II-N}$, and the corresponding distributions of $k_{PHP-II-N,EFF}$.

There are notable differences in the PHP ON state performance between the 1-circuit and 2-circuit configurations. Perhaps most importantly, when Cryocooler-II-N is inactive and PHP-II-N is dry, dryout occurs in PHP-I-N at lower $\dot{Q}_{CCP-N}$ in the 1-circuit configuration relative to the 2-circuit configuration. In the latter, dryout is *not* seen in the remaining operating PHP-I-N up to the maximum tested $\dot{Q}_{CCP-N}=16\,W$, as shown in Figure 2.14. In the 1-circuit configuration,

18 The actual maximum capacity is higher than reported for this configuration because dryout was not seen in this data set.

dryout in PHP-I-N (which shares a common fluid circuit with the always dry PHP-II-N) occurs around $\dot{Q}_{CCP-N} = 9\,W$, as shown by the spike in evaporator temperatures and drop in $k_{PHP-I-N,EFF}$ as $\dot{Q}_{CCP-N}$ approaches this value in Figure 2.15. Higher heat loads are measured in the 2-circuit configuration as its design allows for the development of a net circulation [30][34] in the remaining operating PHP-I-N – its entire tube circuit remains in an advective state. Circulation is *not* possible in the 1-circuit configuration since PI-PHP-II is completely dry, causing a vapor lock with no liquid present in 20 consecutive tubes of the combined 40 tube fluid path. Closely related to this phenomenon, the maximum effective $k_{PHP-I-N,EFF}$ in the 1-circuit configuration with an inactive Cryocooler-II-N is about 20000 W/m-K, significantly lower than the 60000 W/m-K achieved in the 2-circuit configuration. As the $k_{PHP-I-N,EFF}$ and $k_{PHP-II-N,EFF}$ vary little between the 1-circuit and 2-circuit configurations when *both* cryocoolers are active, the 2-circuit configuration is clearly desirable to maximize capacity of the remaining PHP when one of the cryocoolers are inactive.

Furthermore, small differences between the PHP-I-N and PHP-II-N condenser temperatures cause much larger performance changes in the 1-circuit configuration than in the 2-circuit configuration. There are two reasons why $(T_{PHP-I-N,EVAP} - T_{PHP-I-N,COND})$ and $(T_{PHP-II-N,EVAP} - T_{PHP-II-N,COND})$ may be different in this experiment. The first is that $T_{PHP-I-N,EVAP}$ and $T_{PHP-II-N,EVAP}$ may vary due to differences in the contact conductances within the common cold plate assembly (see Section 2.5.4). The second is that that $T_{PHP-I-N,COND}$ and $T_{PHP-II-N,COND}$ may be different since they are located on different cryocoolers and are independently controlled. In the 2-circuit configuration, such a difference between $T_{PHP-I-N,COND}$ and

$T_{PHP-II-N,COND}$ causes the total common cold plate heat load to be split unevenly between the PHPs (that is, $\dot{Q}_{PHP-I-N}$ and $\dot{Q}_{PHP-II-N}$ are in general unequal in this configuration), although $k_{PHP-I-N,EFF}$ and $k_{PHP-II-N,EFF}$ are approximately equal. This means the energy transport through each PHP scales according to the PHP evaporator to condenser temperature difference (PHP-I-N and PHP-II-N have equal evaporator temperatures but their condenser temperatures differ slightly). In the 1-circuit configuration, the total common cold plate heat load is *always* shared equally between the PHPs ($\dot{Q}_{PHP-I-N}$ and $\dot{Q}_{PHP-II-N}$ and are essentially equal for this configuration), although in this configuration $k_{PHP-I-N,EFF}$ and $k_{PHP-II-N,EFF}$ differ. This behavior is caused by the directly coupled fluid dynamics between PHP-I-N and PHP-II-N in the 1-circuit configuration. Even though the PHP-I-N and PHP-II-N condenser temperatures are controlled at different values and the common evaporator temperatures are the same (therefore causing each PHP to have a different driving temperature difference), the heat transfer through each PHP is equal because each experiences the same advective flow.

2.5.3 Switching ratio

The effectiveness of PHP-II-N as a thermal switch is ultimately characterized by its switching ratio as defined in Equation 2.15. Figure 2.19 shows the PHP-II-N switching ratio as a function of ON state PHP-II-N heat load for both the 1-circuit and 2-circuit configurations[19]. The ratio approaches about 2500 for the 2-circuit configuration and 2000 for the 1-circuit configuration, indicating that $k_{PHP-II-N,EFF}$ is over three orders of magnitude larger in the ON (advective) state than in the OFF (dry) state. This clearly demonstrates the effectiveness of PHPs as thermal

19 Again recall that the switching ratio is only measured for PHP-II-N since Cryocooler-I-N is always active to cool the radiation shield.

switches, even when large temperature differences (about 220 K here) are imposed in the OFF switch state between the condenser and evaporator plates.

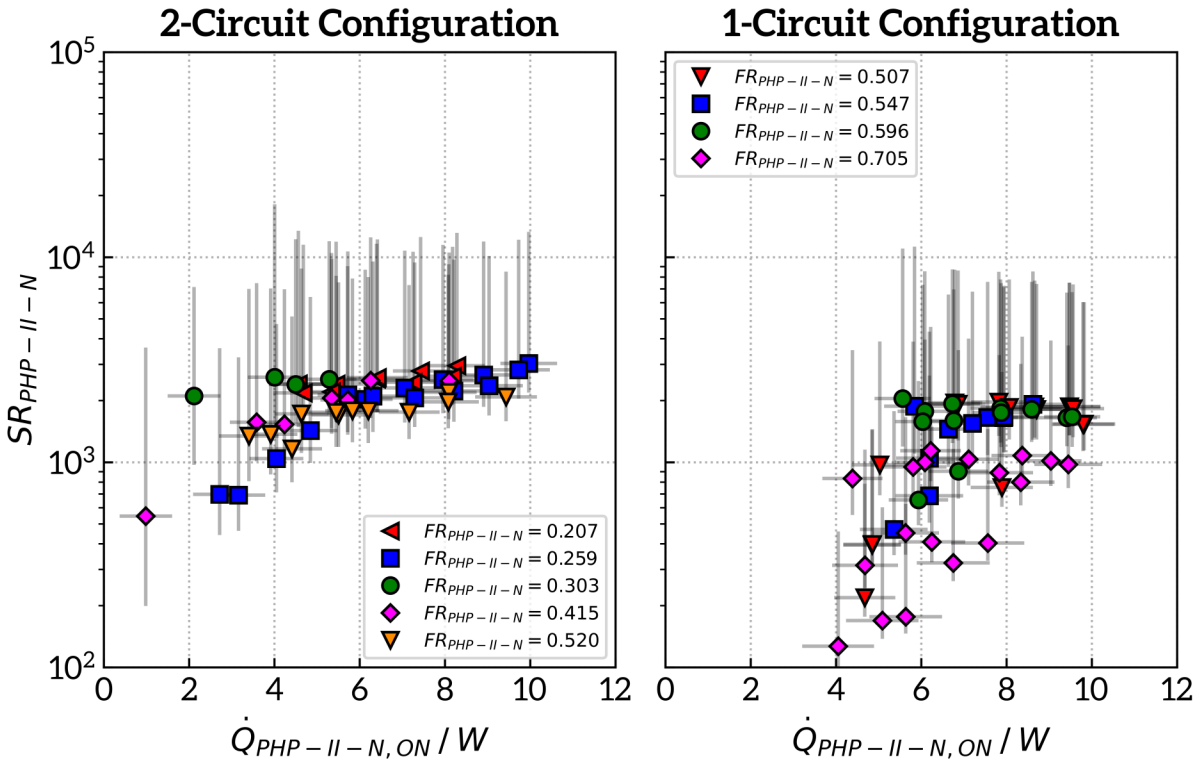

Figure 2.19. Switching ratio as a function of the heat load in the ON state for the PHP-II-N in both the 2-circuit and 1-circuit configurations[20]. Colors and marker shapes in the legends apply exclusively to the corresponding panel.

Two important observations can be made from Figure 2.19. First, the switching ratio isn't sensitive to the PHP fill ratio. This is not unexpected – the PHP effective thermal conductivity in the ON state is typically a fairly weak function of fill ratio (except at fill ratios approaching 0 or 1), while the OFF state effective thermal conductivity is independent of the stagnant gas pressure; this OFF state gas pressure changes as the fill ratio varies – see Section 2.1 for details. Second, a

20 The switching ratio uncertainty is clearly skewed high. This occurs because the ON state conductivity is associated with very small temperature differences between the PHP condenser and evaporator. Since this temperature difference approaches the uncertainty of the temperature sensors, the minimum temperature difference in Equation 2.10 tends to zero, causing the PHP conductance to head towards infinity. For evaluation of switch performance, the maximum uncertainty bound of the switching ratio is far less important than the minimum, which is significantly smaller in magnitude because the denominator of Equation 2.10 is at its largest possible value.

large number of measurements for the 1-circuit configuration occur at high heat loads with relatively low (<1000) values for the switching ratio. This is a result of $k_{PHP-II-N,EFF}$ varying substantially with small differences in PHP-I-N and PHP-II-N condenser temperatures in the ON state, as discussed previously.

2.5.4 Contact conductance in the common cold plate assembly

With Cryocooler-II inactive, $T_{PHP-II-N,EVAP}$ noticeably diverges from $T_{PHP-I-N,EVAP}$ with increasing $\dot{Q}_{CCP-N}$. This is apparent in both the 2-circuit and 1-circuit results shown in the lower right panels of Figure 2.14 and Figure 2.15, respectively, although the effect is much more pronounced in the former. Such behavior is suggestive of a contact conductance between copper components of the common cold plate assembly. To estimate this contact conductance, a simple model of the conduction heat transfer through the common cold plate, shown in Figure 2.20, is solved. Here the contact conductances between all components are assumed to be equal and each copper plate is assumed isothermal. All values in Figure 2.20 are measured or calculated from the experiment results shown in Figure 2.14 and Figure 2.15 except UA_{CONT-N} and T_{CCP-N} – there is no temperature sensor on the evaporator connector plate. Equations 2.17 and 2.18 represent the heat transfer over the connector plate to PHP-I-N evaporator and PHP-II-N evaporator to connector plate joints, respectively, and are solved simultaneously to determine these unknown values for each experiment datum with Cryocooler-II-N inactive.

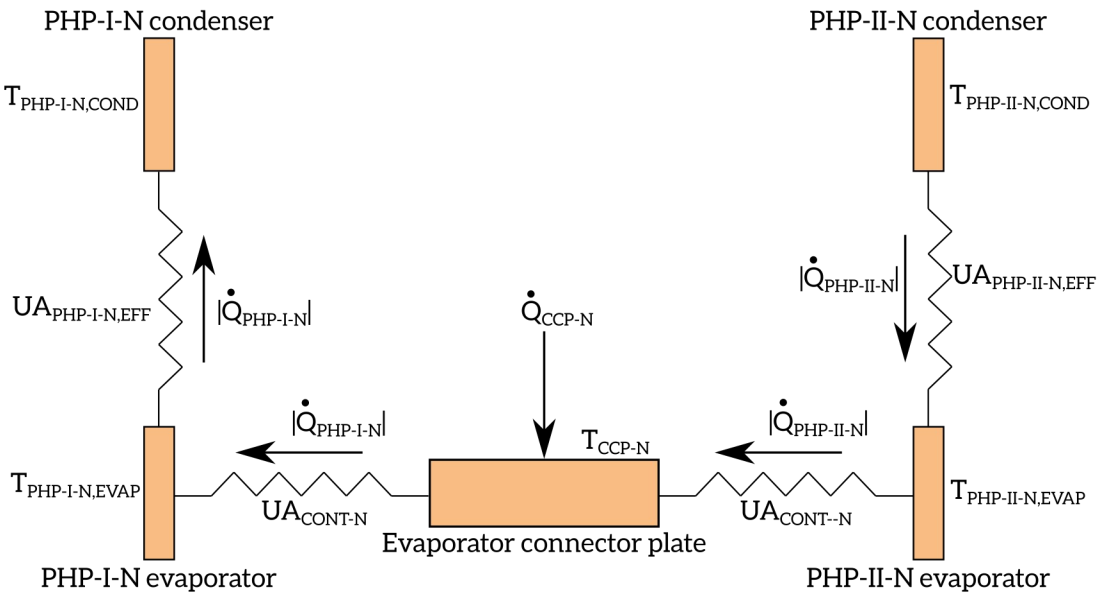

Figure 2.20. Schematic showing heat transfers and conductances in the common cold plate assembly. Arrows indicate positive values of heat transfers when Cryocooler-II-N is inactive.

$$|\dot{Q}_{PHP-I-N}| = \frac{UA_{CONT}}{T_{PHP-II-N,EVAP} - T_{CCP-N}} \tag{2.17}$$

$$|\dot{Q}_{PHP-II-N}| = \frac{UA_{CONT}}{T_{CCP-N} - T_{PHP-I-N,EVAP}} \tag{2.18}$$

Results from the common cold plate contact resistance model are shown in Figure 2.21 and Figure 2.22 for the 2-circuit and 1-circuit plumbing configuration measurement data, respectively. The left panels of the figures show the measured heat transfer over each joint as a function of the associated modeled temperature difference while the right panels show the modeled T_{CCP-N} compared to the $T_{PHP-I-N,EVAP}$ and $T_{PHP-II-N,EVAP}$ measurements. The excellent linear fit in the left panels, for the heat transfers over both common cold plate joints, suggest that the model is representative and that UA_{CONT-N} is constant over the observed temperature range. For the 2-circuit configuration UA_{CONT-N} is an estimated 0.219 W/K; for the 1-circuit configuration the estimate is 0.590 W/K.

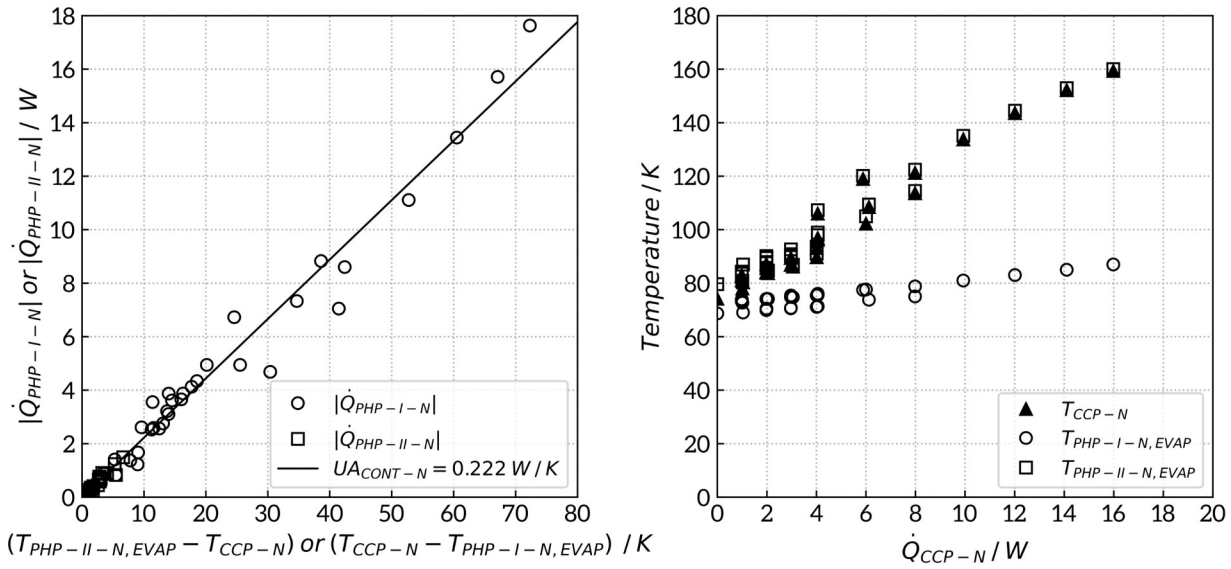

Figure 2.21. Common cold plate contact conductance estimate using experiment data from the 2-Circuit configuration with Cryocooler-II-N inactive (left) and modeled evaporator connector plate temperature $T_{CCP\text{-}N}$ as a function of the common cold plate heat load (right).

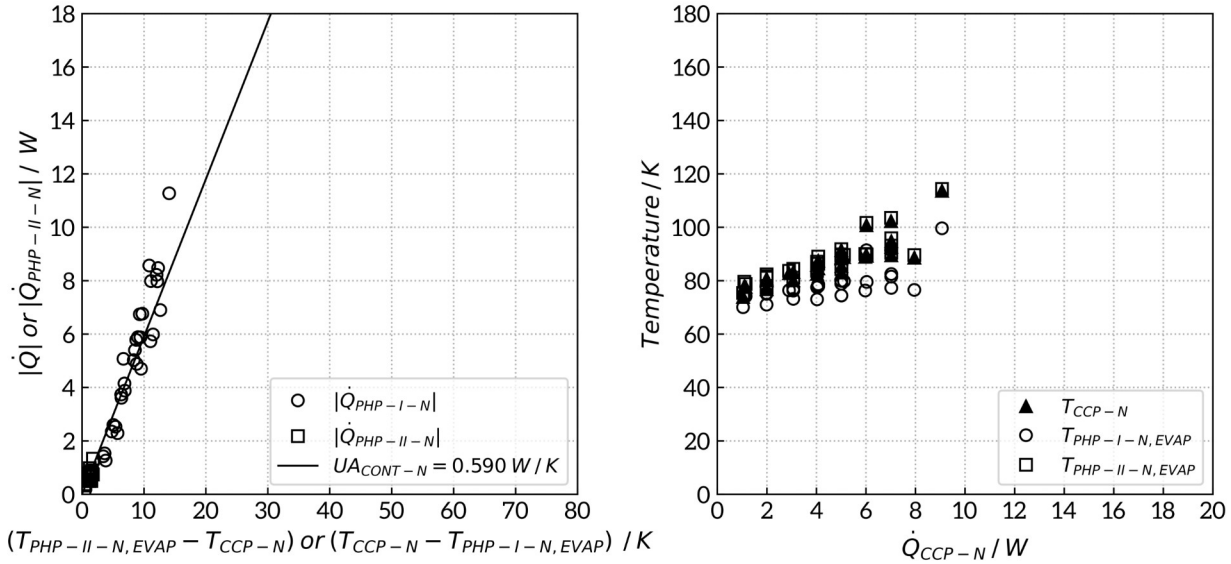

Figure 2.22. Common cold plate contact conductance estimate using experiment data from the 1-Circuit configuration with Cryocooler-II-N inactive (left) and modeled evaporator connector plate temperature $T_{CCP\text{-}N}$ as a function of the common cold plate heat load (right).

The right panels of Figure 2.21 and Figure 2.22 explain the observed increasing temperature gradient between $T_{PHP-II-N,EVAP}$ and $T_{PHP-I-N,EVAP}$ with increasing $\dot{Q}_{CCP-N}$. The contact conductance model suggests the majority of this temperature gradient is over the connector plate to

PHP-I-N evaporator joint, caused by and scaling with $\dot{Q}_{CCP-N}$. The PHP-II-N to connector plate joint, meanwhile, is subjected to the lower magnitude (and almost constant) parasitic heat transfer $|\dot{Q}_{PHP-II-N}|$. T_{CCP-N} and $T_{PHP-II-N,EVAP}$ are therefore always nearly identical. This explanation is consistent with the observation that $T_{PHP-I-N,EVAP}$ and $T_{PHP-II-N,EVAP}$ nearly converge to about 80 K at $\dot{Q}_{CCP-N}=0\,W$ for both plumbing configurations, with the remaining offset due only to the parasitic $|\dot{Q}_{PHP-II-N}|$.

Table 2.10. Comparison of common cold plate contact conductance (modeled via Equations 2.17 and 2.18) to OFF state PHP-II-N conductance (measured per Equation 2.10) for all measurement data

Configuration	**Estimate Bound**	UA_{CONT} **[W/K]**	$UA_{EFF,PHP-II-N,OFF}$ **[W/K]**	$\frac{UA_{CONT}}{UA_{EFF,PHP-II-N,OFF}}$
2-Circuit	Minimum	0.137	0.0010	137
	Mean	0.222	0.0021	106
	Maximum	0.312	0.0046	67
1-Circuit	Minimum	0.331	0.0011	300
	Mean	0.590	0.0034	173
	Maximum	0.802	0.0069	116

Table 2.10 compares the modeled values of UA_{CONT-N} to the experimentally calculated values of $UA_{EFF,PHP-II-N,OFF}$ for all measurements with Cryocooler-II-N inactive. Recall that $UA_{EFF,PHP-II-N,OFF}$ is computed with $(T_{PHP-II-N,COND}-T_{PHP-II-N,EVAP})$, rather than $(T_{PHP-II-N,COND}-T_{CCP-N})$ and therefore does not benefit from the additional temperature gradient within the common cold plate assembly due to the contact conductances. Additionally, the estimated contact conductance UA_{CONT-N} is *much* larger (by about two orders of magnitude) than the measured PHP-II-N OFF state conductance $UA_{EFF,PHP-II-N,OFF}$, suggesting that the pres-

ence of the contact conductance is not significantly deflating the reported values of $UA_{EFF,PHP-II-N,OFF}$.

Insufficient contact area and clamping force are the likely causes of the observed contact conductance in the common cold plate assembly. Note that the 2-circuit configuration testing was performed prior to that of the 1-circuit configuration, and the low contact conductance was suspected as the system underwent conversion to the 1-circuit configuration. Some fasteners clamping the common cold plate components together were discovered to be insufficiently secured at this time and were subsequently tightened before testing of the 1-circuit configuration. This is consistent with the contact conductance more than doubling for the 1-circuit configuration data relative to the 2-circuit configuration data. Although the contact conductances seen here (even for the improved 1-circuit configuration data) would be an issue for an application requiring the common cold plate to remain at a certain design temperature at all $\dot{Q}_{CCP-N}$, based on the preceding analysis they do not preclude the objective of this work: evaluating PHP thermal switch performance. A better designed common cold plate assembly – for instance, with more contact area and polished surfaces between the components) – would alleviate the issue but is not pursued here due to time constraints.

2.5.5 Behavior during Cryocooler-II-N shutdown and subsequent restart

For the OFF state PHP-II-N measurements, the facility is initially in a state with Crycooler-I-N and Cryocooler-II-N active. Cryocooler-II-N is then deactivated and the electric resistance heaters attached to the cold head are utilized to rapidly (in roughly 90 minutes) warm the Cry-

ocooler-II-N cold head and PHP-II-N condenser from about 80 K to 290 K. During the warming of Cryocooler-II-N, Cryocooler-I-N continues operating and PHP-I-N continues removing $\dot{Q}_{CCP}$ from the PHP-I-N evaporator. Typically, if $\dot{Q}_{CCP}$ is larger than about 1 W during this Cryocooler-II-N warm up process, $T_{PHP-I-N,EVAP}$ smoothly transitions from the value measured at this $\dot{Q}_{CCP}$ with Cryocooler-II-N active to the value with Cryocooler-II-N inactive (per Figure 2.14 and Figure 2.15). $T_{PHP-I-N,EVAP}$ is stable during this process and sees no rapid increases, suggesting that the parasitic load $|\dot{Q}_{PHP-II-N}|$ never increases significantly above the reported steady state values in Figure 2.14 and Figure 2.15 and that the switching process (dryout) in PHP-II-N is complete at relatively low values of $T_{PHP-II-N,COND}$. If $\dot{Q}_{CCP}$ is less than about 1W during the Cryocooler-II-N warm up, PHP-I-N operation can become intermittent, causing brief rises in $T_{PHP-I-N,EVAP}$ above the steady values reported in Figure 2.14 and Figure 2.15. For a more thorough accounting of PHP evaporator temperatures, condenser temperatures, and loads during the PHP switching process, see Section 3.6 for results from the helium PHP thermal switch test facility.

3 Helium PHP thermal switch performance characterization in a redundant cryocooler system

The second portion of this project involves the design, fabrication, and performance characterization of *helium* PHP thermal switches (with switching temperatures near 4 K). Demonstrating helium PHP thermal switching at such temperatures is the ultimate goal of the project. With a possible application of such a device allowing improvements in reliability and portability of cooling systems for superconducting electronic systems in terrestrial or aerospace applications [6][7]. As stated previously, a major benefit of first testing the nitrogen PHP thermal switches prior to proceeding with an analogous helium PHP thermal switch test is the ability to burn project risk with a simplified facility operating at relatively high temperatures. With the success of the proof-of-principle nitrogen PHP thermal switch tests demonstrated in Section 2, the follow on helium PHP thermal switch test setup is presented here.

3.1 Test facility overview

The helium PHP thermal switch test facility is similar to, but significantly more complex than, the facility developed previously for the nitrogen PHP thermal switch testing. This is caused by several differing factors: two rather than one actively cooled radiation shields (one each at about 4 K and 70 K, from now on referred to as the ‘4 K’ and ‘70 K’ shields respectively), the desire to allow the 70 K shield to be thermally isolated from a deactivated cryocooler, and longer PHP adiabatic sections. External views of the helium PHP thermal switch test facility with the dewar excluded, are shown as a solid model in Figure 3.1 and as an image of the actual assembly in Figure 3.2. Figure 3.3 offers similar views of the solid model assembly with 70 K shield and nitrogen shield PHPs removed, while Figure 3.4 further removes the 70 K shield support structure.

Figure 3.5 shows a solid model profile view of the assembly with the 4 K shields removed to reveal the detail of the helium PHPs and heat meters.

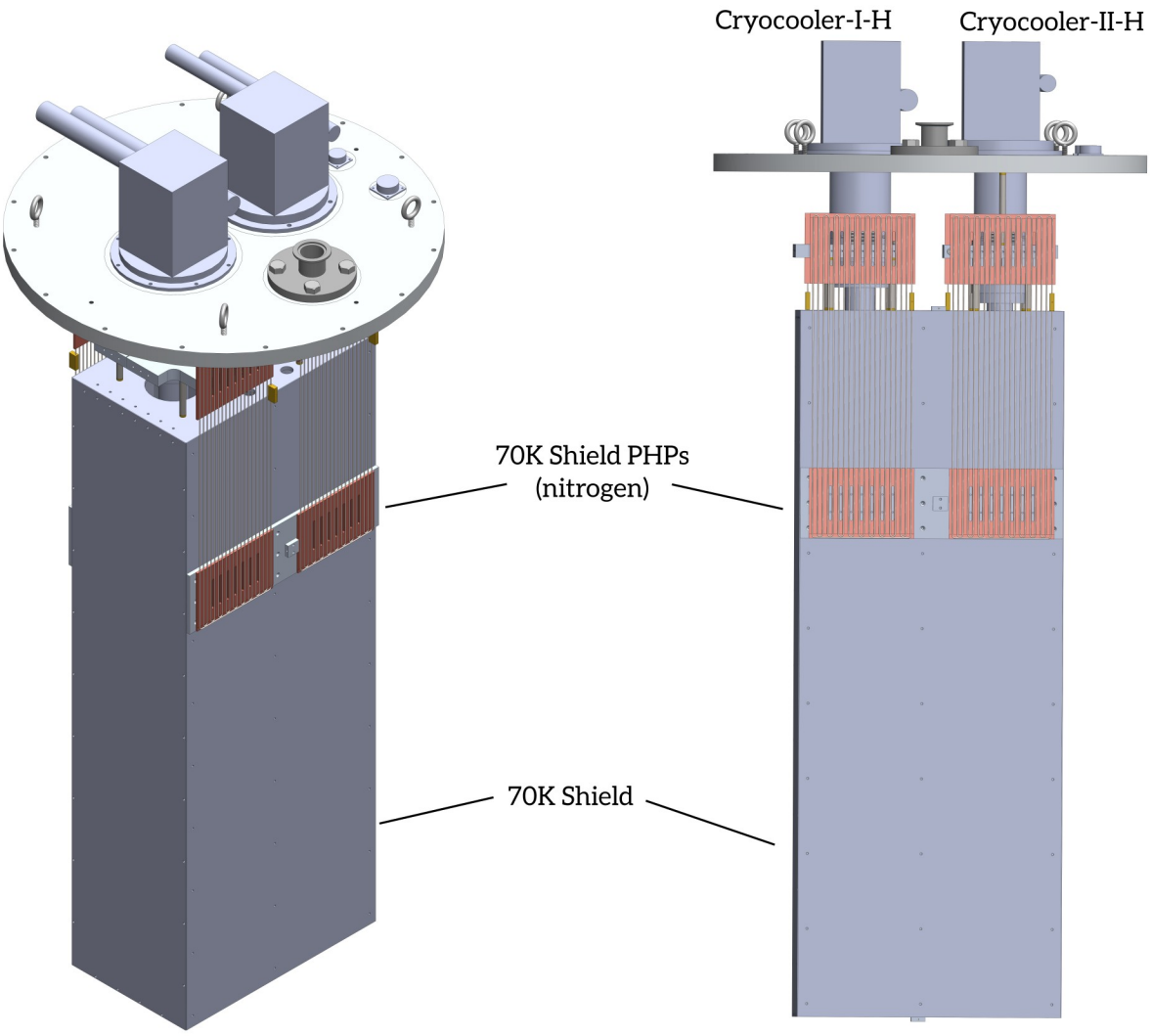

Figure 3.1. Solid model assembly views of the helium PHP thermal switch test facility with the locations of the four nitrogen shield PHPs indicated (dewar not shown).

At the core of the facility are two redundant Gifford-McMahon cryocoolers – a Cryocooler-I-H[21] (a Sumitomo RDK-415D rated for 1.5W at 4.2K) and a Cryocooler-II-H (a Sumitomo RDK-408D2 rated for 1.0W at 4.2K) – each mounted vertically in a common dewar via a common cus-

21 -The 'H' suffix refers to the helium PHP switch test facility

tom designed 6061 aluminum dewar cover plate. In this orientation, the longest axes of the cryocoolers are parallel to the gravity field. The cover plate also includes a single KF-40 ASA flange adapter (Kurt J. Lesker model QF40XASA5G) used as a passthrough for the PHP filling lines, along with three electrical passthrough connectors (one Deteronics DT02H-16-8PN and two DT02H-20-41PN) for thermometer and heater lead passthroughs. Figure 3.1 and Figure 3.6 show views of these dewar cover plate connected components. A KF40 flange for the connection of the vacuum pump system is available directly on the dewar – a full description of the external vacuum and PHP filling plumbing is provided in the Appendix Section 8.2.

Figure 3.2. Images of the helium PHP thermal switch test facility showing the 70 K shield and the nitrogen shield PHPs.

Overall, this facility is significantly larger than that of the nitrogen PHP thermal switch facility in order to accommodate an extra layer of radiation shields and the longer helium PHP adiabatic sections. The helium PHP thermal switch facility dewar dimensions are listed in Table 3.1, which can be compared the nitrogen PHP thermal switch facility dimensions listed in Table 2.1. Figure 3.7 provides an external image of the helium PHP thermal switch facility dewar, highlighting its much large size.

Table 3.1. Nitrogen PHP thermal switch test facility dimensions

Dimension	Value
Dewar internal diameter	60 cm
Dewar internal height	180 cm

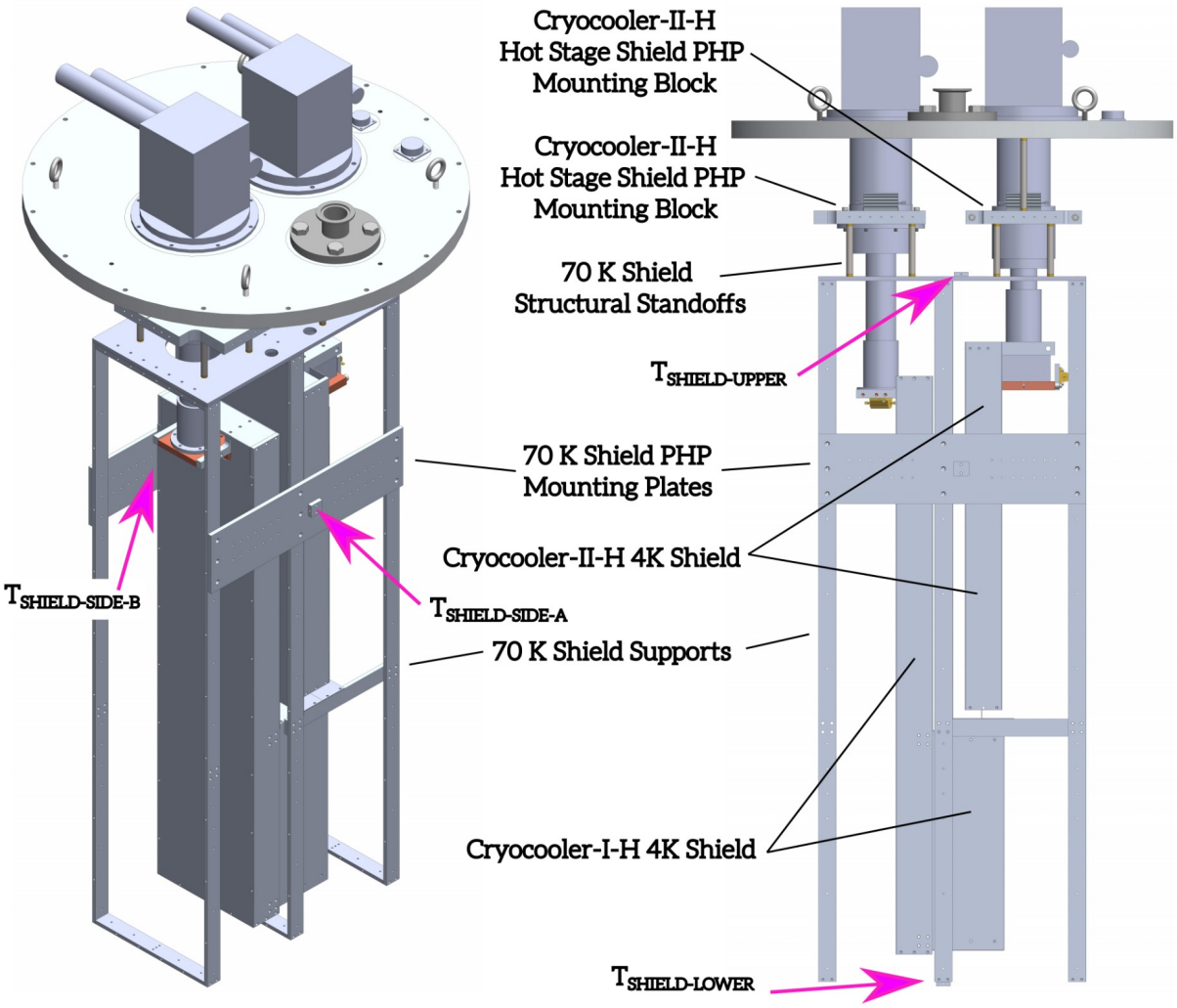

Figure 3.3. Solid model assembly views of the helium PHP thermal switch test facility with the 70 K shield and nitrogen shield PHPs removed. Pink arrows indicate locations of the four temperature sensors attached to the 70 K shield.

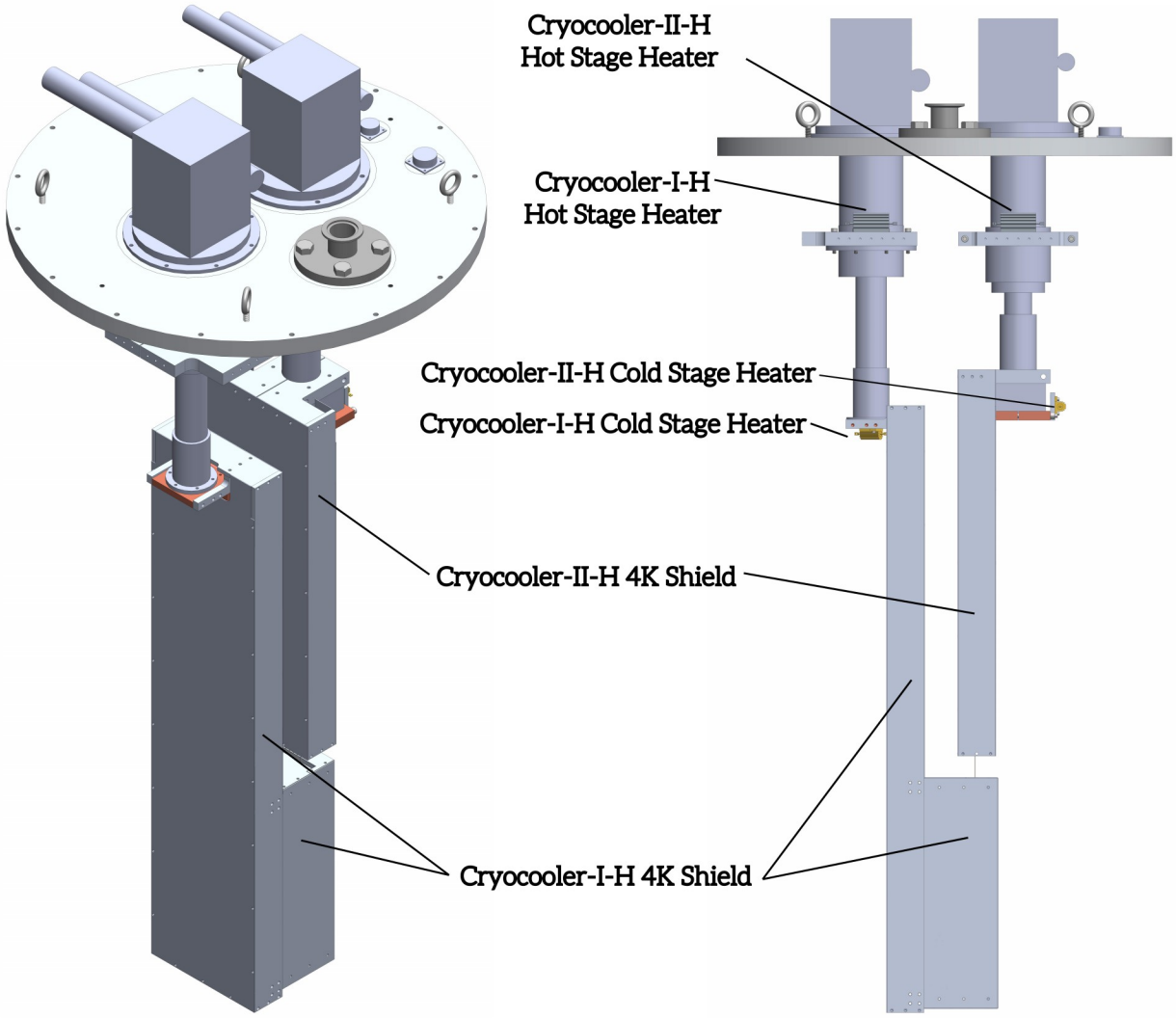

Figure 3.4. Solid model assembly views of the helium PHP thermal switch test facility with all 70 K shields and structure removed.

Perhaps the most immediately obvious new feature for the helium PHP thermal switch facility (relative to the nitrogen PHP switch facility) is the 70 K heat shield design. Here, the 70 K heat shield is thermally sunk to *both* Cryocooler-I-H and Cryocooler-II-H, not with directly mated metal surfaces but rather with two nitrogen PHP thermal switches per cryocooler. This allows the 70 K shield to be passively thermally isolated from an inactive cryocooler. In principle, this design allow the 70 K shield to remain cold at all times using the remaining active cryocooler if

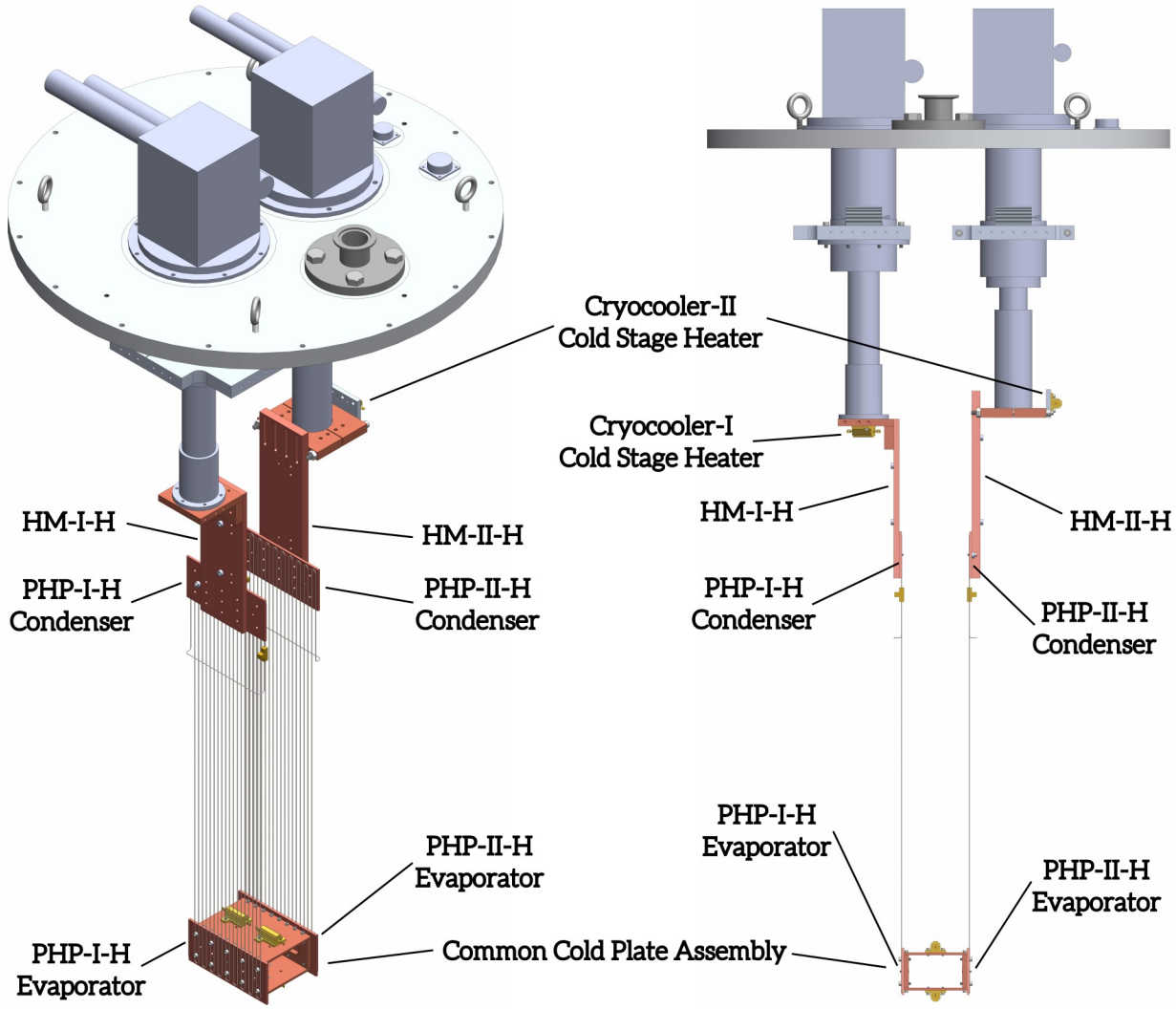

Figure 3.5. Solid model assembly views of the helium PHP thermal switch test facility with all 70 K and 4 K shields and structures removed.

either Cryocooler-I-H *or* Cryocooler-II-H is deactivated[22]. Such a design is not required for performance characterization of the helium PHP thermal switches, but it is required for any actual application of cryogenic PHPs and is included in the facility as a proof-of-principle engineering demonstration. The four nitrogen PHP switches (two each per cryocooler) are nearly identical to

22 Recall that the heat shield is sunk to only the Cryocooler-I-N cold head in the nitrogen PHP thermal switch test facility. This means that Cryocooler-I-N must be always be active during testing of the nitrogen PHPs.

those used in the nitrogen PHP thermals switch test facility, with design details discussed in Section 3.2.

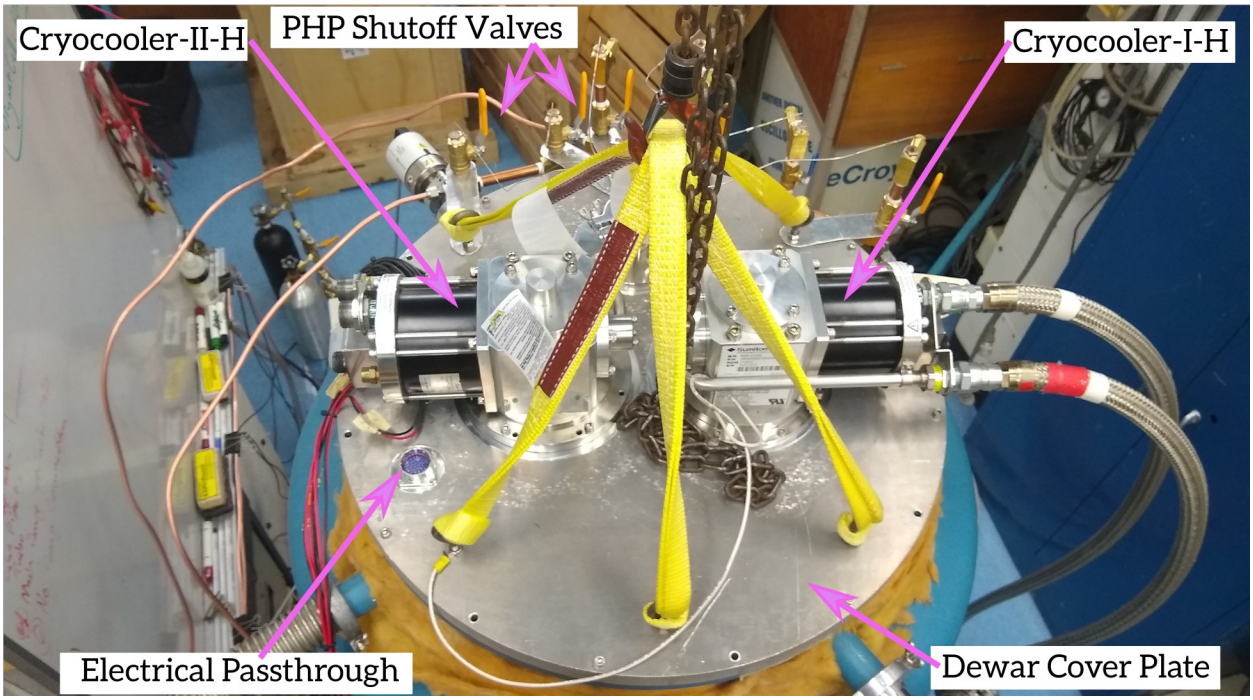

Figure 3.6. Overhead image of the helium PHP thermal switch facility dewar cover plate with annotated components.

The mechanical structure of the 70 K shield varies substantially from the analogous radiation shield in the nitrogen PHP thermal switch test facility in order to implement the PHP thermal switch connections to the hot stages of Cryocooler-I-H and Cryocooler-II-H. Here, the 70 K shield is covered with panels cut from 1.3 mm thickness 6061 aluminum and has a box shape to mate with the nitrogen PHP evaporator plates, as seen in Figure 3.1. A system of 6061 aluminum structural supports secures the shield panels and nitrogen shield PHPs. The shield panels and structural components are joined with 6-32 screws and Apiezon N thermal vacuum grease, with the entire shield assembly mechanically suspended from the cryocooler hot stages with thermally insulating thin-walled stainless steel support rods. The shield temperature is monitored by four

platinum resistance thermometers (uncalibrated Lakeshore Cryotronics model PT-102), located at the top, bottom, and sides (near the nitrogen shield PHP evaporators) of the 70 K shield, as highlighted in Figure 3.2. An approximately 30 layer MLI blanket surrounds the panels of the shield. Details of the 70 K shield assembly structure are shown in Figure 3.8, with an image of the MLI-wrapped assembly shown in Figure 3.7.

Figure 3.7. External view of the helium PHP thermal switch test facility dewar (left) and the test facility removed from the dewar showing MLI-wrapped 70 K shield (right)

Similar to the nitrogen PHP thermal switch test facility, this facility contains two custom designed and fabricated helium PHPs[23] – labeled PHP-I-H and PHP-II-H – which are associated with Cryocooler-I-H and Cryocooler-II-H, respectively. Each helium PHP condenser plate is structurally and thermally linked to its respective cryocooler cold head via custom designed conduction heat meters labeled HM-I-H and HM-II-H. The heat meters are again rectangular copper bars of known length and cross sectional area with thermometers installed near each end of the bar[24]. Both Cryocooler-I-H and Crycooler-II-H have electrical resistance heaters attached to the hot and cold stages – 13 Ω TE Connectivity model HSC7513RJs on the hot stages and 1200 Ω TE Connectivity model HSA251K2Js on the cold stages. Each heater is powered by an independent, programmable direct current power supply and controlled by an independent LabVIEW PID controller. Temperature input for the hot stage controllers are provided by platinum resistance thermometers (uncalibrated Lakeshore Cryotronics model PT-102) mounted on the shield PHP mounting blocks, highlighted in Figure 3.9. Temperature input for the cold stage controllers is provided by the Cernox thermometers (calibrated[25] Lakeshore Cryotronics model CX-1050-CU-HT) mounted on the helium PHP condensers, shown in Figure 3.17. The heater and power supply combinations allow up to 150 W and 2 W to be applied at the hot stage and cold stage of the cryocoolers, respectively, in order to maintain temperature set points at these locations. Figure 3.9 and Figure 3.5 indicated the locations of the hot and cold stage heaters, respectively.

23 See section 3.3 for a full description of the PHP design

24 See section 3.4 for details of heat meter construction and calibration.

25 See Section 8.6 for calibration details

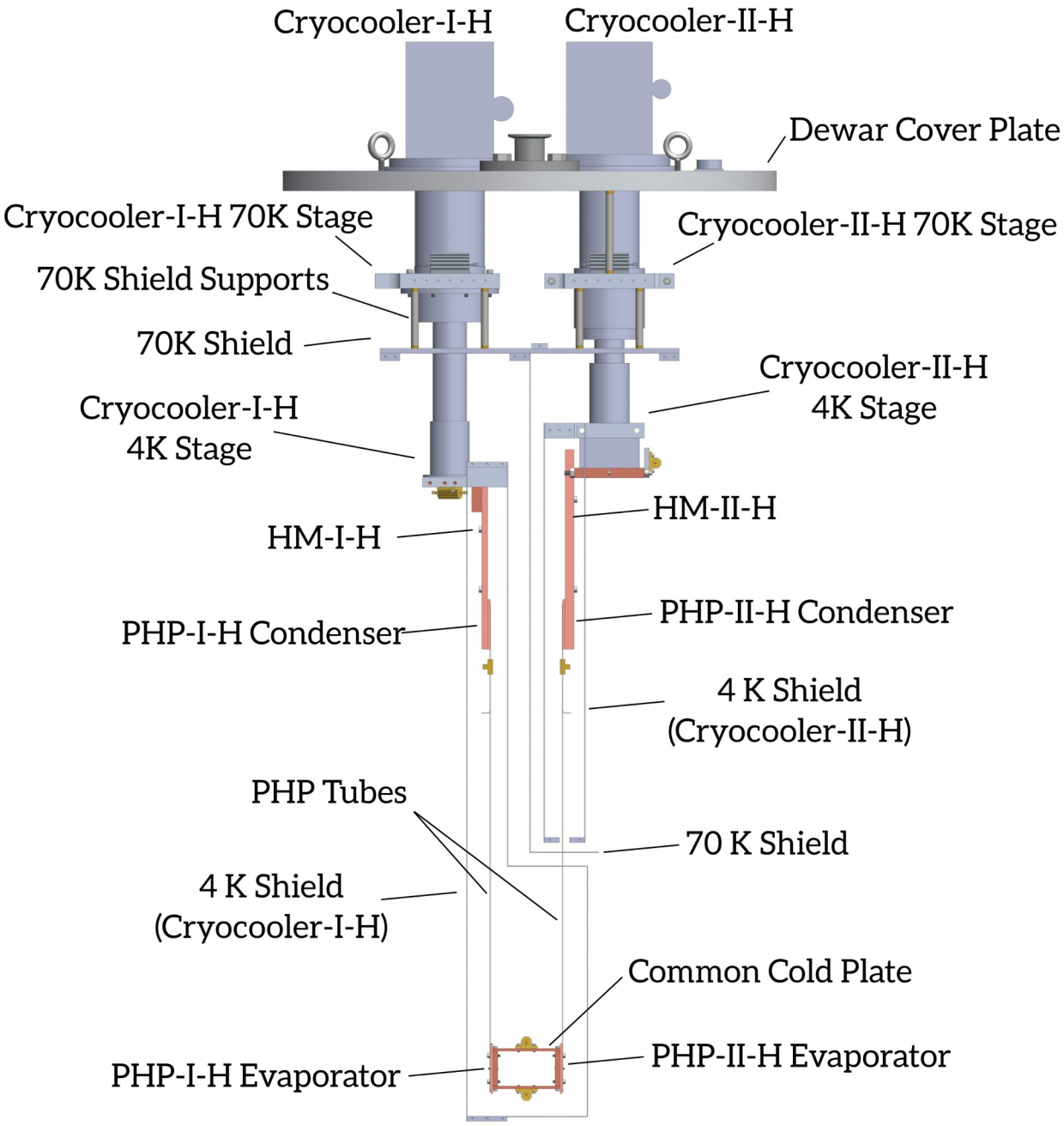

Figure 3.8. Solid model CAD profile view illustrating 4 K heat shielding for the helium PHPs within the helium PHP thermal switch facility. The 70 K shield is excluded from view for clarity (except for its upper plate).

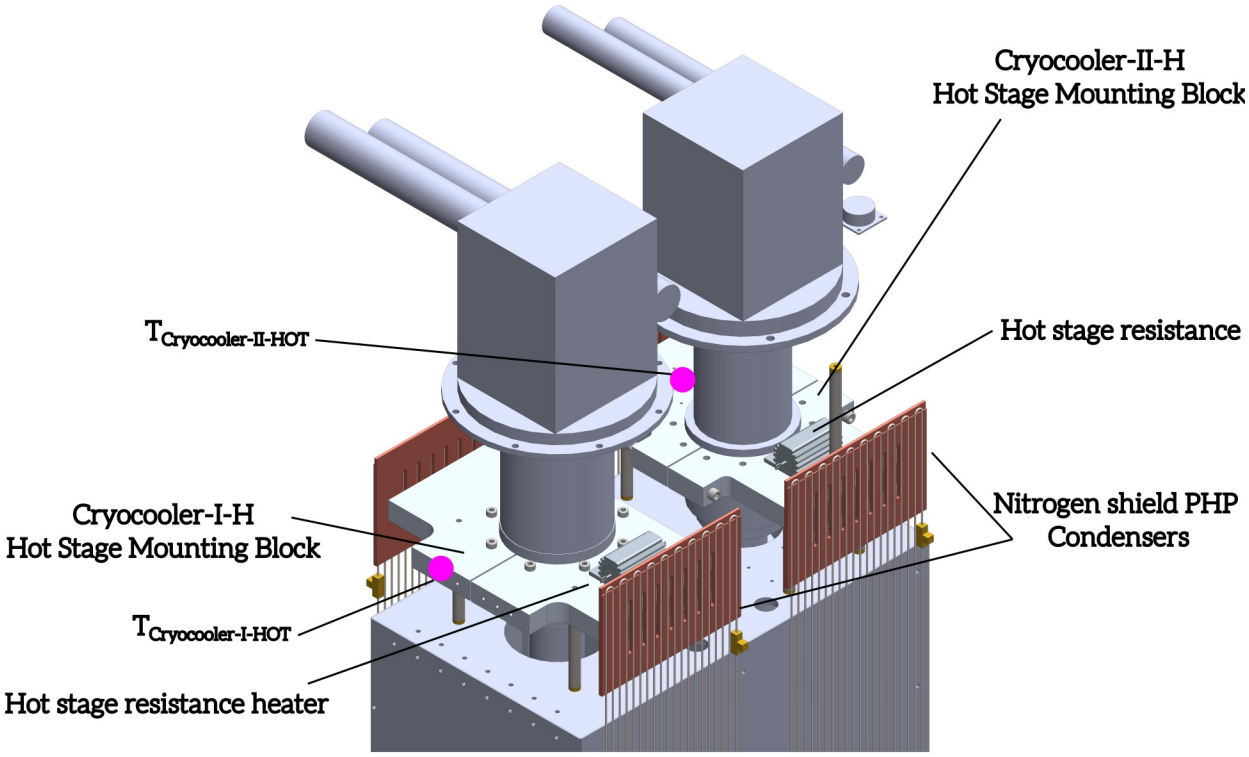

Figure 3.9. Solid model assembly detailing the connection between the nitrogen shield PHPs and the hot stages of Cryocooler-I-H and Cryocooler-II-H. Hot stage temperature sensors locations denoted by the pink markers.

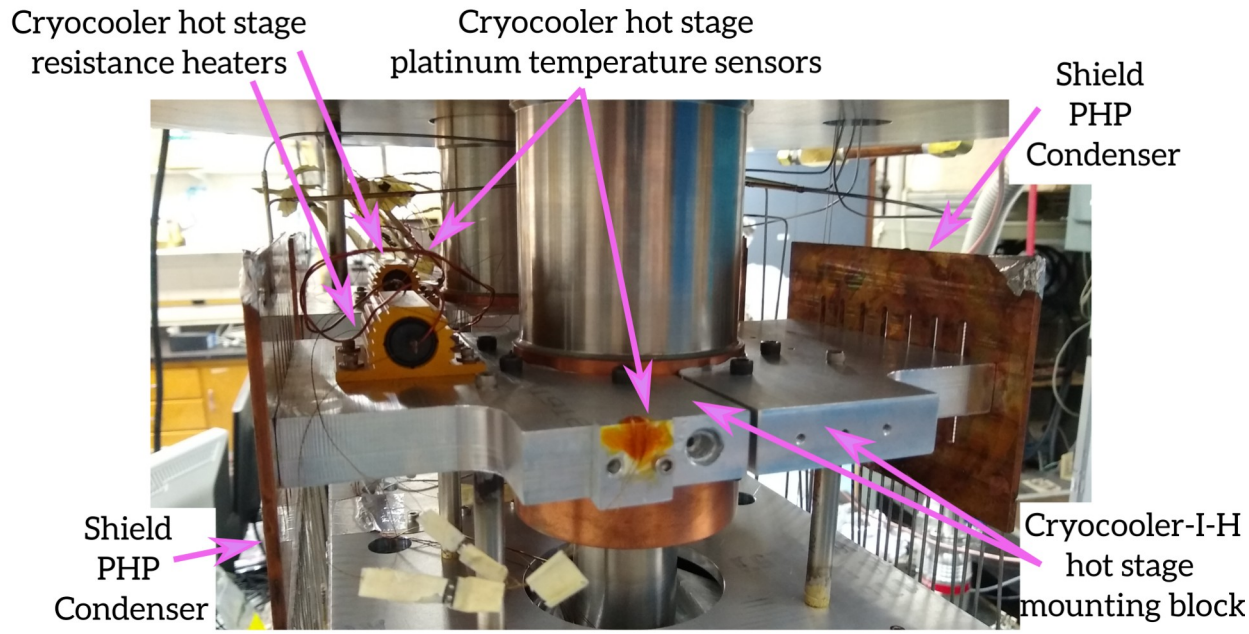

Figure 3.10. Image detailing the connection between the nitrogen shield PHPs and the cryocooler hot stages

A common cold plate assembly, depicted in Figure 3.11 and Figure 3.12, thermally and structurally connects the evaporators of PHP-I-H and PHP-II-H. The design is modified from that in the nitrogen PHP thermal switch test facility to mitigate the contact conductance issues seen in that facility. Here, indium sheets are used for all thermal component joints in the common cold plate assembly. Four electrical resistance heaters (40 Ω TE Connectivity model HSA2550RJ), attached to the common cold plate assembly between the PHP-I-H and PHP-II-H evaporator plates, are wired in series and powered with a programmable Keithley 2200-20-5 direct current power supply to provide the common cold plate heat load. The power supply uses a two wire measurement to accurately measure the power applied the common cold plate resistor, as the circuit is intentionally designed to have sufficiently low current that dissipation in the leads is negligible for all operating conditions.

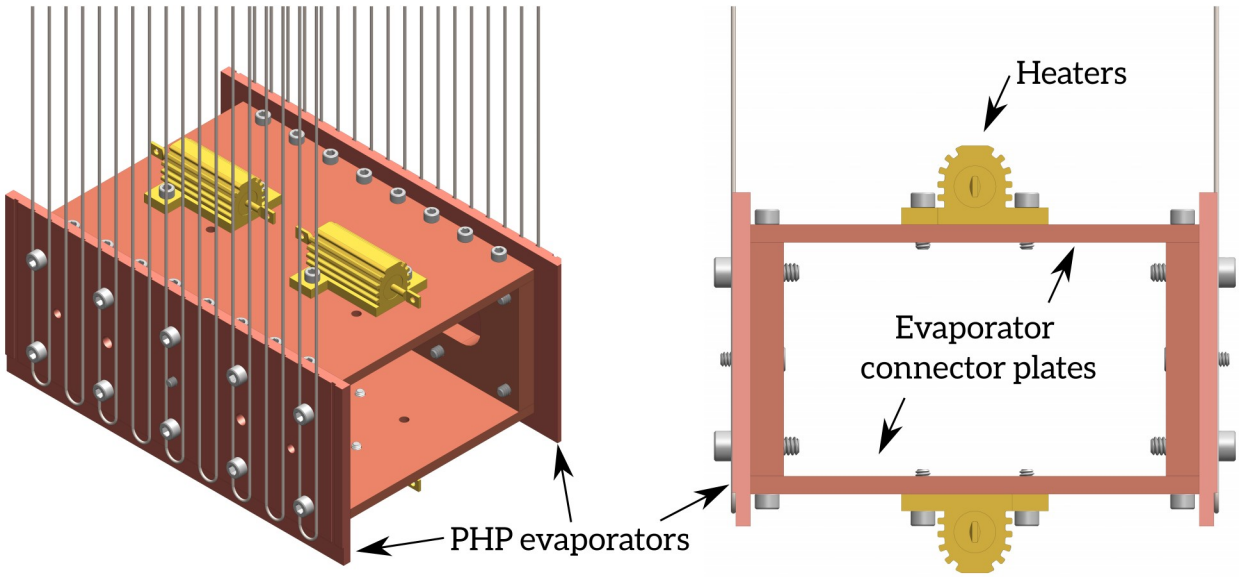

Figure 3.11. Solid model showing the details of helium PHP thermal switch assembly common cold plate

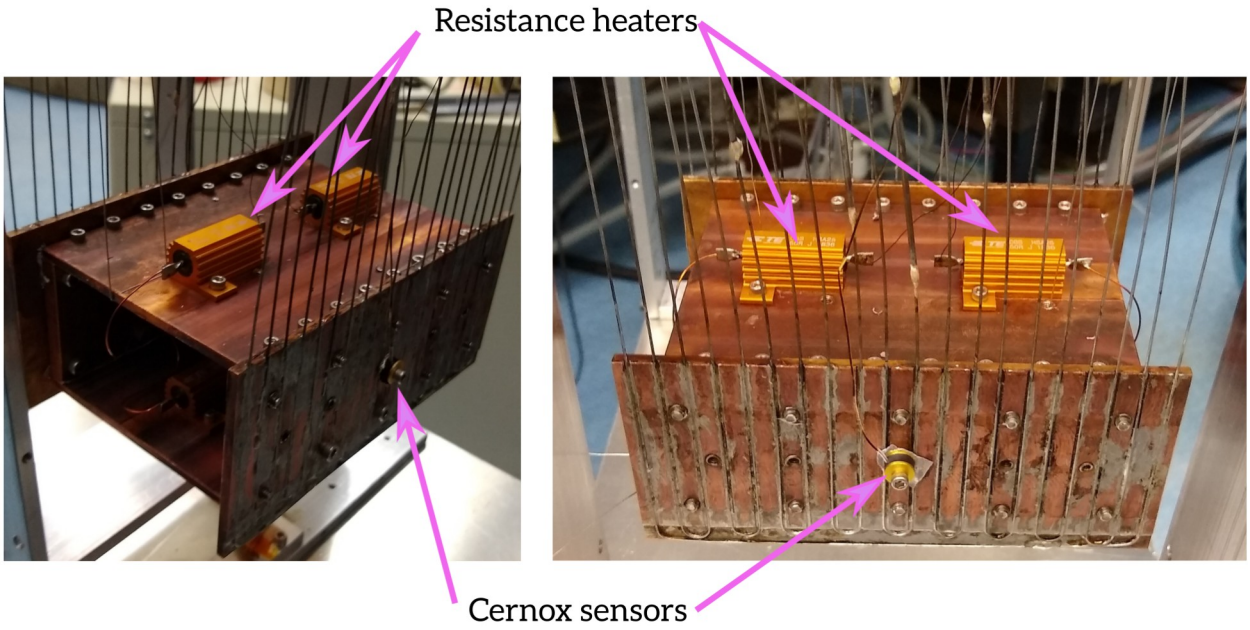

Figure 3.12. Images detailing the helium PHP thermal switch assembly common cold plate

The helium PHP thermal switch test facility also includes a set of actively cooled thermal shields, one directly attached to the cold stage of Cryocooler-I-H and the other directly attached to the cold stage of Cryocooler-II-H, shown in Figure 3.4 and Figure 3.8. These shields are labeled '4 K' shields as they remain at approximately 4 K when the associated cryocooler is active. The 4 K shields are included for a single purpose: allowing energy balances to be carried out on a system consisting of PHP-I-H, PHP-II-H, HM-I-H, HM-II-H, and the common cold plate without concern for the radiation heat transfer between these components and the 70 K shield. The net radiative load from the 70 K surfaces to the 4 K surfaces is expected to be small but on the order of the capacity of the helium PHPs (approximately 100 mW). In an actual engineering application, this small radiative load would be incident on the common cold plate and PHP tubes and would be removed via the PHP advective flow (along with the applied load at the common cold plate). Because this experiment is concerned about careful measurements of only the *advec-*

tive and *conduction* heat transfer modes within the PHP, it is convenient to ensure that the incident radiation load on the system of interest is negligible – hence the 4 K shield to shunt the radiation load around the PHPs, heat meters, and common cold plates and directly to the cryocooler cold stages. The situation is explained by schematic in Figure 3.13.

When the associated cryocooler is deactivated, however, the 4 K shield warms to the temperature of the inactive cold head (typically around 290 K). In addition to the '4 K' label becoming a misnomer in this situation, the situation presents an opportunity for small, non-negligible net radiation load on the PHP adiabatic section to develop. This owes to the large (about 285 K) temperature gradient which develops over the PHP switch adiabatic section in its OFF state. In such a scenario, the coldest parts of the PHP adiabatic tubes (nearest the common cold plate, which is at about 4 K) are much colder than the encapsulating '4 K' shield (now at 290 K), creating the opportunity for a parasitic radiative load between the hot '4 K' shield and the coldest tube surfaces on the OFF state PHP. Figure 3.14 roughly describes the surface temperature of the key components when this occurs. To limit the impact of characterized radiation parasitics clouding the OFF state PHP switch performance measurements, two mitigation steps are taken: OFF state testing is limited to only PHP-II-H[26] and an asymmetric '4 K' shield with a thermal break about midway through the PHP-II-H adiabatic section is used. With these steps, the larger section section of the '4 K' shield – which is attached to the Cryocooler-I-H and completely surrounds PHP-I-H, the common cold plate, and the coldest surfaces of PHP-II-H – always remains at 4 K, while only a

26 This (unfortunately) imposes the same constraint that the nitrogen PHP thermal switch test facility incurred, but for a different reason. Here, however, the limitation is purely related to the thermal management needs for characterizing the PHP switch performance and could easily be lifted for an application where the thermal loads do not need to be accuracy measured.

small section of the ‘4 K’ shield covering the warmest surfaces of PHP-II-H is attached to 290K Cryocooler-II-H. The asymmetric ‘4 K’ shield is shown in Figure 3.8 and Figure 3.4, with the schematic of Figure 3.14 depicting how this design limits the radiation-driving surface temperature differences with Cryocooler-II-H inactive.

Finally, note that 15 to 30 layers of MLI is inserted between all surfaces in the facility which may develop large temperature differences during operation with either Cryocooler-II-H active or inactive. This includes the volume between PHP-II-H and the ‘4 K’ shield attached to Cryocooler-II-H. However, MLI is likely somewhat optically transparent to radiation at wavelengths emitted from a 70 K surface, so the insulating effectiveness may be minimal. Indeed, evidence of a radiation parasitic incident on the adiabatic section of PHP-II-H is observed during testing with Cryocooler-II-H inactive. See Section 3.6.4 and Section 4.3 for a discussion of these results.

Although the 70 K shield is agnostic to which cryocooler is deactivated, the need for accurate energy accounting through the helium PHPs imposes a requirement that Cryocooler-I-H remain operating at all times. This is due to the fact that the 4 K shield encapsulating the common cold plate is sunk directly to the Cryocooler-I-H 4 K stage and must always be cooled to limit the difficult-to-quantify accurately radiation load into the common cold plate. For accurate characterization of the helium PHP switch performance, this radiation load removed through the helium PHPs must always be essentially zero. In an actual application such a shield would be entirely unnecessary; the radiation load would simply be absorbed by the common cold plate and re-

moved through the PHPs, as accurate measurements of the energy transported by the PHPs in this case would not be needed. Figure 3.13 is a schematic which compares these two scenarios.

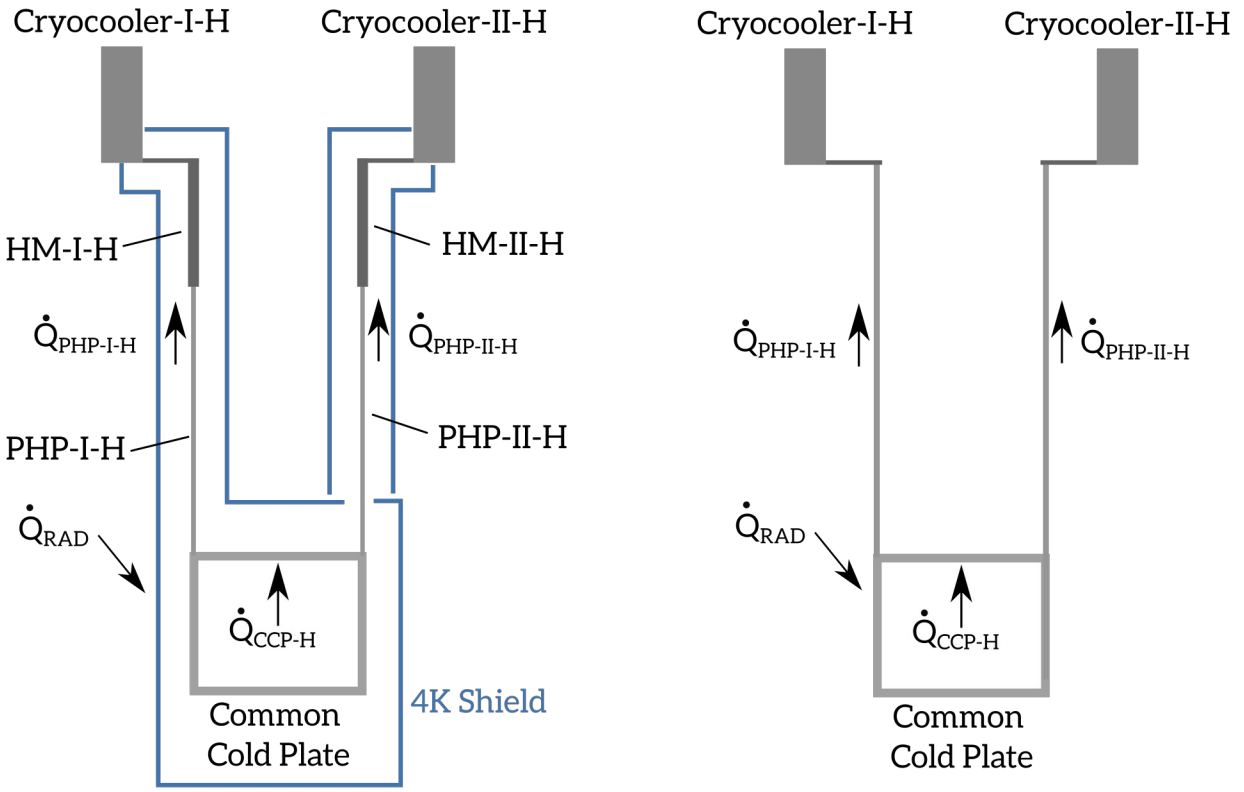

Figure 3.13. Schematic depicting the helium PHP thermal switch facility with 4K heat shield and heat meters (left) and an example application without 4K heat shield and heat meters (right). The radiation heat load indicated is from the 70 K shield to the 4 K shield.

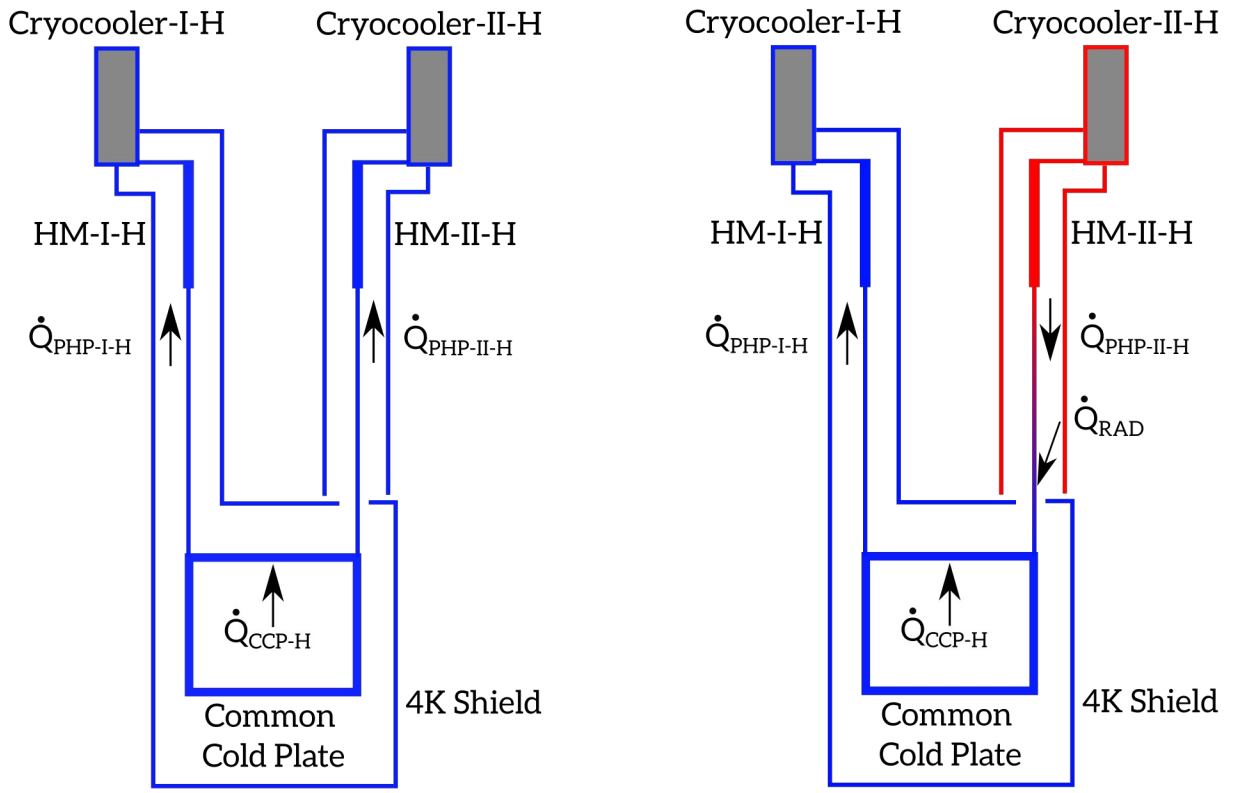

Figure 3.14. Schematic depicting the helium PHP thermal switch facility with 4 K heat shield with Cryocooler-II-H active (left) and inactive (right). 290 K surfaces are indicated by red and 4 K surfaces are indicated by blue, with gradients between these colors indicating an approximate temperature gradient. The radiation heat load indicates a parasitic from the '4 K' shield at 290 K to the cold adiabatic tubes of the PHP-II-H PHP.

3.2 Nitrogen heat shield PHP design and construction

The helium PHP thermal switch test facility uses four nitrogen PHP thermal switches to connect the 70 K shield to the hot stages of Cryocooler-I-H and Cryocooler-II-H. These PHPs are labeled PHP-I-NHS, PHP-II-NHS, PHP-III-NHS, and PHP-IV-NHS – where 'NHS' stands for 'nitrogen heat shield'. These heat shield PHPs are described by annotated solid model and actual assembly images in Figure 3.15 and by the design parameters in Table 3.2. The materials, design, assembly, and construction methods of these PHPs are nearly identical to those developed for the nitrogen PHP thermal switch test facility described previously in Section 2.2. In this application, how-

ever, temperature sensors are absent on the PHP condenser and evaporator plates, and each PHP always has its own dedicated fluid circuit.

Table 3.2. Nitrogen 70K shield PHP design information. X in a symbol subscript can be I, II, III, or IV depending on the PHP name column.

PHP Name → / **Parameter ↓**	**PHP-I-NHS**	**PHP-II-NHS**	**PHP-III-NHS**	**PHP-IV-NHS**
Associated Cryocooler	**Cryocooler-I-H**		**H-Cryocooler-II-H**	
Number of Parallel Tubes, $N_{PHP-X-NHS-TUBES}$	20			
Inner Tube Diameter, d_i [mm]	1.08			
Outer Tube Diameter, $d_{PHP-X-NHS,o}$ [mm]	1.47			
Adiabatic Section Length, $L_{PHP-X-NHS,ADIA}$ [mm]	267.00			
Condenser Section Length, $L_{PHP-X-NHS,COND}$ [mm]	102.00			
Evaporator Section Length, $L_{PHP-X-NHS,EVAP}$ [mm]	102.00			
Tube Spacing (center axis), $L_{PHP-X-NHS,TS}$ [mm]	7.63			
Condenser Section Width, $W_{PHP-X-NHS,COND}$ [mm]	153			
Evaporator Section Width, $W_{PHP-X-NHS,EVAP}$ [mm]	153			
Condenser Section Thickness, $TH_{PHP-X-NHS,COND}$ [mm]	3.56			
Evaporator Section Thickness, $TH_{PHP-X-NHS,EVAP}$ [mm]	3.56			
PHP Volume, $V_{PHP-X-NHS,PHP}$ [mm^3]	8505			

Two nitrogen shield PHPs are connected to each Cryocooler-I-H and Cryocooler-II-H, with the shield PHPs sized such that the entire radiation load on the 70 K shield can be removed by the set of shield PHPs connected to a single active cryocooler (while the other cryocooler is inactive

and its associated PHPs are dry). An initial (very) conservative estimate suggests approximately 30 W for the net radiation load on the 70 K shield. Since similarly sized PHPs used in the nitrogen PHP thermal switch test facility accommodated at least 16 W prior to dryout (see Figure 2.14), two are included per cryocooler here for a minimum heat trasnfer capacity of at least 32 W. The shield PHPs are connected to Cryocooler-I-H and Cryocooler-II-H via a set of mounting blocks, visualized by an annotated solid model assembly in Figure 3.9 and by images of the actual assembly in Figure 3.10. All thermal-mechanical joints in the cryocooler/mounting block/PHP condenser assembly use either an indium sheet or Apeizon N thermal vacuum grease to minimize contact resistance. The Cryocooler-I-H shield PHP mounting blocks are mechanically secured to the cryocooler with threaded fasteners provided on the Cryocooler-I-H cold head itself. However, neither the hot nor cold stage of Cryocooler-II-H has a mechanism for securing an external assembly because as the unit is specialized for cooling a bath of liquid helium rather than cooling experiment hardware. The shield PHP mounting block for Cryocooler-II-H therefore uses a clamping mechanism to grip the cylindrical surface of the hot stage. Finally, the PHP evaporators are thermally and mechanically secured with screws and Apiezon N thermal vacuum grease to the 70 K shield via a mounting plate visible in Figure 3.1 and Figure 3.3.

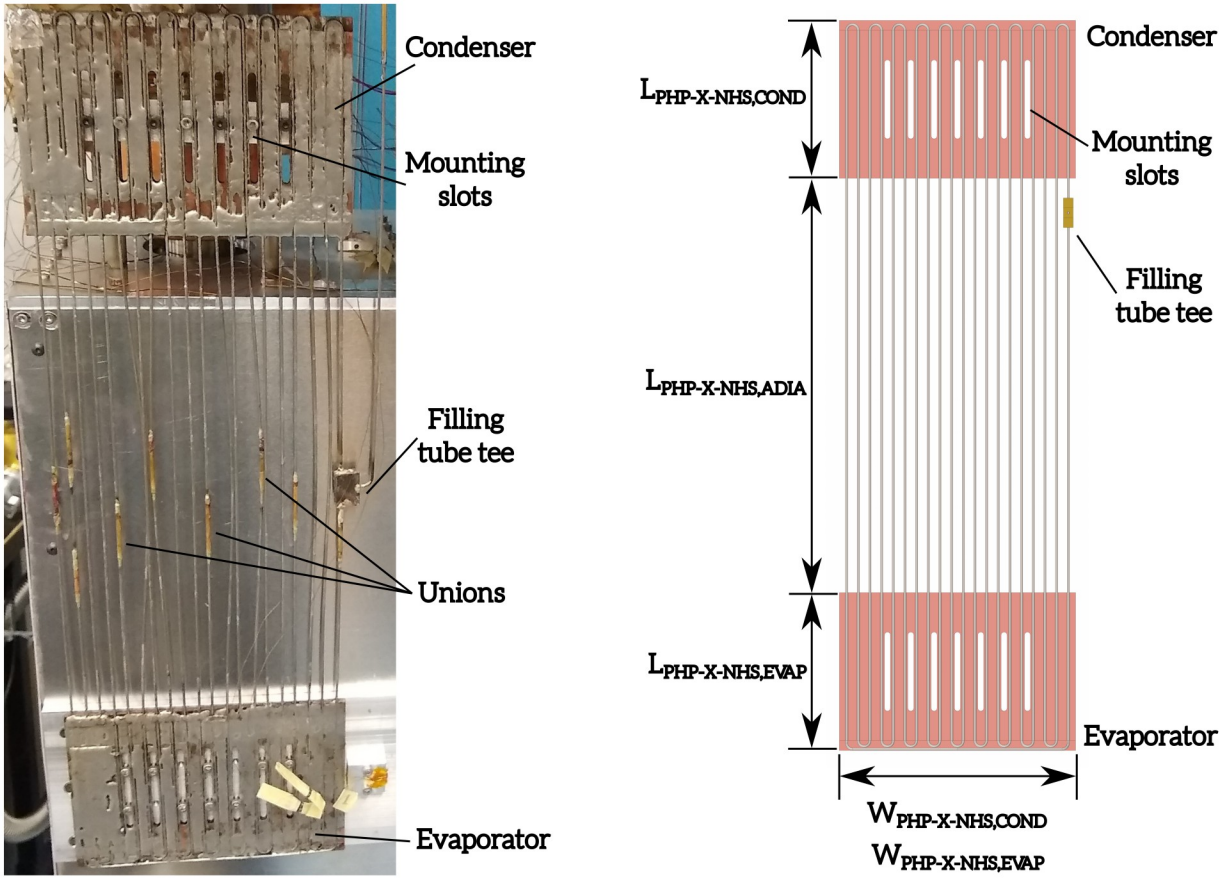

Figure 3.15. Annotated image (left) and solid model (right) of a nitrogen heat shield PHP assembly.

3.3 Helium PHP design and construction

The helium PHPs thermal switches, shown as solid model assemblies in Figure 3.17 and images of the actual assemblies in Figure 3.16, are conceptually similar to the nitrogen PHP switches presented previously in Section 2.2 and Section 3.2. Indeed the fabrication techniques use for construction are identical. However, several key design changes are made to accommodate the helium working fluid and the accompanying larger adiabatic section temperature gradient imposed in the OFF switch state. The most important update is to the PHP inner tube diameter, which is reduced to 0.51 mm from 1.08 mm as helium has a lower critical diameter than nitrogen (approximately 0.50 mm and 1.00 mm respectively, per Equation 1.9 and Figure 1.10). This he-

lium PHP inner diameter leaves much less safety margin than the nitrogen PHP to guarantee thermally driven advective flow (that is, the selected inner tube diameter is much closer to the critical diameter for the helium PHPs compared to the nitrogen PHPs), but successful helium PHP operation has been demonstrated with this geometry [44][45]. Additionally, the helium PHPs feature a single temperature sensor (a calibrated[27] Lakeshore Cryotronics model CX-1050-CU-HT) screwed to each evaporator and condenser plate, with locations indicated in Figure 3.17.

27 See Section 8.6 for calibration details

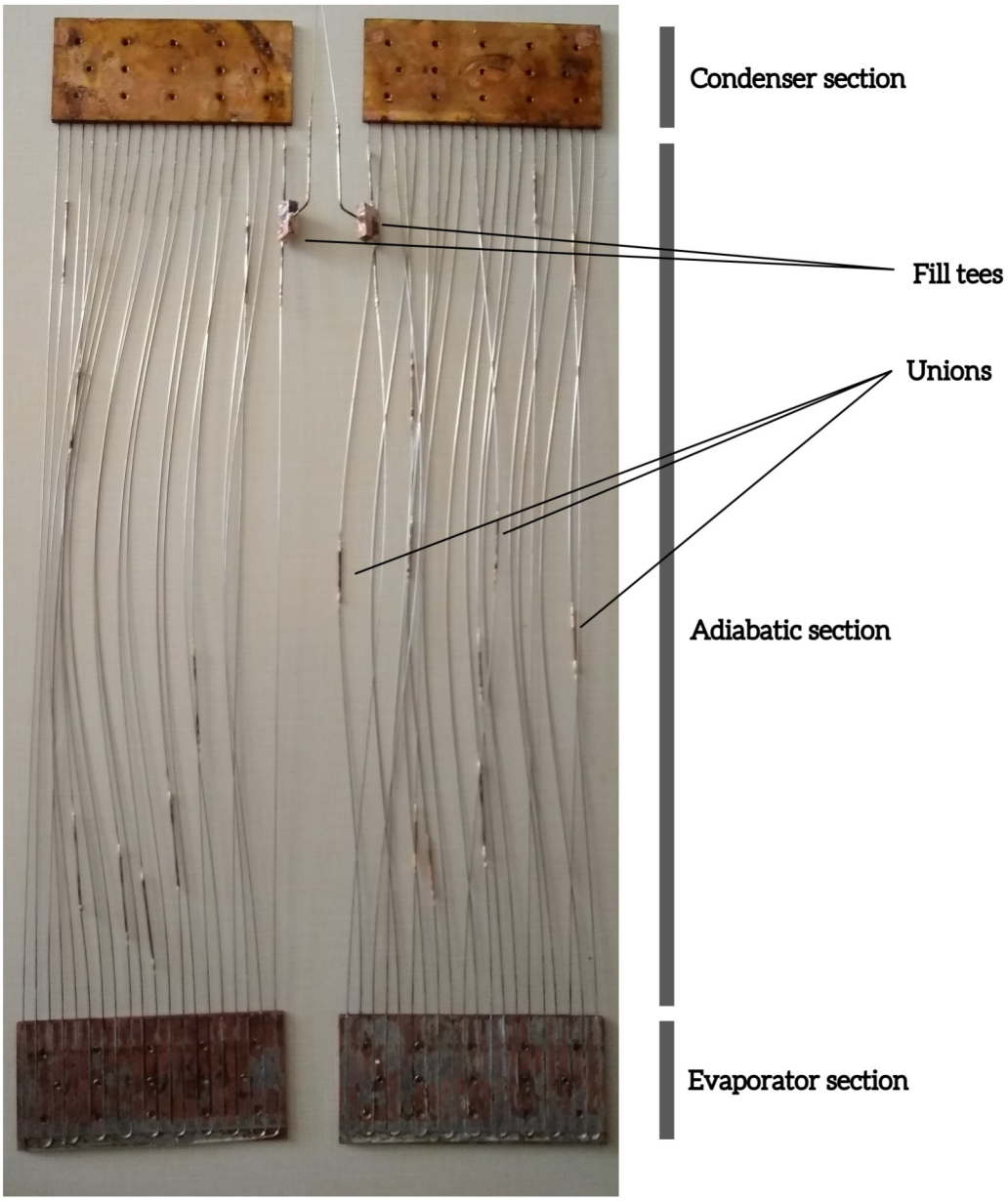

Figure 3.16. Image of the assembled PHP-I-H (right) and HPHP-II-H (left). Note that, prior to testing, the outermost tubes (in which the fill tees are attached) were modified to mach the tube routing of Figure 3.17.

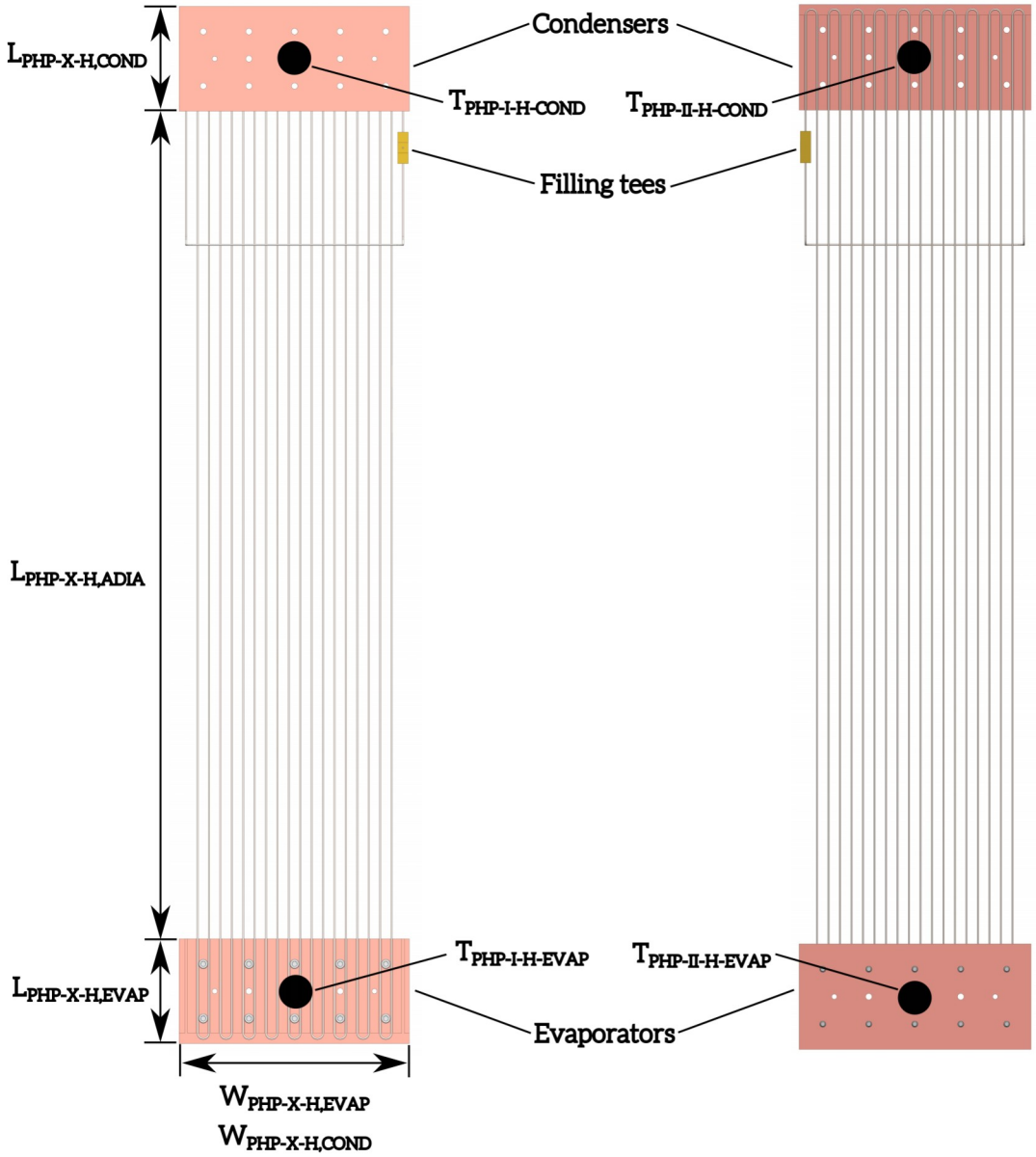

Figure 3.17. Solid model of the assembled PHP-I-H (right) and PHP-II-H (left). Temperature sensor locations indicated by black circles.

Thin sheets of indium between the sensors and PHP plates increase the contact conductance at the joint. This differs from the nitrogen PHP thermal switches where three sensors are used for each evaporator and condenser plate. The reduction in sensor count reflects both budget constraints and the higher accuracy of the Cernox sensors.

As with the nitrogen PHP thermal switches, the helium PHP thermal switch design is based on an approximately scaling of the total maximum PHP heat transfer per internal cross sectional area reported by other helium PHP studies [45][35]. This is intended to *roughly* allow about 0.6 W of heat transfer capacity per PHP before dryout for the PHPs built in the present work. The helium PHP adiabatic lengths are twice as large as those of the nitrogen proof-of-concept PHPs (501 mm versus 254 mm). This change increases the conduction length in the OFF state of the thermal switch (providing better thermal isolation) while negligibly impacting the effective conductance in the ON state [52]. The number of parallel tubes is also decreased slightly (18 vs 20). This is an unintentional change which is the consequence of a fix to resolve performance issues arising from an initial configuration consisting of 20 parallel tubes, a different filling tee location, and an unequal evaporator tube loop length; Section 3.6.5 provides more details regarding this change. Finally, note that the helium PHP thermal switches are only tested in the 2-circuit configuration. The reason for this is multifold but mainly due to the fact that results from the nitrogen PHP thermal switch in the 1-circuit configuration yielded lower ON state performance and indicated no benefit to this configuration. Table 3.3 summarizes the design information for the helium PHP thermal switches and can be compared with the nitrogen PHP thermal switch design described in Table 2.2.

Table 3.3. Helium PHP design information. X in a symbol subscript can be I or II depending on the PHP name column.

PHP Name → / **Parameter ↓**	**PHP-I-H**	**PHP-II-H**
Associated Cryocooler	**Cryocooler-I-H**	**Cryocooler-II-H**
Number of Parallel Tubes, $N_{PHP-X-H-TUBES}$	18	
Inner Tube Diameter, $d_{PHP-X-H,i}$ [mm]	0.51	
Outer Tube Diameter, $d_{PHP-X-H,o}$ [mm]	0.72	
Adiabatic Section Length, $L_{PHP-X-H,ADIA}$ [mm]	501.00	
Condenser Section Length, $L_{PHP-X-H,COND}$ [mm]	57.00	
Evaporator Section Length, $L_{PHP-X-H,EVAP}$ [mm]	57.00	
Tube Spacing (center axis), $L_{PHP-X-H,TS}$ [mm]	6.93	
Condenser Section Width, $W_{PHP-X-H,COND}$ [mm]	140.00	
Evaporator Section Width, $W_{PHP-X-H,EVAP}$ [mm]	140.00	
Condenser Section Thickness, $TH_{PHP-X-H,COND}$ [mm]	3.40	
Evaporator Section Thickness, $TH_{PHP-X-H,EVAP}$ [mm]	3.40	
PHP Volume, $V_{PHP-X-H,PHP}$ [cm^3]	2566	

3.4 Heat meter design, fabrication, and calibration

The conduction heat meters used to independently measure the heat load carried through PHP-I-H and PHP-II-H (HM-I-H and HM-II-H) – shown in Figure 3.18, Figure 3.19, and Figure 3. – are conceptually similar to those used in the nitrogen PHP thermal switch experiment. Again, these instruments are constructed from machined rectangular 110 copper bars to a specified length and cross sectional area, with temperature sensors attached at each end of the device. As with the PHPs themselves, however, there are key design changes made to accommodate several issues which arise from the lower (approximately 4 K) operating temperature. Table 3.4 tabulates the design information for HM-I-H and HM-II-H and can be compared with the analogous speci-

fications for HM-I-N and HM-II-N from the nitrogen PHP thermal switch test facility in Table 2.3.

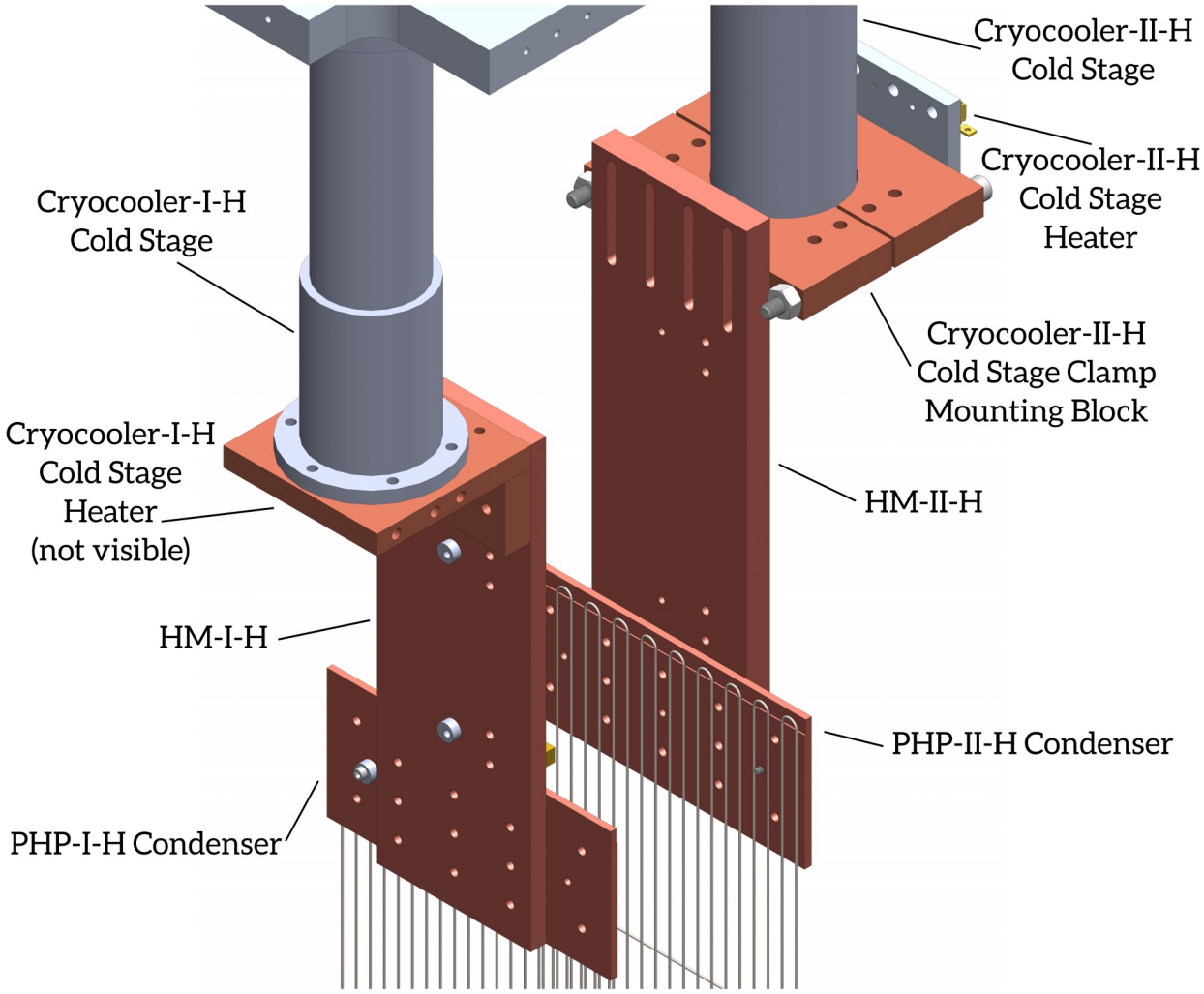

Figure 3.18. Solid model assembly detailing the helium PHP thermal switch to cryocooler connections

Table 3.4. Helium PHP thermal switch test facility heat meter design information.

Heat Meter Name → / **Parameter ↓**	**HM-I-H**	**HM-II-H**
Associated Cryocooler	Cryocooler-I-H	Cryocooler-II-H
Material	110 Copper	
Length between temperature sensors, L_{HM-X-H} [m]	0.076200	0.114300
Area cross section, A_{HM-X-H} [m^2]	0.000567	0.000871
Area to length ratio, $\frac{A_{HM-X-H}}{L_{HM-X-H}}$ [m]	0.007441	0.007620
Calibration Regime	3K – 6K	3K – 6K

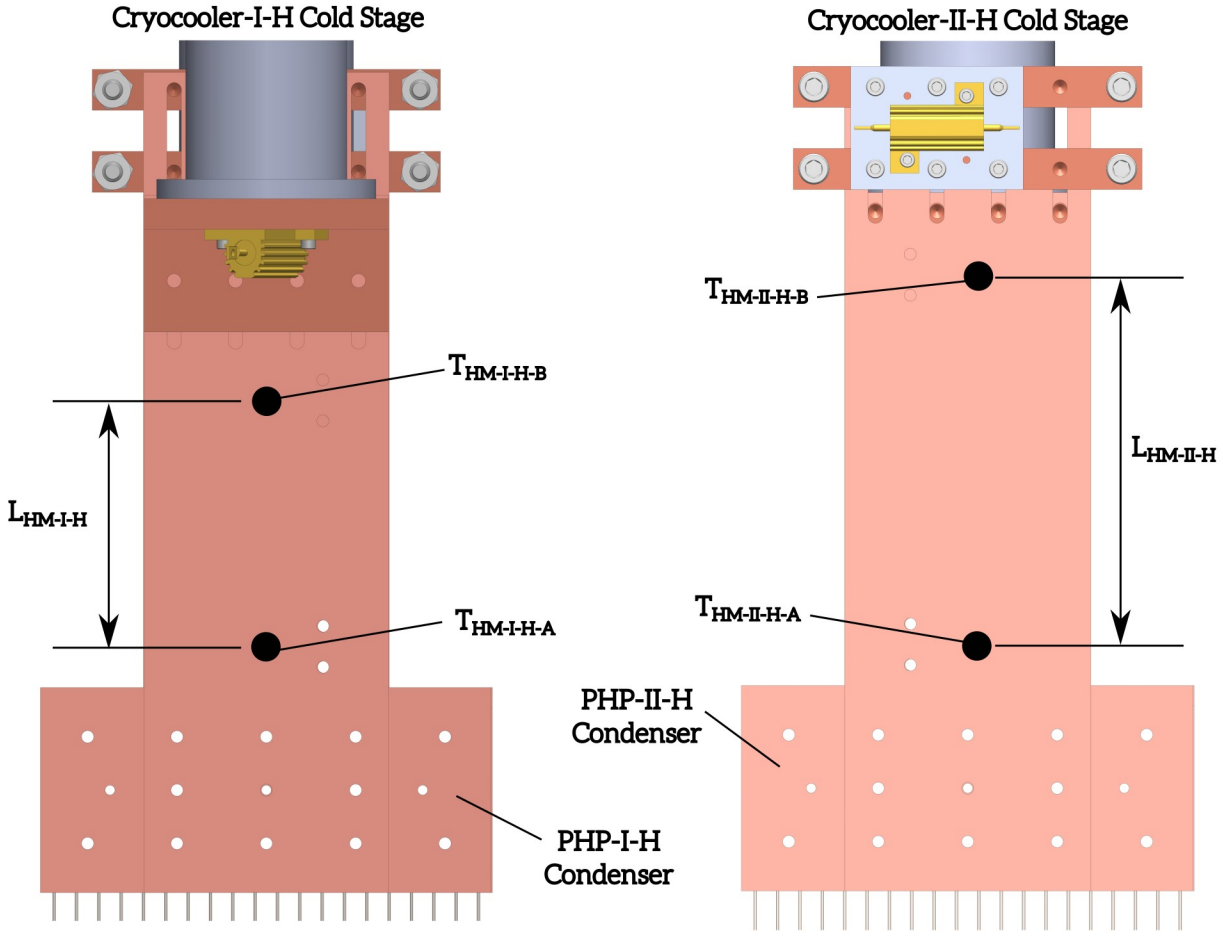

Figure 3.19. Solid model assembly of the helium PHP thermal switch heat meters HM-I-H (left) and HM-II-H (right) showing the location of the Cernox temperature sensors.

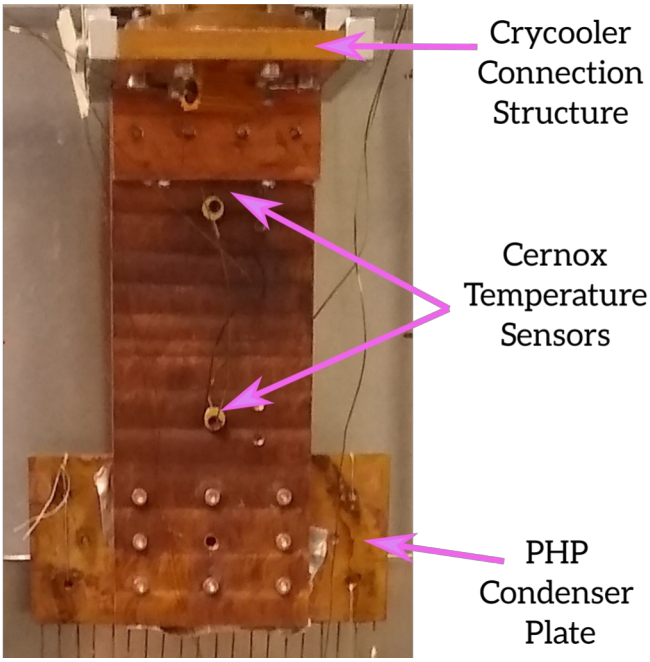

Figure 3.20. Image of the helium PHP thermal switch HM-I-H and its mating components.

The most important design criteria for the HM-I-H and HM-II-H is balancing the conflicting needs of high sensitivity and accuracy of the conduction measurement (which requires a larger temperature drop over the meter) and maintaining a high temperature at the cryocooler cold head such that sufficient cooling power is available to remove the load from the heat meter (which requires a low temperature drop over the meter). This compromise is highlighted in Figure 3.21, which shows decreasing relative uncertainty in the heat flow measurement and increasing temperature drop as the heat load increases through the meter; various area-to-length ratios are plotted, with 0.0075 m selected for the actual HM-I-H and HM-II-H design in order to keep the temperature drop below 0.150 K at the expected maximum heat load of 0.75 W. Note that in principle this same balance is also required for heat meters HM-I-N and HM-II-N in the nitrogen PHP thermal switch test facility, but the higher operating temperature in that case (approximately 80

K) means the cryocoolers retain sufficient cooling power well below 40 K, easily allowing temperature drops of up to 10 K over the heat meters, decreasing the relevancy of the issue.

The heat meters in the helium PHP thermal switch test facility use Cernox temperature sensors (calibrated[28] Lakeshore Cryotronics model CX-1050-CU-HT) as opposed to the platinum temperature sensors (Lakeshore Cryotronics model PT-102[29]) used in the nitrogen PHP thermal switch test facility. Two reasons drive this change: the need for higher accuracy (±0.003 mK vs ±0.250 mK) and the need to read temperatures near 4 K. The increased accuracy is necessary to allow allow measurements of the conduction heat flux with the small (approximately 0.150 K) temperature drop expected over the heat meter, while the abandonment of platinum is necessary because the electrical resistivity sensitivity of the metal versus temperature plummets at temperatures lower than 25 K, prohibiting their use in such a temperature range. The Cernox temperature bobbins are attached to the heat meters via screws and a thin layer of indium to increase contact conductance between the sensor and heat meter.

28 See the Appendix, Section 8.6 for calibration details

29 See the Appendix, Section 8.4 for calibration details.

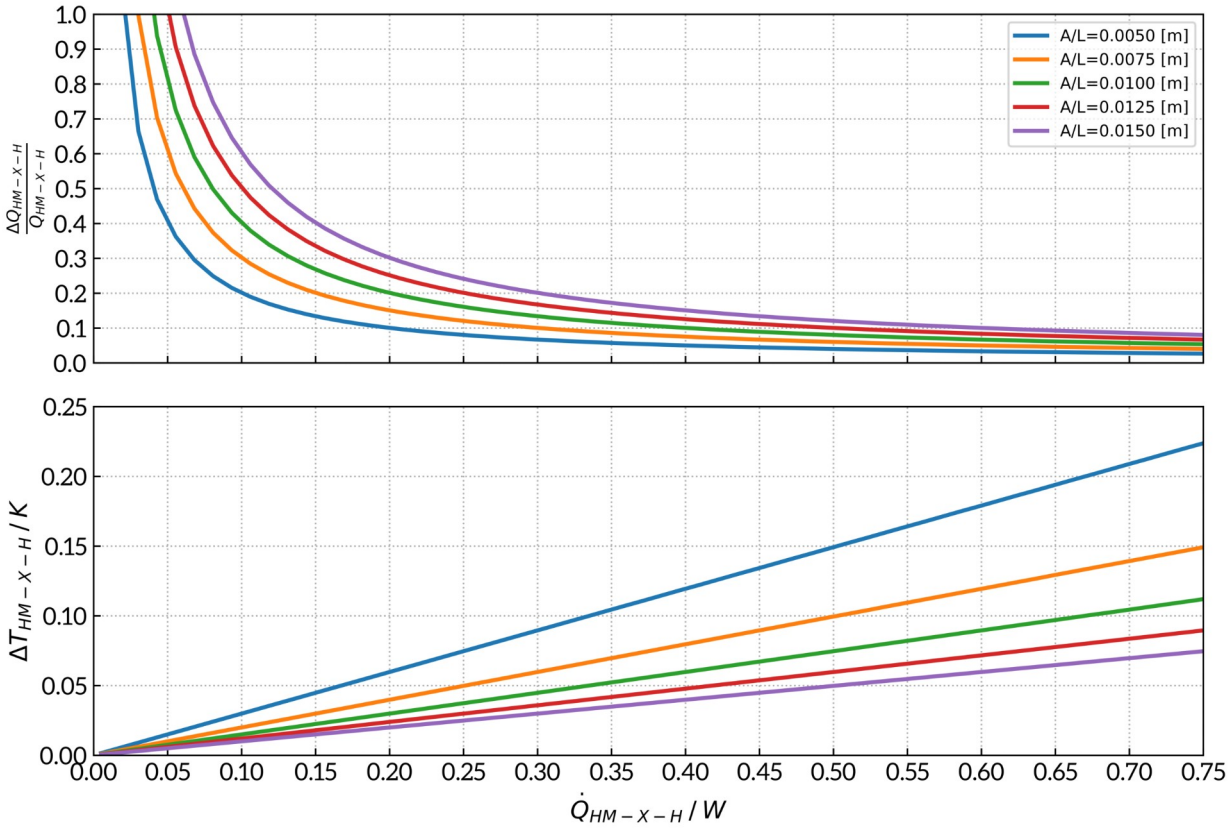

Figure 3.21. Modeled helium PHP thermal switch heat meter relative accuracy (top) and temperature drop (bottom) as a function of heat load for different area-to-length ratios. Assumes constant thermal conductivity of RRR100 copper at 4.2 K. Uncertainties reflect manufacturer long-term repeatability for the Cernox sensors (+- 3 mK).

The heat meter conductance, which is again temperature and impurity dependent at the temperatures of interest for the helium PHP thermal switch experiments, is calibrated for both HM-I-H and HM-II-H in the range 3 K to 6 K. The heat meter calibration setup varies slightly from the facility setup described in this section to this point, with PHP-I-H and PHP-II-H physically removed from the facility and a resistance heater instead installed at the former locations of the PHP-I-H and PHP-II-H condensers. All radiation shielding remains unchanged for this modified calibration facility setup. In this arrangement, the resistance heaters supply a known, well characterized heat load to the heat meters for calibration. To calibrate the heat meters, a series of measurements are obtained with sweeps of both the supplied electric heat load and the heat meter

temperature furthest from the cryocoolers ($T_{HM-I-H-A}$ and $T_{HM-II-H-A}$). The calibration points are then fit using a least squares regression to the function forms of

$$\dot{Q}_{PHP-I-H} = A_I T_{HM-I-H,A} + B_I T_{HM-I-H,B} + C_I T_{HM-I-H,A}^2 + D_I T_{HM-I-H,B}^2 + E_I \quad (3.1)$$

$$\dot{Q}_{PHP-II-H} = A_{II} T_{HM-II-H,A} + B_{II} T_{HM-II-H,B} + C_{II} T_{HM-II-H,A}^2 + D_{II} T_{HM-II-H,B}^2 + E_{II} \quad (3.2)$$

. The idea here is that the functional form of the conductance should be *roughly* quadratic in the temperature difference across the meter for temperatures between 3 K and 6 K as the thermal conductivity of copper is approximately linear with temperature in this range. The heat flow can be calculated by integrating the (temperature-linear) thermal conductivity while accounting for any bias stemming from electrical noise in the temperature sensor electrical signals

$$\dot{Q}_{PHP-I-H} = -\int_{T_{HM-I-H,A}}^{T_{HM-I-H,B}} k_{HM-I-H}(T) \frac{A_{HM-I-H}}{L_{HM-I-H}} dT + \dot{Q}_{OFFSET,HM-I-H} \quad (3.3)$$

$$\dot{Q}_{PHP-II-H} = -\int_{T_{HM-II-H,A}}^{T_{HM-II-H,B}} k_{HM-II-H}(T) \frac{A_{HM-II-H}}{L_{HM-II-H}} dT + \dot{Q}_{OFFSET,HM-II-H} \quad (3.4)$$

. The integrated result should be represented well over the narrow 3 K to 6 K temperature range by Equation 3.1 and Equation 3.2. Table 3.5 shows the range of heat loads and temperature ranges sampled for each heat meter for the calibration and the calibrated regression coefficients for use in Equation 3.1 and Equation 3.2.

Table 3.5. Helium PHP thermal switch test facility heat meter calibration details. X in a symbol subscript can be I or II depending on the column.

Heat meter name→	HM-I-H	HM-II-H
Parameter ↓ **Calibration regime→**	3K–6K	3K–6K
Number of calibration samples in data set	230	173
Range of supplied electric heat loads [W]	0.00 to 1.2	0.00 to 0.80
Fit Coefficient A_X	0.73918258	-3.55284524
Fit Coefficient B_X	-0.88219318	3.74612241
Fit Coefficient C_X	0.54248548	1.09735214
Fit Coefficient D_X	-0.52587252	-1.12000867
Fit Coefficient E_X	0.17656371	-0.42656031

Since the Cernox sensors lack sensitivity near room temperature, HM-II-H is not calibrated near 290 K. Instead, the parasitic heat load through PHP-II-H in the OFF switch state is calculated during the PHP performance experiments by a system energy balance

$$\dot{Q}_{PHP-II-H} = \dot{Q}_{CCP-H} - \dot{Q}_{PHP-I-H} \tag{3.5}$$

, where $\dot{Q}_{PHP-I-H}$ is the heat load through PHP-I-H, $\dot{Q}_{PHP-II-H}$ is the heat load through PHP-II-H, and $\dot{Q}_{CCP-H}$ is the electric head load applied to the common cold plate. This is possible because the radiation load on HM-I-H, PHP-I-H, and the common cold plate is negligible due to the always active 4 K shield (see Figure 3.14) and the fact that both the measurements of $\dot{Q}_{CCP-H}$ and $\dot{Q}_{PHP-I-H}$ are highly accurate, therefore allowing an accurate calculation of $\dot{Q}_{PHP-II-H}$.

Figure 3.22 plots the error between the actual applied heat load through the heat meter and the calibration fit predicted heat load through heat meter (from Equation 3.1 and Equation 3.2), for each calibration point, as a function of the applied heat load during the calibration. This shows

that most of the calibration points are associated with heat loads lower than about 0.6 W, which corresponds to the maximum heat load expected through each helium PHP based on data gathered from similarly constructed devices [52,45]. However, the helium PHPs tested in this work under some conditions measured larger heat loads before dryout (see Section 3.6.2), requiring a small amount of extrapolation beyond the calibrated domain. Section 3.6.1 discusses the accuracy of these extrapolations.

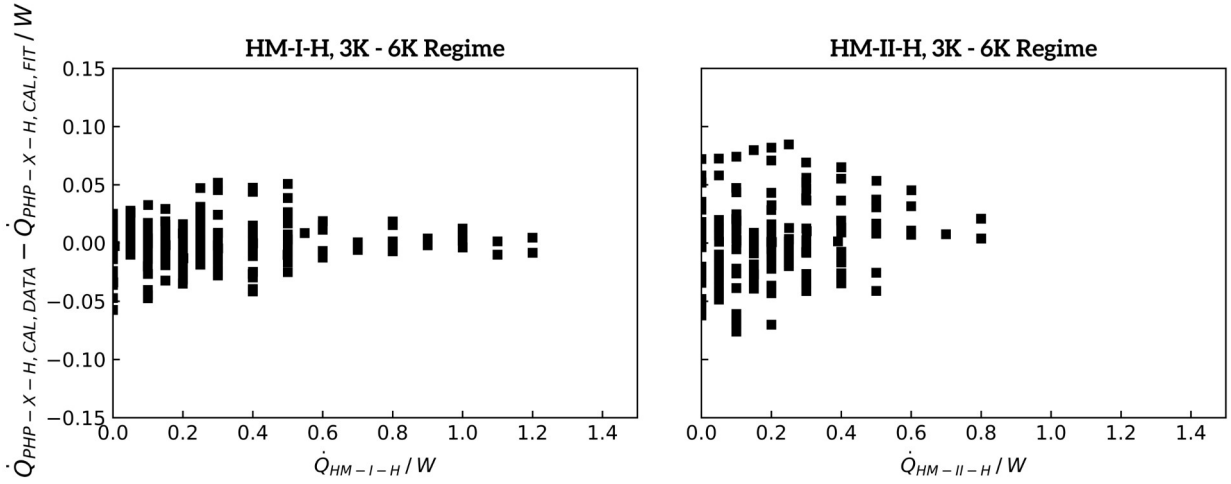

Figure 3.22. Difference between applied heat load and the calibration fit predicted heat load as a function of the for the heat meters in the helium PHP thermal switch test facility. HM-I-H and HM-II-H calibration measures are in the 3K-6K regime.

Figure 3.23 slightly recasts the calibration data of Figure 3.22 to show the distribution of errors in histogram form. The normal-looking distribution suggests that calibration error is related to the random noise from the temperature measurements and not caused by the fitting procedure or choice of equation. Based on the results in this plot, the uncertainty in the heat meter measurements is estimated at ±0.050 W for HM-I-H and ±0.075 W for HM-II-H, independent of the temperature measurements.

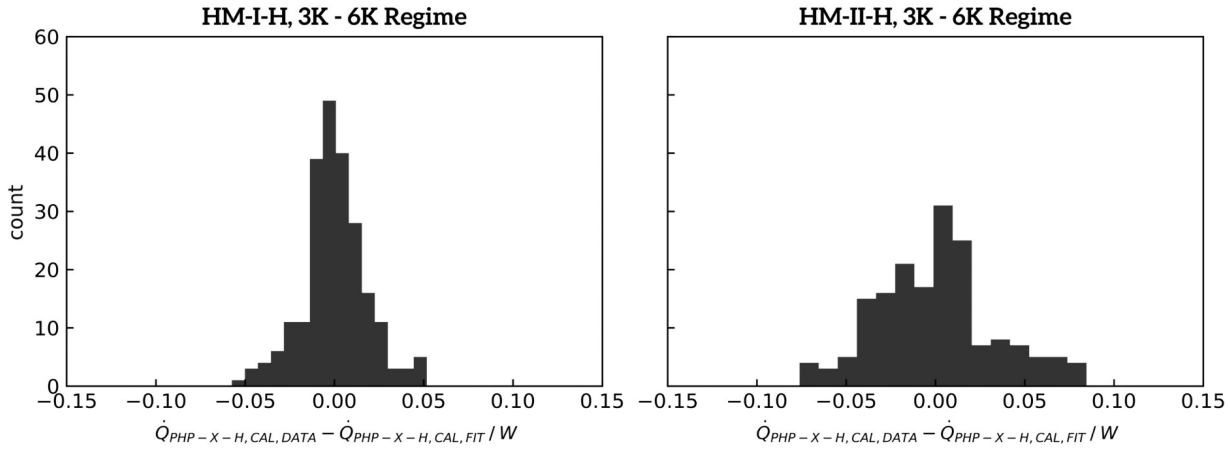

Figure 3.23. HM-I-H and HM-II-H histogram of errors. HM-I-H and HM-II-H calibration measures are in the 3K-6K regime.

3.5 Measurements and performance characteristics

To test the helium PHP thermal switch performance in both the ON and OFF switch states, the facility allows measurements or calculations of several key experiment parameters listed in Table 3.6. These are similar to the measurements and calculations in the nitrogen PHP thermal switch facility, with a few modifications and additions.

There are now four measurements – via uncalibrated platinum temperature sensors – which monitor the temperature at various locations on the 70 K shield. The purpose of these is to ensure the shield is at a sufficiently uniform temperature and check that the nitrogen shield PHPs are operating nominally. Two additional uncalibrated platinum temperature sensor measurements monitor provide temperature measurements of the Cryocooler-I-H and Cryocooler-II-H hot stage temperature and are used as feedback for the respective temperature controllers.

Table 3.6. Measurements provided by the helium PHP thermal switch test facility

Quantity	Measurement Devices(s)	Comments
$T_{SHIELD-UPPER}$	Uncalibrated Lakeshore Cryotronics PT-102 sensor	See Figure 3.3 and Figure 3.9 for locations
$T_{SHIELD-LOWER}$		
$T_{SHIELD-SIDE-A}$		
$T_{SHIELD-SIDE-B}$		
$T_{Crycooler-I-HOT}$		
$T_{Crycooler-II-HOT}$		
$T_{HM-I-H-A}$	Lakeshore Cryotronics CX-1050-CU-HT Cernox sensor	See Figure 3.19 for locations See Appendix 8.6 for calibration details
$T_{HM-I-H-B}$		
$T_{HM-II-H-A}$		
$T_{HM-II-H-B}$		
$T_{PHP-I-H,COND}$		See Figure 3.17 for locations See Appendix 8.6 for calibration details
$T_{PHP-II-H,COND}$		
$T_{PHP-I-H,EVAP}$		
$T_{PHP-II-H,EVAP}$		
$\dot{Q}_{CCP-H}$	Keithley-2200-20-5 direct current power supply	See Table 3.8
$\dot{Q}_{PHP-I-H}$	Not applicable – calculated quantity	See Equation 3.1 [+] indicates heat flow from common cold plate to the Cryocooler-I-N cold head.
$\dot{Q}_{PHP-II-H}$		See Equations 3.2 and 3.5 [+] indicates heat flow from common cold plate to the Cryocooler-II-N cold head [-] indicates heat flow direction from Cryocooler-II-N cold head to common cold plate (parasitic)
$k_{PHP-I-H,EFF}$		See Equation 3.6
$k_{PHP-II-H,EFF}$		See Equation 3.7
$UA_{PHP-I-H,EFF}$		See Equation 3.8
$UA_{PHP-II-H,EFF}$		See Equation 3.9
$SR_{PHP-II-H}$		See Equation 3.10
$FR_{PHP-I-H}$		See Equation 1.14 with $T_{SAT}=3.6\,K$ and Appendix 8.3
$FR_{PHP-II-H}$		

These six platinum temperature sensors are not used in calculations which determine the helium PHP switch performance. All temperature measurements used in the helium PHP switch performance calculations are obtained with calibrated Cernox CX-1050-CU-HT sensors. These include the temperatures on the evaporators and condensers of PHP-I-H and PHP-II-H and those at each end of HM-I-H and HM-II-H.

Heat flows through HM-I-H and HM-II-H ($\dot{Q}_{PHP-I-H}$ and $\dot{Q}_{PHP-II-H}$) are defined by Equation 3.1, Equation 3.2, and the coefficients of Table 3.5. These quantities again are defined with signs indicating the direction of heat flow through the PHP (positive indicates a heat transfer moving from the 'evaporator' to the 'condenser', and negative indicates a parasitic load moving from the 'condenser' the 'evaporator'). The electric heat load applied to the common cold plate, $\dot{Q}_{CCP-H}$, is measured directly by the Keithley-2200-20-5 power supply driving the resistance heater. The effective thermal conductivity and effective conductance of the helium PHP thermal switches are defined in the same sense as for the nitrogen PHP thermal switches

$$k_{PHP-I-H,EFF} = \frac{|\dot{Q}_{PHP-I-H}|}{|T_{PHP-I-H,COND} - T_{PHP-I-H,EVAP}|} \frac{L_{PHP-I-H,ADIA}}{N_{PHP-I-H,TUBES}\,\pi\left(\frac{d_{PHP-I-H,o}}{2}\right)^2} \tag{3.6}$$

$$k_{PHP-II-H,EFF} = \frac{|\dot{Q}_{PHP-II-H}|}{|T_{PHP-II-H,COND} - T_{PHP-II-H,EVAP}|} \frac{L_{PHP-II-H,ADIA}}{N_{PHP-I-H,TUBES}\,\pi\left(\frac{d_{PHP-II-H,o}}{2}\right)^2} \tag{3.7}$$

$$UA_{PHP-I-H,EFF} = \frac{|\dot{Q}_{PHP-I-H}|}{|T_{PHP-I-H,COND} - T_{PHP-I-H,EVAP}|} \tag{3.8}$$

$$UA_{PHP-II-H,EFF} = \frac{|\dot{Q}_{PHP-II-H}|}{|T_{PHP-II-H,COND} - T_{PHP-II-H,EVAP}|} \tag{3.9}$$

. Finally, the switching ratio is again measured only for PHP-II-H – due to the 4 K shielding energy balance constraints discussed previously – and is defined as

$$SR_{PHP-II-H} = \frac{UA_{PHP-II-H,EFF,ON}}{UA_{PHP-II-H,EFF,OFF}} \tag{3.10}$$

. As is the case with the nitrogen PHP thermal switch measurements, in general, both the numerator and denominator of Equation 2.15 can vary with the PHP condenser and evaporator temperatures, heat load, and fill ratio. However, since the OFF state condenser and evaporator temperature difference of PHP-II-H is very large relative to that in the ON state, $UA_{PHP-II-H,EFF,OFF}$ is several orders of magnitude smaller than $UA_{PHP-II-H,EFF,ON}$ and remains relatively constant with changes in $\dot{Q}_{CCP-H}$. Therefore, in the calculation of the switching ratio via Equation 3.10, $UA_{PHP-II-N,EFF,OFF}$ is considered a constant which is calculated as the mean of all experiment measurements over all evaporator loads, fill ratios, and PHP plumbing configurations.

A worst case uncertainty analysis for the calculated quantities helium PHP thermal switch performance quantities is presented in Table 3.7. This approach is identical to that used for the nitrogen PHP thermal switch measurements and accounts for possible bias in the measurement variables that would not contribute to the error in a sum of squares method and results in asymmetric uncertainty bands. Again, the superscripts (+) and (-) denote the upper and lower uncertainty limits. Uncertainties due to digital-to-analog conversion in the data acquisition hardware are negligible relative to the measured variable uncertainty and are therefore not treated here. Table 3.8 lists measured variable uncertainties. A few differences in the measurement variable uncertainties are noteworthy relative to those in the nitrogen PHP thermal switch facility (Table 2.7):

- the uncertainty for $\dot{Q}_{PHP-I-H}$ and $\dot{Q}_{PHP-II-H}$ are now considered temperature independent and are based on the analysis in Figure 3.1,
- the uncertainty for $\dot{Q}_{CCP-H}$ is quite small as the uncertainty of the on-board power supply electronics are far more accurate than the current shunt used in the nitrogen PHP thermal switch experiment, and
- the Cernox sensors are far more accurate than the calibrated platinum resistance temperature sensors.

Table 3.7. Uncertainty definitions for calculated quantities in the helium PHP thermal switch test facility.

Quantity	Upper(+) and lower(-) uncertainty limits
$k_{PHP-I-H,EFF}$	$k^{+}_{PHP-I-H,EFF}=\frac{\lvert\dot{Q}_{PHP-I-H}+\dot{Q}_{PHP-I-H}\rvert}{\lvert(T_{PHP-I-H,COND}-\Delta T_H)-(T_{PHP-I-H,EVAP}+\Delta T_H)\rvert}\frac{(L_{PHP-I-H,ADIA}+\Delta L_{ADIA-H})}{N_{PHP-I-H,TUBES}\,\pi\left(\frac{(d_{PHP-I-H,o}-\Delta d_{o-H})}{2}\right)^2}$
	$k^{-}_{PHP-I-H,EFF}=\frac{\lvert\dot{Q}_{PHP-I-H}-\dot{Q}_{PHP-I-H}\rvert}{\lvert(T_{PHP-I-H,COND}+\Delta T_H)-(T_{PHP-I-H,EVAP}-\Delta T_H)\rvert}\frac{(L_{PHP-I-H,ADIA}-\Delta L_{ADIA-H})}{N_{PHP-I-H,TUBES}\,\pi\left(\frac{(d_{PHP-I-H,o}+\Delta d_{o-H})}{2}\right)^2}$
$k_{PHP-II-H,EFF}$	$k^{+}_{PHP-II-H,EFF}=\frac{\lvert\dot{Q}_{PHP-II-H}+\dot{Q}_{PHP-II-H}\rvert}{\lvert(T_{PHP-II-H,COND}-\Delta T_H)-(T_{PHP-II-H,EVAP}+\Delta T_H)\rvert}\frac{(L_{PHP-II-H,ADIA}+\Delta L_{ADIA-H})}{N_{PHP-II-H,TUBES}\,\pi\left(\frac{(d_{PHP-II-H,o}-\Delta d_{o-H})}{2}\right)^2}$
	$k^{-}_{PHP-II-H,EFF}=\frac{\lvert\dot{Q}_{PHP-II-H}-\dot{Q}_{PHP-II-H}\rvert}{\lvert(T_{PHP-II-H,COND}+\Delta T_H)-(T_{PHP-II-H,EVAP}-\Delta T_H)\rvert}\frac{(L_{PHP-II-H,ADIA}-\Delta L_{ADIA-H})}{N_{PHP-II-H,TUBES}\,\pi\left(\frac{(d_{PHP-II-H,o}+\Delta d_{o-H})}{2}\right)^2}$
$UA_{PHP-H,EFF}$	$UA^{+}_{PHP-I-H,EFF}=\frac{\lvert\dot{Q}_{PHP-I-H}+\Delta\dot{Q}_{PHP-I-H}\rvert}{\lvert(T_{PHP-I-H,COND}-\Delta T_H)-(T_{PHP-I-H,EVAP}+\Delta T_H)\rvert}$
	$UA^{-}_{PHP-I-H,EFF}=\frac{\lvert\dot{Q}_{PHP-I-H}-\Delta\dot{Q}_{PHP-I-H}\rvert}{\lvert(T_{PHP-I-H,COND}+\Delta T_H)-(T_{PHP-I-H,EVAP}-\Delta T_H)\rvert}$
$UA_{PHP-II-H,EFF}$	$UA^{+}_{PHP-II-H,EFF}=\frac{\lvert\dot{Q}_{PHP-II-H}+\dot{Q}_{PHP-II-H}\rvert}{\lvert(T_{PHP-II-H,COND}-\Delta T_H)-(T_{PHP-II-H,EVAP}+\Delta T_H)\rvert}$
	$UA^{-}_{PHP-II-H,EFF}=\frac{\lvert\dot{Q}_{PHP-II-H}-\dot{Q}_{PHP-II-H}\rvert}{\lvert(T_{PHP-II-H,COND}+\Delta T_H)-(T_{PHP-II-H,EVAP}-\Delta T_H)\rvert}$
$SR_{PHP-II-H}$	$SR^{+}_{PHP-II-H}=\frac{UA^{+}_{PHP-II-H,EFF,ON}}{UA^{-}_{PHP-II-H,EFF,OFF}}$
	$SR^{-}_{PHP-II-H}=\frac{UA^{-}_{PHP-II-H,EFF,ON}}{UA^{+}_{PHP-II-H,EFF,OFF}}$
$FR_{PHP-I-H}$	See Appendix 8.3
$FR_{PHP-II-H}$	See Appendix 8.3

Table 3.8. Uncertainty definitions for measured quantities in the nitrogen PHP thermal switch test facility

Quantity	Uncertainty limits
$\dot{Q}_{CCP-H}$	$\pm\Delta\dot{Q}_{CCP-H}=0.003\,W$
$\dot{Q}_{PHP-I-N}$	$\pm\Delta\dot{Q}_{PHP-I-H}=0.050\,W$
$\dot{Q}_{PHP-II-N}$	$\pm\Delta\dot{Q}_{PHP-II-H}=0.075\,W$ (ON state) $\pm\Delta\dot{Q}_{PHP-II-H}=0.053\,W$ (OFF state)
$d_{PHP-I-H,o}$	$\pm\Delta d_{o-H}=\pm0.013\,mm$
$d_{PHP-II-H,o}$	
$L_{PHP-I-H,ADIA}$	$\pm\Delta L_{ADIA-H}=\pm0.2\,mm$
$L_{PHP-II-H,ADIA}$	
$T_{HM-I-H-A}$, $T_{HM-I-H-B}$, $T_{HM-II-H-A}$, $T_{HM-II-H-B}$, $T_{PHP-I-H,COND}$, $T_{PHP-II-H,COND}$, $T_{PHP-I-H,EVAP}$, $T_{PHP-II-H,EVAP}$	$\pm\Delta T_H=\pm0.005\,K$
$T_{Crycooler-II-HOT}$, $T_{Crycooler-I-HOT}$, $T_{SHIELD-SIDE-B}$, $T_{SHIELD-SIDE-A}$, $T_{SHIELD-LOWER}$, $T_{SHIELD-UPPER}$	$\pm\Delta T_{SHIELD}=\pm1.0\,K$

3.6 Experimental results

Experimental results characterizing the performance of the helium PHP thermal switches are presented here closely mirror the results for the nitrogen PHP thermal switches presented previously in Section 2.6. Measurements of $\dot{Q}_{PHP-I-H}$, $\dot{Q}_{PHP-II-H}$, $k_{PHP-I-H,EFF}$, $k_{PHP-II-H,EFF}$, $UA_{PHP-I-H,EFF}$, $UA_{PHP-II-H,EFF}$, $T_{PHP-I-H,COND}$, $T_{PHP-I-H,EVAP}$, $T_{PHP-II-H,COND}$, $T_{PHP-II-H,EVAP}$, and $SR_{PHP-II-H}$ are shown here for a range of $\dot{Q}_{CCP-H}$, $FR_{PHP-I-H}$, $FR_{PHP-II-H}$, and cryocooler operating statuses. Note that the helium PHPs are only tested in the 2-circuit configuration and *not* in the 1-circuit configuration. Table 3.9 summarizes the test-

ing parameters, and the corresponding fill ratio uncertainties are listed in Table 3.10. Experiment measurements are plotted in Figure 3.24 as functions of the applied common cold plate heat load $\dot{Q}_{CCP-H}$ and Cryocooler-II-H status.

Table 3.9. Helium PHP thermal switch test system operating parameters

PHP circuit configuration	**Cryocooler-I-H status**	**Cryocooler-II-H status**	$FR_{PHP-I-H}, FR_{PHP-II-H}$	$m_{PHP-I-H}, m_{PHP-II-H}$ **[kg]**	$\dot{Q}_{CCP-H}$ **[W]**
2-circuit	Active	Active	0.203, 0.187	0.000083, 0.000078	0 to 1.4
		Inactive	0.287, 0.302 0.432, 0.406 0.478, 0.500 0.470, 0.479 0.589, 0.577 0.489, 0.194	0.000108, 0.000113 0.000152, 0.000144 0.000166, 0.000173 0.000164, 0.000166 0.000199, 0.000196 0.000169, 0.000080	0 to 0.4

Table 3.10. Helium PHP thermal switch test system fill ratio uncertainties (see Appendix 8.3 for definitions)

Configuration	$FR_{PHP-I-H}$	$FR^{+}_{PHP-I-H}$	$FR^{-}_{PHP-I-H}$	$FR_{PHP-II-H}$	$FR^{+}_{PHP-II-H}$	$FR^{-}_{PHP-II-H}$
2-circuit	0.203	0.259	0.191	0.187	0.242	0.178
	0.287	0.355	0.268	0.302	0.373	0.282
	0.432	0.520	0.399	0.406	0.491	0.376
	0.478	0.574	0.442	0.500	0.599	0.462
	0.470	0.564	0.434	0.479	0.574	0.443
	0.589	0.699	0.542	0.577	0.685	0.531
	0.489	0.585	0.451	0.194	0.249	0.184

All data are obtained at steady PHP operating conditions, meaning that the PHP condenser and evaporator temperatures are time independent over the approximately 20 minute data collection interval (obviously ignoring the smaller scale, high frequency pulsing associated with PHP operating). Furthermore, the measurements are obtained with no regard to the ramping (up or down) application of $\dot{Q}_{CCP-H}$, as the PHP performance changes are found to be negligible whether the prior $\dot{Q}_{CCP-H}$ in a measurement sequence is a higher or lower value. Measurements at different

$FR_{PHP-I-H}$ and $FR_{PHP-II-H}$ are obtained by raising the cold stage temperatures of both crycoolers above the critical temperature of helium (to purge the majority of helium charge from the PHP tubes and allow an estimate of the remaining mass) and refilling to the new fill ratio. Due to the time required to warm Cryocooler-II-H to 290 K (about 36 hours), only two PHP-II-H fill ratios – of about 0.20 and 0.50 – are tested in the OFF state. Based on the ON state performance, these tested OFF state fill ratios represent practical extrema charges for which the ON state PHP would operate with a design application and therefore offer representative performance bounds for OFF switch state.

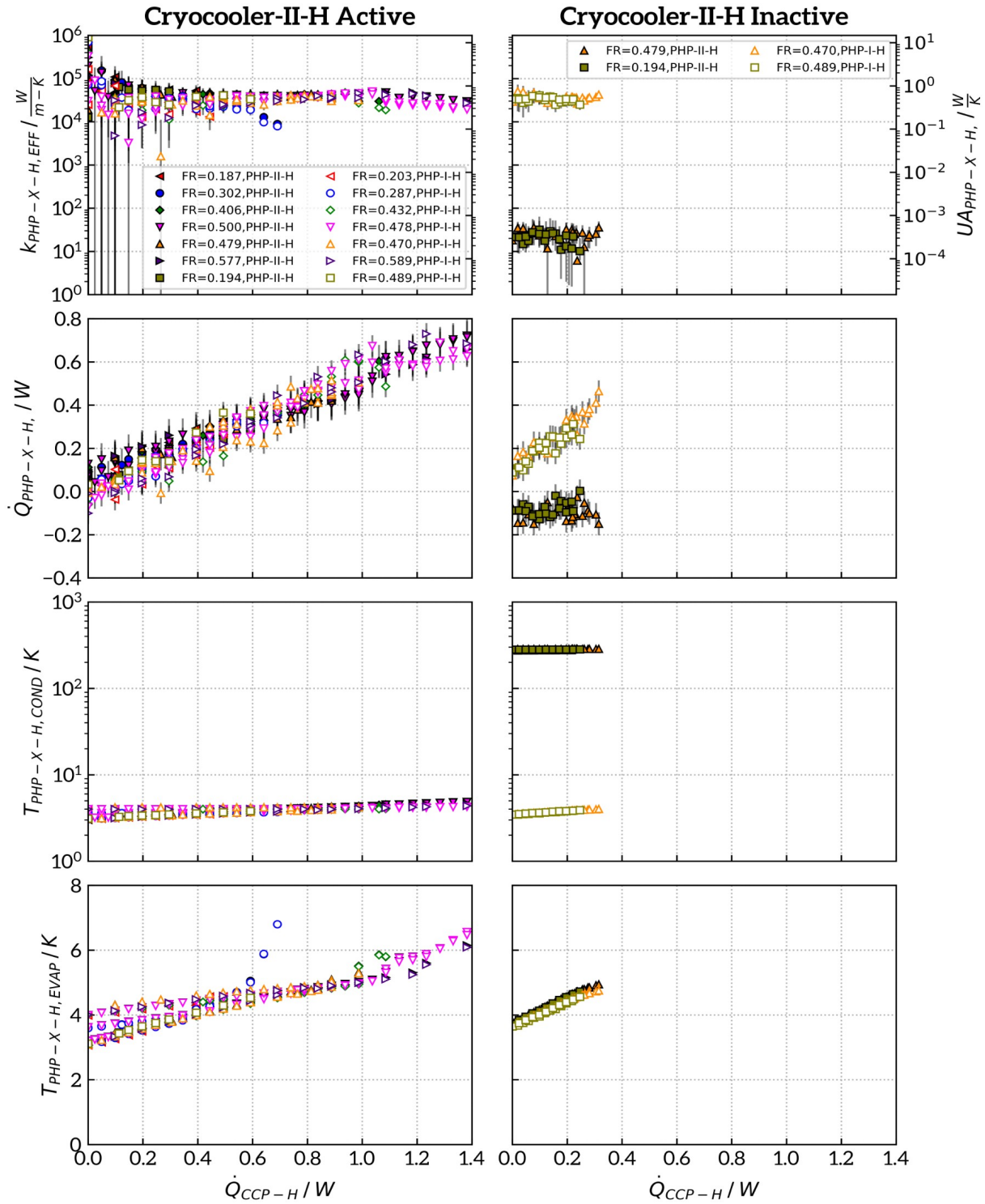

Figure 3.24. Effective conductivity, conductance, heat transfer, condenser temperature, and evaporator temperature over a range of common cold plate heat loads for PHP-I-H and PHP-II-H in the 2-circuit configuration.

3.6.1 Confirmation of heat meter calibrations

The data presented in Figure 3.24 contains simultaneous measurements from HM-I-H, HM-II-H and the applied electric heat power on the common cold plate. These simultaneous measurements, along with a system energy balance, can be used to help verify the accuracy of the heat meter calibrations when Cryocooler-II-H is active. The energy balance used for this is

$$\dot{Q}_{CCP-N} = \dot{Q}_{PHP-I-N} + \dot{Q}_{PHP-II-N} \tag{3.11}$$

, depicted by diagram in Figure 3.25, holds nearly within the uncertainty bands for each measurement point. This is shown in Figure 3.26, which plots the sum of $\dot{Q}_{PHP-I-H}$ and $\dot{Q}_{PHP-II-H}$ as a function of $\dot{Q}_{CCP-H}$ for all helium PHP thermal switch operation data with Cryocooler-II-H active along with the expected perfect energy balance for comparison.

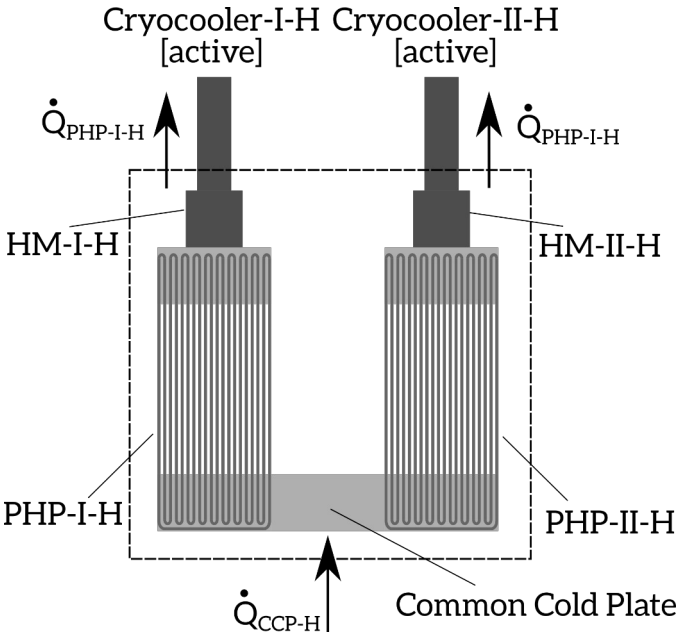

Figure 3.25. Schematic showing energy balance (neglecting radiation) on a system consisting of PHP-I-H, PHP-II-H, HM-I-H, HM-II-H, and the common cold plate.

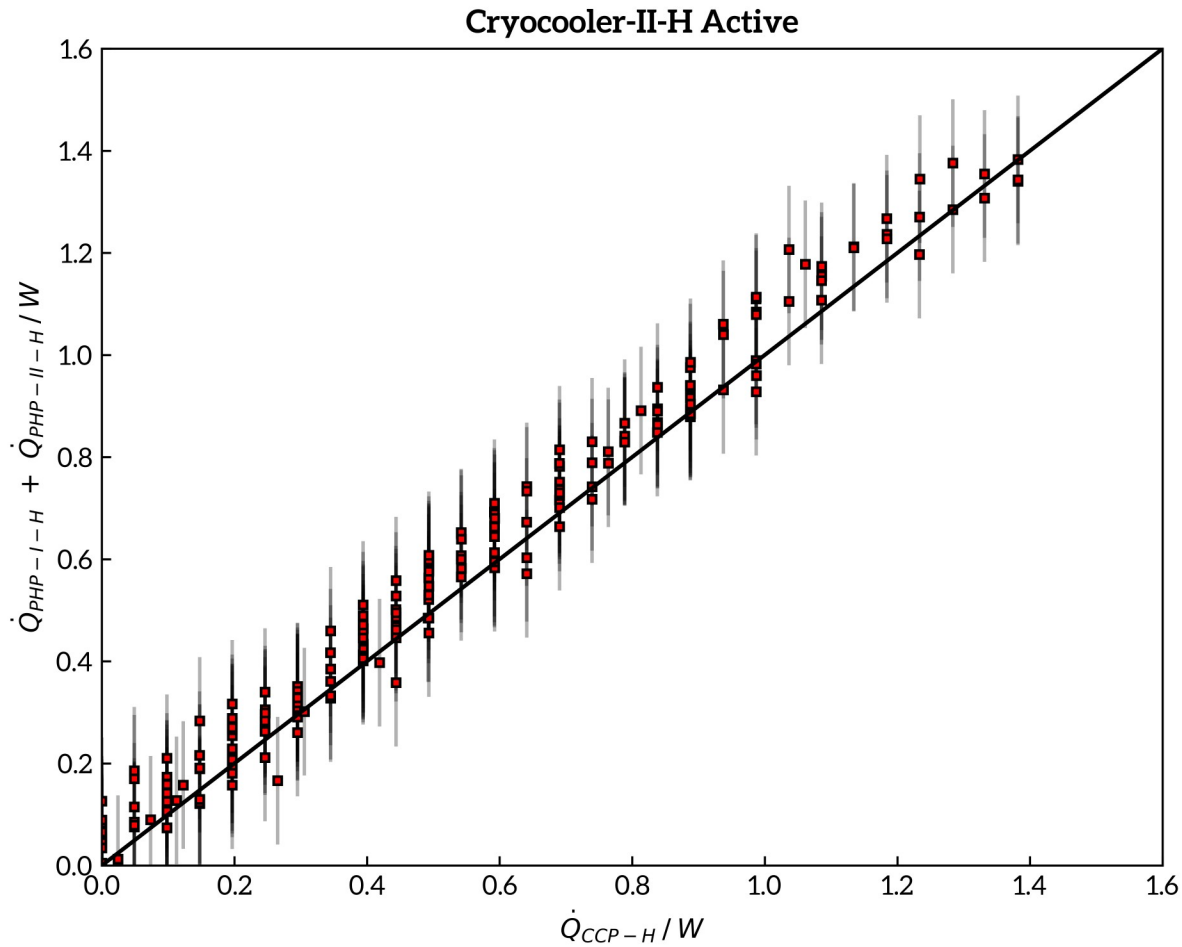

Figure 3.26. Sum of heat meter measurements from HM-I-H and HM-II-H as a function of the common cold plate heat load for measures with both Cryocooler-I-H and Cryocooler-II-H active.

The excellent agreement over all $\dot{Q}_{CCP-H}$ provides an independent confirmation of the accuracy of the heat meter calibrations. Based on the calibration data for HM-I-H and HM-II-H presented in Figure 3.22, it is likely that the points in Figure 3.26 above approximately $\dot{Q}_{CCP-H} = 1.2\,W$ are extrapolated beyond the calibration sample domain. This is feasible because the calibration fit functions for $\dot{Q}_{PHP-I-H}$ and $\dot{Q}_{PHP-II-H}$ – Equation 3.1 and Equation 3.2, respectively – are inherently defined outside of the calibration domain. However, the independent energy balance check in Figure 3.26 shows that the accuracy of the extrapolation matches closely to those points within the calibration domain. Note that the calibration check is *not* provided for measurements

when Cryocooler-II-H is inactive. This differs from the situation for the nitrogen PHP thermal switch tests because HM-II-H is not calibrated at room temperature here due to lack of sensitivity of the Cernox sensors at 290 K (see Section 3.4). Instead the same energy balance of Equation 3.11 is used to directly calculate the OFF state $\dot{Q}_{PHP-II-H}$, per Equation 3.5, which then prevents the use of the energy balance as an independent check on the calibration.

3.6.2 PHP heat transfer, effective conductivity, and evaporator/condenser temperature difference in the ON and OFF switch states

As seen in Figure 3.24, when both Cryocooler-I-H and Cryocooler-II-H are active, the majority of effective thermal conductivity measurements for both PHP-I-H and PHP-II-H fall between 10000 W/m-K and 50000 W/m-K. The corresponding effective conductance values are between about 0.10 W/K and 0.75 W/K. These ON state performance values are consistent with those for other helium PHPs of similar size reported in the literature [43,44,45,52]. A few caveats of the ON state effective thermal conductivity and conductance data in Figure 3.24 must be mentioned, however. First, at $\dot{Q}_{CCP-H}$ lower than about 0.30 W, the heat meter calibrations become relatively inaccurate per Figure 3.21. When this inaccuracy is combined with the small temperature difference between the PHP condenser and evaporator plates which occur at low $\dot{Q}_{CCP-H}$, the uncertainty in the effective thermal conductivity and conductance data is amplified per the analysis in Table 3.7. The peak in these values at low $\dot{Q}_{CCP-H}$ should be viewed as an artifact of the uncertainty rather than a real phenomena. Furthermore, ON state data is provided for a wide range of fill ratios here for the purpose of ensuring the optimum conductance of the ON state helium PHPs is identified rather than to closely detail the difference performances and dryout con-

ditions of each fill ratio. Discerning differences between different fill ratios from Figure 3.24 is difficult due to the log scaling and the large number of sample points; however, the scaling allows a clear visual comparison between the conductances for PHP-I-H and PHP-II-H when Cryocooler-II-H is both active and inactive – the main goal of this investigation.

The optimum ON state conductance of both PHP-I-H and PHP-II-H occurs at a fill ratio of about 0.50 and $\dot{Q}_{CCP-H}$ of about 1.1 W. This corresponds to $\dot{Q}_{PHP-I-H}$ and $\dot{Q}_{PHP-II-H}$ each equal to about 0.550 W, as the load applied at the common cold plate is roughly split equally between the two PHPs. This is again inline with similarly sized PHP performance describe in the literature. For instance, helium PHPs with 14 parallel tubes and adiabatic section lengths of 300 mm and 1000 mm have been measured with an optimum conductance of 0.38 W/K at a load of about 0.26 W [52]. The same paper noted that the adiabatic length between 300 mm and 1000 mm had negligible effect on the optimum conductance. The larger optimum conductance seen in this testing is therefore likely associated with the larger count of parallel tubes (18 vs 14) rather than the different adiabatic length (501 mm vs 300 mm and 1000 mm).

The parasitic heat leak through the OFF state PHP-II-H $\dot{Q}_{PHP-II-H}$ is nearly constant overall all measurements at widely varying fill ratios – behavior identical to that observed previously with the nitrogen PHP thermal switch PHP-II-N. The mean of these OFF state $\dot{Q}_{PHP-II-H}$ measurements is about -0.080 W, which are obtained over a range of applied applied common cold plate heat loads $\dot{Q}_{CCP-H}$ between 0.00 W and 0.32 W[30] while the evaporator and condenser tempera-

30 The applied $\dot{Q}_{CCP-H}$ is limited such that $T_{PHP-II-H,EVAP}$ remains safely below the critical temperature of helium when Cryocooler-II-H is inactive. This ensures the helium in the OFF state PHP-II-H evaporator remains liquid and helps avoid overpressuring the helium PHP and fill line system, whose solder joints and valves are

tures of PHP-II-H are at approximately 4 K and 290 K, respectively. Again this is due to the large temperature difference between the PHP-II-H condenser and evaporator which develops when Cryocooler-II-H is inactive; this temperature difference varies little while the thermal conductivity of the contained static helium vapor is very low. Note that because the PHP geometry is also fixed, a constant $\dot{Q}_{PHP-II-H}$ implies that $k_{PHP-II-H,EFF}$ and $UA_{PHP-II-H,EFF}$ are also constant per Equation 3.7 and Equation 3.9.

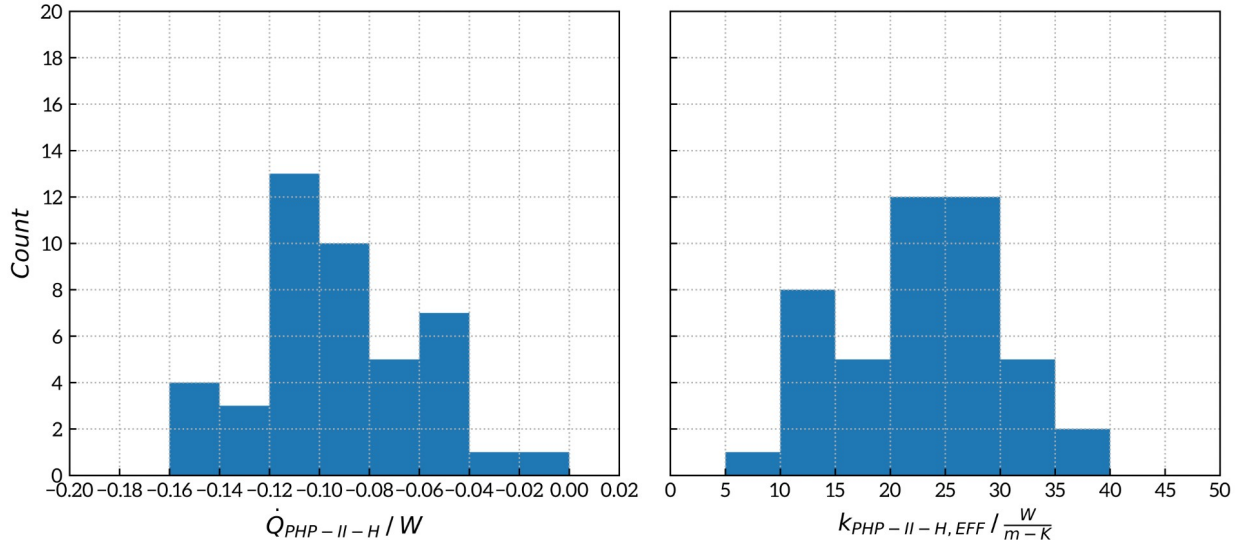

Figure 3.27. Distribution of parasitic heat leak through the OFF state PHP-II-H, $\dot{Q}_{PHP-II-H}$, and the corresponding distributions of $k_{PHP-II-H,EFF}$.

Figure 3.27 shows the distributions of $\dot{Q}_{PHP-II-H}$ and $k_{PHP-II-H,EFF}$ for all measurements with Cryocooler-II-H inactive – that is, with PHP-II-H in the OFF state. The distributions are almost normal and notably not multi modal, suggesting that there is no unforeseen dependence of the OFF state heat leak on the fill ratio over the range tested here. Comparison of theses measured OFF state heat leaks $\dot{Q}_{PHP-II-H}$ to modeled predictions are presented in Section 4.3. It is worth

not necessary capable of handling the high pressures associated with evaporating the complete PHP charge within the restricted PHP volume.

mentioning that OFF state heat leak for the helium PHP (-0.080 W) is nearly an order of magnitude smaller than that observed for the nitrogen PHP (-0.54 W). This is mostly due to design changes in the PHP construction – a longer adiabatic section and smaller total tube cross sectional area – which result in lower OFF state conduction through the tube walls and static gas. Note that the parasitic load of about -0.080 W through the OFF state PHP-I-H $\dot{Q}_{PHP-II-H}$, which must be removed from the common cold plate entirely through the ON state PHP-I-H and Cryocooler-I-H, is about 13 percent of the maximum demonstrated capacity of PHP-I-H and 9 percent of the available capacity of Cryocooler-I-H after accounting for the radiation load incident on the 4 K heat shield load. Like the nitrogen PHPs then, the PHP-II-H here is functioning effectively as a thermal switch, providing insulation to protect the common evaporator plate from the hot PHP-II-H condenser plate while allowing Cryocooler-I-H to continue cooling the evaporator load.

A minor final point here is that, for measurements with Cryocooler-II-H inactive, there is very little temperature gradient over the evaporator (that is, $T_{PHP-II-H,EVAP} - T_{PHP-I-H,EVAP}$ is small) for all measurements with PHP-II-H in the OFF state. Two factors contribute to this – the first and most important being the large reduction in contact resistances within the common cold plate assembly relative to those experienced with the nitrogen PHP thermal switch experiment. Secondly, the heat loads $\dot{Q}_{CCP-H}$ applied at the evaporator here are far small smaller (0 W to about 0.32 W) than those $\dot{Q}_{CCP-N}$ applied in the nitrogen experiment (0 W to about 16 W), which limits the temperature gradient that can develop over the contact resistance which remains. Since the experiment evidence suggests there is no significant contact resistance in the common

cold plate assembly, a contact resistance model is not provided for the helium PHP measurements as for the nitrogen PHP measurements.

3.6.3 Switching ratio

PHP-II-H's effectiveness as a thermal switch is characterized by its switching ratio in Figure 3.28, which plots the PHP-II-H switching ratio as a function of ON state PHP-II-H heat load $\dot{Q}_{PHP-II-H}$ for the same experiment test data from Figure 3.24. The ratio for the 2-circuit helium PHP thermal switch approaches about 2000, as compared with about 2500 for the 2-circuit nitrogen PHP thermal switch presented previously. As with the nitrogen PHP thermal switches, this means that the ON state switch conductance $UA_{PHP-II-H,EFF,ON}$ is about three orders of magnitude larger than the OFF (dry) state conductance $UA_{PHP-II-H,EFF,OFF}$, demonstrating the effectiveness of the helium PHPs as thermal switches even with an OFF state temperature difference imposed (approximately 285 K versus 220 K) between the condenser and evaporator plates well exceeding that of the nitrogen PHP switches. In addition to the larger temperature gradient, recall that the helium PHPs have different geometry (adiabatic lengths, tube inner and outer diameters, and parallel tube count) from the nitrogen PHPs, all of which combine to cause the differences in switching ratio. The OFF state helium PHPs are also likely subjected to a small, yet important, radiative load which is likely contributing to the lower switching ratios. An analysis regarding this is provided in Section 3.6.4 and Section 4.3.

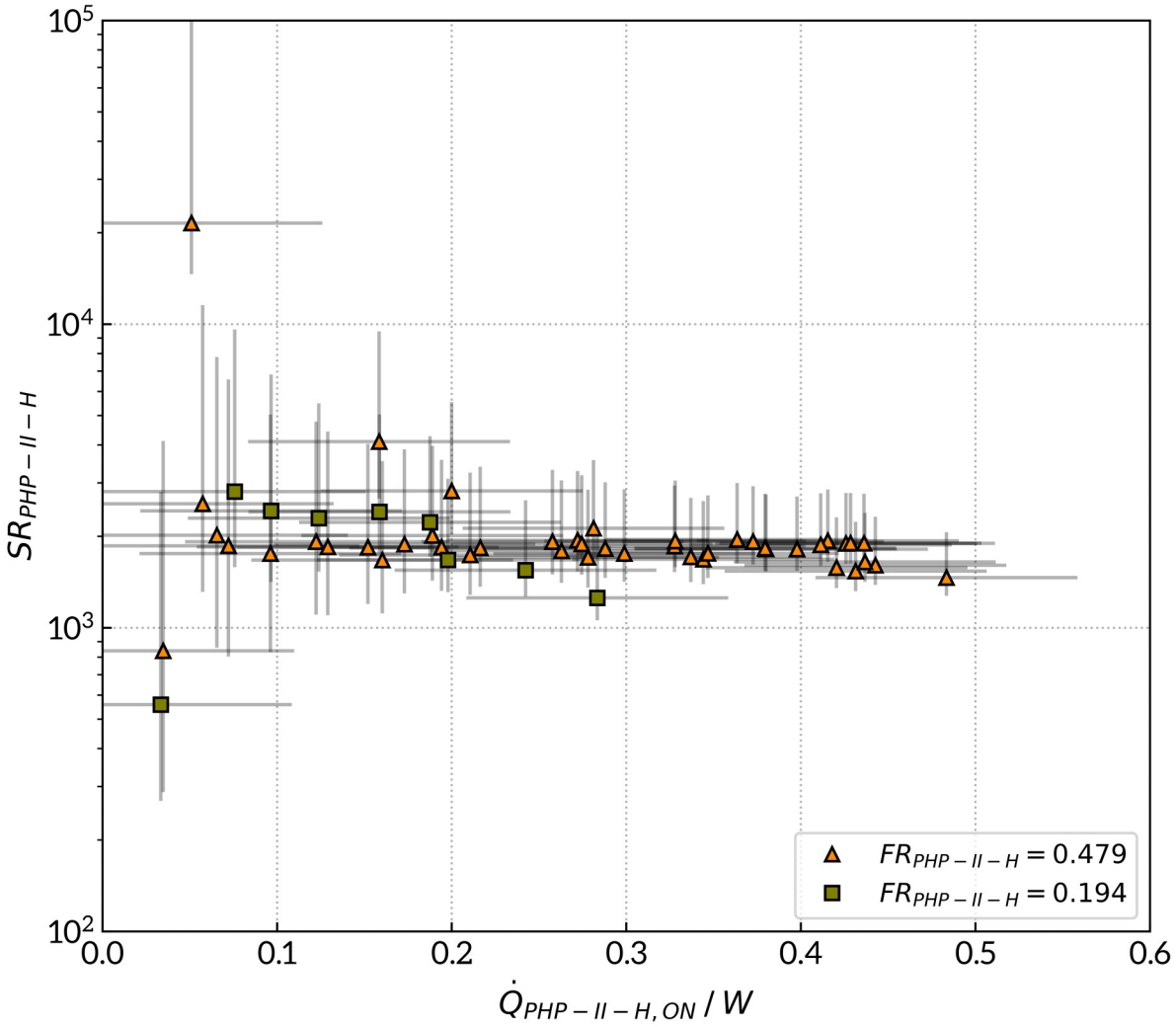

Figure 3.28. Switching ratio as a function of the heat load in the ON state for PHP-II-H

With the helium PHP switches, the switching ratio is again insensitive to the PHP fill ratio. This is again expected since working fluid swap does not change the fact that the PHP effective thermal conductivity in the ON state is typically a fairly weak function of fill ratio (except at fill ratios approaching 0 or 1), while the OFF state effective thermal conductivity is independent of the stagnant gas pressure (which changes as the fill ratio varies). Section 4.3 has further analysis regarding the parasitic heat leak dependence on charge pressure for the helium PHP switches.

3.6.4 Behavior during Cryocooler-II-H shutdown and subsequent restart

The behavior of key experiment quantities during the transition of the PHP-II-H thermal switch from the ON to OFF to ON states is plotted in Figure 3.29. This time series corresponds to a system operation sequence starting with both cryocoolers active (at time = 0 hr), moving to Cryocooler-II-H inactive (0 hr < time < 48 hr), and then moving back again to both cryocoolers active (time > 48 hr). The upper panel shows the PHP-I-H and PHP-II-H evaporator and condenser temperatures, the middle panel shows the heat leak through PHP-II-H $\dot{Q}_{PHP-II-H}$, and the lower panel shows the 70 K shield and cryocooler hot stage temperatures as a function of time during the Cryocooler-II-H ON-OFF-ON cycle.

During the warming of the Cryocooler-II-H cold heads (0 hr < time < 48 hr), the electric heaters on both the hot stage and cold stage of Crycooler-II-H are fully powered at approximately 150 W and 2 W, respectively, to assist in warming the cold stage to 290 K as rapidly as possible. The results in the hot stage reaching 290 K fairly quickly – in about 2 hours – while the cold stage requires much longer – about 48 hours. This is purely due to the fact that the cold stage electric resistance heater is primarily designed for the small power and current necessary for temperature control during the ON state rather than rapid warming to reach the OFF state. Per Figure 3.29, $|\dot{Q}_{PHP-II-H}|$ increases slowly from about 0 W to 0.08 W as Cryocooler-II-H warms in time; when Cryocooler-II-H is reactivated, $|\dot{Q}_{PHP-II-H}|$ returns to 0 W. Note that the noise in the $\dot{Q}_{PHP-II-H}$ signal in Figure 3.29 is on the order of the random error of the heat meter calibrations in Figure 3.23 – which is about ±0.050 W for HM-I-H, on which the OFF state $\dot{Q}_{PHP-II-H}$ is based per Equation 3.5.

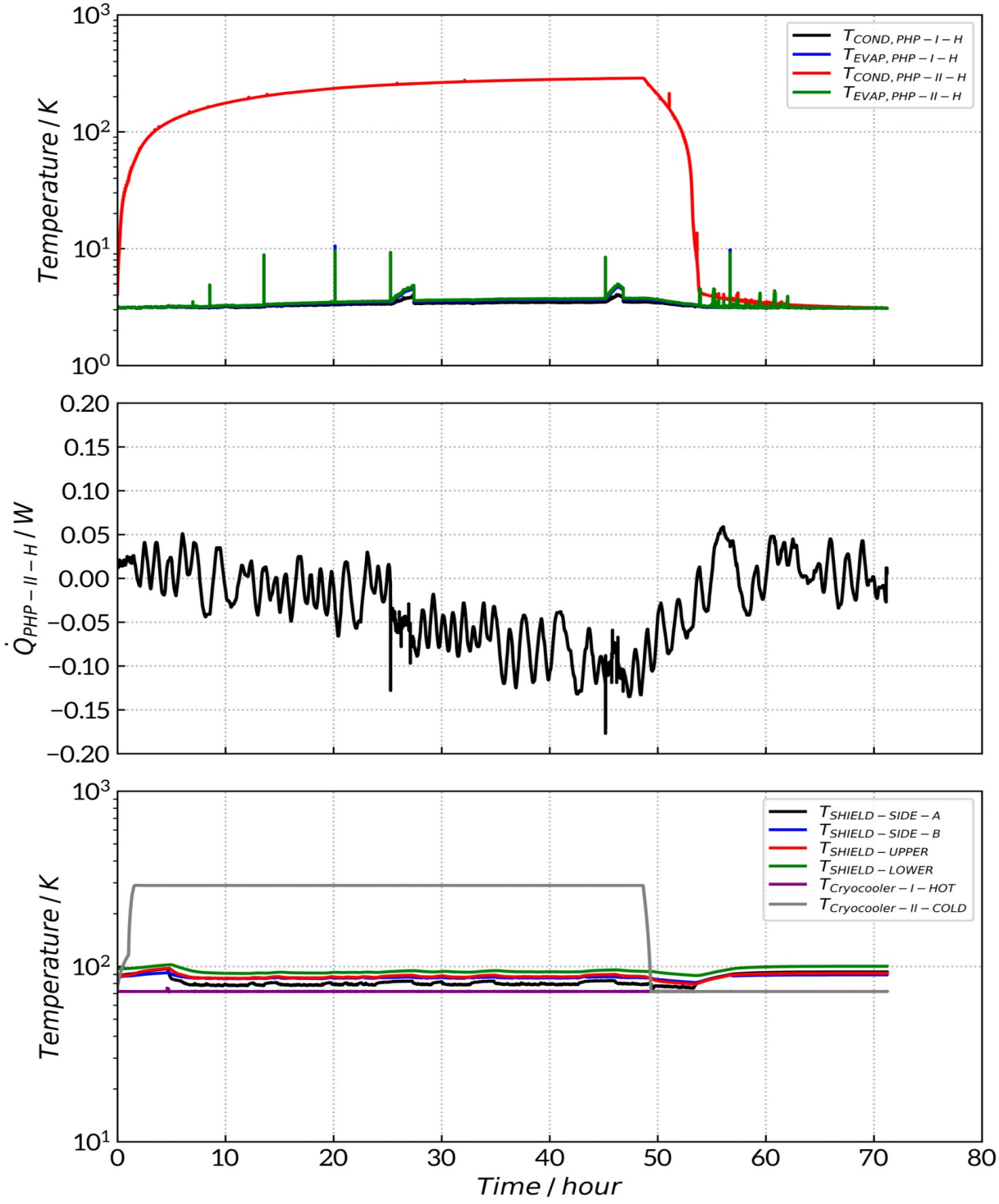

Figure 3.29. PHP-I-H and PHP-II-H condenser and evaporator temperatures, PHP-II-H parasitic load, and 70 K shield temperatures during deactivation and reactivation of Cryocooler-II. $FR_{PHP-I-H} = 0.470$ and $FR_{PHP-II-H} = 0.479$.

During both the Cryocooler-II-H warm up period and subsequent cool down period, several instances of brief spikes in the evaporator temperatures $T_{PHP-I-H,EVAP}$ and $T_{PHP-II-H,EVAP}$ are observed. During warm up, the first of four of these spikes (at about time = 7 hr, 8 hr, 14 hr, and 20 hr) are likely associated with heat transfer to the PHP-II-H evaporator from the condenser due to fluid movement caused by liquid boiling within the PHP tube. The following two spikes at about 25 hrs and 45 hrs are associated with the initial application of $\dot{Q}_{CCP-H}$ for a series of testing the $\dot{Q}_{PHP-II-H}$ at various common cold plate heat loads in the OFF state, as shown in Figure 3.24. There are a few possible explanations for these latter two events: one is that some finite time is necessary to increase the velocity of helium in the ON state PHP-I-H when after $\dot{Q}_{CCP-H}$ is increased; another is that the initial application of $\dot{Q}_{CCP-H}$ is enough to cause a small movement of fluid in the OFF state PHP-II-H, in turn condensing some vapor in within the evaporator and causing a nearly instantaneous load increase for the ON state PHP-I-H. All of the evaporator temperature spikes during the cooldown period are again caused by applications of $\dot{Q}_{CCP-H}$. It is important to note that, during each of these temperature spikes, the ON state PHP-I-H is capable of removing the energy from the common cold plate even though the temperature peaks well above the critical temperature of helium (at about 10 K max). Finally, it is worth mentioning that the shield temperatures during the entire Cryocooler-II-H shutdown and restart sequence in Figure 3.29 consistently remain between about 70 K and 100 K. This is evidence that the nitrogen shield PHPs are sized sufficiently such that the two attached to the active Cryocooler-I-H are capable of removing the incident radiation while the two attached to the inactive Cryocooler-II-H are in the OFF switch state.

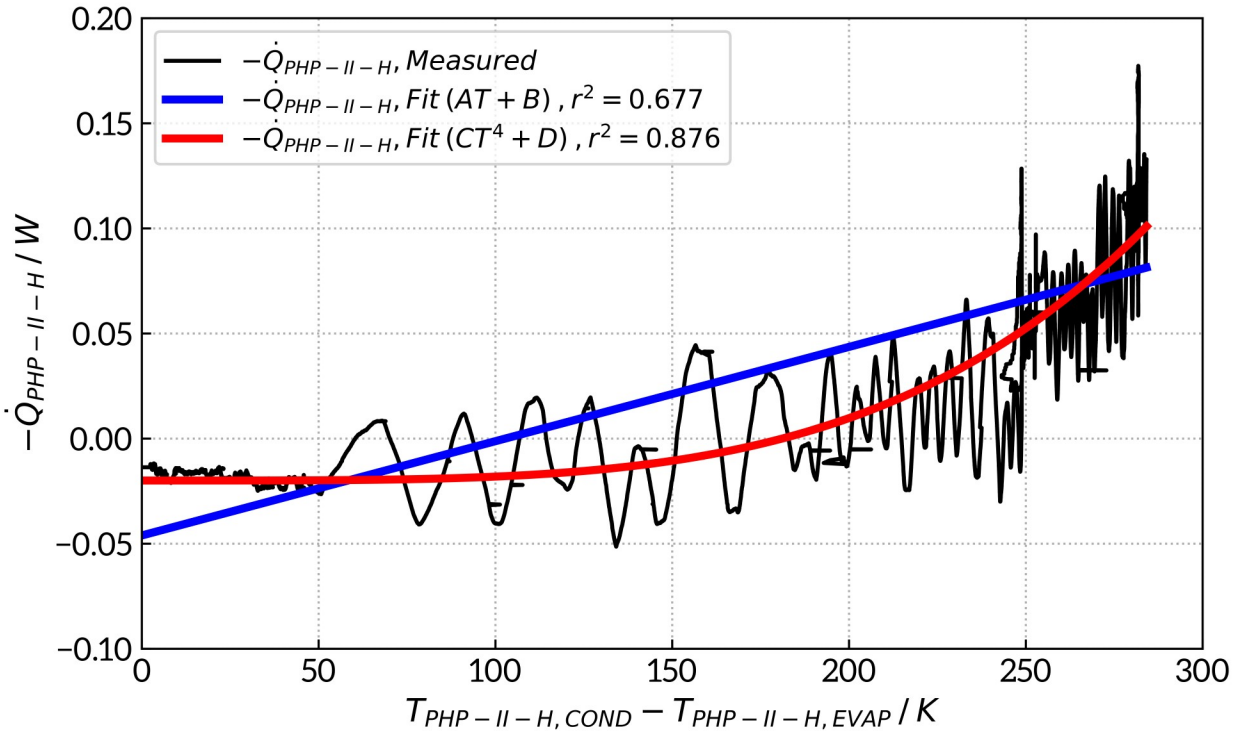

Figure 3.30. Measured relation between the OFF state parasitic load through PHP-II-H and ($T_{PHP-II-H,COND} - T_{PHP-II-H,EVAP}$) during the slow psuedo-steady state Cryocooler-II-H warm up shown in Figure 4.29. Linear and quadratic fits and their coefficients of determination (r^2) are shown. A, B, C, and D in the legend are constants determined by the regression.

A useful consequence of the long warm up period shown in Figure 3.29 is that the parasitic heat load through PHP-II-H $\dot{Q}_{PHP-II-H}$ is sampled over a range of psuedo-steady state Cryocooler-II-H cold head temperatures $T_{PHP-II-H,COND}$ (essentially from 4 K to 290 K). This allows an estimate of the functional dependence of the OFF state $\dot{Q}_{PHP-II-H}$ on $(T_{PHP-II-H,COND} - T_{PHP-II-H,EVAP})$ to be computed. Figure 3.30 accomplishes this via two regression fits of the experiment measurements: one a linear fit ($|\dot{Q}_{PHP-II-H}| = f(T_{PHP-II-H,COND} - T_{PHP-II-H,EVAP})$) intended to check if the measurements roughly correspond to a conduction parasitic, and one a quartic fit ($|\dot{Q}_{PHP-II-H}| = f(T_{PHP-II-H,COND} - T_{PHP-II-H,EVAP})^4$) to check if the measurements roughly corre-

spond to a radiative parasitic. The quartic fit is superior, suggesting that imperfect radiation shielding is responsible for much of the measured OFF state heat leak $|\dot{Q}_{PHP-II-H}|$ through PHP-II-H and therefore also responsible for the offset between the experiment measurements and modeled values where $T_{PHP-II-H,EVAP}$ is approximately 290 K.

3.6.5 Modification of PHP fluid circuit design to resolve initial performance issues

The helium PHP thermal switches in this work are the product of an important design iteration that is worthy of a brief discussion. Originally, the helium PHP thermal switches described in Section 3.3 were intended to include 20 parallel tubes and have a filling tee in the adiabatic section, completely analogous to the nitrogen shield PHPs shown in Figure 3.15. This is clearly different than the 18 parallel tube final PHP design shown in Figure 3.17, which features the filling tube in a short adiabatic section connected to the condenser at each end. Figure 3.31 compares the initial helium PHP switch design to the revised final version.

The helium PHP plumbing change was made in an effort to overcome severe performance issues: the initial design essentially failed to operate as a PHP, with dryout in both PHP-I-H and PHP-II-H at $\dot{Q}_{CCP-H} < 0.050\,W$. This is an order of magnitude lower than the design expectations for the critical heat load and indeed an order of magnitude lower than the actual critical head load measured with the final modified helium PHP design. One plausible reason for the under performance is that the initial design had one evaporator tube section of approximately twice the length of the other evaporator tube section. An evaporator tube section here is a single U-shaped portion of the PHP tube that is soldered to the evaporator plate. These can be seen in Figure 3.31; there

are 10 such sections in the initial design and 9 in the revised design. The 10^{th} section in the initial design connects the two outermost adiabatic tube sections, requiring an extra length of tube spanning nearly the entire width of the evaporator plate. In the initial design then, this extra long evaporator tube section is more likely to dry out than the other 9 shorter evaporator tube sections, which could plausibly prevent a net fluid circulation from developing in the PHP loop. That is, a liquid slug could survive a pass through each of the 9 shorter evaporator tube sections, but may evaporate completely in the longer section.

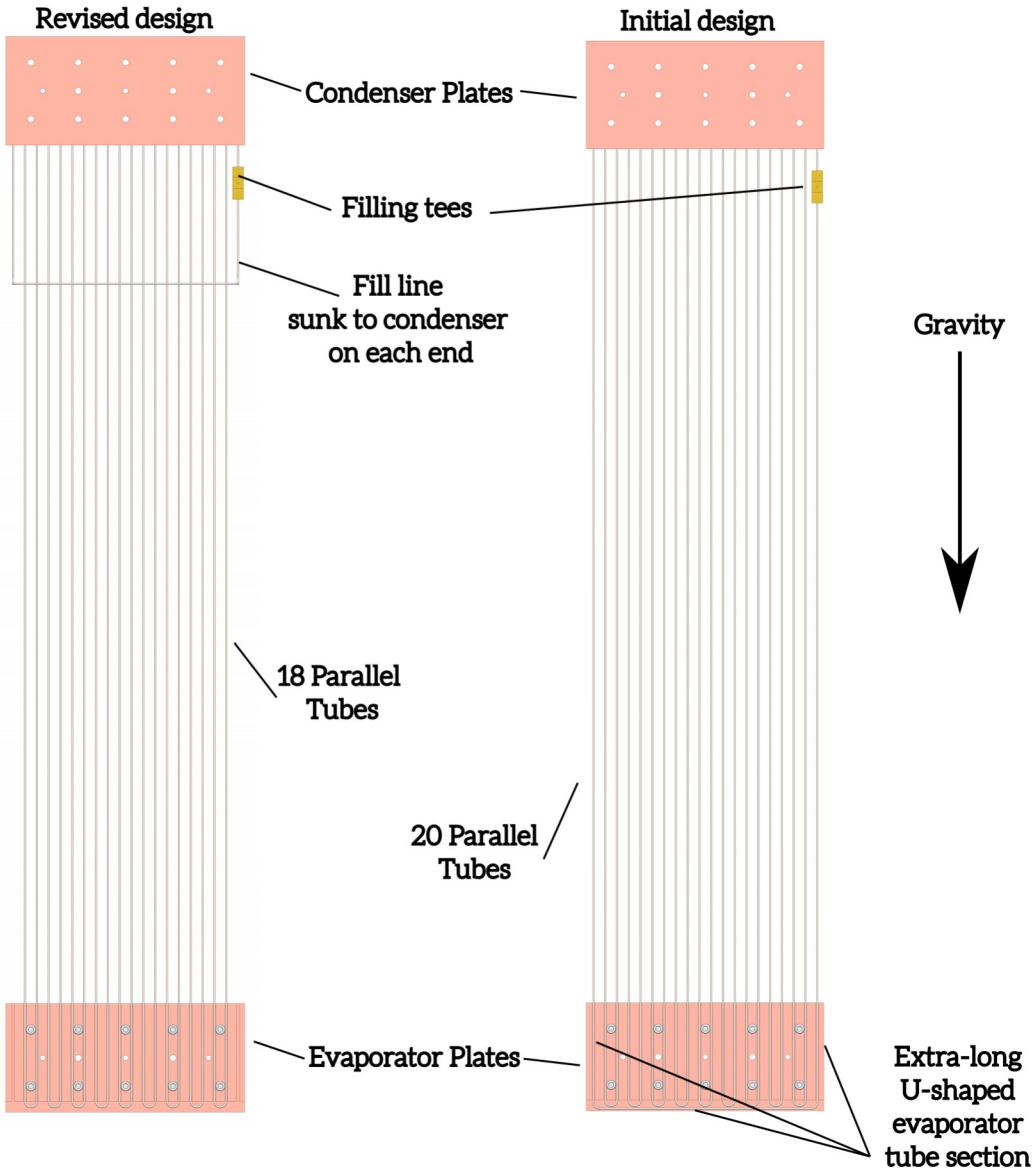

Figure 3.31. Revised helium PHP design (left) and initial PHP design (right).

4 Development of a PHP thermal switch OFF state performance model

4.1 Model definition

To assess whether the measured OFF state parasitic loads $|\dot{Q}_{PHP-II-N}|$ are reasonable, a simple resistance network conduction heat transfer model for an OFF state PHP switch is developed[31]. Four major assumptions are taken in deriving this model:

1) an OFF state PHP has no advective flow since the temperatures in the condenser and the majority of the adiabatic section are far above the critical temperature and therefore any liquid remaining in the evaporator flashes before penetrating any significant distance into the adiabatic section;
2) the working fluid is in hydrostatic equilibrium throughout the PHP tube;
3) radiation is negligible; and
4) the system is in a steady state.

With these assumptions in mind, there are two parallel conduction paths between the evaporator and condenser plates to consider – through the tube wall and through the stagnant working fluid vapor within the tube. These parallel conduction paths are modeled with a single thermal conductivity by weighting the contributions by fraction of the contributed area cross section. This approach is an isothermal one dimensional approximation to a two dimension conduction problem which results in a lower bound of the actual resistance [53]. The conduction problem is discretized in the tube axis dimension to account for the temperature dependent thermal conductivity of both the tube wall material and the working fluid. Figure 4.1 is a schematic that highlights

31 The model is described within this section in general terms so it may be applied to both the nitrogen and helium PHP thermal switches

key features of the conduction problem, describes the discretization, and relates the boundary temperatures to the evaporator and condenser temperatures.

By a steady state global energy balance, the PHP switch OFF state heat transfer between any two nodes in Figure 4.1 must be equivalent. The heat transfer between any two adjacent nodes can be described then by the one dimensional conduction equation

$$\dot{Q}_{PHP,OFF,MODEL} = k_{MODEL}\left(\frac{N_{NODES}-1}{L_{PHP,ADIA}}\right)\pi\left(\frac{d_{PHP,o}}{2}\right)^2 N_{PHP,TUBES}\left(T_i - T_{i+1}\right) \quad \text{for } i = 0 \text{ to } N_{NODES}-1 \tag{4.1}$$

, where $\dot{Q}_{PHP,OFF,MODEL}$ is the modeled PHP thermal switch OFF state parasitic heat transfer, k_{MODEL} is the weighted thermal conductivity of the tube wall and vapor between the nodes, $d_{PHP,o}$ is the outer diameter of the PHP tube, $L_{PHP,ADIA}$ is the PHP adiabatic section length, $N_{PHP,TUBES}$ is the number of parallel tubes in the PHP, T_i is the temperature at the i^{th} discretized node, and N_{NODES} is the number of discretized nodes. Importantly, k_{MODEL} is a function of the local temperature and has cross section weighted contributions from both the tube wall material and the working fluid

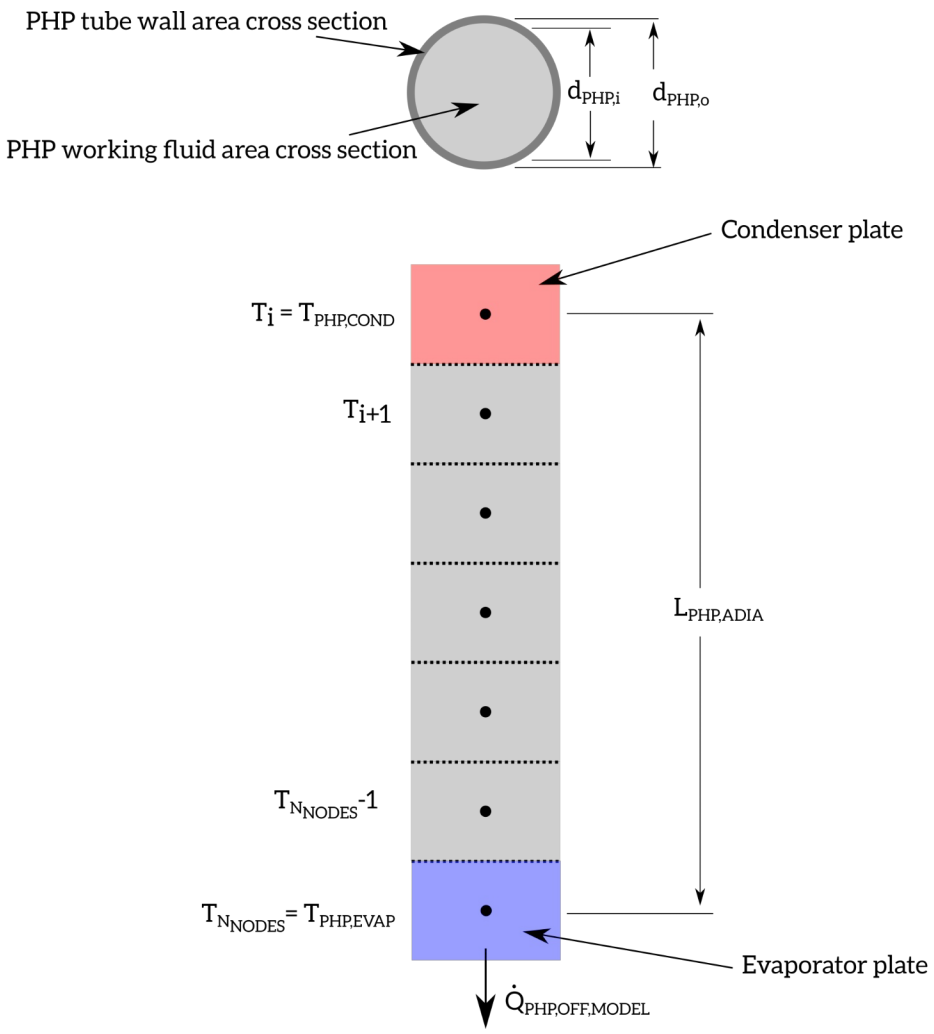

Figure 4.1. Geometry for PHP switch OFF state performance model (not drawn to scale)

$$k_{MODEL} = k_{FLUID}\left(P_{PHP,OFF,MODEL}, \frac{T_i + T_{i+1}}{2}\right)\left(\frac{d_{PHP,i}^2}{d_{PHP,o}^2}\right) + k_{WALL}\left(\frac{T_i + T_{i+1}}{2}\right)\left(\frac{d_{PHP,o}^2 - d_{PHP,i}^2}{d_{PHP,o}^2}\right) \quad (4.2)$$

, where k_{FLUID} is the pressure and temperature dependent conductivity of the working fluid, k_{WALL} is the temperature dependent conductivity of the wall, and $P_{PHP,OFF,MODEL}$ is the pressure of the PHP working fluid in the OFF switch state. Note that the brackets following the conductivity terms in Equation 4.2 bound function arguments for the conductivities and are not

meant to show multiplication. Equation 4.2 clearly shows how the fluid and wall material conductivity contributions are weighted in proportional to their respective cross sectional areas.

The pressure of the PHP in the OFF switch state is determined in one of two ways. The first represents a case where the PHP shutoff valve (see Figure 8.1) remains closed at all times. This means the ON state charge mass must remain in the local PHP tubing during the OFF state. In this case the pressure must rise (significantly) as the condenser temperature rises as the charge mass and volume are fixed. A mass balance between the ON and OFF switch states representing this is

$$m_{PHP} = \sum_{0}^{N_{NODES}} \frac{L_{PHP,ADIA} N_{PHP,TUBES} \pi \left(\frac{d_{PHP,i}}{2} \right)^2}{N_{NODES} v_{FLUID}\left(P_{PHP,OFF,MODEL}, T_i\right)} + \frac{V_{PHP,COND}}{v_{FLUID}\left(P_{PHP,OFF,MODEL}, T_{PHP,COND}\right)} + \frac{V_{PHP,EVAP}}{v_{FLUID}\left(P_{PHP,OFF,MODEL}, T_{PHP,EVAP}\right)} \tag{4.3}$$

, where m_{PHP} is the ON state charge mass, v_{FLUID} is the temperature and pressure dependent specific volume of the working fluid, $T_{PHP,COND}$ is the OFF state PHP condenser temperature, $T_{PHP,EVAP}$ is the OFF state PHP evaporator temperature, $V_{PHP,COND}$ is the internal PHP tube volume contained in the condenser, and $V_{PHP,EVAP}$ is the internal PHP tube volume contained in the evaporator. Here the ON state charge mass must remain in the condenser (at the condenser temperature), in the evaporator (at the evaporator temperature), or in the adiabatic section (at the discretized temperatures determine by the conduction model). This approach allows the specific volume of the working fluid to vary with position in the adiabatic section tubes. Note that, if

$P_{PHP,OFF,MODEL}$ is below the critical pressure, any node at a temperature lower than the corresponding saturation temperature is assumed to be saturated liquid.

In a second scenario, the PHP shutoff valve is opened when the PHP switch actuates from the ON to the OFF state. Such an action occurs for some of the OFF state PHP experiment data in this work, for instance, with the purpose of limiting the pressure applied to the PHP tubing joints (for structural integrity purposes) in the experimental facility. When the shutoff valve is opened, the filling system (again see Figure 8.1) is assumed to have sufficient volume so that $P_{PHP,OFF,MODEL}$ reaches about 1 bar. With $P_{PHP,OFF,MODEL}$ set explicitly in this case, Equation 4.3 determine can be used to determine the OFF state working fluid mass in the PHP.

The nonlinear equation set representing the model, resulting from Equations 4.1 through 4.3, are solved numerically using the boundary conditions for the conduction model

$$T_0 = T_{PHP,COND} \tag{4.4}$$

$$T_{N_{NODES}} = T_{PHP,EVAP} \tag{4.5}$$

, resulting in a prediction of the OFF switch state parasitic heat load $\dot{Q}_{PHP,OFF,MODEL}$, the corresponding temperature and specific volume profiles of the working fluid in the PHP adiabatic section, and either the OFF switch state working fluid pressure $P_{PHP,OFF,MODEL}$ or OFF switch state mass remaining in the PHP m_{PHP}, depending on the scenario chosen for actuating the PHP shutoff valve. The modeled PHP switch OFF state conductivity and conductance are found by

$$k_{PHP,EFF,OFF,MODEL} = \frac{|\dot{Q}_{PHP,OFF,MODEL}|}{|T_{PHP,COND} - T_{PHP,EVAP}|} \frac{L_{PHP,ADIA}}{N_{PHP,TUBES}\pi\left(\frac{d_{PHP,o}}{2}\right)^2} \tag{4.6}$$

and

$$UA_{PHP,EFF,OFF,MODEL} = \frac{|\dot{Q}_{PHP,OFF,MODEL}|}{|T_{PHP,COND} - T_{PHP,EVAP}|} \tag{4.7}$$

. Finally, a pseudo-modeled switching ratio is computed using the modeled value of $UA_{PHP,EFF,OFF,MODEL}$ along with corresponding experimentally measured values of the ON state conductance $UA_{PHP,EFF,ON,EXPERIMENT}$

$$SR_{PHP,MODEL} = \frac{UA_{PHP,EFF,ON,EXPERIMENT}}{UA_{PHP,EFF,OFF,MODEL}} \tag{4.8}$$

.

4.2 Comparison of the nitrogen PHP thermal switch OFF state measurements to OFF state performance model

The PHP switch OFF state model developed in the previous section is solved here using the parameters listed in Table 4.1 which are associated with the nitrogen PHP thermal switches presented in Section 2.2. Prior to reviewing the model predictions for the parasitic heat load and effective conductivity of the OFF state PHP switch, it is worthwhile to check the model's predicted temperature and specific volume profiles through the length of the adiabatic section tubes. Figure 4.2 shows these predictions for five of the experimentally tested 2-circuit fill ratio measurements listed in Table 2.8 and Figure 2.14. A few observations from the profiles are particular noteworthy.

Table 4.1. Parameters for nitrogen PHP switch OFF state performance model

Model Parameter	Description	Value
k_{FLUID}	Thermal conductivity of PHP working fluid as a function of temperature and pressure	Nitrogen [54]
v_{FLUID}	Specific volume of PHP working fluid as a function of temperature and pressure	Nitrogen [55]
k_{WALL}	Thermal conductivity of PHP tube wall material	304 Stainless Steel [56]
N_{NODES} [32]	Model node count	200
m_{PHP}	Mass of working fluid within the PHP	$m_{PHP-II-N}$ measurements per Table 2.8.
$T_{PHP,COND}$	PHP condenser temperature	$T_{PHP-II-N,COND}$ measurements per Figures 2.14 and 2.15
$T_{PHP,EVAP}$	PHP evaporator temperature	$T_{PHP-II-N,EVAP}$ measurements per Figures 2.14 and 2.15
$V_{PHP,COND}$	PHP condenser internal volume	1813 mm^3
$V_{PHP,EVAP}$	PHP evaporator internal volume	1813 mm^3
$L_{PHP,ADIA}$	PHP adiabatic section length	$L_{PHP-II-N,ADIA}$ per Table 2.2
$d_{PHP,i}$	PHP tube internal diameter	$d_{PHP-II-N,i}$ per Table 2.2
$d_{PHP,o}$	PHP tube external diameter	$d_{PHP-II-N,o}$ per Table 2.2
$N_{PHP,TUBES}$	Number of PHP parallel tubes	$N_{PHP-II-N,TUBES}$ per Table 2.2
$UA_{PHP,EFF,ON,EXPERIMENT}$	PHP ON state conductance measurements	$UA_{PHP-II-N}$ measurements per Figures 2.14 and 2.15 with Cryocooler-II-N active

At the higher fill ratios and their associated higher OFF state PHP pressures, the mean specific volume in the PHP decreases and liquid or high density supercritical nitrogen is predicted to encroach into the end of the adiabatic tubes closest to the common cold plate. The higher the fill ratio (and OFF state pressure), the further the impingement. This result is consistent with the need to contain the larger fluid charge mass associated with higher fill ratios within the same PHP volume. However, the temperature profiles in the adiabatic section for each of these fill ratios are

32 An informal nodal converge study confirms that the chosen value of N_{NODES} is plenty large to provide sufficient solution accuracy.

nearly identical, even though the high density nitrogen at the cold end of the adiabatic section should result in enhanced conduction in the associated locations.

This is explained by the fact that k_{MODEL} in Equation 4.2 is dominated by the thermal conductivity of the tube wall (the stainless steel conductivity is roughly 7.4 W/m-K at 70 K while that for saturated liquid nitrogen roughly 0.16 W/m-K), even though the tube wall contributes a smaller fraction of the tube cross section. The practical consequence of this is that the fill ratio or actuation of the PHP shutoff valve with the deactivation of Cryocooler-II-N does not significantly affect the parasitic heat load $\dot{Q}_{PHP-II-N}$ through the OFF state PHP-II-N. Indeed this independence of $\dot{Q}_{PHP-II-N}$ is seen in the experiment results for both circuit configurations (see Figure 2.14 and Figure 2.15).

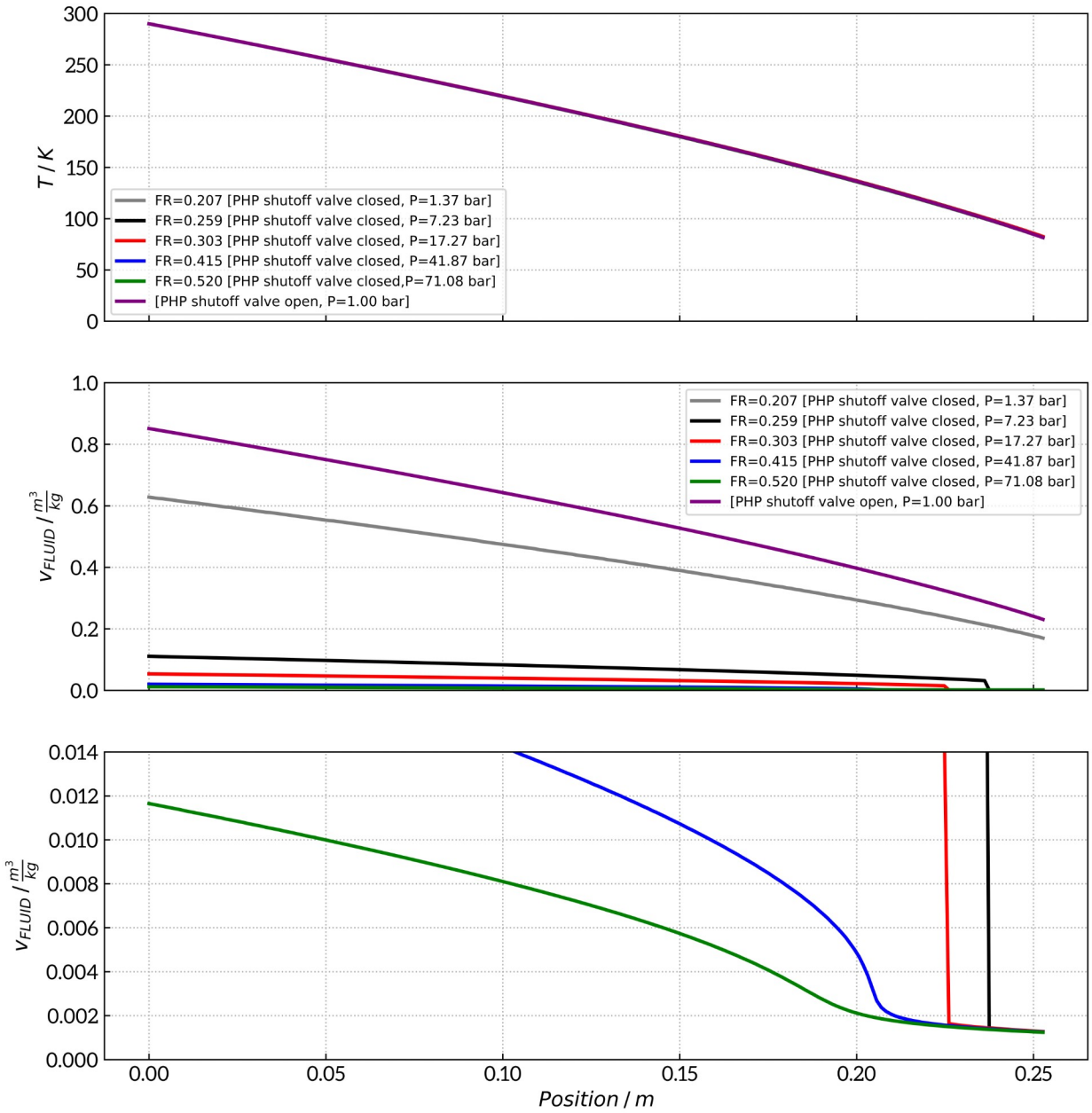

Figure 4.2. Modeled temperature (top panel) and specific volume profiles (middle and bottom panels at different scales) in the adiabatic section of the OFF state PHP-II-N. All curves use $T_{PHP\text{-}II\text{-}N,COND}$ = 290 K, $T_{PHP\text{-}II\text{-}N,EVAP}$ = 80 K, and the fill ratios from the experiment data per Table 2.8.

Modeled parasitic heat loads $\dot{Q}_{PHP,OFF,MODEL}$ through the OFF state PHP-II-N, and the OFF state parasitic load $\dot{Q}_{PHP-II-N}$ measurements from Figure 2.14 and Figure 2.15, are shown together in Figure 4.3 as a function of the corresponding measurement of the load through the cor-

responding ON state PHP-I-N $\dot{Q}_{PHP-I-N}$. Each modeled parasitic load is calculated at the same fill ratio, condenser temperature, and evaporator temperature as the corresponding measurement. Perhaps the most important observation here is that that both the modeled and experimentally measured parasitic vary little with the small changes in operating conditions between the measurement points. Such a result is not surprising since the difference between the evaporator and condenser temperature is large and does not vary greatly within the experiment data. Additionally, a majority of the modeled parasitic loads fall within the uncertainty bands of the corresponding measured parasitic loads.

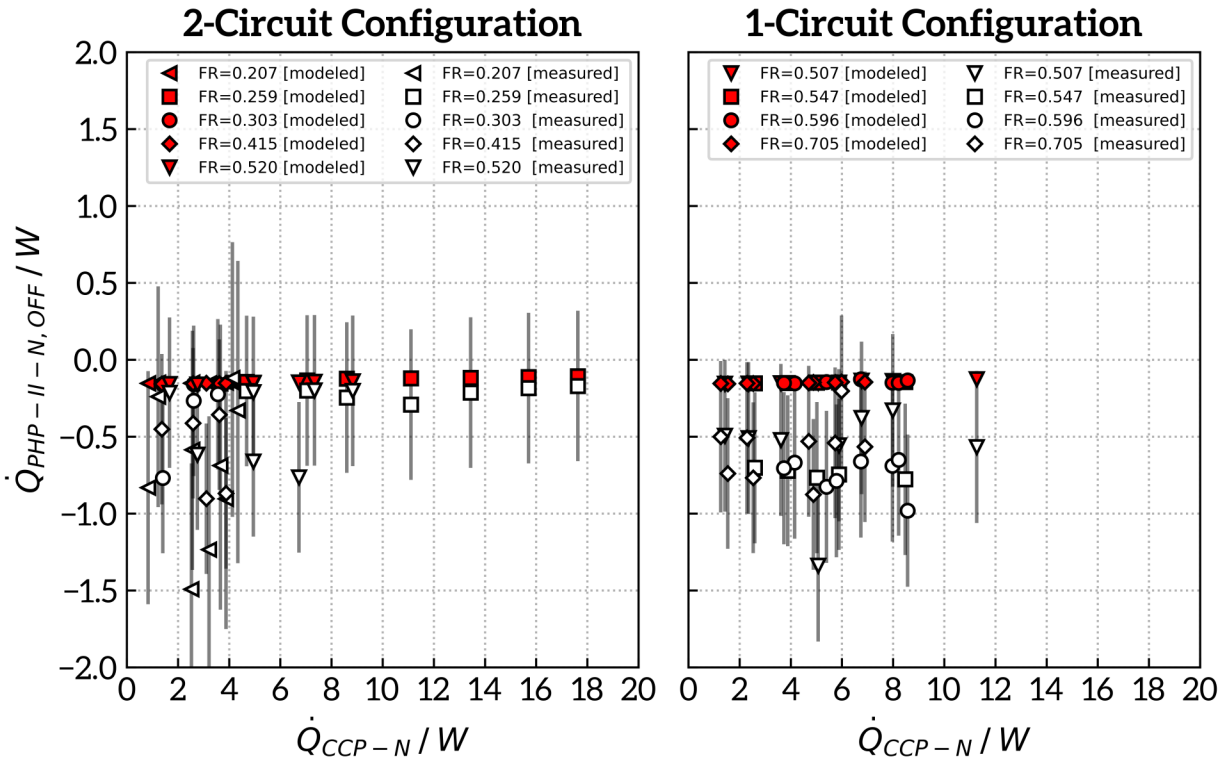

Figure 4.3. Modeled and measured parasitic heat loads through the OFF state PHP-II-N as a function of the heat flow through the ON state PHP-I-N. 2-circuit configuration models are for the PHP shutoff valve closed (PHP pressure varies with fill fraction) and 1-circuit configuration models are with the PHP shutoff valve open (PHP pressure is 1 bar).

There is, however, a small systematic error causing the measured parasitic loads to be consistently larger in magnitude than the modeled values. This bias appears to be *slightly* larger in the 1-circuit configuration than in the 2-circuit configuration. There are two likely causes driving this discrepancy: a systematic error in the temperature measurements (present for both the 1-circuit and 2-circuit results), and a small amount of fluid movement within the OFF state 1-circuit PHP-II-N. The latter is plausible because the PHP-II-N circuit shares a common fluid loop with the PHP-I-N, the latter which continues to operate in the advective slug-plug flow regime while the former is (mostly) dry. A reasonable hypothesis for the 1-circuit configuration is that some of the moving liquid slugs from the connected ON state PHP-I-N oscillate into the adiabatic section of the OFF state PHP-II-N before evaporating, effectively shortening the length of adiabatic section and slightly increasing the effective thermal conductivity relative to the 2-circuit configuration and model.

Figure 4.4 shows the modeled and measured effective thermal conductivities corresponding to the parasitic loads of Figure 4.3. The results are as expected from the preceding discussion regarding the parasitic loads – the measured effective conductivities are nearly constant for all measured data and are biased slightly higher than the corresponding measurement values, yet mostly fall within the uncertainty bands. Again the 1-circuit configuration shows slightly higher bias in the effective thermal conductivity than the 2-circuit configuration.

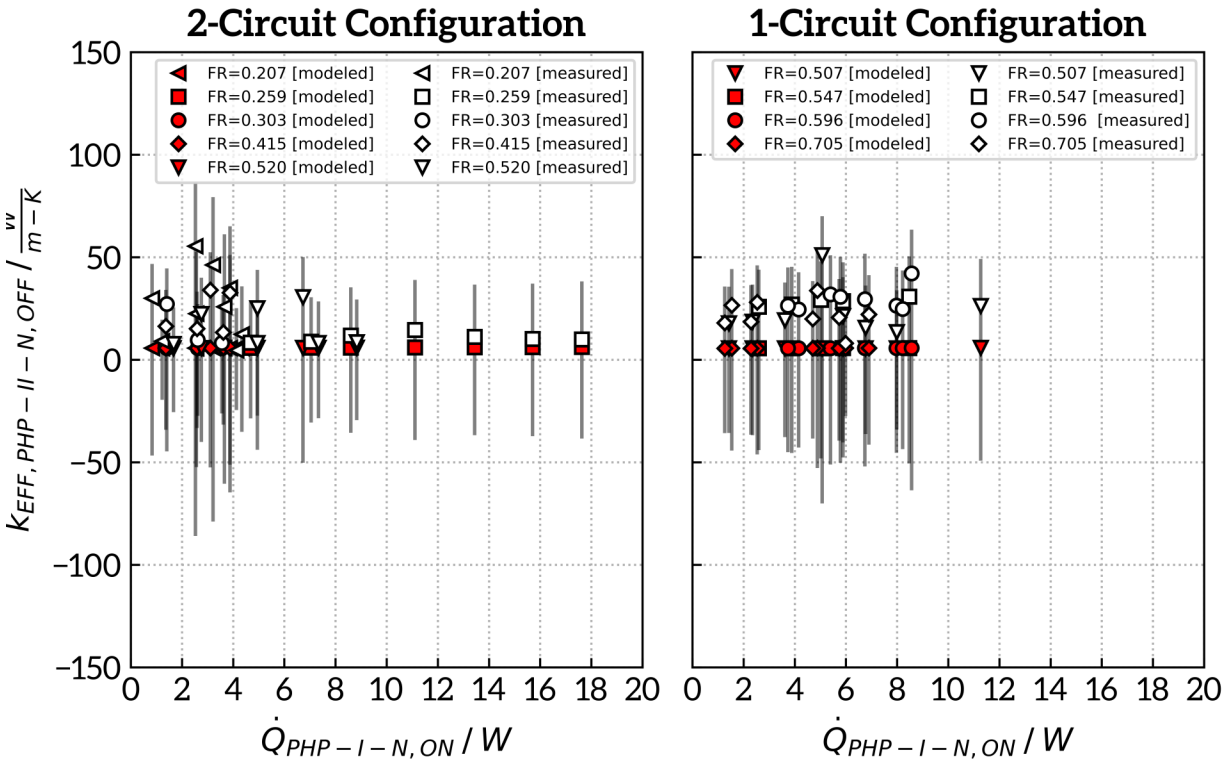

Figure 4.4. Modeled and measured effective thermal conductivity through the OFF state PHP-II-N as a function of the heat flow through the ON state PHP-I-N. 2-circuit configuration models are for the PHP shutoff valve closed (PHP pressure varies with fill fraction) and 1-circuit configuration models are with the PHP shutoff valve open (PHP pressure is 1 bar).

Finally, Figure 4.5 compares the measured and psuedo-modeled switching ratios for PHP-II-N for all ON state PHP-II-N heat loads. Consistent with the relation between the modeled and experiment measurements for the parasitic load and effective thermal conductivies, the modeled switching ratios are systematically higher than the experimental measurements. For the 2-circuit configuration, the modeled switching ratios mostly fall within the experimentally uncertainty bands. The modeled switching ratios for the 1-circuit configuration consistently fall on the margins of the error bars for the experiment data. The larger gap between the model and experiment data for the 1-circuit data is again likely explained by a small amount of advective flow occurring within the adiabatic section while in the OFF state, which is not considered in the model.

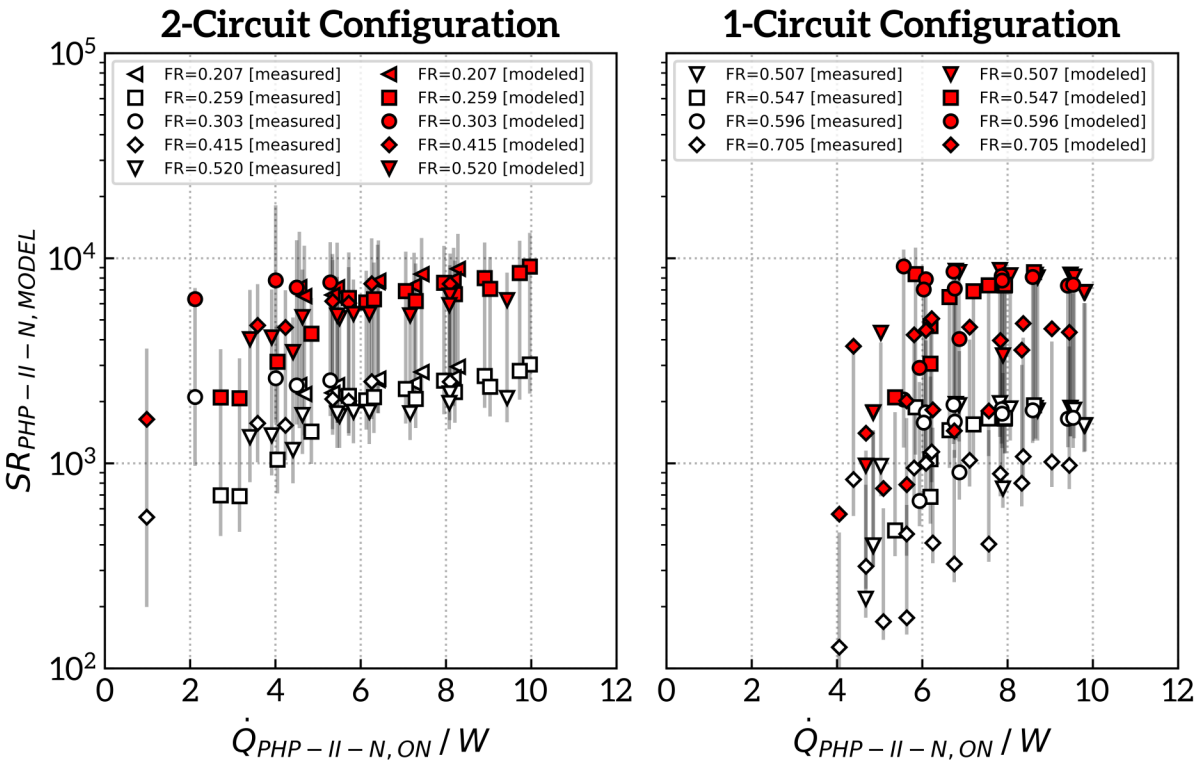

Figure 4.5. Modeled and measured switching ratio for PHP-II-N as a function of the heat flow through the ON state PHP-I-N. 2-circuit configuration models are for fill valve closed (PHP pressure varies with fill fraction) and 1-circuit configuration models are with fill valve open (PHP pressure is 1 bar).

Overall, the simple OFF state PHP performance model presented in Section 4.1 appears to agree well with the nitrogen PHP thermal switch test data. This agreement suggests that there is no large unexpected OFF state advective thermal communication between the evaporator and condenser plates for the 2-circuit configuration. For the 1-circuit configuration, a small amount of advective communication perhaps remains in the switch OFF state due the plumbing shared with the remaining ON state PHP. However, it is entirely plausible that much of disagreement between the model and experiment results is simply due to systematic bias in the measurement system.

4.3 Comparison of the helium PHP thermal switch OFF state measurements to OFF state performance model

Here the PHP switch OFF stat model is applied to the helium PHP thermal switches developed in Section 3 and solved using the parameters listed in Table 4.2. Model predictions of the temperature and specific volume profiles through the adiabatic section tubes of the helium PHPs are shown in Figure 4.6. Simulation results are shown for both PHP-II-H fill ratios tested in the OFF state per Table 4.9 and Figure 3.24. The behavior of these curves is similar to those of the nitrogen PHP thermal switch OFF state model with some small but important differences.

Table 4.2. Parameters for helium PHP switch OFF state performance model

Model Parameter	Description	Value
k_{FLUID}	Thermal conductivity of PHP working fluid as a function of temperature and pressure	Helium [57]
v_{FLUID}	Specific volume of PHP working fluid as a function of temperature and pressure	Helium [58]
k_{WALL}	Thermal conductivity of PHP tube wall material	304 Stainless Steel [56]
N_{NODES} [33]	Model node count	200
m_{PHP}	Mass of working fluid within the PHP	$m_{PHP-II-H}$ measurements per Table 3.9
$T_{PHP,COND}$	PHP condenser temperature	$T_{PHP-II-H,COND}$ measurements per Figure 3.24
$T_{PHP,EVAP}$	PHP evaporator temperature	$T_{PHP-II-H,EVAP}$ measurements per Figure 3.24
$V_{PHP,COND}$	PHP condenser internal volume	24.6 mm^3
$V_{PHP,EVAP}$	PHP evaporator internal volume	24.6 mm^3
$L_{PHP,ADIA}$	PHP adiabatic section length	$L_{PHP-II-H,ADIA}$ per Table 3.3
$d_{PHP,i}$	PHP tube internal diameter	$d_{PHP-II-H,i}$ per Table 3.3
$d_{PHP,o}$	PHP tube external diameter	$d_{PHP-II-H,o}$ per Table 3.3
$N_{PHP,TUBES}$	Number of PHP parallel tubes	$N_{PHP-II-H,TUBES}$ per Table 3.3
$UA_{PHP,EFF,ON,EXPERIMENT}$	PHP ON state conductance measurements	$UA_{PHP-II-H}$ measurements per Figure 3.24 with Cryocooler-II-H active

33 An informal nodal converge study confirms that the chosen value of N_{NODES} is plenty large to provide sufficient solution accuracy.

At higher fill ratios and their associated higher OFF state PHP pressures, the mean specific volume of the helium in the PHP decreases. This is identical to the modeled behavior of the OFF state nitrogen PHPs, as the relation between lower specific volume and higher fill ratios remains consistent with the need to contain more fluid mass with higher fill ratios within the same PHP volume, even with the change in fluid type. With the helium, however, there is no liquid encroachment into the adiabatic section of the PHP. This difference in behavior is associated with the much lower critical temperature for helium (5.19 K) compared with nitrogen (126.2 K).

The temperature profiles in the adiabatic section for each of the fill ratios shown in Figure 4.6 are nearly identical, which is reasonable given that there is no liquid present in the adiabatic section for any of the modeled fill ratios. Note that the predicted OFF state pressures for the tested fill ratios are quite high (about 141 bar for the FR=0.194 and 280 bar for FR=0.479). There is no available sensor in the experiment facility to measure the pressure in the OFF state PHP-II-H with its shutoff valve (see Section 8.2) closed, so the pressure at which the OFF state experiment results are obtained is unknown. It is possible that the PHP tubes and filling lines, with its solder joints and shutoff valve seals as its weakest mechanical structures, could survive such pressures intact. It is also possible that some high density liquid helium liquid is stored on the evaporator end of the adiabatic section to an extent not predicted by the model, which would have the effect of lowering the OFF state pressure compared to the model prediction.

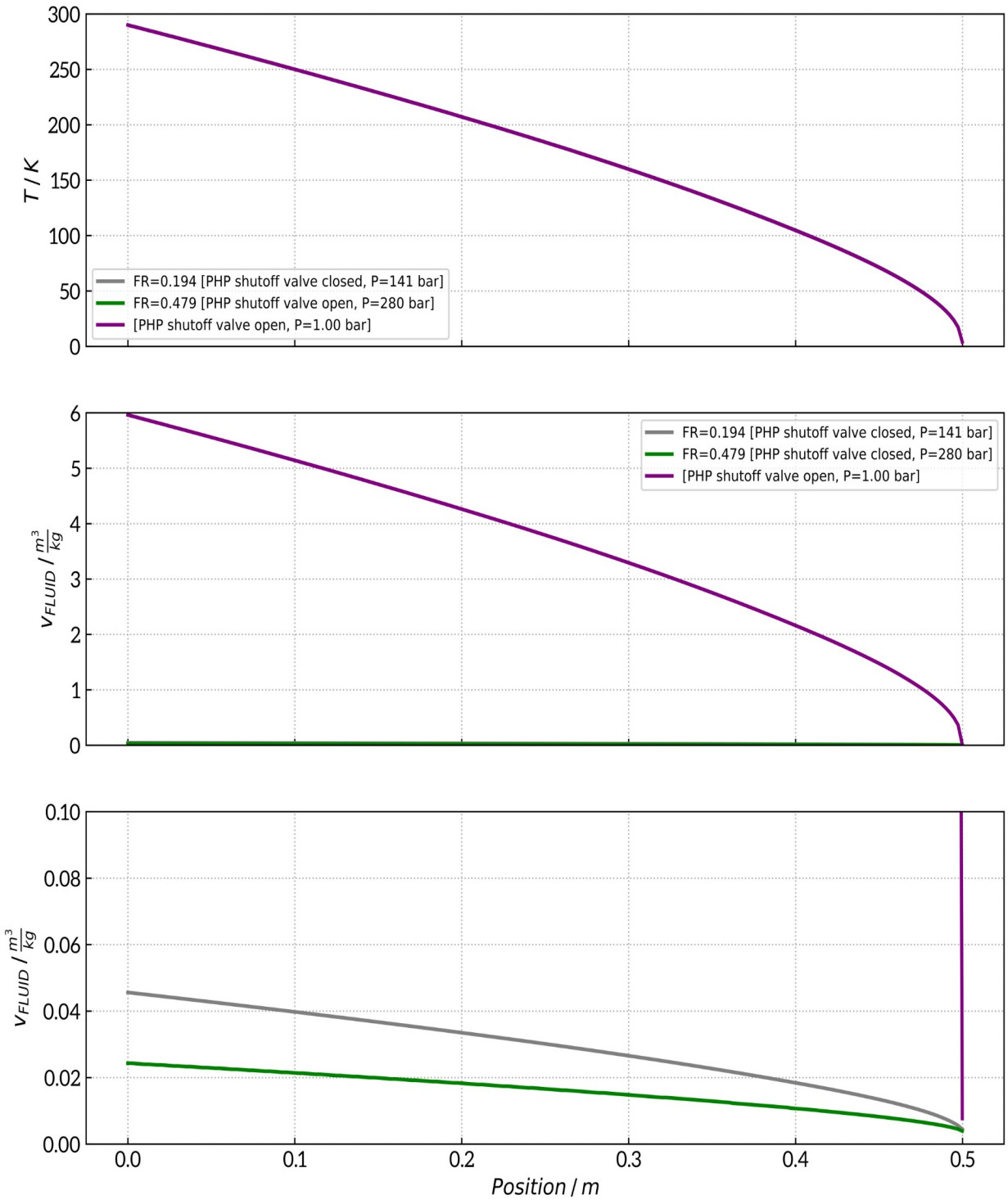

Figure 4.6. Modeled temperature (top panel) and specific volume profiles (middle and bottom panels at different scales) in the adiabatic section of the OFF state PHP-II-H. All curves use $T_{PHP\text{-}II\text{-}H,COND}$ = 290 K, $T_{PHP\text{-}II\text{-}H,EVAP}$ = 4 K, and the fill ratios from the experiment data per Table 3.2.

Modeled parasitic heat loads $\dot{Q}_{PHP,OFF,MODEL}$ through the OFF state PHP-II-H, and the OFF state parasitic load $\dot{Q}_{PHP-II-H}$ measurements from Figure 3.24 are shown together in Figure Figure 4.7 as a function of the corresponding measurement of the load through the ON state PHP-I-H $\dot{Q}_{PHP-I-H}$. Each modeled parasitic load is calculated at the same fill ratio, condenser temperature, and evaporator temperature as the corresponding measurement. As expected from the OFF state nitrogen PHP model and experiment data, the most important observation here is that that both the modeled and experimentally measured parasitic vary little with the small changes in operating conditions between the measurement points. Again this is not a surprising result since the difference between the evaporator and condenser is even larger than seen with the nitrogen PHP switches (about 285K versus 220 K) and does not vary greatly within the experiment data.

Diverging from the comparison with the nitrogen PHP switch model results, the majority of the modeled parasitic heat loads $\dot{Q}_{PHP-II-H}$ for the helium PHPs shown in Figure 4.7 are slightly out side of the uncertainty bands for the corresponding measured parasitic loads, with the model consistently predicting a smaller magnitude $|\dot{Q}_{PHP-II-H}|$ than measured. Recall that a similar bias is present in the nitrogen PHP OFF state parasitic load measurements – explainable by systematic error in the heat meter temperature measurements. Here, however, the discrepancy is likely caused by a net radiative, rather than conductive, parasitic load into the PHP-II-H evaporator, visualized previously in Figure 3.14. Evidence for this is discussed in Section 3.6.4, where a $\dot{Q}_{PHP-II-H} \propto T^4_{PHP-II-H,COND}$ relationship is found, suggesting that a radiative leak from the '4 K'

shield (now at 290 K) to the coldest surfaces of PHP-II-H nearest the evaporator (remaining near 4 K) is responsible for much of the measured $\dot{Q}_{PHP-II-H}$.

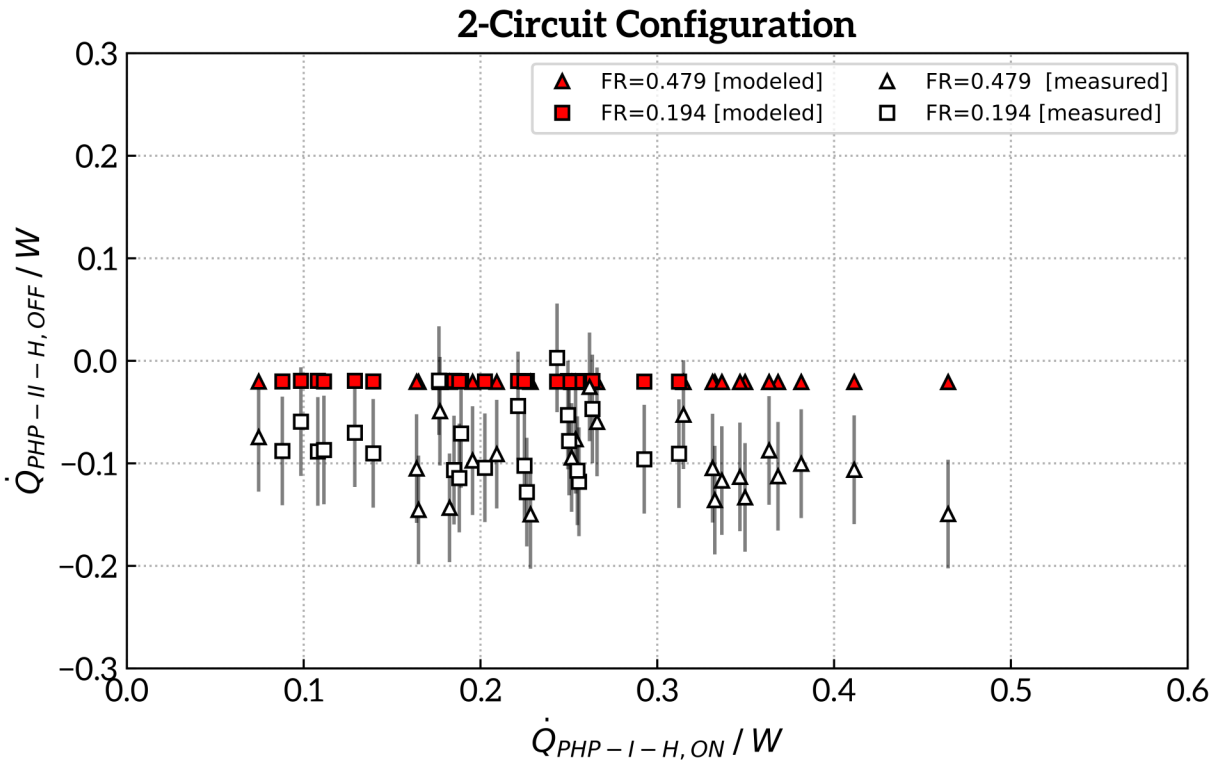

Figure 4.7. Modeled and measured parasitic heat loads through the OFF state PHP-II-H as a function of the heat flow through the ON state PHP-I-H with the PHP shutoff valve closed.

Figure 4.8 shows the modeled and measured effective thermal conductivities corresponding to the parasitic loads shown in Figure 4.7. The results are as expected from the preceding discussion regarding the parasitic loads – the measured effective thermal conductivities are nearly constant for all measured data but are biased slightly higher and generally just outside of the uncertainty bands compared to the corresponding measurement values.

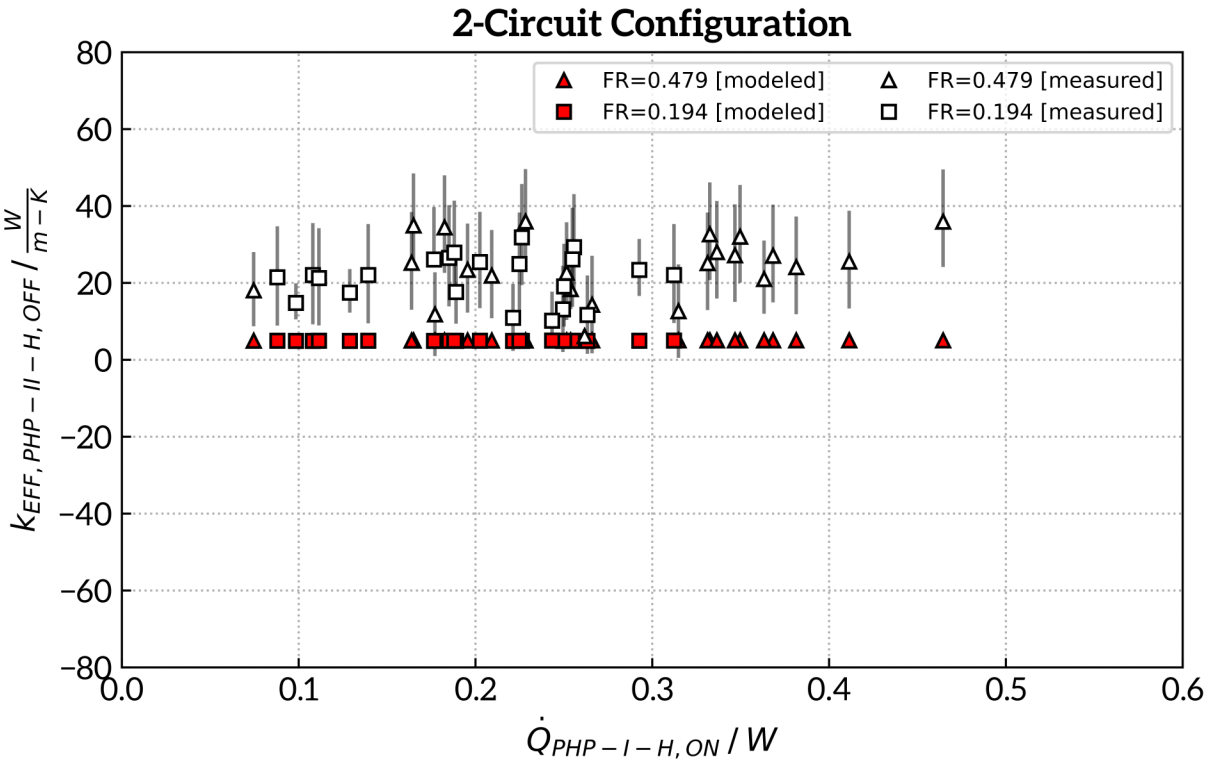

Figure 4.8. Modeled and measured effective thermal conductivity through the OFF state PHP-II-H as a function of the heat flow through the ON state PHP-I-H with the PHP shutoff valve closed.

Lastly, Figure 4.9 compares the measured and psuedo-modeled switching ratios for PHP-II-H for all ON state PHP-II-H heat loads $\dot{Q}_{PHP-II-H}$. The modeled switching ratios are systematically higher than the experimental measurements, which is consistent with results from the modeled parasitic loads and OFF state thermal conductivities presented previously. The modeled switching ratios consistently fall above the error bars for the experiment data, which is again likely explained by the radiative leak which is not considered by the model.

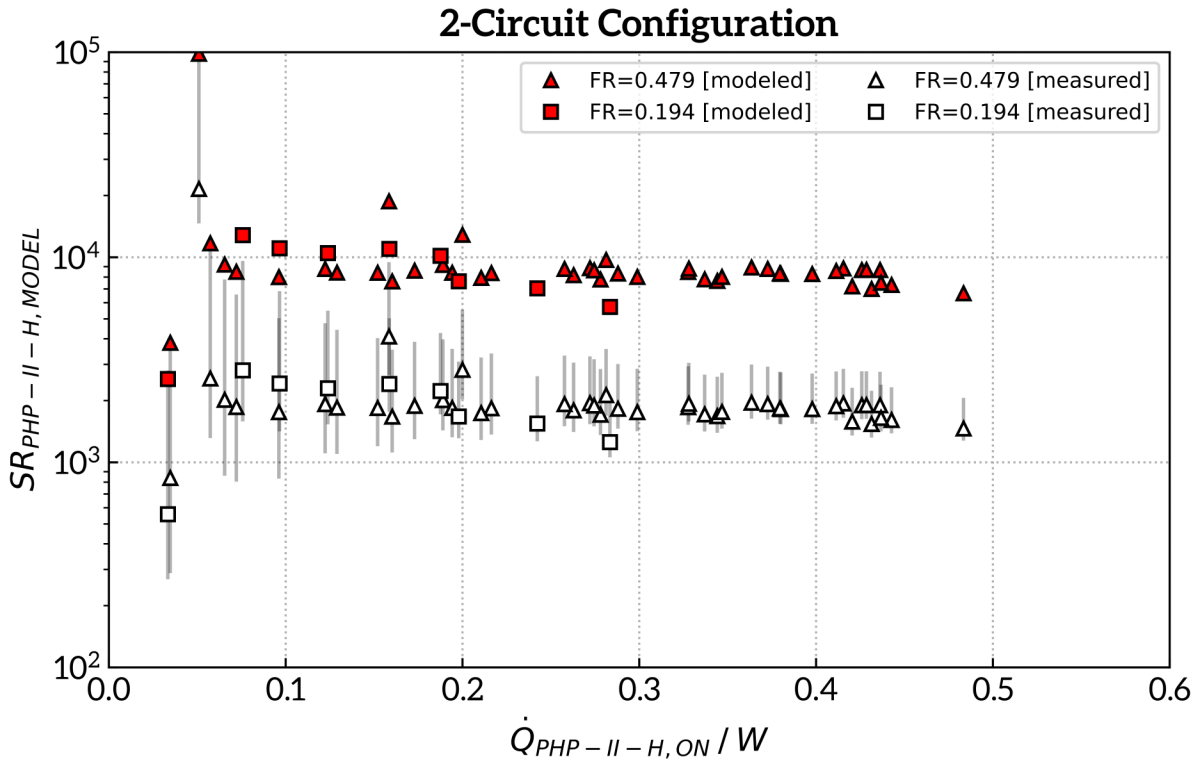

Figure 4.9. Modeled and measured switching ratio for PHP-II-H as a function of the heat flow through the ON state PHP-I-H with the PHP shutoff valve closed.

Qualitatively, the OFF state performance model developed in Section 4.1 is shown now to agree *quite well* with both the nitrogen PHP thermal switch test data (from Section 2.5) and *fairly well* with the helium PHP thermal switch test data (from Section 3.6). With independent devices, two different working fluids, and two different operating temperature ranges, the good agreement overall suggests that there is no large unexpected OFF state advective thermal communication between the evaporator and condenser plates for independent (2-circuit) PHP tubing configurations; all deviations between the OFF state models and the experiment results can be explained by the experiment measurement uncertainties and imperfect radiation shielding. The radiation shielding issue certainly has practical consequences, however, as a helium PHP thermal switch intended for a real application would likely require a smaller parasitic than observed in this

proof-of-principle facility. Reducing the OFF state radiation parasitic is not an insurmountable issue, however, but is rather an engineering design and construction issue, requiring greater care in construction of the 70 K shield and MLI.

5 Development of a PHP thermal switch ON state performance model

Modeling the advective flow in PHPs (the ON state for the thermal switches in this work) is, in general, a complicated three dimensional and time dependent multi-physics problem involving two phase fluid dynamics and thermal conduction. To make the problem tractable and solvable in a way which allows parametric studies to be completed within reasonable simulation times on desktop workstation computers, the dimensionality of the problem must be reduced from that of the general case without sacrificing the fidelity of the fundamental physics on which the PHP operates.

5.1 Model definition

5.1.1 Model physics

The approach used here is the so-called mass-spring-damper PHP model, first developed by Shafii and Faghri [59] and subsequently modified in various ways by Ma [60], Gürsel [61], Fonseca [35], and Sun [62]. The core simplification in such models is the assumption that the inner PHP tube diameter is below the critical diameter (see Equation 1.9) and therefore liquid slugs always span the cross section of the PHP tube. In this case, the positions and velocities of individual liquid slugs within the PHP are restricted to a single dimension along the axis of the PHP tube, as depicted in Figure 5.1.

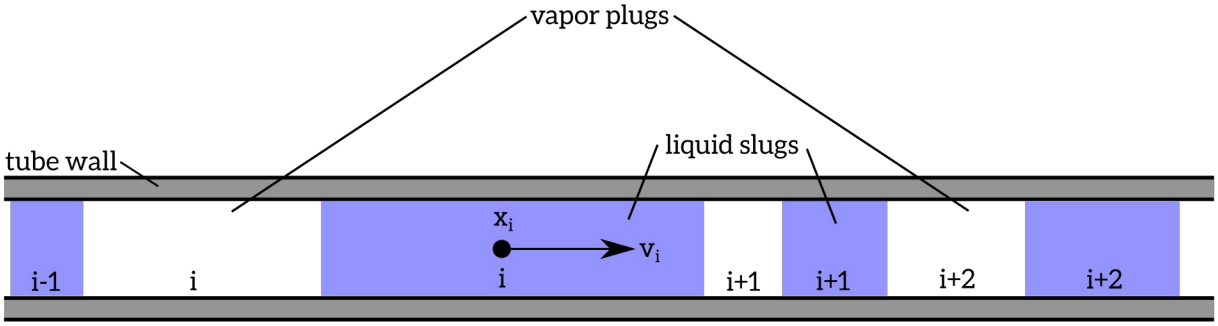

Figure 5.1. Schematic showing liquid slugs and vapor plugs in a PHP tube as considered in a mass-spring-damper -style PHP model

A momentum balance can be written for each (the i^{th}) *liquid* slug

$$\frac{d}{dt}\left(m_i v_i\right) = F_{p,i} + F_{g,i} + F_{v,i} + F_{c,i} \qquad \text{where i is a liquid slug} \tag{5.1}$$

, where t is time, m_i is the slug mass, v_i is the slug velocity, $F_{p,i}$ is the net force on the liquid slug from the adjacent vapor plugs, $F_{g,i}$ is the buoyancy force, $F_{v,i}$ is the viscous force, and $F_{c,i}$ is the capillary force. These pressure and buoyancy forces are defined by

$$F_{p,i} = A_i\left(P_i - P_{i+1}\right) \tag{5.2}$$

$$F_{g,i} = m_i g f_i \cos\left(\alpha\right) \tag{5.3}$$

where A_i is the inner cross sectional area of the tube through which the fluid flows, P_{i+1} and P_i are the pressures of the adjacent *vapor* plugs[34], g is the gravitational constant, f_i is +1 or -1 depending on the direction of the gravity force relative to the tube axial tube position vector in which the cell resides (which flips every parallel tube section), and α is the angle of the PHP tube plain (0 is vertical, π/2 is horizontal). Figure 5.2 shows illustrates the gravity related parameters of the PHP geometry. The viscous and capillary forces are given in Equation 5.21 and

34 Note that the liquid and vapor cells share indices (i.e. there is both a liquid and vapor index i).

5.23, but further development of the model framework must be developed prior to their definition.

The momentum balance of Equation 5.1 can be solved for the velocity time derivative

$$\frac{dv_i}{dt} = \left(F_{p,i} + F_{g,i} + F_{v,i} + F_{c,i} - v_i \frac{dm_i}{dt} \right) \frac{1}{m_i} \qquad \text{where i is a liquid slug} \tag{5.4}$$

, which is related to the position time derivative by

$$\frac{dx_i}{dt} = v_i \qquad \text{where i is a liquid slug} \tag{5.5}$$

. Given this equation set, it is straightforward to see that the mass-spring-damper derives its name from the analogous mechanical dynamic system: here the mass is the liquid slug mass, the (non-linear) spring is the related to the energy stored in the adjacent vapor plugs, and the damper is the viscous loss.

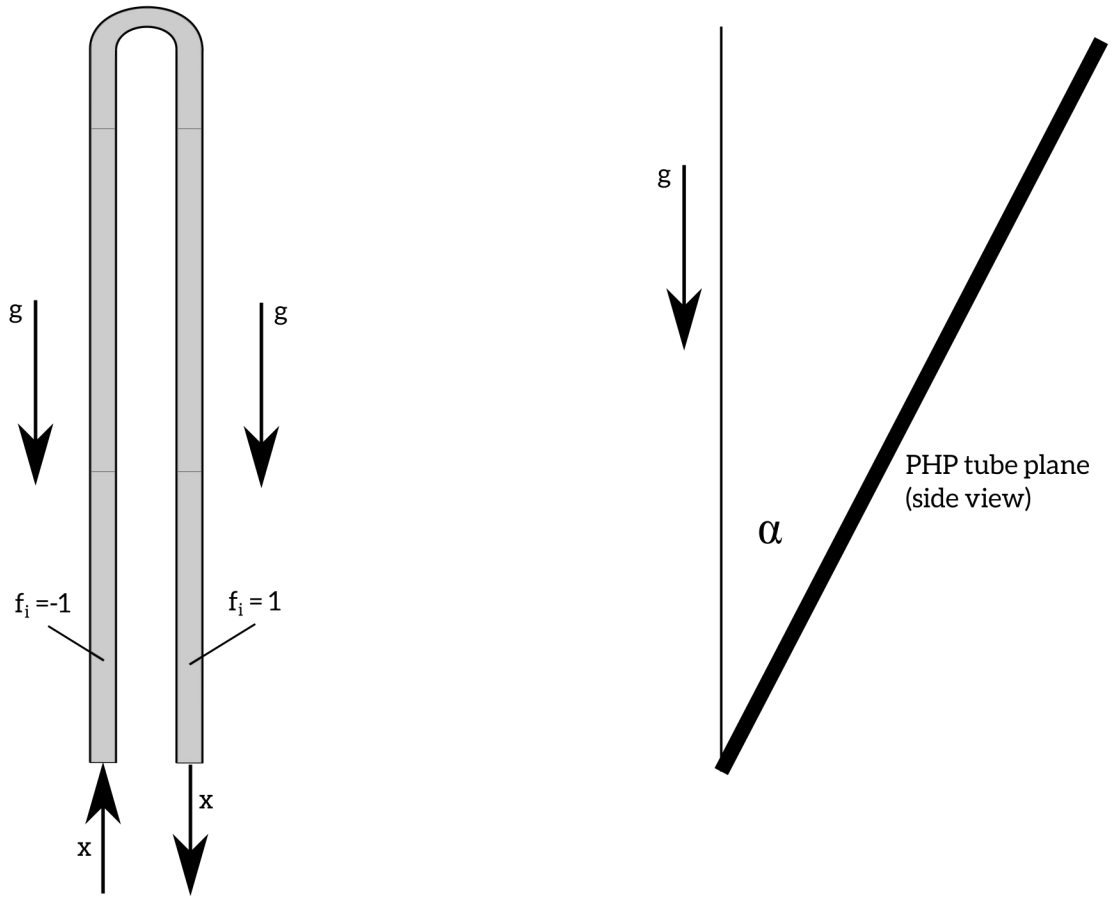

Figure 5.2. Illustration showing the gravity vector and axial tube vector for consecutive tube passes (left panel) and tilt angle (right panel)

The momentum equation must be complemented with a thermal model to describe the heat and mass transfer within the fluid, tube walls, evaporator plate, and condenser plate. To do this, the tube walls, liquid slugs, and vapor plugs are discretized further into smaller cells as depicted in Figure 5.3. Here the control volumes of the fluid move in time (due to the momentum equation) relative to the stationary tube wall cells. Liquid cells are assumed incompressible and saturated – meaning that the internal energy, enthalpy, and thermal conductivity are functions of temperature only; vapor cells use real fluid properties from a reduced-Helmholtz equation of state (See Section 5.1.4 for more details regarding this).

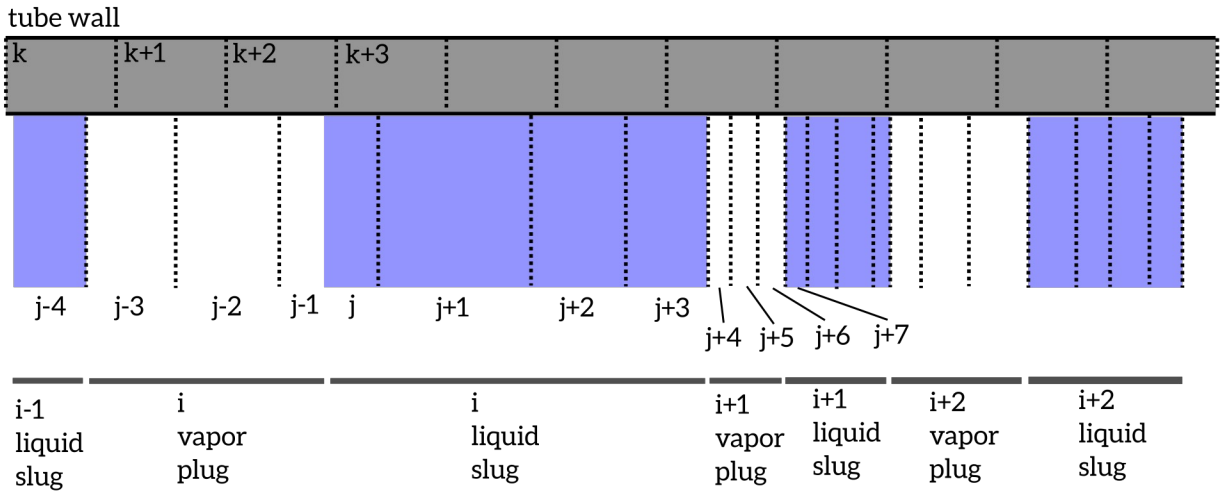

Figure 5.3. Schematic showing the discretization of the PHP tube walls, liquid slugs, and vapor plugs used for the thermal model. Momentum equation discretization index is i (only the liquid slugs), fluid thermal cell index is j (may be liquid or vapor), and wall thermal cell index is k.

The 1st law applied to the jth fluid cell control volume of Figure 5.4 (which may in general be liquid or vapor) as

$$\begin{aligned}\frac{dU_j}{dt} = &\left(\frac{\lambda_{fluid}(T_j)+\lambda_{fluid}(T_{j-1})}{2}\right)A_i\left(\frac{T_{j-1}-T_j}{x_j-x_{j-1}}\right)+\\ &\left(\frac{\lambda_{fluid}(T_{j+1})+\lambda_{fluid}(T_j)}{2}\right)A_i\left(\frac{T_{j+1}-T_j}{x_{j+1}-x_j}\right)+\\ &F_{v,j}v_j+\dot{H}_{in}-\dot{H}_{out}+\sum_{k_a}^{k_b}h_j A_{s,jk}(T_k-T_j)-P_j\frac{d\,Vol_j}{dt}\end{aligned} \tag{5.6}$$

where U_j is the internal energy of the jth fluid cell, T_j is the temperature of the jth fluid cell, $\lambda_{fluid}(T_k)$ is the temperature dependent thermal conductivity of the jth fluid cell, x_j is the center position of the jth fluid cell, $F_{v,j}$ is the viscous force on the ith fluid cell, v_i is the velocity of the ith fluid cell, $\dot{H}_{in}$ is the total enthalpy flux inbound to the jth fluid cell due to evaporation (if cell j is vapor) or condensation (if cell j is liquid) in nearby cells, $\dot{H}_{out}$ is the enthalpy flux outbound from the jth fluid cell due to evaporation (if cell j is liquid) or condensation (if cell

j is vapor) within the j^{th} fluid cell, k_a through k_b are the range of wall cell indices in contact with the j^{th} fluid cell, h_j is the heat transfer coefficient for the j^{th} fluid cell in contact with the k^{th} tube wall cell, $A_{s,jk}$ is the surface area for the j^{th} fluid cell in contact with the k^{th} tube wall cell, T_k is the temperature of the k^{h} wall cell, P_j is the pressure of the j^{th} fluid cell, and $\frac{dVol_j}{dt}$ is the time derivative of the volume change for the j^{th} fluid cell. Equation 5.6 captures the physics of axial conduction in the fluid, viscous dissipation, enthalpy flux due to evaporation and condensation, convective heat transfer with the tube wall, and the compression/expansion work.

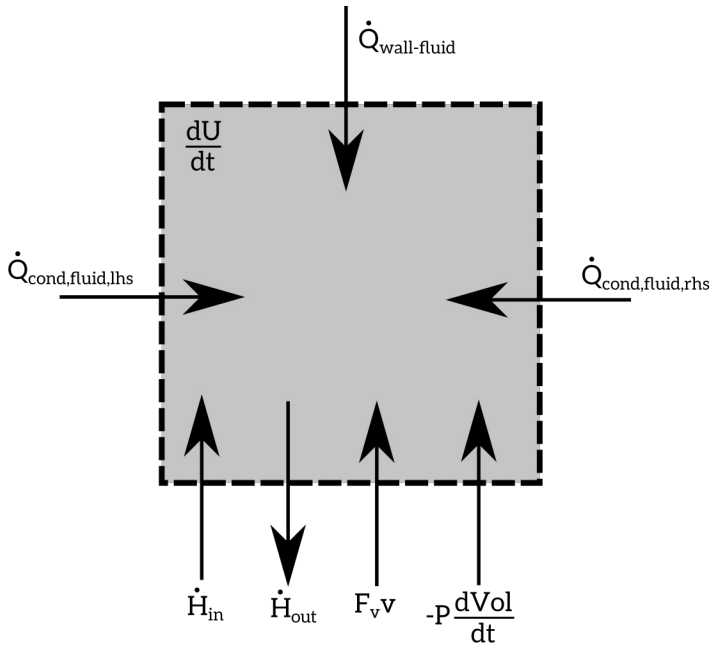

Figure 5.4. Schematic of a fluid cell control volume showing rates of energy flows into or out of the cell

The compression / expansion work term in Equation 5.6 is determined for the vapor cells from the velocities and volumes of the adjacent i-indexed liquid plugs. The volume change of an i-in-

dexed vapor plug is distributed equally over all of its discretized j-indexed fluid cells; the term is zero for the incompressible liquid cells.

The outbound enthalpy flux term in Equation 5.6 is related to the mass transfer rate by

$$\begin{aligned} \dot{H}_{out,j} &= \dot{m}_{out,j} h_{sat,liquid}(T_j) \quad \text{if j is a vapor cell} \\ \dot{H}_{out,j} &= \dot{m}_{out,j} h_{sat,vapor}(T_j) \quad \text{if j is a liquid cell} \end{aligned} \tag{5.7}$$

, where $\dot{m}_{out,j}$ is the mass flow rate out of the j^{th} cell, $h_{sat,liquid}$ is the saturated liquid enthalpy, and $h_{sat,vapor}$ is the saturated vapor enthalpy. This implies that mass can only leave a liquid cell if it is evaporated, and mass can only leave a vapor cell if it is condensed. Evaporated vapor leaving a liquid cell is distributed equally to the cells composing the immediate adjacent vapor plugs, while condensed liquid leaving a vapor cell is distributed equally to the cells composing the nearest liquid plugs. This process is depicted in Figure 5.5. This simple mass distribution model means that the j^{th} cell can receive condensed liquid from the cells comprising the immediate neighboring vapor cells (if it is liquid) or receive evaporated vapor from the cells comprising the neighboring liquid cells (if it is vapor). The inbound enthalpy flux for the j^{th} cell is then

$$\begin{aligned} \dot{H}_{in,j} &= \sum_{s_a}^{s_b} \dot{m}_{out,s} h_{sat,vapor}(T_s) \quad \text{if j is a vapor cell} \\ \dot{H}_{in,j} &= \sum_{s_a}^{s_b} \dot{m}_{out,s} h_{sat,liquid}(T_s) \quad \text{if j is a liquid cell} \end{aligned} \tag{5.8}$$

, where s_a and s_b indicate the range of neighboring fluid cell indices feeding mass to the j^{th} cell.

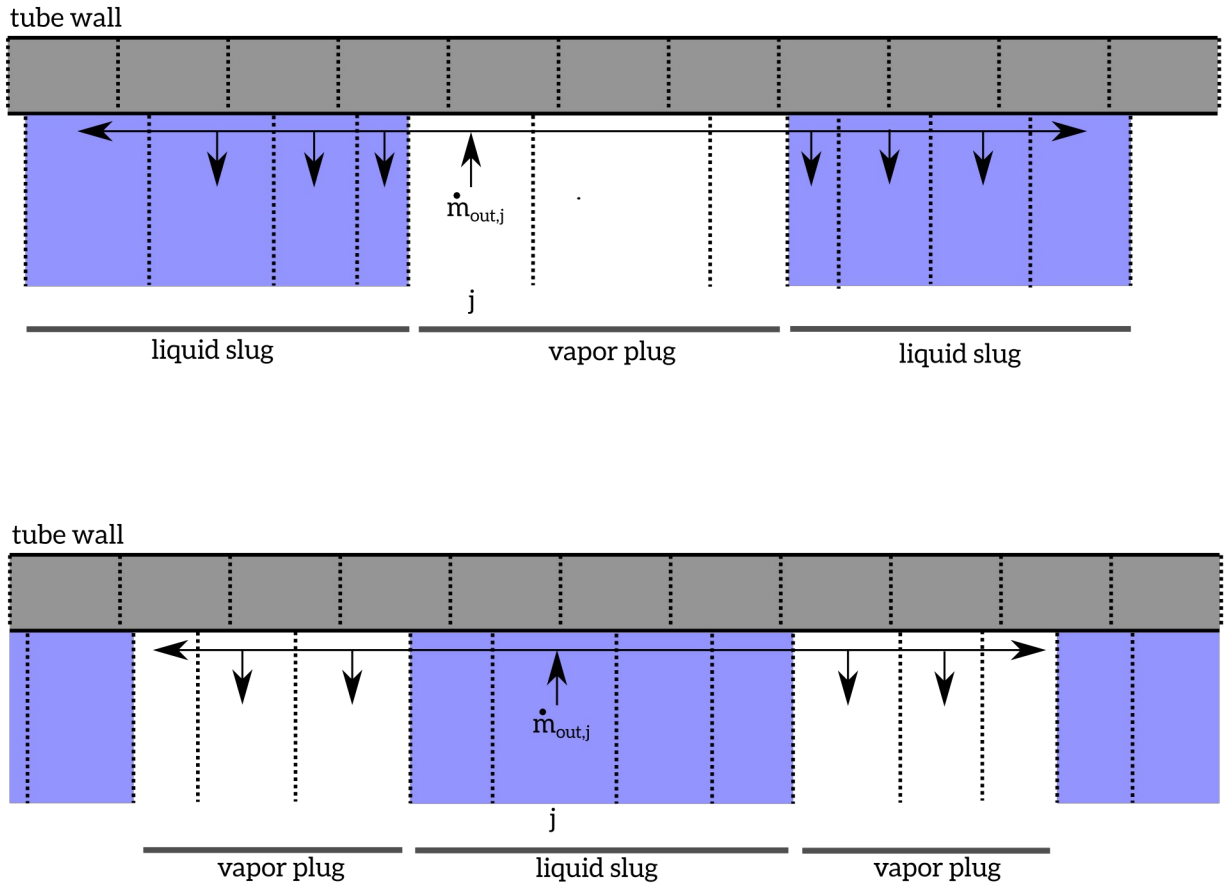

Figure 5.5. Schematic showing the distribution of condensate leaving vapor cell j (upper panel) and evaporate leaving liquid cell j (lower panel)

The heat transfer coefficients used for the convective term in Equation 5.6 vary with fluid cell type and its position in the PHP per

If j is either **liquid** or **vapor** and in the **adiabatic** section:

$$h_j = 3.66 \frac{k_j}{d_i}$$

If j is **liquid** and in the **evaporator** section [63]:

$$h_j = 3.66 \frac{k_j}{d_i} \left(12 + 3000\, Bo^{0.86}\right)$$

where

$$Bo = \frac{\sum_{k_a}^{k_b} h_j A_{s,jk} \left(T_k - T_j\right)}{\left(\frac{dm_j}{dt}\left(h_{sat,vapor}\left(T_j\right) - h_{sat,liquid}\left(T_j\right)\right)\right)}$$

If j is **vapor** and in the **evaporator** section [62][64][65][59]:

$$h_j = k_j \frac{1 + 3.335\, Ca_j^{2/3}}{0.67\, d_i\, Ca_j^{2/3}}$$

where

$$Ca_j = 0.5\left(\frac{\mu_{j_a} v_{j_a}}{\sigma_{j_a}} + \frac{\mu_{j_b} v_{j_b}}{\sigma_{j_b}}\right) \quad (5.9)$$

with j_a and j_b the nodes of the nearest liquid cells on each side of the j^{th} vapor cell

If j is **liquid** and in the **condenser** section:

$$h_j = 3.66 \frac{k_j}{d_i}$$

If j is **vapor** and in the **condenser** section [62][64][65][59]:

$$h_j = k_j \frac{1 + 3.335\, Ca_j^{2/3}}{0.67\, d_i\, Ca_j^{2/3}}$$

where

$$Ca_j = 0.5\left(\frac{\mu_{j_a} v_{j_a}}{\sigma_{j_a}} + \frac{\mu_{j_b} v_{j_b}}{\sigma_{j_b}}\right)$$

with j_a and j_b the nodes of the nearest liquid cells on each side of the j^{th} vapor cell

, where Ca_j is the capillary number of the j^{th} fluid cell. With this approach, the heat transfer coefficient for all fluid cells in locations undergoing only sensible energy transfer is (rather crudely) estimated by assuming fully developed single phase flow with constant heat flux from the wall. In the evaporator, liquid cells see heat transfer enhancement due to boiling (using the Gungor and Winteron correlation [63]) and vapor cells due to conduction through a thin evaporating liquid film which coats the tube wall (see [62][64][59][65]). An analogous condensing film also occurs on the tube wall surface of vapor cells in the condenser, which uses the same correlation for heat transfer enhancement. Note that such liquid films are not explicitly included in this model in terms of mass transfer, however. Because of this, any enhanced heat transfer in vapor cells due to evaporation in these wall films is instead distributed equally to the nearest adjacent liquid plugs where it can drive evaporation from a liquid fluid cell. Figure 5.6 illustrates the thin films which form at the tube wall-vapor cell interface and how the heat transfer enhancement is directed to the neighboring liquid cells in the evaporator.

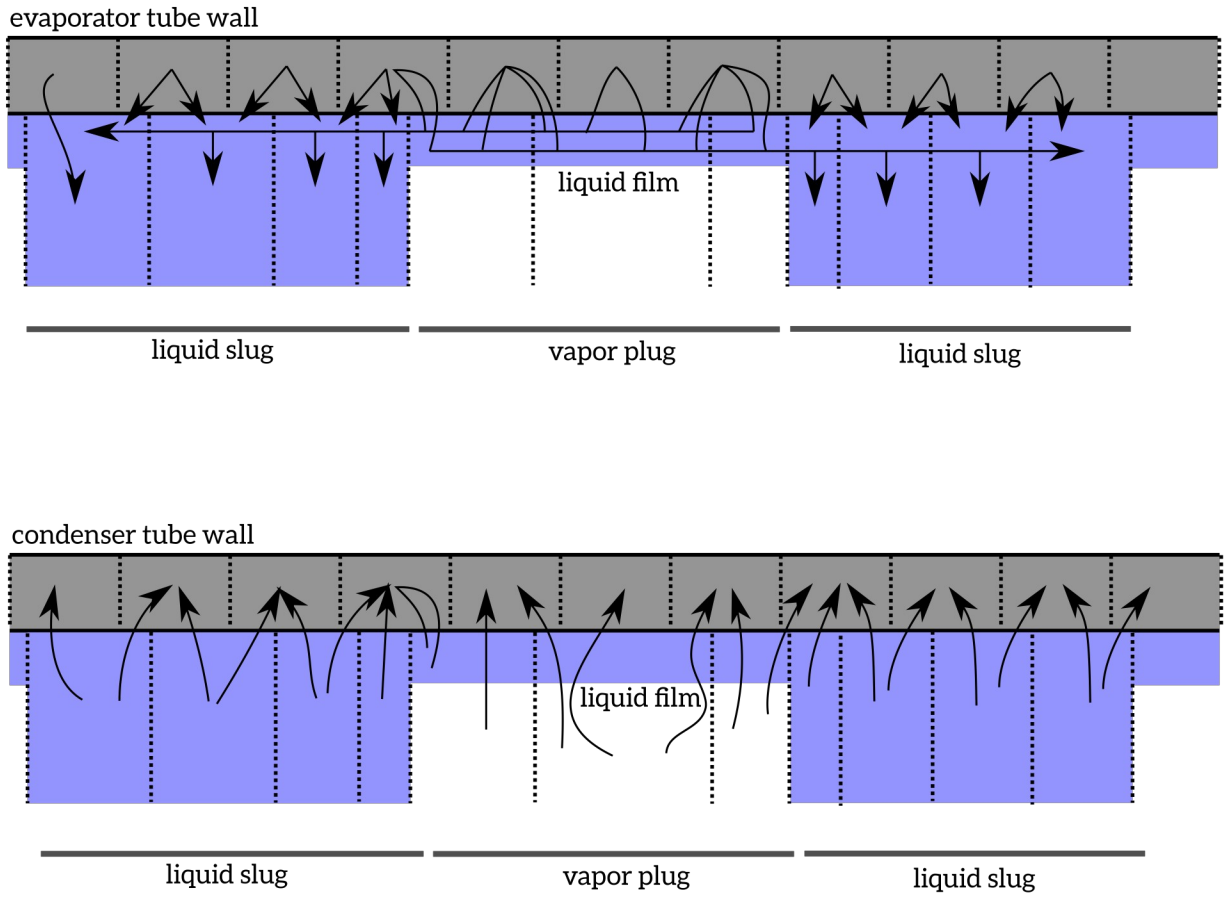

Figure 5.6. Schematic depicting thin liquid films coating the tube wall over the vapor cells along with the effective heat flow paths between the tube wall and fluid cells in the evaporator (upper panel) and condenser (lower panel)

The evaporation and condensation mass flow rates leaving a fluid cell, $\dot{m}_{out,j}$, are determined by a simple criteria: if the cell is liquid and its pressure falls below the saturation pressure associated with its temperature, any net heat transfer *into* the cell contributes *only* to evaporation; if the cell is vapor and its pressure rises above the saturation pressure associated with its temperature, any net heat transfer *out of* the cell contributes *only* to condensation. Under any other conditions, the net heat transfer into or out of a fluid cell results in sensible heating/cooling rather than latent heating/cooling. This is captured by

If j is a **liquid** cell, $P_j < P_{sat}(T_j)$, and the bracketed net heat transfer term is positive: evaporation occurs via

$$\dot{m}_{out,j} = \frac{1}{h_{sat,vapor}(T_j) - h_{sat,vapor}(T_j)} \left[\left(\frac{\lambda_{fluid}(T_j) + \lambda_{fluid}(T_{j-1})}{2} \right) A_i \left(\frac{T_{j-1} - T_j}{x_j - x_{j-1}} \right) + \left(\frac{\lambda_{fluid}(T_{j+1}) + \lambda_{fluid}(T_j)}{2} \right) A_i \left(\frac{T_{j+1} - T_j}{x_{j+1} - x_j} \right) + F_{v,j} v_j + \sum_{k_a}^{k_b} h_j A_{s,jk} (T_k - T_j) \right]$$

If j is a **vapor** cell, $P_j > P_{sat}(T_j)$, and the bracketed net heat transfer term is negative: condensation occurs via (5.10)

$$\dot{m}_{out,j} = \frac{-1}{h_{sat,vapor}(T_j) - h_{sat,vapor}(T_j)} \left[\left(\frac{\lambda_{fluid}(T_j) + \lambda_{fluid}(T_{j-1})}{2} \right) A_i \left(\frac{T_{j-1} - T_j}{x_j - x_{j-1}} \right) + \left(\frac{\lambda_{fluid}(T_{j+1}) + \lambda_{fluid}(T_j)}{2} \right) A_i \left(\frac{T_{j+1} - T_j}{x_{j+1} - x_j} \right) + F_{v,j} v_j + \sum_{k_a}^{k_b} h_j A_{s,jk} (T_k - T_j) \right]$$

Else no mass transfer occurs

$$\dot{m}_{out,j} = 0$$

.

Finally, the mass time derivative of the liquid cells is expressed as

$$\frac{dm_j}{dt} = -\dot{m}_{j,out} + \sum_{s_a}^{s_b} \dot{m}_{out,s} \tag{5.11}$$

,where s_a and s_b indicate the range of neighboring fluid cell indices feeding mass to the j^{th} cell.

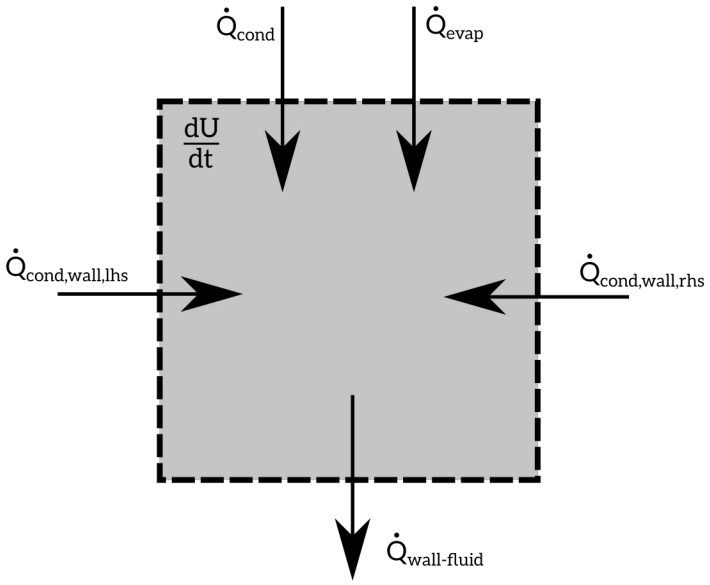

Figure 5.7. Schematic of a tube wall cell control volume

The 1st law must also be applied to each of the discretized tube wall cells. For the k^{th} tube wall cell of the control volume in Figure 5.7, this is

$$\begin{aligned}\frac{dU_k}{dt} &= \frac{d}{dt}\left(m_k c_k(T_k) T_k\right) = \\ &\left(\frac{\lambda_{tube}(T_k)+\lambda_{tube}(T_{k-1})}{2}\right)(A_o - A_i)\left(\frac{T_{k-1}-T_k}{x_k - x_{k-1}}\right) + \\ &\left(\frac{\lambda_{tube}(T_{k+1})+\lambda_{tube}(T_k)}{2}\right)(A_o - A_i)\left(\frac{T_{k+1}-T_k}{x_{k+1}-x_k}\right) - \\ &\sum_{j_a}^{j_b} h_j A_{s,kj}(T_k - T_j) + UA_{cond}(T_{cond} - T_k) + UA_{evap}(T_{evap} - T_k)\end{aligned} \tag{5.12}$$

where U_k is the internal energy of the k^{th} tube wall cell, T_k is the tube wall cell temperature, $c_k(T_k)$ is the temperature dependent specific heat capacity of the tube wall, $\lambda_{tube}(T_k)$ is the temperature dependent thermal conductivity of the tube wall, A_o is the entire cross sectional area of the tube (including tube and flow path), A_i is the inner cross sectional area of the tube through which the fluid flows, x_k is the center position of the k^{th} tube wall cell, j_a

through j_b represent the range of fluid cell indices in contact with the k^{th} tube wall cell, h_j is the heat transfer coefficient for the j^{th} fluid cell in contact with the k^{th} tube wall cell, $A_{s,kj}$ is the surface area for the j^{th} fluid cell in contact with the k^{th} tube wall cell, T_j is the temperature of the j^{th} fluid cell, T_{cond} is the temperature of the condenser plate, and T_{evap} is the temperature of the evaporator plate. Assuming $c_k(T_k)$ varies slowly with temperature, this can be arranged to solve for the time varying temperature of the tube wall cells

$$\frac{dT_k}{dt}=\frac{1}{m_k c_k(T_k)}\left[\left(\frac{\lambda_{tube}(T_k)+\lambda_{tube}(T_{k-1})}{2}\right)(A_o-A_i)\left(\frac{T_{k-1}-T_k}{x_k-x_{k-1}}\right)+\left(\frac{\lambda_{tube}(T_{k+1})+\lambda_{tube}(T_k)}{2}\right)(A_o-A_i)\left(\frac{T_{k+1}-T_k}{x_{k+1}-x_k}\right)+\sum_1^m h_m A_{s,km}(T_m-T_k)+UA_{cond}(T_{cond}-T_k)+UA_{evap}(T_{evap}-T_k)\right] \tag{5.13}$$

.

The condenser and evaporator plates are lumped capacitance models with temperatures T_{cond} and T_{evap}, thermally connected to the tube wall cells contained within the condenser and evaporator using large conductances UA_{cond} and UA_{evap}, respectively. These conductances change with location within the PHP per Table 5.1. Figure 5.8 shows the heat flow routing between the tube wall cells and the evaporator and condenser lumped capacitance blocks.

Table 5.1. Values of UA_{cond} and UA_{evap} at different PHP locations

Location	UA_{cond}	UA_{evap}
Evaporator	0	10 W/K
Adiabatic	0	0
Condenser	10 W/K	0

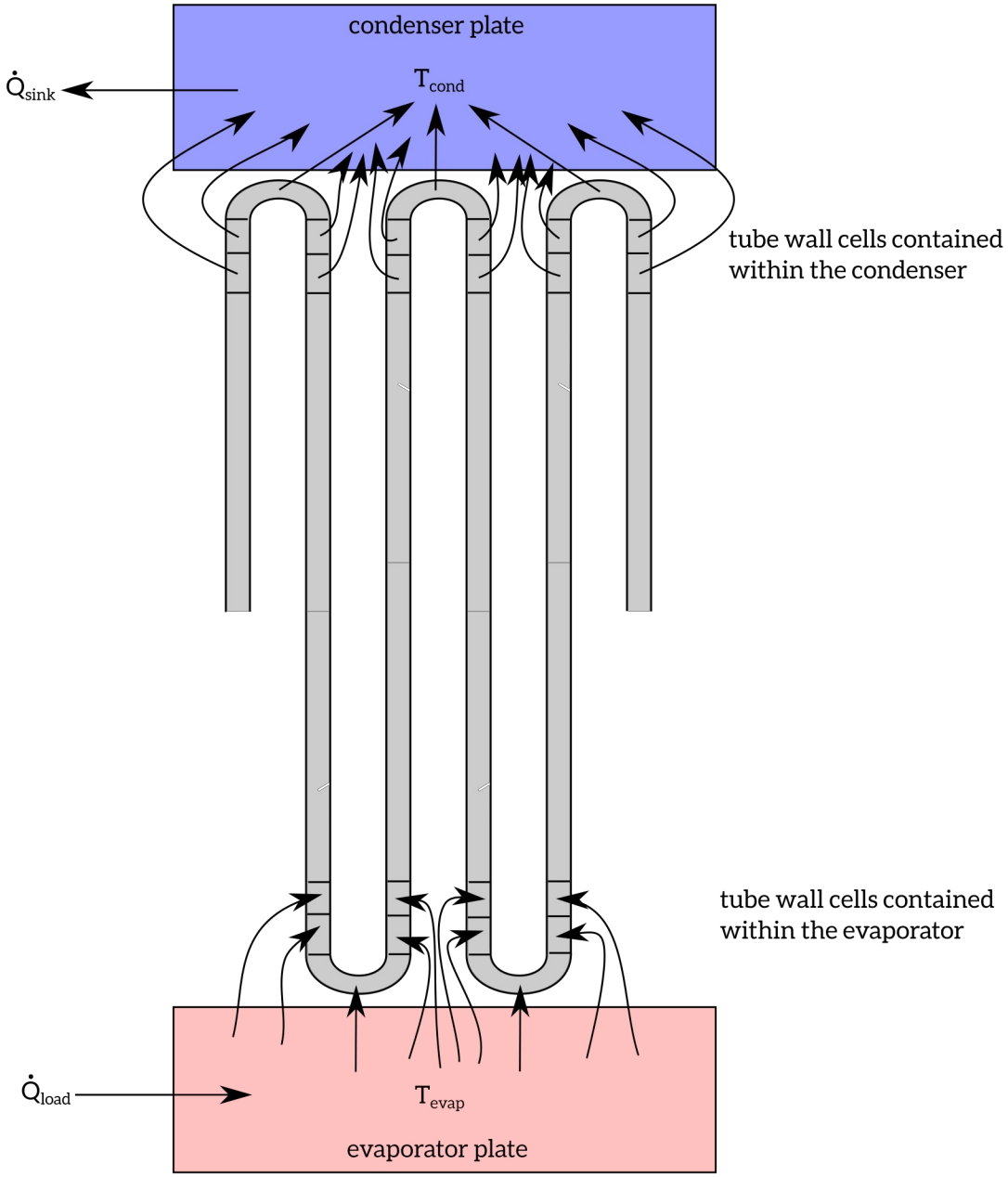

Figure 5.8. Illustration of the lumped capacitance evaporator and condenser plates showing heat flows to the PHP tube wall cells

The energy balances on these lumped capacitance models are

$$\frac{dU_{cond}}{dt} = \frac{d}{dt}\left(m_{cond}\, c_{cond}\left(T_{cond}\right) T_{cond}\right) = -\dot{Q}_{sink} + \sum_{k_a}^{k_b} UA_{cond}\left(T_k - T_{cond}\right) \tag{5.14}$$

$$\frac{dU_{evap}}{dt} = \frac{d}{dt}\left(m_{evap}\, c_{evap}\left(T_{evap}\right) T_{evap}\right) = \dot{Q}_{load} - \sum_{k_a}^{k_b} UA_{evap}\left(T_{evap} - T_k\right) \tag{5.15}$$

, where m_{cond} is the condenser mass, c_{cond} is the temperature dependent condenser specific heat, m_{evap} is the evaporator mass, c_{evap} is the temperature dependent evaporator specific heat $\dot{Q}_{load}$ is the load applied to the evaporator, and $\dot{Q}_{sink}$ is the load removed from the condenser. Again assuming the specific heats change slowly with temperature, the temperature time derivatives can be isolated

$$\frac{dT_{cond}}{dt} = \frac{1}{m_{cond}\, c_{cond}\left(T_{cond}\right)}\left[-\dot{Q}_{sink} + \sum_{k_a}^{k_b} UA_{cond}\left(T_k - T_{cond}\right)\right] \tag{5.16}$$

$$\frac{dT_{evap}}{dt} = \frac{1}{m_{evap}\, c_{evap}\left(T_{evap}\right)}\left[\dot{Q}_{load} - \sum_{k_a}^{k_b} UA_{evap}\left(T_{evap} - T_k\right)\right] \tag{5.17}$$

. Note that, when the system is in a periodic steady state, the time averages of $\dot{Q}_{load}$ and $\dot{Q}_{sink}$ are equivalent by energy balance on the entire PHP. The modeled conductance and effective thermal conductivity (either instantaneous or time averaged) are computed using

$$UA_{PHP,ON,MODEL} = \frac{\dot{Q}_{load}}{T_{evap} - T_{cond}} \tag{5.18}$$

$$k_{EFF,PHP,ON,MODEL} = \frac{\dot{Q}_{load}}{T_{evap} - T_{cond}} \frac{L_{ADIA}}{N_{tubes} A_o} \tag{5.19}$$

. The time averaged values of $\dot{Q}_{load}$ and $\dot{Q}_{sink}$ are equivalent to the quantity $\dot{Q}_{PHP,ON,MODEL}$ which is used elsewhere in this work to refer to the heat transfer capacity of the experimental PHPs

$$\dot{Q}_{PHP,ON,MODEL} = \frac{\int_{t_i}^{t_f} \dot{Q}_{load}\, dt}{t_f - t_i} = \frac{\int_{t_i}^{t_f} \dot{Q}_{sink}\, dt}{t_f - t_i} \tag{5.20}$$

.

Now that the thermal cells are defined, the viscous and capillary forces on the momentum cells can be revisited and expressed as

$$F_{v,i} = -8\pi v_i \sum_{j_a}^{j_b} \mu_j L_j \tag{5.21}$$

where j_a through j_b represent the range of fluid cell indices contributing to the viscous force on the i^{th} liquid slug, μ_j is the viscosity of the j^{th} fluid cell, and L_j is the length of the j^{th} fluid cell. The range of fluid cells j_a through j_b consists of all the liquid cells in the i^{th} liquid slug, along with contributions from the nearest half the adjacent vapor cells in the i^{th} and i^{th+1} vapor plugs. Similarly, the i^{th} slug mass contains contributions from all the liquid cells in the i^{th} liquid slug as well as contributions from the nearest half the adjacent vapor cells in the i^{th} and i^{th+1} vapor plugs

$$m_i = \sum_{j_a}^{j_b} m_j \tag{5.22}$$

. Finally, the capillary force on the i^{th} liquid slug is defined by

$$F_{c,i} = \frac{4 A_i}{d_i}\left(\sigma_{receding,i}\cos(\theta_{receding,i}) - \sigma_{advancing,i}\cos(\theta_{advancing,i})\right) \tag{5.23}$$

, where d_i is the inner diameter of the tube, $\sigma_{\text{receding},i}$ and $\sigma_{\text{advancing},i}$ are the surface tensions at the receding and advancing edges of the i^{th} liquid slug obtained from the corresponding j^{th} index, and $\theta_{\text{receding},i}$ and $\theta_{\text{advancing},i}$ are the receding and advancing dynamic contact angles of the i^{th} liquid slug. The dynamic angles are defined in terms of the static contact angle (a material property) and the capillary number by

$$\theta_{\text{receding},i} = \theta_{\text{static}} - 72\frac{\text{Ca}_{\text{receding},i}}{3\theta_{\text{static}}^2} \tag{5.24}$$

$$\theta_{\text{advancing},i} = \theta_{\text{static}} - 72\frac{\text{Ca}_{\text{advancing},i}}{3\theta_{\text{static}}^2} \tag{5.25}$$

$$\text{Ca}_{\text{receeding},i} = \frac{\mu_{\text{receding},i}\, v_i}{\sigma_{\text{receeding},i}} \tag{5.26}$$

$$\text{Ca}_{\text{advancing},i} = \frac{\mu_{\text{advancing},i}\, v_i}{\sigma_{\text{advancing},i}} \tag{5.27}$$

[35][66]. For the surface tension force, advancing refers to the "front" side of the liquid slug while receding refers to the "back" side of the plug, relative to its velocity. This means the capillary force changes directions when the velocity changes directions.

5.1.2 Boundary conditions, initial conditions, applied loads, and discretization details

The state equations represented by Equations 5.4, 5.5, 5.6, 5.11, 5.12, 5.16, and 5.17 represent a system discretized ordinary differential equations and partial differential equations and therefore require initial conditions (and boundary conditions for the PDEs) to be solved.

First, the number of liquid slugs (and an equal number of vapor plugs) N_{slugs} used for the momentum equation is defined, allowing the length of the slug velocity and position vectors to be calculated

$$v_i \quad \text{for } i = 1..N_{SLUGS} \tag{5.28}$$

$$x_i \quad \text{for } i = 1..N_{SLUGS} \tag{5.29}$$

. The initial values at t=0 seconds are

$$v_i = v_{ini} \tag{5.30}$$

$$x_i = x_{ini,i} \tag{5.31}$$

. The initial velocity v_{ini} for all slugs is typically 0 m/s. However, some initial conditions result in high heat transfer rates and mass transfer rates, rapidly depleting all fluid mass from a cell. Due to this, along with the fact that estimating steady state performance is the ultimate goal of the model, better convergence is obtained with a non-zero value for v_{ini} between 0 m/s and 1 m/s. Due to viscous dissipation, initial velocities are rapidly damped and do not affect the steady state solution.

The initial positions of the liquid slug centers $x_{ini,i}$ are equally distributed throughout the length of the serpentine PHP tube $L_{PHP,TUBE}$. The initial volume for each of the slugs are equal and determined by

$$vol_i = FR \frac{L_{TUBE} A_i}{N_{SLUGS}} \quad \text{where } i \text{ is a liquid slug} \tag{5.32}$$

, where Vol_i is the volume of the liquid slug and FR is the liquid fill ratio. The vapor plugs fill the remaining volume of the tube.

Unlike the liquid slug momentum equation, the energy balances for the fluid and wall cells are discretized PDEs which require initial conditions as well as boundary conditions. Here the number of fluid cells $N_{FLUIDCELLS}$ and number of wall cells $N_{WALLCELLS}$ define the vector lengths for the fluid cell internal energy and wall cell temperature

$$U_j \quad \text{for } j = 1..N_{FLUIDCELLS} \tag{5.33}$$

$$T_k \quad \text{for } k = 1..N_{WALLCELLS} \tag{5.34}$$

. The number of fluid cells is determined by the number of fluid cells specified for each liquid slug and vapor plug

$$N_{FLUIDCELLS} = N_{SLUGS}\left(N_{LIQUID-PER-SLUG} + N_{VAPOR-PER-PLUG}\right) \tag{5.35}$$

. The initial temperatures of the fluid cells and wall cells at t=0 seconds are

$$T_j = T_{ini,j} \tag{5.36}$$

$$T_k = T_{ini,k} \tag{5.37}$$

, where the fluid temperature is related to the internal energy by

$$\begin{aligned} U_j &= m_j u_j = vol_j \rho_{sat,liquid}(T_{ini,j})\, u_{sat,liquid}(T_{ini,j}) \quad \text{where j is a liquid cell} \\ U_j &= m_j u_j = vol_j \rho_{sat,vapor}(T_{ini,j})\, u_{sat,vapor}(T_{ini,j}) \quad \text{where j is a vapor cell} \end{aligned} \tag{5.38}$$

where ρ is the mass density and vol_j is the volume of the fluid cell. Notice that Equation 5.38 also defines the initial mass in each fluid cell

$$\begin{aligned} m_j &= \mathrm{vol}_j \rho_{sat,liquid}(T_{ini,j}) \quad \text{where j is a liquid cell} \\ m_j &= \mathrm{vol}_j \rho_{sat,vapor}(T_{ini,j}) \quad \text{where j is a vapor cell} \end{aligned} \tag{5.39}$$

.

The initial fluid cell temperatures $T_{ini,j}$ are based on their initial location in the PHP and the wall cell temperatures $T_{ini,k}$ on their permanent location in the PHP, per Table 5.2.

Table 5.2. Values of $T_{ini,j}$ and $T_{ini,k}$ at different PHP locations

Location	Value
Evaporator	T_{EVAP}
Adiabatic	$0.5(T_{EVAP}+T_{COND})$
Condenser	T_{COND}

Boundary conditions must enforce the condition that the first and last cells in both the fluid and tube wall are actually adjacent (and share a boundary) due to the closed loop PHP geometry. In the context of Equation 5.6 and Equation 5.12 this means that

$$\begin{aligned} &\text{when } j = N_{FLUIDCELL}+1, \text{ replace with } j = 1 \\ &\text{when } j = -1, \text{ replace with } j = N_{FLUIDCELL} \end{aligned} \tag{5.40}$$

$$\begin{aligned} &\text{when } k = N_{WALLCELL}+1, \text{ replace with } k = 1 \\ &\text{when } k = -1, \text{ replace with } k = N_{WALLCELL} \end{aligned} \tag{5.41}$$

.

Finally, the initial temperatures of the evaporator and condenser block are set by

$$T_{COND} = T_{COND,ini} \tag{5.42}$$

$$T_{EVAP} = T_{EVAP,ini} \tag{5.43}$$

. For all of the simulations presented here, the evaporator and condenser temperatures are held constant in time, with $\dot{Q}_{PHP,ON,MODEL}$ being computed as the model output. Note that the model is capable, however, of setting $\dot{Q}_{PHP,ON,MODEL}$ and either T_{COND} or T_{EVAP}, thereby calculating the other plate temperature as the model output.

5.1.3 Fluid properties and state update procedure

Fluid properties are provided from the open source Coolprop package [67], allowing access to high accuracy reduced-Helmholtz equations of state as well as transport properties for a wide variety of real fluids including nitrogen and helium. Temperature dependent thermal conductivity and specific heat capacity for the stainless steel tube wall [56] and copper evaporator and condenser plates [38] are obtained from NIST.

The solution procedure to update the state equations at each time is as follows. At each time step, integration of Equations 5.4, 5.5, 5.6, 5.11, 5.12, 5.16, and 5.17 provides values for the liquid slug velocities v_i, liquid slug center positions x_i, fluid thermal cell internal energies U_j, fluid thermal cell masses m_j, wall cell temperatures T_k, evaporator block temperature T_{evap}, and condenser block temperature T_{cond}. The specific internal energies of the all (liquid or vapor) fluid cells are calculated first using

$$u_j = \frac{U_j}{m_j} \tag{5.44}$$

, after which all other *liquid* cell properties *other than the actual cell pressure* are calculated assuming saturated conditions

$$T_j = T_{sat,liquid}(u_j) \text{ where j is a liquid cell} \tag{5.45}$$

$$\rho_j = \rho_{sat,liquid}(u_j) \quad \text{where j is a liquid cell} \tag{5.46}$$

$$h_j = h_{sat,liquid}(u_j) \quad \text{where j is a liquid cell} \tag{5.47}$$

$$\lambda_j = \lambda_{sat,liquid}(u_j) \quad \text{where j is a liquid cell} \tag{5.48}$$

$$\mu_j = \mu_{sat,liquid}(u_j) \quad \text{where j is a liquid cell} \tag{5.49}$$

$$P_{sat,j} = P_{sat}(T_j) \quad \text{where j is a liquid cell} \tag{5.50}$$

, where ρ_j is the mass density. Knowing the density and mass of the liquid fluid cells (j-indices) and the center positions of the liquid slugs (i-indices), the total volume $vol_{i,liquid}$ of the liquid slugs are calculated. This in turn provides the volumes for each of the vapor plugs $vol_{i,vapor}$ adjacent to the liquid momentum slugs, which are either compressed or expanded relative to the prior time step.

Each vapor plug pressure P_i is now calculated assuming the plug is in hydrodynamic equilibrium (i.e. all of its contained thermal j-indexed cells have the same pressure) but not thermal equilibrium (each j-indexed cell has a different internal energy). This is expressed by the implicit relation

$$vol_i = \sum_{j_a}^{j_b} \frac{m_j}{\rho_j(u_j, P_i)} \qquad \text{where i is a vapor slug} \tag{5.51}$$

, where $j_a \ldots j_b$ is the range of fluid cell indices comprising the i^{th} vapor plug and the density is determined by the equation of state for the vapor. Equation 5.51 must be solved for each vapor plug with a nonlinear equation solution algorithm. With the internal energies and pressures known for each vapor cell, all other vapor cell properties are determined by

$$T_j = T(u_j, P_j) \qquad \text{where j is a vapor cell} \tag{5.52}$$

$$\rho_j = \rho(u_j, P_j) \qquad \text{where j is a vapor cell} \tag{5.53}$$

$$h_j = h(u_j, P_j) \qquad \text{where j is a vapor cell} \tag{5.54}$$

$$\lambda_j = \lambda(u_j, P_j) \qquad \text{where j is a vapor cell} \tag{5.55}$$

$$\mu_j = \mu(u_j, P_j) \qquad \text{where j is a vapor cell} \tag{5.56}$$

$$P_{sat,j} = P_{sat}(T_j) \qquad \text{where j is a vapor cell} \tag{5.57}$$

.

Finally, the actual pressure of each liquid fluid cell is estimated using the adjacent vapor plug pressures and assuming a linear pressure drop over the i^{th} liquid slug

$$P_j = P_i + \frac{(P_{i+1} - P_i)}{x_{i+1} - x_i}(x_j - x_i) \qquad \text{where j is a liquid cell between vapor plugs i and i+1} \tag{5.58}$$

. The estimated actual liquid fluid cell pressure in Equation 5.58 is compared with its saturation pressure from Equation 5.50 to determine whether or not evaporation occurs (see Equation 5.10).

With all of the properties now determined, the all of the rates (energy transfer, mass transfer, momentum change, etc) described in the preceding text can be determined for the time step.

5.1.4 Implementation and solution algorithms

The model defined by the system of ordinary differential equations of Equations 5.4, 5.5, 5.6, 5.11, 5.12, 5.16, and 5.17 is implemented in the Julia [68] programming language and solved using the DifferentialEquations package [69] to solve the ODE system and the Nlsolve package [70] to solve the nonlinear system for the vapor plug pressures (Equation 5.51). The language is chosen for its mature collection of scientific numerical computing packages and execution speed which rivals C, as well as the feature-rich and high performance DifferentialEquations package which implements a plethora of ODE algorithms. The simulations presented here are solved with an explicit time adaptive Adams method (JVODE_Adams), except for stiffer helium PHP simulations which are solved with an implicit method (Implicit Euler). The greater stiffness of the helium PHP models is likely due to the lower amount of thermal mass at its approximately 4K operating temperature. Both the JVODE_Adams and Implicit Euler methods use adaptive time stepping with both the absolute and relative error tolerances set to 1E-1; the maximum time step is set to 2.5E-4 seconds. For more on the algorithms and error control, see [69].

Each of the model results presented here are run for 20 simulated seconds, with a periodic state achieved in just a few real time seconds. The presented values of $\dot{Q}_{PHP,ON,MODEL}$, $UA_{PHP,ON,MODEL}$, and $k_{EFF,PHP,ON,MODEL}$ correspond to time averages over the last 15 seconds (of the 20 second total) simulation time.

5.1.5 Novel features relative to existing models

As stated earlier, the ON state PHP model developed here is an evolution of similar mass-spring-damper -type models developed previously by other authors [59][60][61][35]. For a variety of reasons, several noteworthy modifications to the existing models are applied. Some of these features are completely new, while others are implemented in other models but are combined together here for the first time. These updates include:

- the inclusion of the evaporator and condenser plate thermal masses in the form of lumped capacitance models (which interact via conduction with the attached tube walls)
- fully temperature-dependent thermal conductivity and specific heat capacity for the PHP tube wall material and evaporator/condenser block materials
- fully temperature-dependent properties for the liquid slugs
- capture of the viscous losses and inertia of *vapor* plugs in the momentum equation
- the use of a high accuracy reduced-Helmoltz equation of state and the ability to easily change working fluids
- the determination of vapor plug pressures assuming *pressure* equilibrium but not *thermal* equilibrium

- a mechanism which allows the fluid cell masses to be depleted and refilled, allowing (1) the effective merging of liquid slugs when the interstitial vapor plug is fully condensed (or the merging of vapor plugs when the interstitial liquid slug is fully evaporated) and (2) the effective nucleation of vapor plugs when two adjacent liquid slugs evaporate (or the nucleation of liquid slugs when two adjacent vapor plugs condense)
- and the ability to easily use a variety of high order (explicit or implicit) integration methods.

Furthermore, existing models tend to present extremely limited validation data to confirm their accuracy. For instance, both Shafii and Faghri [59] and Ma [60] are purely numerical analyzes and do not compare their model results to expeirment data. Gürsel [61] compares model results to 14 experiment data points using two PHPs with two working fluids (ethanol and water), while Sun [35] compares model results with 6 experiment data points on a single PHP and working fluid (hydrogen). The model presented here is validated with 4 cryogenic working fluids and 75 experimental data points spanning a wide range PHP design parameters and applied loads.

5.1.6 ON state model validation

To validate the ON state model, experiment data from a variety of PHP experiments is utilized. This includes a subset of experiment data from the present work – both the nitrogen experiments presented in Section 2.5 and the helium experiments presented in Section 3.6. In an effort to more broadly sample important design parameters such as the working fluid, adiabatic/evaporator/condenser section lengths, tube diameters, heat loads, fill ratios, evaporator/condenser temperatures, and the number of parallel tubes, additional experiment data performed by other

sources is also used. The validation data sources and their corresponding PHP design parameters are summarized in Table 5.3. Note that, due to resource limitations, the validation data set is a subset of the total experiment data in these sources. However, the subset is sampled such that the important design parameters are varied widely across the range present in the experiments. Importantly, data from sources other than the present work are gathered from published plots (as the actual values corresponding to experiment operating points are not published as numerical values by any of the references), which introduces additional error to the analysis.

Table 5.3. Experiment parameters for validation simulations presented in Figure 5.9 and Figure 5.10

Working fluid	**Source**	N_{TUBES}	d_i [mm]	d_o [mm]	L_{ADIA} [mm]	L_{COND} [mm]	L_{EVAP} [mm]	FR	T_{EVAP} [K]	T_{COND} [K]	$\dot{Q}_{load}$ [W]	Samples
nitrogen	Present work	20	1.08	1.47	254	102	102	0.259 to 0.520	75.30 to 87.00	72.49 to 84.70	4.72 to 17.62	18
	Jiao 2009 [39]	16	1.65	3.18	100	60	40	0.480	79.15 to 83.65	85.65 to 100.65	22.50 to 125.70	5
helium	Present work	18	0.51	0.72	501	57	57	0.190 to 0.590	3.34 to 4.26	3.44 to 4.98	0.07 to 0.58	19
	Fonseca 2016 [35]	14	0.50	0.80	300	90	30	0.700	3.33 to 4.20	3.60 to 4.80	0.05 to 0.18	4
					1000			0.580				4
hydrogen	Sun 2020 [71]	4	2.3	3.3	500	55	55	0.340	19.00 to 27.50	19.25 to 30.30	0.40 to 12.00	6
		10										10
argon	Uzoma 2021 [72]	40	0.51	0.72	265	50	50	0.200	88.98 to 89.10	91.90 to 101.77	1.00 to 6.00	9

Models of the experiment data points summarized in Table 5.3 are simulated by setting the evaporator and condenser temperatures T_{COND} and T_{EVAP} to the corresponding values measured in the experiments and solving for a time averaged, period steady state $\dot{Q}_{load}$ per the model pro-

cedure defined in Section 5.1.4. This makes defining the mass and specific heat capacity of the evaporator and condenser plates in the model irrelevant, which is helpful since this ancillary information is not typically published for PHP tests. Table 5.4 lists key model parameters used for the validation simulations.

Table 5.4. Parameters used for ON state model simulations

Parameter	**Value**
N_{SLUGS}	Majority at 60, some less
$N_{LIQUID-PER-SLUG}$	6
$N_{VAPOR-PER-SLUG}$	16
$N_{WALLCELLS}$	$\frac{L_{PHP}}{0.8\,mm}$
α	0 (Vertical bottom heated mode)

The validation study probes the model both in terms of its ability to predict the heat transfer capacity of the PHP and the conductance. Figure 5.9 shows the experimental ON state heat transfer capacity $\dot{Q}_{PHP,ON,EXPERIMENT}$ as a function of the model predicted heat transfer capacity $\dot{Q}_{PHP,ON,MODEL}$ for each of the validation data points, while Figure 5.10 shows the experimental conductance $UA_{PHP,ON,EXPERIMENT}$ as a function of the model conductance $UA_{PHP,ON,MODEL}$; Table 8.34 in Appendix 8.9 tabulates the data displayed in these plots. A line is shown on each of these plots to indicate the location of points where the model perfectly predicts the experiment result.

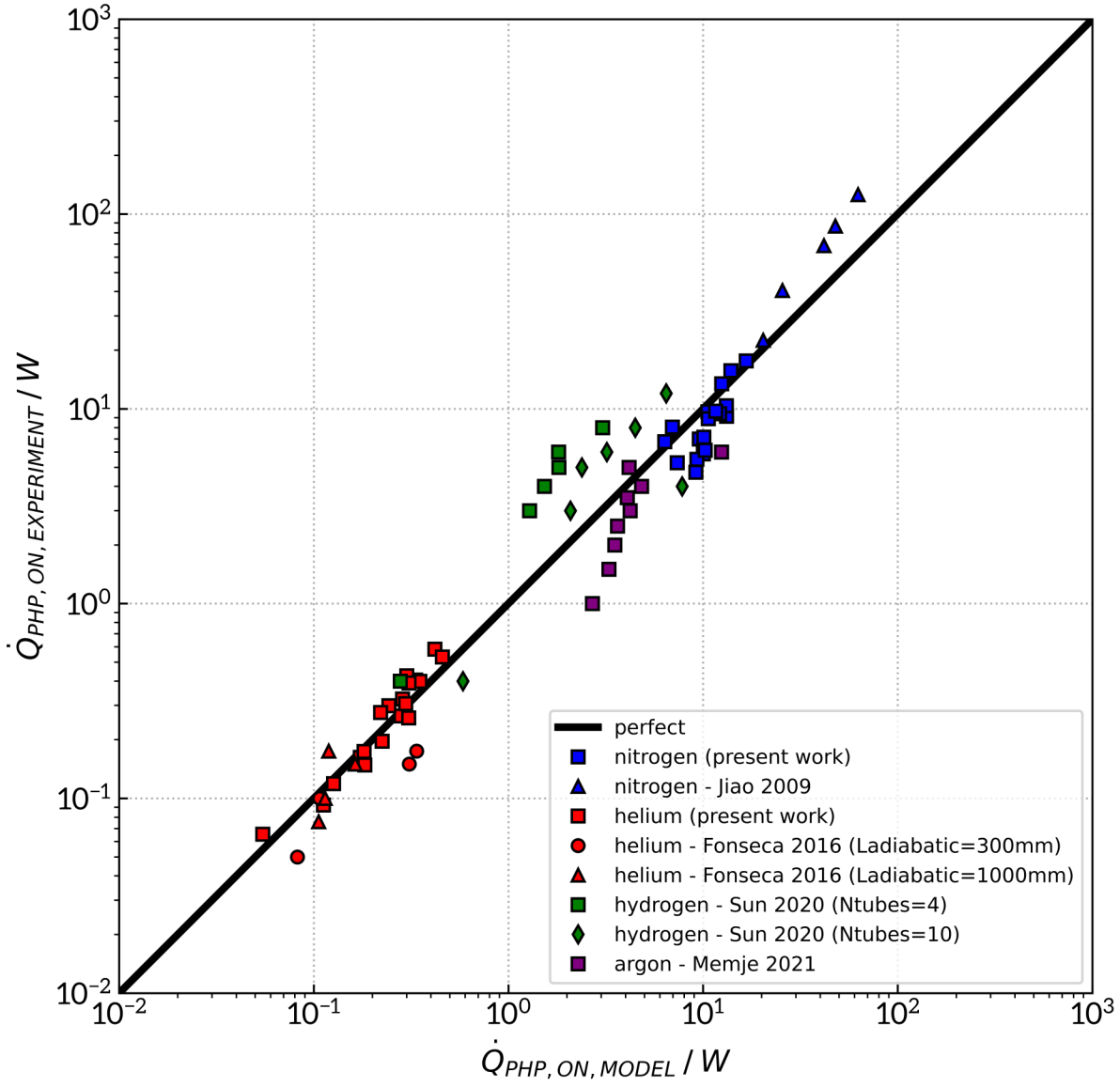

Figure 5.9. Comparison of modeled-predicted PHP heat transfer $\dot{Q}_{PHP,MODEL}$ with the measured experimental PHP heat transfer $\dot{Q}_{PHP,EXPERIMENT}$ for a sample of operating points from a variety of published cryogenic PHP operating data.

Several characteristics of the model-to-experiment relation can be immediately seen by observation of Figure 5.9 and Figure 5.10. First is that error between the model prediction and the experimental data for both the PHP heat transfer capacity and the conductance is remarkably unbiased

– that is, the data points seem to fall fairly evenly above and below the line of perfect agreement. In fact, the distribution of relative error for the model-experiment comparison data set shown in Figure 5.9 and Figure 5.10 is nearly normal (with a slight skew) with a mean and standard deviation of -13.29% and 59.10%, respectively, and is shown in Figure 5.11. This indicates a slight model over prediction of the cooling power and conductance on average, with nearly all of the validation test points being within ± 100% of the predicted value. Because the relative error is essentially unchanged with the PHP heat transfer capacity, the width of scatter of the data band in the log-log axes of Figure 5.9 and Figure 5.10 is essentially constant over the entire sampled range. Note that the heat transfer capacity and conductance errors in relative terms are equal since the condenser and evaporator temperatures are identical for both the model and experiment

$$\dot{Q}_{PHP,ON,RelativeError} = \frac{\dot{Q}_{PHP,ON,MODEL} - \dot{Q}_{PHP,ON,EXPERIMENT}}{\dot{Q}_{PHP,ON,MODEL}} = \frac{UA_{PHP,ON,MODEL}(T_{EVAP} - T_{COND}) - UA_{PHP,ON,EXPERIMENT}(T_{EVAP} - T_{COND})}{UA_{PHP,ON,MODEL}(T_{EVAP} - T_{COND})} = \frac{UA_{PHP,ON,MODEL} - UA_{PHP,ON,EXPERIMENT}}{UA_{PHP,ON,MODEL}} = UA_{PHP,ON,RelativeError} \tag{5.59}$$

.

For such a simple PHP model (relative to, say, a three-dimensional two-phase fluid CFD analysis), this is a noteworthy predictive capability considering the range of fluids and design parameters included in the validation data. Although additional validation – especially with higher temperature working fluids and large heat transfer capacities – should be carried out to increase confidence in the modeling approach, this study shows that simple mass-spring-damper -type PHPs models may be utilized as a design tool to quite confidently predict performance of a PHP to

within ± 100% of the desired cooling power and conductance. The value in the approach is even clearer when considering that the required simulation time for a single operating point, on a typical modern desktop computer, is on the order of 10 to 30 minutes.

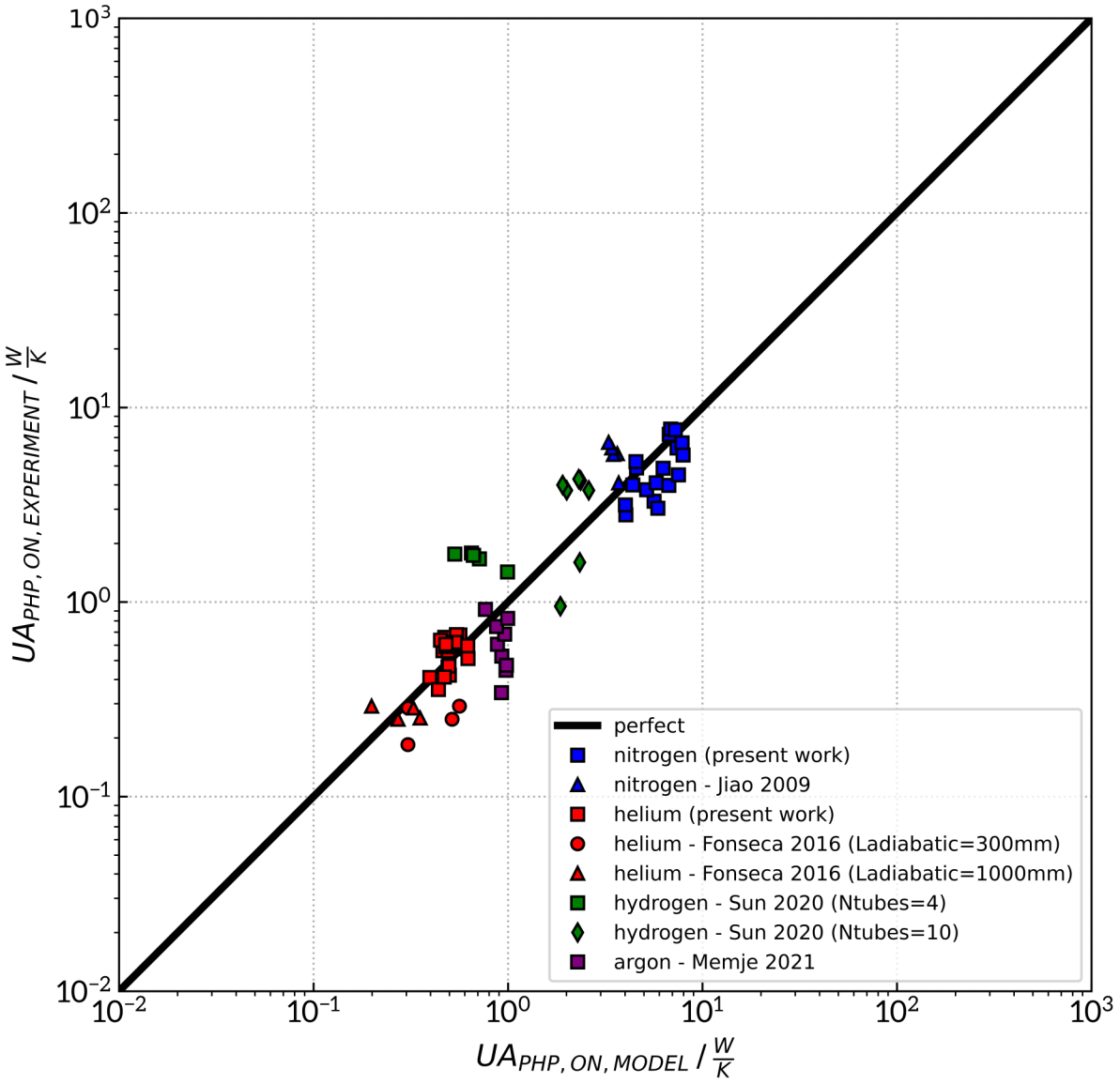

Figure 5.10. Comparison of modeled-predicted PHP conductance UA_{MODEL} with the measured experimental PHP conductance $UA_{EXPERIMENT}$ for a sample of operating points from a variety of published cryogenic PHP operating data.

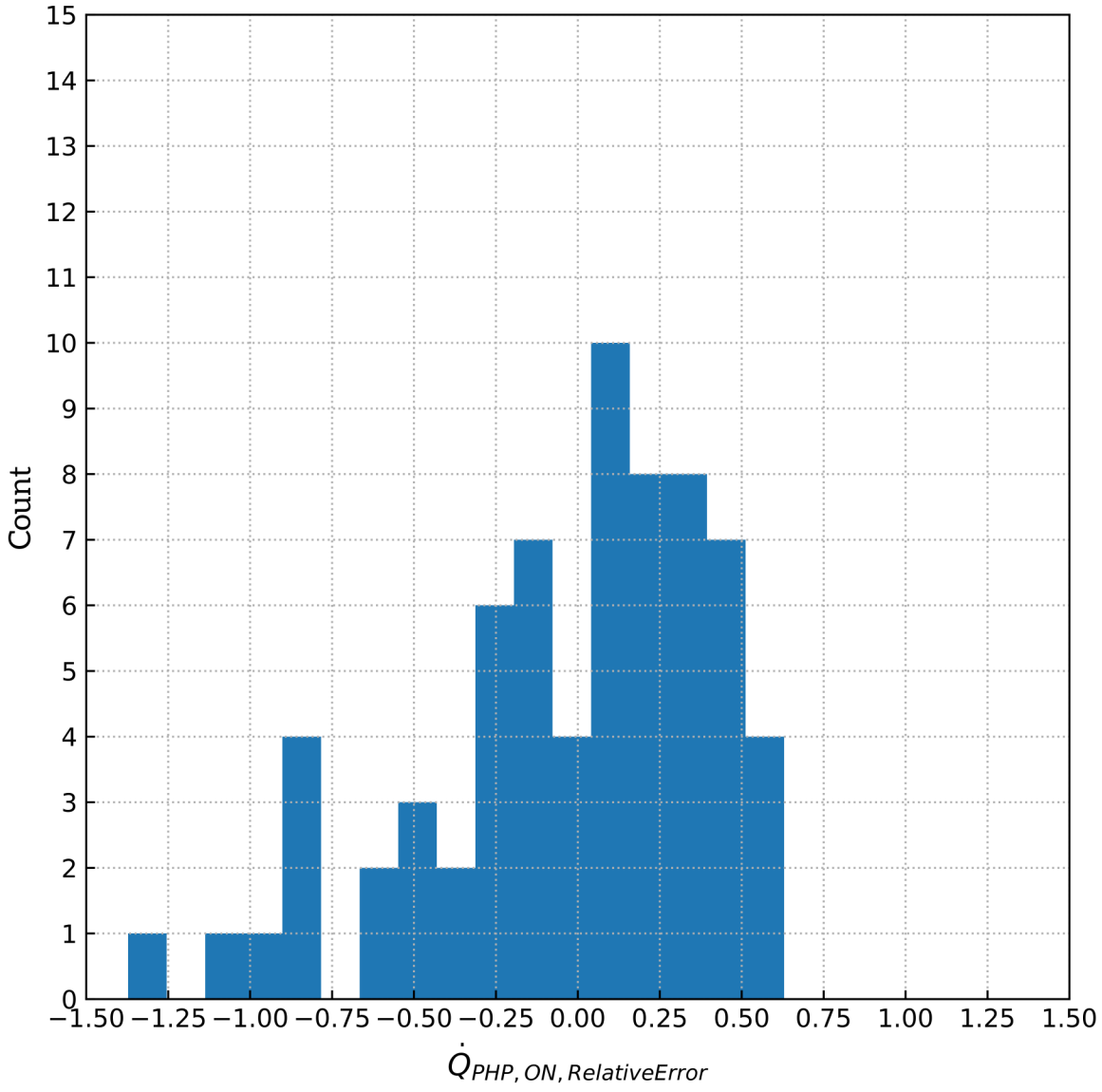

Figure 5.11. Distribution of the relative error in PHP heat transfer capacity between the experiment data and model predictions for the data in Figure 5.9

In addition to the validation of the model via existing experimental PHP data, several sanity-check simulations are performed to ensure the model is capturing key behavior that is intuitively expected or known to occur from experimental data. The first of these is an investigation of the dependence of the PHP conductance and heat transfer capacity on the number of parallel tubes,

shown in Figure 5.12 for a nitrogen PHP and Figure 5.13 for a helium PHP. Other than the number of parallel tubes, the devices in these simulations are identical to the nitrogen and helium PHP designs of Section 2 and Section 3 of this work, with simulations at each value of $N_{PHP,TUBES}$ run with the same values of T_{EVAP} and T_{COND}. For the nitrogen case in Figure 5.12, there is a nearly perfect linear scaling of both the heat transfer capacity and conductance with $N_{PHP,TUBES}$ – an intuitive and expected result, as one could simply install additional isolated fluid loop PHPs in parallel between temperature reservoirs and see the same scaling of *total* heat transfer rate and conductance summed over each of the parallel devices. However, a single PHP fluid loop presents an opportunities for secondary effects to modify this expected scaling, as the fluid contained in an added parallel tube is coupled to the physics of the larger fluid loop. Indeed, the analogous simulation set using helium as the working fluid (Figure 5.13) shows a slightly sub-linear relation for both the heat transfer capacity and conductance, especially at the larger tube counts. One possible reason for the degradation in this relation is that the net viscous losses are increased in the coupled momentum equation; another is that the length of the initial liquid slugs relative to the adiabatic length shrinks as $N_{PHP,TUBES}$ increases. For both fluids, however, the model produces consistent general scaling increasing heat transfer capacity and conductance with the count of parallel tubes, which is consistent with a high level assessment of the problem physics and suggestive that the model is capturing key behavior of the system.

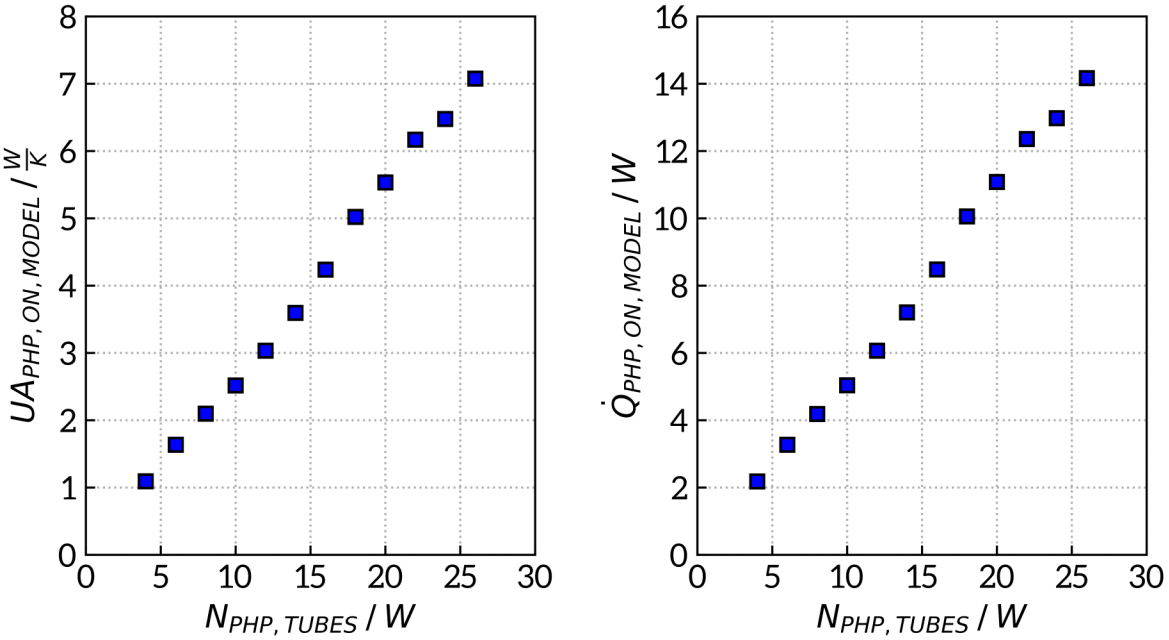

Figure 5.12. Variation of PHP conductance and heat transfer as a function of the number of parallel PHP tubes with nitrogen as the working fluid. PHP design parameters (other than $N_{PHP,TUBES}$) are as stated in Table 2.2.

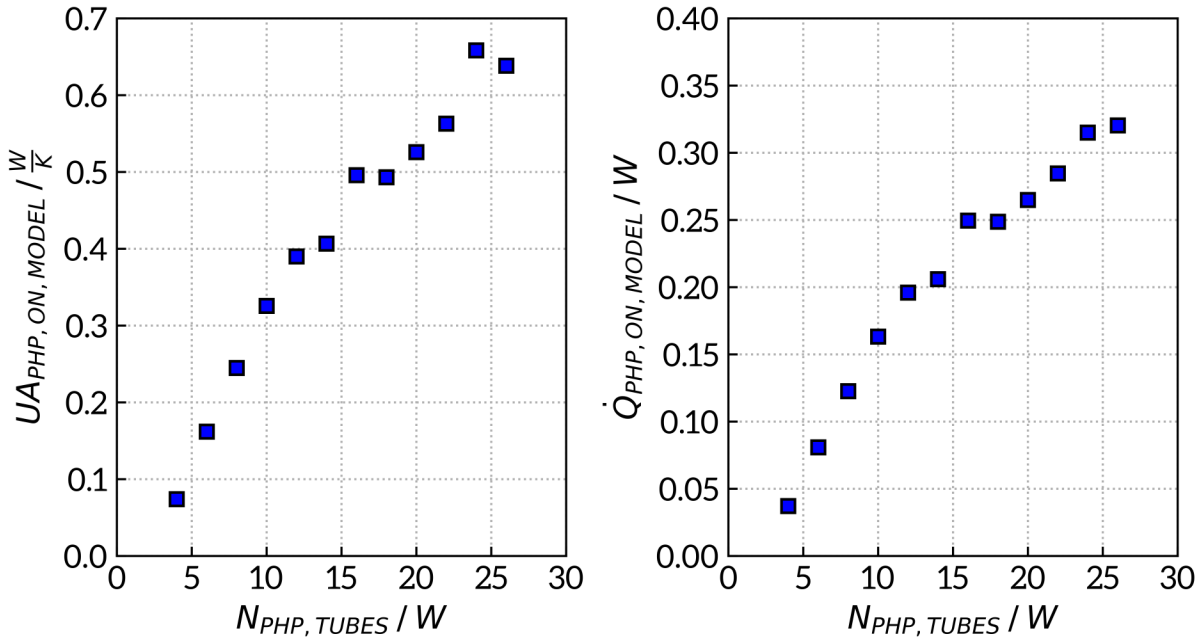

Figure 5.13. Variation of PHP conductance and heat transfer as a function of the number of parallel PHP tubes with helium as the working fluid. PHP design parameters (other than $N_{PHP,TUBES}$) are as stated in Table 3.3.

A second check of model behavior – the dependence of the conductance and effective thermal conductivity on the adiabatic length $L_{PHP,ADIA}$ – is shown in Figure 5.14 and Figure 5.15 for nitrogen and helium working fluids, respectively. Again, other than the adiabatic lengths, the devices in these simulations are identical to the nitrogen and helium PHP designs of Section 2 and Section 3 of this work, with simulations at each value of $L_{PHP,ADIA}$ run with the same values of T_{EVAP} and T_{COND}. For both the nitrogen and helium PHPs, it is evident that the effective thermal conductivity approximately scales slightly sub-linearly and *almost directly proportionally* with the adiabatic length. Considering that T_{EVAP} and T_{COND} remain constant for these simulations, and also the relation between $k_{EFF,PHP,ON,MODEL}$ and $UA_{PHP,ON,MODEL}$ in Equation 5.18 and Equation 5.19, this dictates that both $\dot{Q}_{PHP,ON,MODEL}$ and $UA_{PHP,ON,MODEL}$ must decrease *slightly* as the adiabatic length increases. Small decreases in $UA_{PHP,ON,MODEL}$ with increases in $L_{PHP,ADIA}$ are indeed seen for both the nitrogen and helium simulations shown here. Experiments which vary the PHP adiabatic length show similar behavior [52]. This behavior is therefore another indication that the model has captured key operating physics of the PHP.

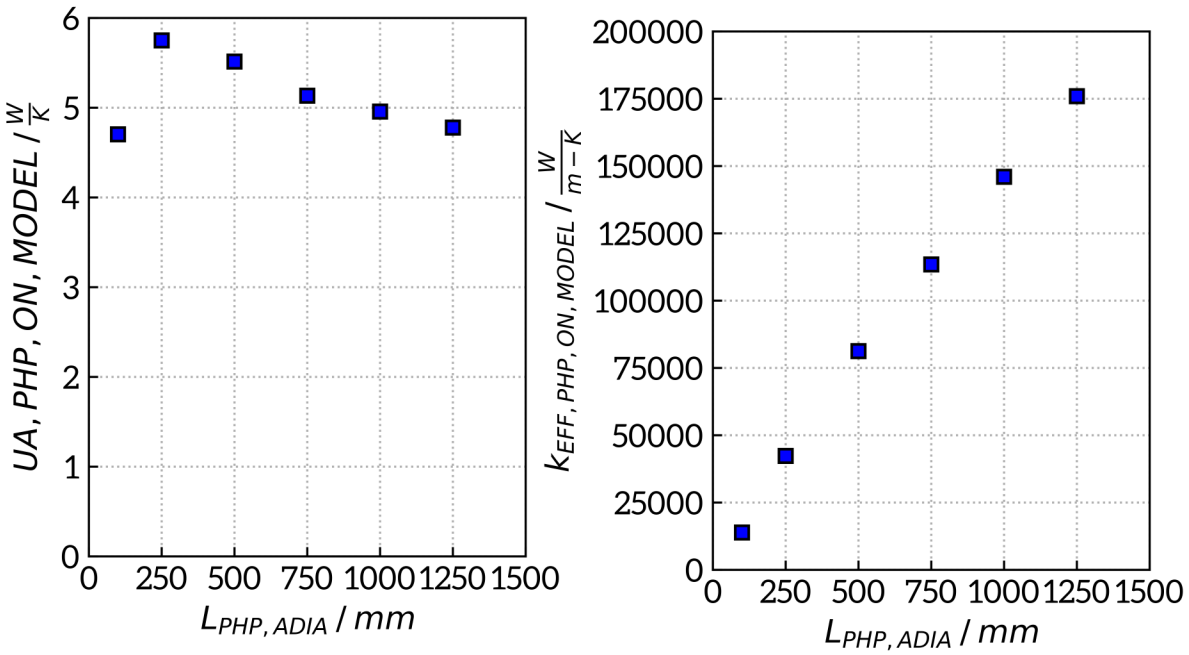

Figure 5.14. Variation of PHP conductance and effective thermal conductivity as a function of the number of the PHP adiabatic length with nitrogen as the working fluid. PHP design parameters (other than N_{TUBES}) are as stated in Table 2.2.

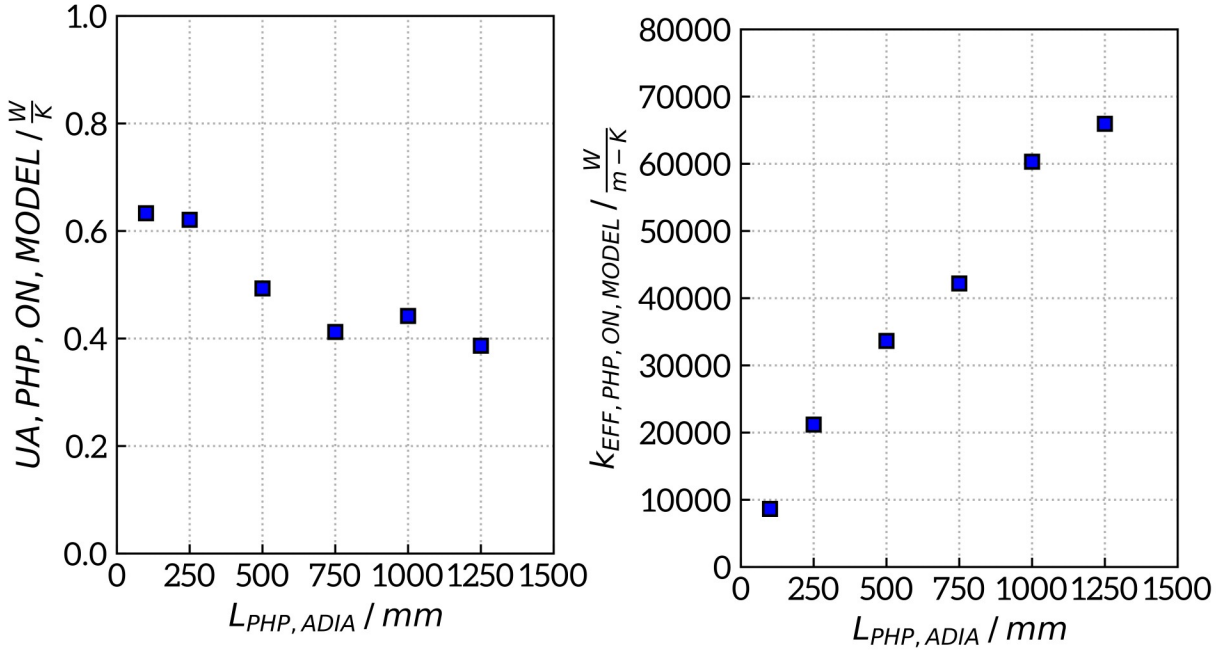

Figure 5.15. Variation of PHP conductance and effective thermal conductivity as a function of the number of the PHP adiabatic length with helium as the working fluid. PHP design parameters (other than $L_{PHP,ADIA}$) are as stated in Table 3.3.

5.1 Comparison of the nitrogen PHP thermal switch ON state measurements to ON state performance model

The ON state PHP thermal switch model developed in Section 5.1 begs a comparison between the experiment measurements and model predictions of the key PHP switch performance metrics: the PHP heat transfer capacities, the corresponding ON state PHP conductances, and the switching ratios. For the nitrogen PHPs tested in Section 2, a subset of the ON state heat transfer capacities and conductance measurements are directly compared to the modeled predictions in the previous section within the cloud of validation data from numerous PHPs and working fluids of Figure 5.9 and Figure 5.10, respectively. Discussion regarding the agreement of the experiment and modeled values for the heat transfer capacities and conductance is provided in that section and not repeated here. However, a comparison between a pure model PHP switching ratio and a subset of the nitrogen PHP experimental measurements is provided here for the first time in Figure 5.16, overlaid on the plot of pseudo-modeled and experimental switching ratio values first presented with the development of the OFF state PHP thermal switch model in Figure 4.5. Here the pure modeled switching ratio is defined by

$$SR_{PHP,MODEL,PURE} = \frac{UA_{PHP,EFF,ON,MODEL}}{UA_{PHP,EFF,OFF,MODEL}} \tag{5.60}$$

, where $UA_{PHP,EFF,ON,MODEL}$ is the conductance predicted by the ON state model and $UA_{PHP,EFF,OFF,MODEL}$ is the conductance predicted by the OFF state model. For the nitrogen PHPs, the pure modeled switching ratio over predicts the experiment value by approximately the same margin as the psuedo-modeled switching ratio.

This because the ON state modeled conductance and heat transfer capacity for the PHP-II-N subset are quite accurate – falling near the middle of the relative error distribution in Figure 5.11

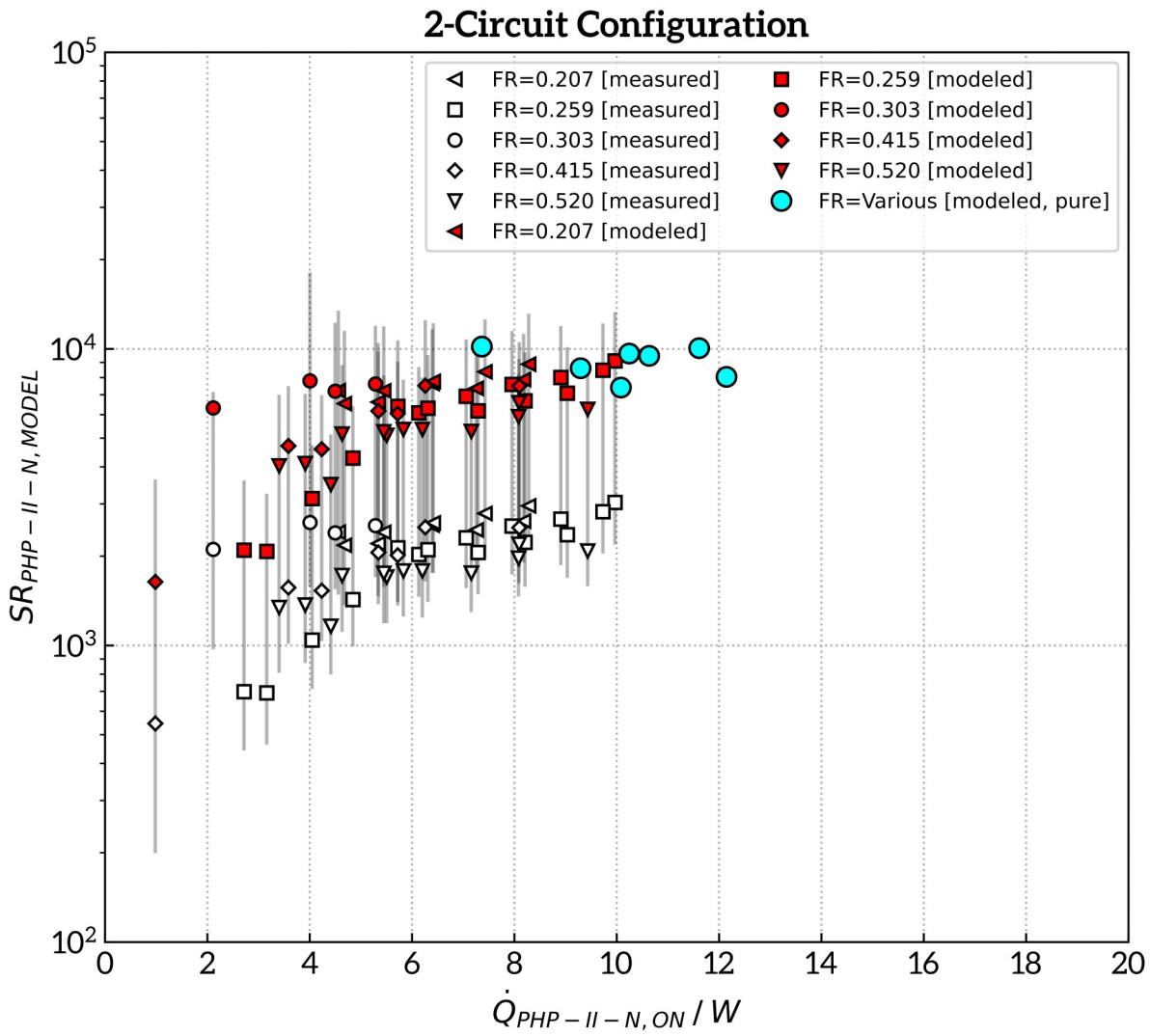

Figure 5.16. Measured and modeled switching ratios for PHP-II-N (in the 2-circuit configuration only) as a function of the heat flow through the ON state PHP-I-N with the PHP shutoff valve closed. Open points are experimental measurements. Red points are the hybrid OFF state model / ON state experiment switching ratio defined in Equation 4.8 and shown in Figure 4.5. Blue points are the pure model switching ratio defined in Equation 5.60.

with values between -40.8% and -16.2%. Note that the pure model switching ratio points don't have corresponding experimental values of $\dot{Q}_{PHP-II-N,ON}$; rather, the modeled points are simulated at the same T_{EVAP} and T_{COND} as the experiment, which results in the heat transfer capacities $\dot{Q}_{PHP,ON,MODEL}$ being different from experiment points. Much of the error between the pure

model and experimental values for the switching ratio, then, is caused by the error in the OFF state conductance model (which is predicted to be somewhat lower than the measurements show).

5.2 Comparison of the helium PHP thermal switch ON state measurements to ON state performance model

For the helium PHPs tested in Section 3, a subset of the ON state heat transfer capacities and conductance measurements are directly compared to the modeled predictions in Figure 5.9 and Figure 5.10, respectively. Pure modeled switching ratios for the helium PHPs, again defined by Equation 5.60, are shown in Figure 5.17 overlaid on the plot of pseudo-modeled and experimental switching ratio values from Figure 4.9. Similarly to the nitrogen PHP simulations, the pure modeled switching ratio over predicts the experiment value by approximately the same margin as the psuedo-modeled switching ratio. The ON state modeled conductance and heat transfer capacity for the PHP-II-H examined subset are fairly accurate with values between -19.0% and 42.0%, which are similar to the values found for the Nitrogen PHP thermal switches. This again means the culprit for the disagreement between the pure model and experiment switching ratio values is due to the OFF state conductance model under predicting the actual measured conductance by a small but non-negligible amount. Note that the pure model switching ratio points don't have corresponding experimental values of $\dot{Q}_{PHP-II-H,ON}$ because the modeled points are simulated at the same T_{EVAP} and T_{COND} as the experiment, resulting in the heat transfer capacities varying between the model and experiment points.

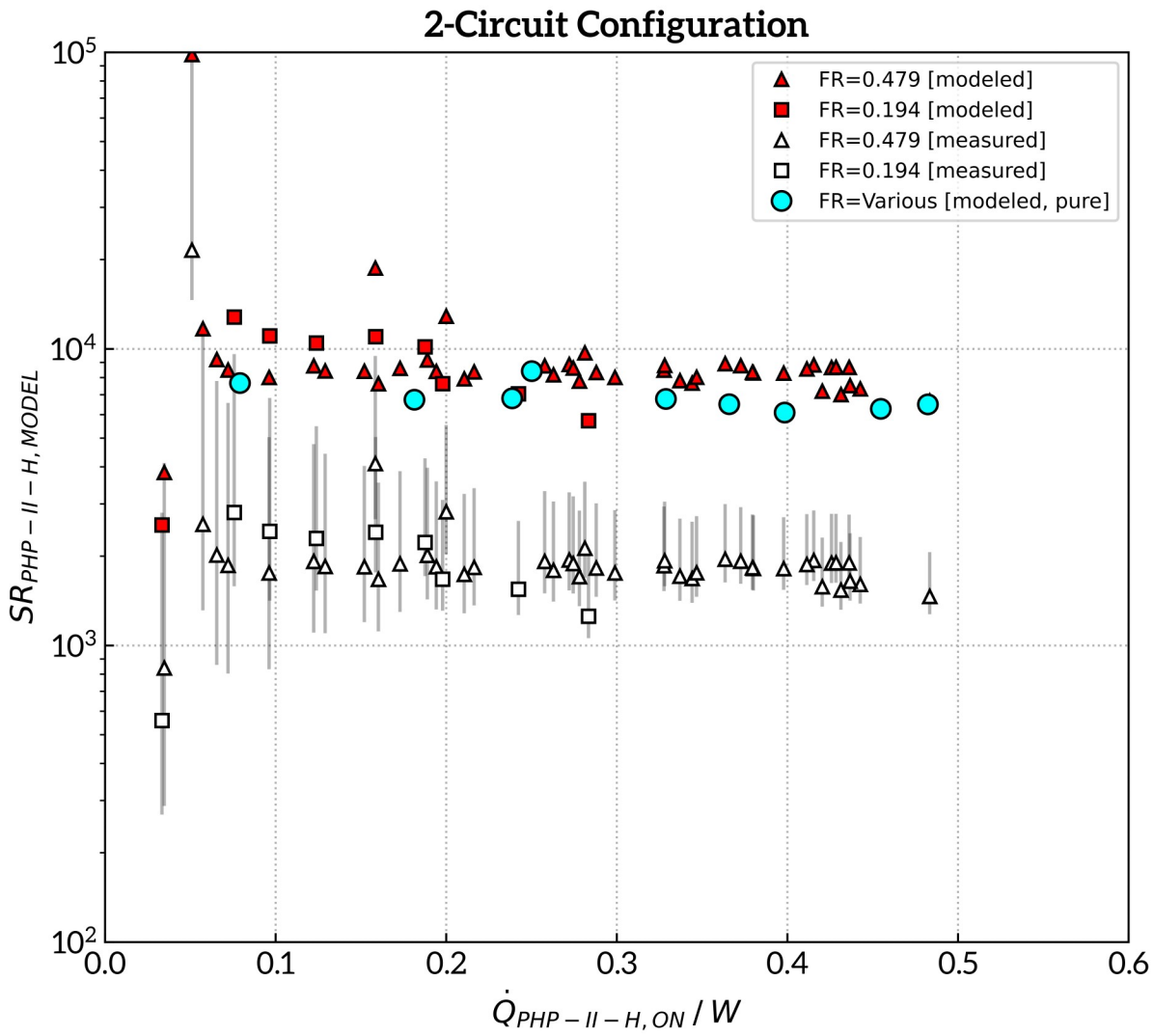

Figure 5.17. Measured and modeled switching ratios for PHP-II-H as a function of the heat flow through the ON state PHP-I-H with the PHP shutoff valve closed. Open points are experimental measurements. Red points are the hybrid OFF state model / ON state experiment switching ratio defined in Equation 4.8 and shown in Figure 4.5. Blue points are the pure model switching ratio defined in Equation 5.60.

6 Comparison of tested PHP thermal switch performance to competing technologies

With test results in hand from both the nitrogen and helium PHP proof-of-principle thermal switches, it is useful to compare their performance to that of existing thermal switch technologies by revisiting the analysis presented in Section 1.1. Recall that Table 1.3 summarizes typical performance data for various thermal switch technologies. This data is reproduced in Table 6.1, with results from the nitrogen and helium PHP thermal switch performance data appended for comparison. Because the heat transfer capacity $\dot{Q}_{switch,ON}$ and the approximate switching temperature vary substantially for each of the example devices listed in Table 6.1, direct comparisons on any individual parameter are difficult to draw. However, some overall observations can be made.

First, the nitrogen and helium PHPs constructed for this work each have large heat transfer capacities relative to the technology examples at similar switching temperatures. For instance, the nitrogen PHP thermal switch, the thermal expansion -driven mechanical contact switch, and the traditional heat pipe diode all have switching temperatures between approximately 80 K to 100 K, but their heat transfer capacities are approximately 16000 mW, 500 mW, and 500 mW, respectively. The helium PHP thermal switch has a similar switching temperature to the piezoelectric -driven mechanical switch, the gas gap switch, and the magnetoresistive switch – all are between about 4 K and 10 K. Again, the helium PHP switch has a much higher heat transfer capacity (550 mW) versus the other devices (50 mW, 50 mW, and 100 mW, respectively). The very high heat transfer capacities of the PHPs are somewhat due to their physically larger overall device sizes (see the enclosure volume V_{switch}), but mostly due to the very large UA_{ON} values inherent to PHPs due to their advantageous slug-plug advective flow operating physics.

Table 6.1. Example performance of existing cryogenic thermal switch technologies (same as Table 1.3), with the results of the nitrogen and helium PHP thermal switches from this work appended. Parameters are approximate and represent devices in the listed references. The examples listed may not represent the full capability of the technologies.

Thermal switch type	**Switch mass [g]**	**Approximate switching temperature [K]**	**ON state conductance UA_{ON}, [mW/K]**	**OFF state conductance UA_{OFF}, [mW/K]**	**Switching ratio** SR	**Enclosure volume V_{switch}, [cm^3]**	**ON state load capacity $\dot{Q}_{switch,ON}$, [mW]**	**Source**
Piezoelectric - driven mechanical contact[35]	400	4.0 to 10	2.6 to 5.5	0.0280	93 to 196	1500	50	[18] [28]
Thermal expansion - driven mechanical contact	25	100	890	1.6000	556	21	500	[17] [19]
Gas gap[36]	215	1.2	30	0.1000	300	0.05	50	[21] [22] [23]
Traditional heat pipe diode[37]	49	100	1	0.4125	2100	18	500	[25] [26]
Magneto-resistive[38]	1.4	< 10	20	0.2000 to 0.0025	100 to 8000	0.25	100	[27]
PHP (nitrogen)	1748	80	7000	2.8000	2500	519	16000	This work
PHP (helium)	523	4	750	0.3750	2000	246	550	This work

With the relative sizes of worked out, the next useful (and important) metric to compare is the switching ratio. Here, the PHPs switches are very competitive as well, with the only the traditional heat pipe diode offering performance parity and the magnetoresisitive switch offering superior performance. The nearly equivalent switching ratio of the traditional heat pipe diode to the PHP switches seems reasonable, given the fact that switching mechanism, operating physics, and device structures are similar – as each use advective fluid flows to transfer energy in the ON state and depend on dryout to limit heat heat in the OFF state. Recall that the traditional heat pipe

35 Roughly estimated using a typical ADR heat rejection power of 50 mW from the listed sources

36 Roughly estimated using a typical ADR heat rejection power of 50 mW from the listed sources

37 Estimated (very roughly) using volumes in the reference and an aluminum density of 2700 kg/m^3

38 Estimated (very roughly) using volumes in the reference and a gallium density of 5900 kg/m3. Switch mass and volume do not include a necessary 1.5 T electromagnetic field source.

diode switch is a relatively complex device from a design and fabrication perspective compared to a PHP, as it requires an internal wick and condensate chamber to prevent reverse heat flow. Likewise, the high switching ratios of the magnetoresistive switches come at the cost of requiring a switchable 1.5 T magnetic field (which is not included in the device mass or volume in Table 6.1) and switching range to temperatures below 10 K.

Finally, both the nitrogen and helium PHPs tested in this work have high mass and volume compared to the other technology examples. This is mostly due to practical experiment constraints – both the PHP mass and volume can be substantially reduced for an actual application use case with little impact to the other performance parameters. For instance, the PHP masses listed in Table 6.1 are almost entirely due to the dense copper used in the evaporator and condenser plates. In an application requiring mass minimization (e.g., aerospace), the plates could be thinned and constructed from a less dense material – aluminum perhaps. Relatively thick copper plates are used in this work for a single reason: ease of fabrication. Machining copper and joining copper to the stainless steel PHP tubes is a fairly straightforward task. Machining thinner plates and joining aluminum to stainless steel is feasible for an actual PHP thermal switch application but would add additional and unnecessary complexity to the proof-of-principle devices tested here. Alternatively, in a real application, the PHP evaporator and condenser section tubes could be integrated into an existing assembly, eliminating the necessity for metal ‘plates’ altogether. Note that, like the PHP switch mass, the PHP switch volume is also inflated due to experiment constraints. Thinning the PHP evaporator and condenser plates to reduce the mass (as discussed above) simultaneously reduces the overall switch volume. Additionally, the adiabatic section tubes could

be bundled in a much tighter formation than the sparsely populated in-plane layout used for the PHP switches (see Figure 2.8 for instance) in this work. Reducing the spacing between the PHP tube in such a way can drastically reduce the overall device volume, as the spacing between the tubes occupies a much larger volume than the tubes themselves.

Overall, the both the nitrogen and helium PHP thermal switches tested in this work compare quite well against the competing technologies. This is especially true with regards to the ON state heat transfer capacity, ON state conductance, and switching ratio. Although advantages in terms of mass and volume are not realized in the prototypes tested here, they are very likely to be attained in an optimized application design.

7 Proposal for future work

The PHP thermal switches presented here are very much proof-of-principle devices. A minimal amount of performance testing is presented in this work to show that cryogenic PHPs can indeed function very well as thermal switches. That is, for the tested PHP geometry (vertical, bottom headed, and no external inertial forces applied), there is little evidence of advective thermal communication between the PHP condenser and evaporator in the OFF switch state. There are, however, several important open questions which may need to be addressed in order to qualify PHP thermal switches for use in certain applications.

Most of these open questions relate to whether or not more extreme conditions imparted on the PHP can induce some level of intolerable advective thermal communication between the evaporator and condenser plates in the OFF switch state. One example is tilt angle: if the PHP tube plane is rotated to be horizontal, or flipped to a vertical top heated mode (with the condensers located directly above the evaporators) relative to the gravity field vector, will the resulting adverse buoyancy forces induce partial fluid movement and therefore an enhanced and unacceptable OFF state parasitic load? Related to this, it is well established that rotations in the PHP tilt angle relative to the gravity field vector result in decreased ON state PHP heat transfer capacity by up to 50 percent [73] compared to the vertical bottom heated orientation used in this experiment. A similar reduction in heat transfer capacity would occur in microgravity applications. Would a combination of reduced ON state heat transfer capacity and a potential increased OFF state parasitic load render the PHP thermal switch unusable from a switching ratio standpoint? One possible remedy for these issues, if they exist, is simply increasing the adiabatic section length of the

PHP. At least for helium PHPs, increasing the adiabatic to at least 1000 mm is shown to have very little effect on the conductance of the ON state PHP [52]. It would, however, serve as both a longer static conduction path in the OFF switch state and a buffer of sorts to keep the liquid further away from the hot condenser in the OFF switch state.

Another non-ideal PHP thermal switch operating scenario relates to disturbances, or applied external inertial forces, to the PHP switch during operation. Disturbance events may emanate from PHPs that are operating as thermal switches in portable dewars within a variety of applications. For instance, a dewar may be moved on a vehicle or dolly and experience vibrations sourced from the ground-to-wheel interaction which are then transmitted via the rigid dewar structure to the PHP tubes. Another possible source may be engine, flight, or ocean wave vibrations if the dewar and PHP switch are located on an aircraft or ship. While these kinds of transient disturbances are unlikely to cause issues to the ON state operation of a PHP switch, the may induce temporary fluid motion in the state OFF state, in turn causing transient spikes in the OFF state parasitic load. This may be especially important to consider for systems operating at liquid helium temperatures, where, combined with the very low heat capacity of the system components, transient load spikes can cause rapid temperature spikes at the common cold plate. Could the vibrations of the PHP structure cause significance increases in the OFF state parasitic load due to the possible induced fluid motion?

Another possibility for additional investigation is to confirm if PHP heat switches retain their switching ratios at reduced heat transfer capacities. In other words, can PHP thermal switches

scale to ‘smaller’ sizes without sacrificing the switching ratios measured from the fairly ‘large’ devices used in this work? Smaller devices may be desirable for applications requiring lower OFF state parasitic loads than measured in the PHP switches tested at present, or for applications with stringent mass and volume constraints. There are two main approaches to achieve lower ON state heat transfer capacities – smaller inner tube diameters to reduce the cross sectional area for the advective flow, and fewer parallel tubes connecting the evaporator and condenser plates. Reducing the OFF state parasitic loads requires thinner tube walls (as most of the load is due to conduction through the tube wall rather than the fluid vapor) or longer adiabatic sections. The former is far more difficult to practically achieve than the latter due to the already thin-walled capillary tubing used for the helium PHPs in this work. Furthermore, as shown earlier, radiation coupling is important to consider for PHPs operating at 4 K; any design attempting to achieve a lower total OFF state parasitic load than measured in this work will very likely need to focus on reducing the OFF state radiation rather than conduction parasitic. Can all of these possible issues ‘size’ or scaling issues be overcome while maintaining the switching ratios measured in the proof-of-concept devices measured here?

Lastly, it is important to experimentally characterize the pressures developed in the OFF state PHPs, as high OFF state pressures could cause structural failures in the PHP tube walls or union joints within a device that is intended to have very high reliability. The PHP switches tested in the present investigation do not have pressure sensors within the PHP circuit, so the model-predicted OFF state pressures (presented in Figure 2.2 and Figure 3.6) remained unconfirmed. It can be stated that both the soft solder union joints in the PHP fill lines and the silver braze union

joints in the PHP adiabatic section survived testing in the OFF state with no failures. Without experimental confirmation, however, the magnitude and potential impacts of the OFF state pressures can not be known. Are the OFF state pressures in agreement with the OFF state model predictions, and what implications does this have for the engineering of the PHP for long term reliability?

Additional testing is clearly needed to answer the aforementioned questions if a PHP thermal switch will be subject to such conditions in a real application. The following investigations are therefore recommended for any future research:

1. Measurements of nitrogen and helium ON and OFF state heat transfer, conductance, and switching ratio at tilt angles ranging a full 180 degrees from the vertical bottom heated orientation investigated in this work
2. Measurements of nitrogen and helium ON and OFF state heat transfer, conductance, and switching ratio while imparting transient vibrations or oscillating motion to the PHP structure
3. Develop and test PHP thermal switches of ‘smaller’ size both in terms of ON state heat transfer capacity (smaller inner tube diameters and fewer parallel tubes) and OFF state parasitic load (longer adiabatic sections and thinner tube walls) to check for impacts on switching ratio
4. Test PHP thermal switches with pressure sensors installed in the fluid loop to fully characterized the pressures which develop in the OFF switch state.

8 Appendix

8.1 Nitrogen PHP thermal switch test facility vacuum and filling systems

A schematic of the nitrogen PHP thermal switch facility external plumbing (for PHP filling and dewar evacuation) is shown in Figure 8.1, with an image highlighting the locations of key components in the setup shown in Figure 8.2. Related component descriptions are given in Table 8.1. A rotary vane vacuum pump is used to evacuate both the dewar and PHP filling lines, with a turbomolecular pump installed inline to achieve a higher vacuum in the dewar. A vacuum gauge is attached to the dewar to monitor system pressure. The PHP filling system is fed by a high purity nitrogen source tank and contains a series of valves, a pressure sensor, and a filling tank to meter the nitrogen charge to the PHPs.

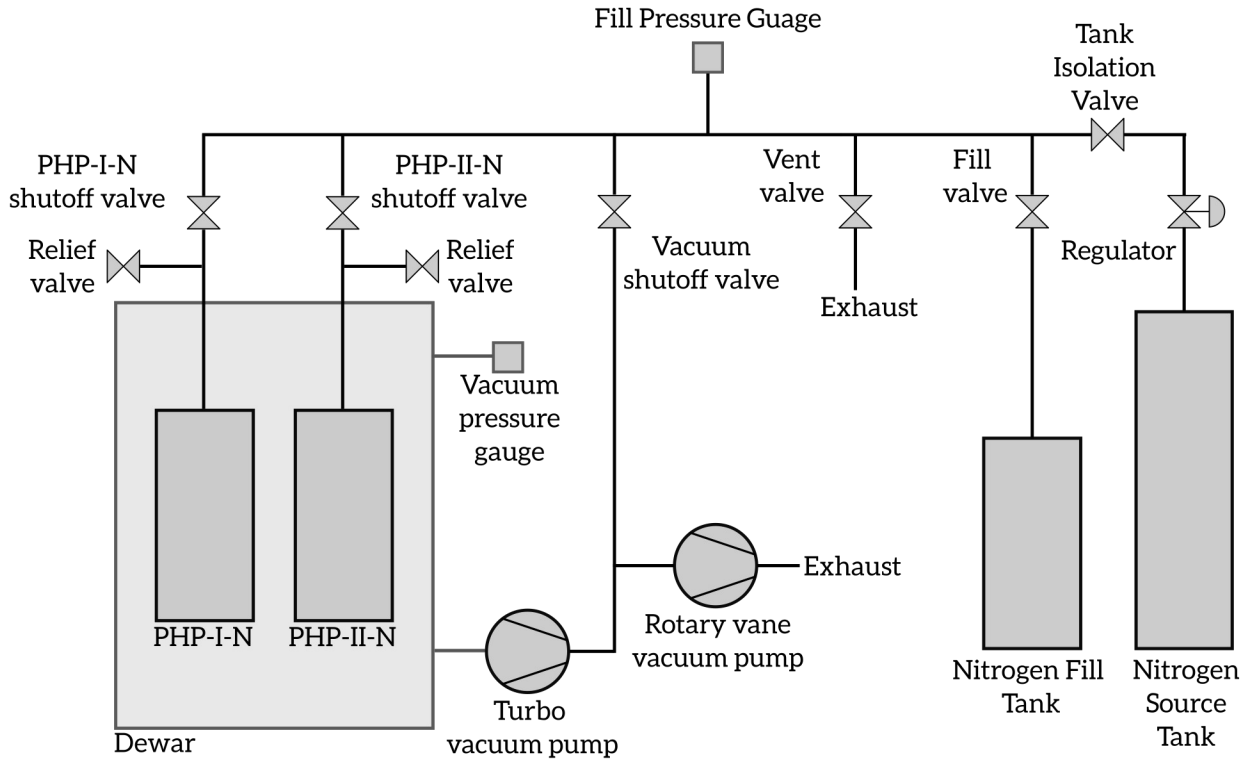

Figure 8.1. Schematic of vacuum and filling system for the nitrogen PHP thermal switch test facility.

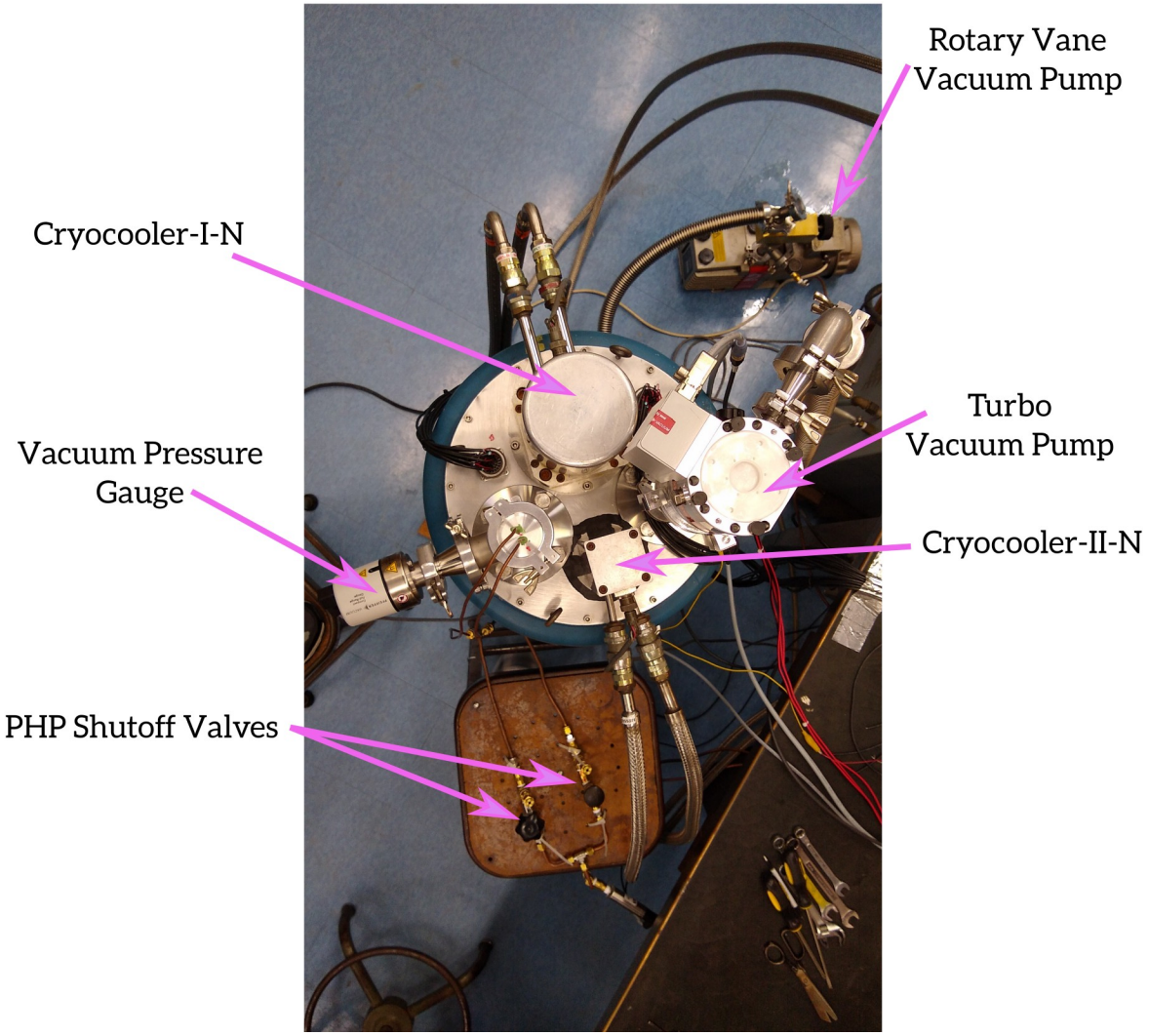

Figure 8.2. Photo showing the vacuum and filling system for the NPHP thermal switch test facility

Table 8.1. Nitrogen PHP thermal switch test facility external plumbing component descriptions.

Component	Manufacturer	Model	Description
Rotary Vane Vacuum Pump	Edwards	E2M2	
Turbo Vacuum Pump	Pfieffer	Hi Pace 80	
Vacuum Pressure Gauge	Pfeiffer	PKR 251	
Fill Pressure Gauge	Omega	PX419-050A5V	
Nitrogen Fill Tank			Known fill volume for (relatively) low pressure mass metering into the nitrogen PHPs
Nitrogen Source Tank			High purity nitrogen source

8.2 Helium PHP thermal switch test facility vacuum and filling systems

A schematic of the helium PHP thermal switch facility external plumbing (for PHP filling and dewar evacuation) is shown in Figure 8.3, with an images highlighting the locations of key components in the setup shown in Figure 8.4 and Figure 8.5. Related component descriptions are given in Table 8.2. A rotary vane vacuum pump is used to evacuate both the dewar and PHP filling lines, with a turbomolecular pump installed inline to achieve a higher vacuum in the dewar. A vacuum gauge is attached to the dewar to monitor system pressure. The PHP filling systems – fed by source tanks of high purity helium and nitrogen – contain a series of valves, pressure sensors, and filling tanks to meter the gas charges to the PHPs. Note here that the helium PHP filling lines between to the PHPs and the shutoff valve do not have relief valves (to minimize leaks) and are sunk to both the hot and cold stages of the cryocoolers via heat exchangers.

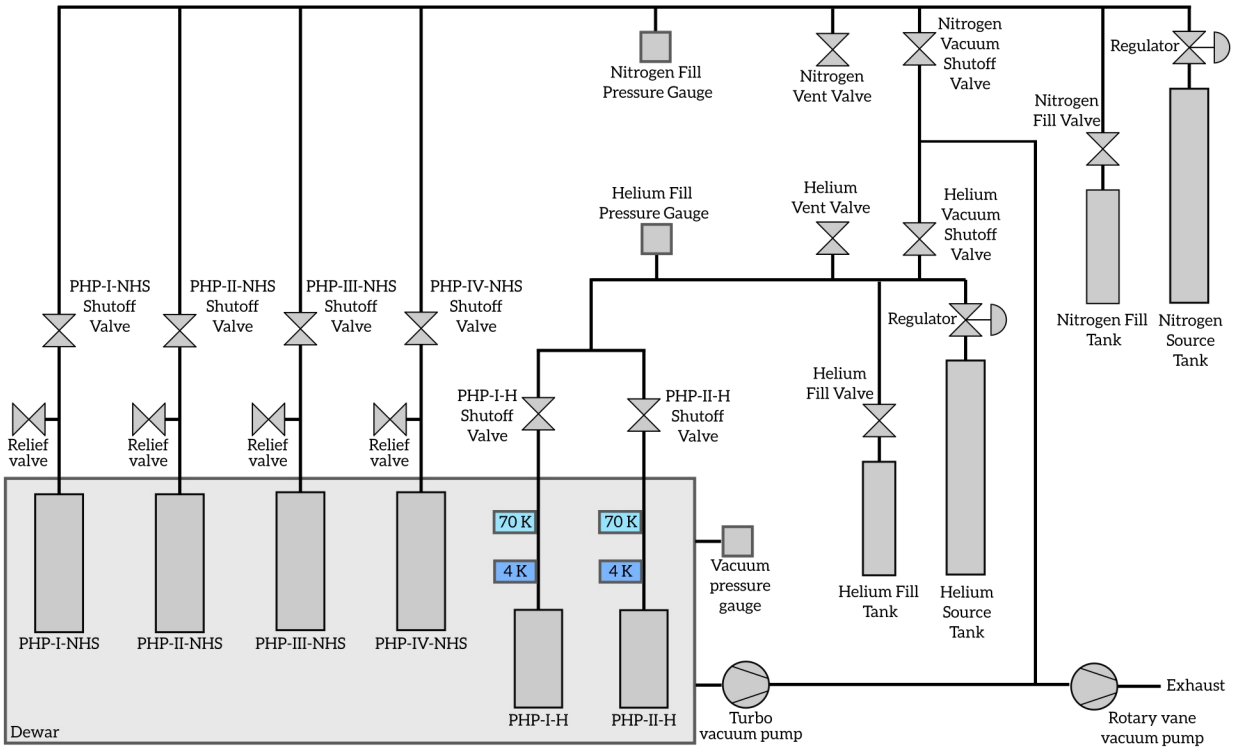

Figure 8.3. Schematic of vacuum and filling system for the helium PHP thermal switch test facility.

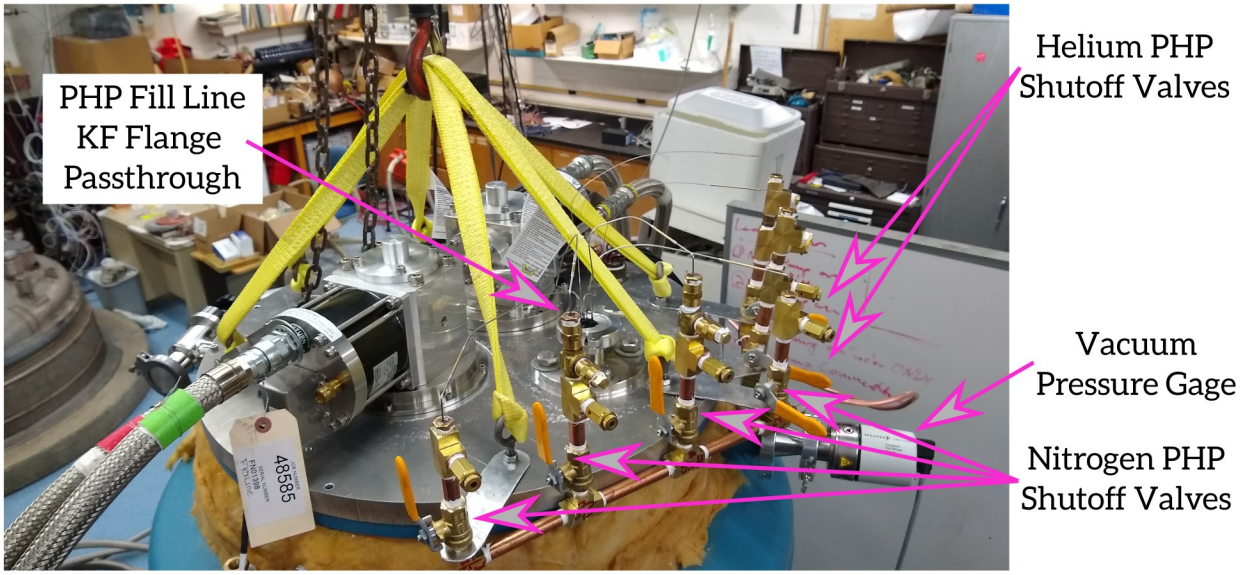

Figure 8.4. Annotated image of the helium PHP switch test facility nitrogen and helium fill system dewar headers and PHP shutoff valves.

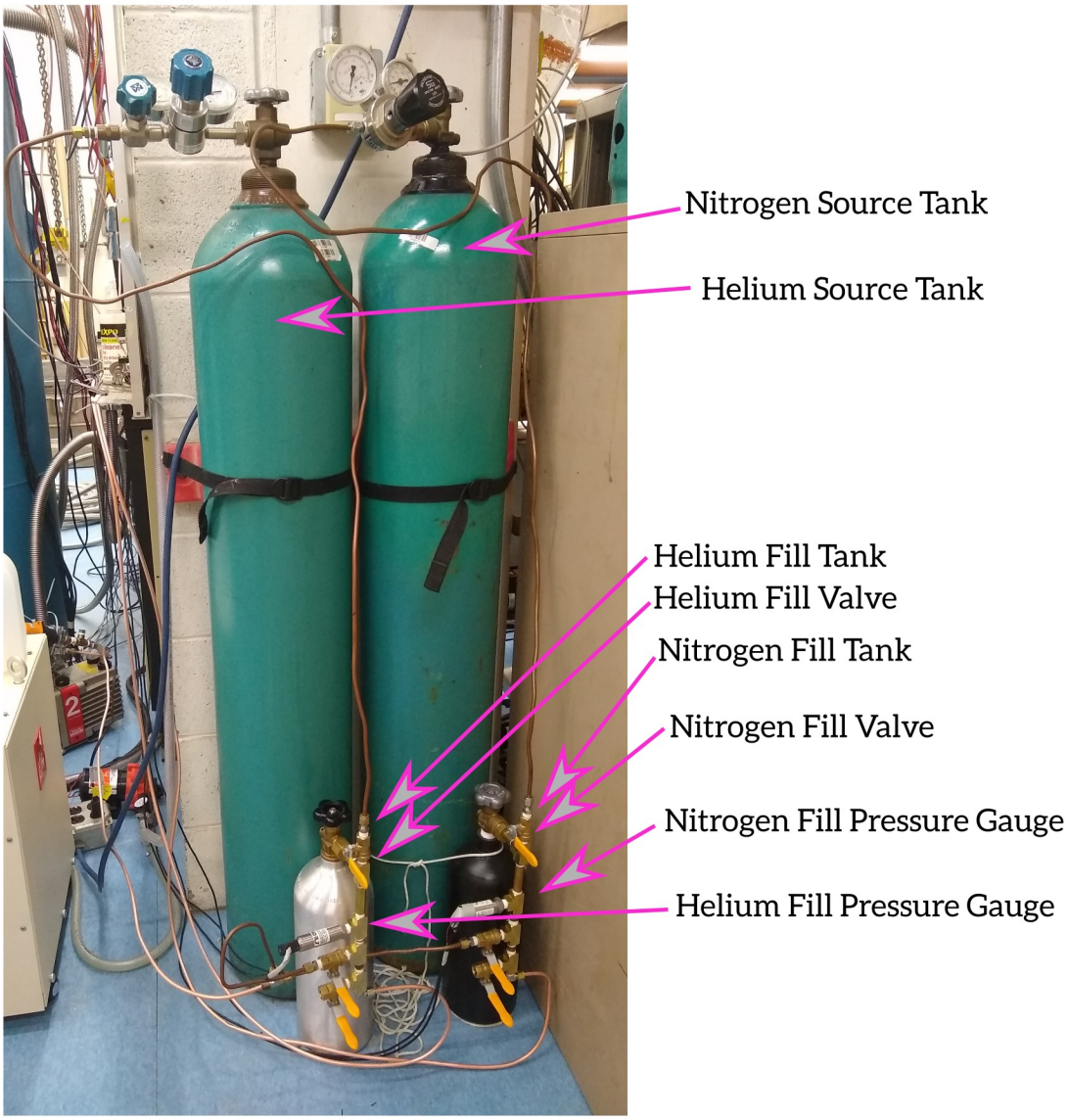

Figure 8.5. Annotated image of the helium PHP switch test facility nitrogen and helium fill system fill tank headers and PHP shutoff valves.

Table 8.2. Helium PHP thermal switch test facility external plumbing component descriptions.

Component	Manufacturer	Model	Description
Rotary Vane Vacuum Pump	Edwards	E2M2	
Turbo Vacuum Pump	Pfieffer	Hi Pace 80	
Vacuum Pressure Gauge	Pfeiffer	PKR 251	
Helium Fill Pressure Gauge	Omega	PX419-050A5V	
Nitrogen Fill Pressure Gauge	Transducers Direct	TD1200CCA005003D002X	
Nitrogen Fill Tank			Known fill volume for (relatively) low pressure mass metering into the nitrogen PHPs
Nitrogen Source Tank			High purity nitrogen source
Helium Fill Tank			Known fill volume for (relatively) low pressure mass metering into the helium PHPs
Helium Source Tank			High purity helium source

8.3 PHP filling calculation

Note: All nomenclature in this section is general as to apply to all PHPs in this work. When referenced in other sections, subscripts are added to refer to specific components.

All PHPs in this work are filled with the same general procedure:

1. With the entire system at ambient temperature T_{AMB} :
    a) Open the vacuum shutoff valve to evacuate the PHP, filling system lines, and filling tanks using the rotary vane vacuum pump
    b) Close the vacuum shutoff valve
    c) Fill the PHP, filling system lines, and filling tanks with working fluid vapor (nitrogen or helium)
2. Repeat step 1 three times

3. Open the vacuum shutoff valve to evacuate the PHP, filling system lines, and filling tanks using the rotary vane vacuum pump
4. Close the vacuum shutoff valve
5. Close All PHP fill valves (on the fill lines immediately external to the dewar). PHPs are now under vacuum.
6. Cool the PHP condensers to the operating temperature (~70K for the nitrogen PHPs and ~4K for the helium PHPs):
7. Fill each PHP individually:
    a) Choose a target fill ratio
    b) Open the regulator and meter a charge of working fluid vapor into the fill tank and filling system line, bringing it to pressure $P_{FILL,EXT,INI}$. This is limited to 345 kPa absolute by the fill pressure gauge. Close the regulator when $P_{FILL,EXT,INI}$ is obtained.
    c) Choose a target fill ratio FR and corresponding saturation temperature in the PHP T_{SAT}.
    d) Determine the final pressure of the filling system $P_{FILL,EXT}$, which corresponds to the correct amount of working fluid mass m_{PHP} transferred to the PHP.
    e) Open the PHP shutoff valve. As vapor condenses in the PHP, the pressure in the filling system decreases. Shut the PHP shutoff valve when the pressure reaches $P_{FILL,EXT}$.

To determine the relation between $P_{FILL,EXT,INI}$, $P_{FILL,EXT}$, and FR, a mass balance is applied to the filling system. First, the working fluid mass necessary to obtain the desired filling ratio at specified saturation temperature T_{SAT} is

$$m_{PHP} = \frac{(FR)V_{PHP}}{v_{SAT,LIQ}(T_{SAT})} + \frac{(1-FR)V_{PHP}}{v_{SAT,VAP}(T_{SAT})} \tag{8.1}$$

, where V_{PHP} is the internal volume of the PHP, $v_{SAT,LIQ}(T_{SAT})$ is the specific volume of the saturated liquid working fluid at the saturation temperature, and $v_{SAT,VAP}(T_{SAT})$ is the specific volume of the saturated vapor working fluid at the saturation temperature. Assuming the PHP is fully evacuated, a mass balance over the filling process is

$$\begin{aligned} m_{PHP} &= m_{FILL,EXT,INI} - m_{FILL,EXT} - m_{FILL,INT} \\ &= \frac{V_{FILL,EXT}}{v(T_{AMB},P_{FILL,INI})} - \frac{V_{FILL,EXT}}{v(T_{AMB},P_{FILL})} - \frac{V_{FILL,INT,T_{AMB}}}{v(T_{AMB},P_{FILL})} - \frac{V_{FILL,INT,70K}}{v(70\,K,P_{FILL})} - \frac{V_{FILL,INT,4K}}{v(4\,K,P_{FILL})} \end{aligned} \tag{8.2}$$

, where $m_{FILL,EX,INI}$ is the mass of working fluid in the fill lines and filling tank at the start of the filling process, $m_{FILL,EX}$ is the mass of working fluid in the fill lines and filling tank at the end of the filling process, and $m_{FILL,INT}$ is the mass of working fluid that remains between the PHP tubing and shutoff valve at the end of filling process. For the helium PHPs, the filling tube contains precooling heat exchangers, per Figure 8.3, which remain at low temperatures during PHP operation; the retained fluid mass in these sections is estimated and accounted for in Equation 8.2. The equation is decomposed into the corresponding volumes and specific volumes at the start and end states of the filling process.

Equations 8.1 and 8.2 are combined and solved explicitly for the filling ratio

$$FR = \frac{\left(\frac{V_{FILL,EXT}}{v(T_{AMB},P_{FILL,INI})} - \frac{V_{FILL,EXT}}{v(T_{AMB},P_{FILL})} - \frac{V_{FILL,INT,T_{AMB}}}{v(T_{AMB},P_{FILL})} - \frac{V_{FILL,INT,70K}}{v(70\,K,P_{FILL})} - \frac{V_{FILL,INT,4K}}{v_{SAT,LIQ}(4\,K)}\right)\frac{v_{SAT,LIQ}(T_{SAT})}{V_{PHP}} - \frac{v_{SAT,LIQ}(T_{SAT})}{v_{SAT,VAP}(T_{SAT})}}{1-\frac{v_{SAT,LIQ}(T_{SAT})}{v_{SAT,VAP}(T_{SAT})}} \quad (8.3)$$

Which is a function of $P_{FILL,EXT,INI}$, $P_{FILL,EXT}$, T_{SAT}, the system volumes, and the working fluid properties. The upper and lower bounds of the fill ratio uncertainty are

$$FR^{+} = \frac{\left(\frac{V_{FILL,EXT}+\Delta V_{FILL,EXT}}{v(T_{AMB},P_{FILL,INI}+\Delta P_{FILL})} - \frac{V_{FILL,EXT}-\Delta V_{FILL,EXT}}{v(T_{AMB},P_{FILL}-\Delta P_{FILL})} - \frac{V_{FILL,INT,T_{AMB}}-\Delta V_{FILL,INT,T_{AMB}}}{v(T_{AMB},P_{FILL}-\Delta P_{FILL})} - \frac{V_{FILL,INT,70K}-\Delta V_{FILL,INT,70K}}{v(70\,K,P_{FILL}-\Delta P_{FILL})} - \frac{V_{FILL,INT,4K}-\Delta V_{FILL,INT,4K}}{v_{SAT,LIQ}(4K)}\right)\frac{v_{SAT,LIQ}(T_{SAT})}{V_{PHP}-\Delta V_{PHP}} - \frac{v_{SAT,LIQ}(T_{SAT})}{v_{SAT,VAP}(T_{SAT})}}{1-\frac{v_{SAT,LIQ}(T_{SAT})}{v_{SAT,VAP}(T_{SAT})}} \quad (8.4)$$

and

$$FR^{-} = \frac{\left(\frac{V_{FILL,EXT}-\Delta V_{FILL,EXT}}{v(T_{AMB},P_{FILL,INI}-\Delta P_{FILL})} - \frac{V_{FILL,EXT}+\Delta V_{FILL,EXT}}{v(T_{AMB},P_{FILL}+\Delta P_{FILL})} - \frac{V_{FILL,INT,T_{AMB}}+\Delta V_{FILL,INT,T_{AMB}}}{v(T_{AMB},P_{FILL}+\Delta P_{FILL})} - \frac{V_{FILL,INT,70K}+\Delta V_{FILL,INT,70K}}{v(70\,K,P_{FILL}+\Delta P_{FILL})} - \frac{V_{FILL,INT,4K}+\Delta V_{FILL,INT,4K}}{v_{SAT,LIQ}(4K)}\right)\frac{v_{SAT,LIQ}(T_{SAT})}{V_{PHP}+\Delta V_{PHP}} - \frac{v_{SAT,LIQ}(T_{SAT})}{v_{SAT,VAP}(T_{SAT})}}{1-\frac{v_{SAT,LIQ}(T_{SAT})}{v_{SAT,VAP}(T_{SAT})}} \quad (8.5)$$

. Volumes and related uncertainties for each of the experimental facilities are listed in Table 8.3.

Table 8.3. Filling system volumes and uncertainties for each test facilities

Quantity	**Nitrogen PHP thermal switch test facility**		**Helium PHP thermal switch test facility (helium)**		**Helium PHP thermal switch test facility (nitrogen shield)**	
	PHP-I-N	**PHP-II-N**	**PHP-I-H**	**PHP-II-H**	**PHP-I-NHS**	**PHP-II-NHS**
$V_{FILL,EXT}$	3432000 mm^3		3521559 mm^3		3875939 mm^3	
$V_{FILL,INT,T_{AMB}}$	9369 mm^3		1059 mm^3		No Uncertainty Analysis	
$V_{FILL,INT,70K}$	N/A		365 mm^3		N/A	
$V_{FILL,INT,4K}$	N/A		270 mm^3		N/A	
V_{PHP}	8550 mm^3		2566 mm^3		8505 mm^3	
$\pm\Delta V_{FILL,EXT}$	34320 mm^3		35216 mm^3		No Uncertainty Analysis	
$\pm\Delta V_{FILL,INT,T_{AMB}}$	169 mm^3		53 mm^3		No Uncertainty Analysis	
$\pm\Delta V_{FILL,INT,70K}$	N/A		18 mm^3		N/A	
$\pm\Delta V_{FILL,INT,4K}$	N/A		13 mm^3		N/A	
$\pm\Delta V_{PHP}$	622 mm^3		273 mm^3		No Uncertainty Analysis	
$\pm\Delta P_{FILL}$	0.28 kPa					

8.4 Nitrogen PHP thermal switch test facility platinum resistance temperature sensor calibrations and measurements

The Lakeshore Cryotronics PT-102 platinum resistance thermometers are calibrated with a two point calibration using the standard Callendar-Van Dusen polynomial, with the temperature explicit form

$$T_S=\left(\frac{1}{2B_S}\right)\left(-A_S+\sqrt{A_s^2-4B_S\left(1-\frac{R_S}{R_{S,0}}\right)}\right)K+273.15\,K \tag{8.6}$$

, where T_S is the temperature, A_S and B_S are fitting parameters, $R_{S,0}$ is the electrical resistance at the freezing point of water, and R_S is the measured resistance of the sensor at T_S. The resistance is measured with the sensor voltage V_S, supplied current I_S, and voltage offset $V_{S,OFFSET}$

$$R_S=\frac{\left(V_S-V_{S,OFFSET}\right)}{I_S} \tag{8.7}$$

, with the voltages read by a National Instruments USB-6218 or National Instruments USB-6210 data acquisition unit. A calibrated Lakeshore Cryotronics 120CS current source provides the current at 100 mA, while B_S is taken as the general value for platinum resistance thermometers. $R_{S,0}$ and A_S are determined by measuring the sensor resistance while submerged in a bath of ice water and boiling liquid nitrogen, respectively, at known temperature and pressure (T=273.15 K and P=1.013 bar for the ice water and T=77.36 K and P=1.013 bar for the boiling liquid). Table 8.4 summarizes these calibration parameters for each these thermometers.

The voltage offsets – caused by electrical noise from the cryocoolers, vacuum pumps, power supplies, and the use of multiple data acquisition boards – are mostly constant but do have some

variation between measurements. Temperature measurement errors are propagated from the measurement uncertainties in V_S and I_S, as well as a fitting error of ±0.25 K associated with the use of Equation 8.6 [74]. Figure 8.6 shows the typical agreement of all the calibrated platinum resistance temperature sensors used in the nitrogen PHP thermal switch test facility at approximately 70 K and 295 K.

Table 8.4. Temperature sensor calibration data.

Temperature sensor name	**Calibration data**			
	A_S	B_S	$R_{S,0}$	$V_{S,OFFSET}$
$T_{PI\text{-}HM\text{-}I\text{-}1}$	0.0039585485	-0.0000005775	99.9272346517	0.0002300350
$T_{PI\text{-}HM\text{-}I\text{-}2}$	0.0039577773		100.0038948358	-0.0002300350
$T_{PI\text{-}PHP\text{-}I\text{-}COND\text{-}1}$	0.0039577720		99.9839047481	0.0006032019
$T_{PI\text{-}PHP\text{-}I\text{-}COND\text{-}2}$	0.0039580602		99.9917049758	0.0008683348
$T_{PI\text{-}PHP\text{-}I\text{-}COND\text{-}3}$	0.0039569170		99.9992888242	0.0012567902
$T_{PI\text{-}HM\text{-}II\text{-}1}$	0.0039583682		99.9862601016	0.0001540467
$T_{PI\text{-}HM\text{-}II\text{-}2}$	0.0039568157		99.9744329452	-0.0001540467
$T_{PI\text{-}PHP\text{-}II\text{-}COND\text{-}1}$	0.0039583547		99.9489307577	0.0009736271
$T_{PI\text{-}PHP\text{-}II\text{-}COND\text{-}2}$	0.0039588960		99.9989016427	0.0008344841
$T_{PI\text{-}PHP\text{-}II\text{-}COND\text{-}3}$	0.0039591169		99.9579445478	0.0007430019
$T_{PI\text{-}PHP\text{-}I\text{-}EVAP\text{-}1}$	0.0039579340		100.0373822550	-0.0002170038
$T_{PI\text{-}PHP\text{-}I\text{-}EVAP\text{-}2}$	0.0039579881		100.0073432127	-0.0000469437
$T_{PI\text{-}PHP\text{-}I\text{-}EVAP\text{-}3}$	0.0039559463		99.9989332285	-0.0000338812
$T_{PI\text{-}PHP\text{-}II\text{-}EVAP\text{-}1}$	0.0039574866		100.0036097690	-0.0000575361
$T_{PI\text{-}PHP\text{-}II\text{-}EVAP\text{-}2}$	0.0039566296		99.9667850245	-0.0000628376
$T_{PI\text{-}PHP\text{-}II\text{-}EVAP\text{-}3}$	0.0039587657		99.9949247251	-0.0000171480

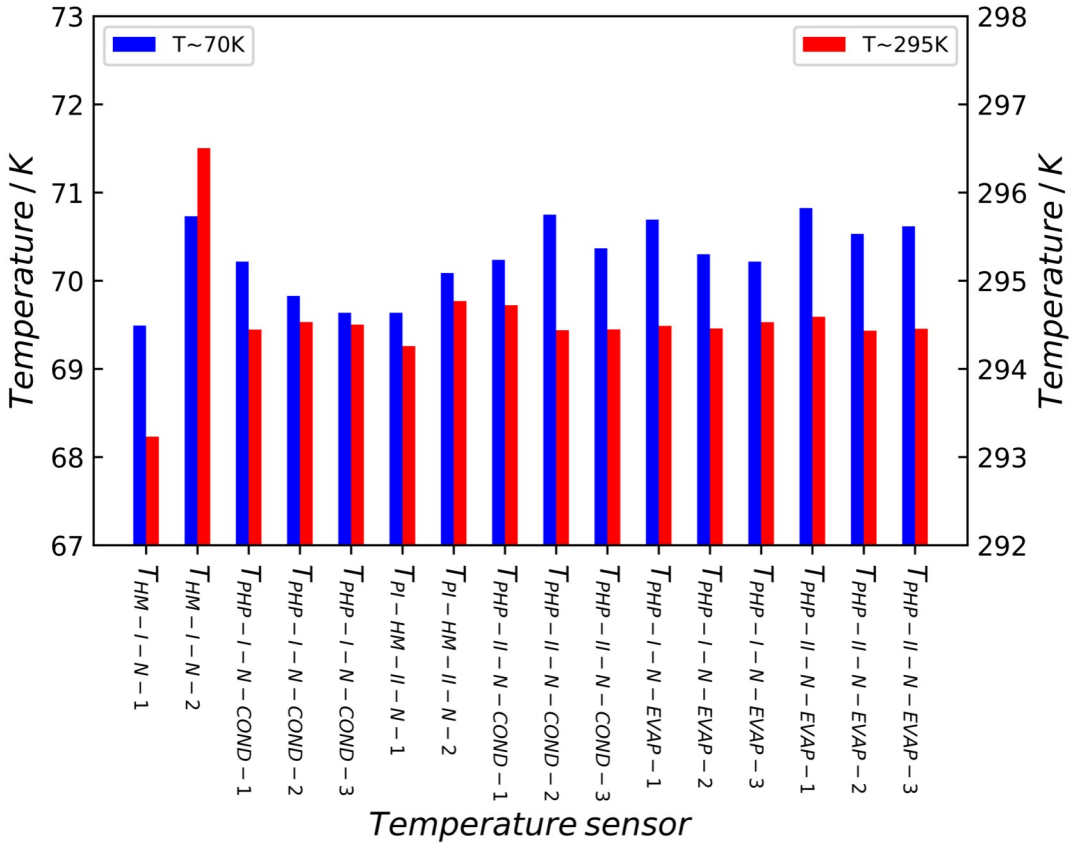

Figure 8.6. Agreement between sensors at approximately 70K and 295K with a common cold plate heat load of 0 W. For the ~70 K measurements, PHP-I-N and PHP-II-N are filled with nitrogen. The voltage offsets are calibrated to minimize variance between the set of sensor measurements at ~70K

8.5 Nitrogen PHP thermal switch test facility heat meter RRR and conductivity calculation

The copper RRR for PI-HM-I is determined by the solution of

$$k_{HM-I-N,MEAN}\frac{A_{HM-I-N}}{L_{HM-I-N}}\left(T_{HM-I-N,MAX}-T_{HM-I-N,MIN}\right)= \int_{T_{HM-I-N,MIN}}^{T_{HM-I-N,MAX}}\left[f_{HM-I-N}k_{RRR\,50}(T)+(1-f_{HM-I-N})k_{RRR\,100}(T)\right]\frac{A_{HM-I-N}}{L_{HM-I-N}}dT \tag{8.8}$$

For f_{HM-I-N}, with the remaining parameters defined in Table 2.3 and Table 2.4. The parameter f_{HM-I-N} results from a linear interpolation between the thermal conductivity of RRR50 and RRR100 copper [37][38]. The interpolated copper RRR for the HM-I-N is then

$$RRR_{HM-I-N} = (f_{HM-I-N})50 + (1 - f_{HM-I-N})100 \tag{8.9}$$

resulting in a thermal conductivity for HM-I-N of

$$k_{HM-I-N}(T) = (f_{HM-I-N})k_{RRR50}(T) + (1 - f_{HM-I-N})k_{RRR100}(T) \tag{8.10}$$

. Likewise the copper RRR for HM-II-N is determined by the solution of

$$k_{HM-II-N,MEAN}\frac{A_{HM-II-N}}{L_{HM-II-N}}(T_{HM-II-N,MAX} - T_{HM-II-N,MIN}) = \int_{T_{HM-II-N,MIN}}^{T_{HM-II-N,MAX}} \left[f_{HM-II-N}k_{RRR50}(T) + (1 - f_{HM-II-N})k_{RRR100}(T)\right]\frac{A_{HM-II-N}}{L_{HM-II-N}}dT \tag{8.11}$$

with

$$RRR_{HM-II-N} = (f_{HM-II-N})50 + (1 - f_{HM-II-N})100 \tag{8.12}$$

and

$$k_{HM-II-N}(T) = (f_{HM-II-N})k_{RRR50}(T) + (1 - f_{HM-II-N})k_{RRR100}(T) \tag{8.13}$$

8.6 Helium PHP thermal switch test facility Cernox sensor calibrations and measurements

A suite of eight Cernox sensors (Lakeshore Cryotronics model CX-1050-CU-HT) are used for thermometry in the helium PHP thermal switch test facility. Four of these sensors are used to measure the heat meter temperatures (sensors $T_{HM-I-H-A}$, $T_{HM-I-H-B}$, $T_{HM-II-H-A}$, and

$T_{HM-II-H-B}$) and four are used to measure the helium PHP evaporator and condenser plate temperatures (sensors $T_{PHP-I-H,COND}$, $T_{PHP-I-H,EVAP}$, $T_{PHP-II-H,COND}$, and $T_{PHP-II-H,EVAP}$). Locations of these thermometers are shown in Figure 3.19 and Figure 3.17. One of the sensors – $T_{PHP-II-H,EVAP}$ – is factory calibrated. The other sensors are calibrated relative to this factory calibrated sensor using the setup shown in Figure 8.7.

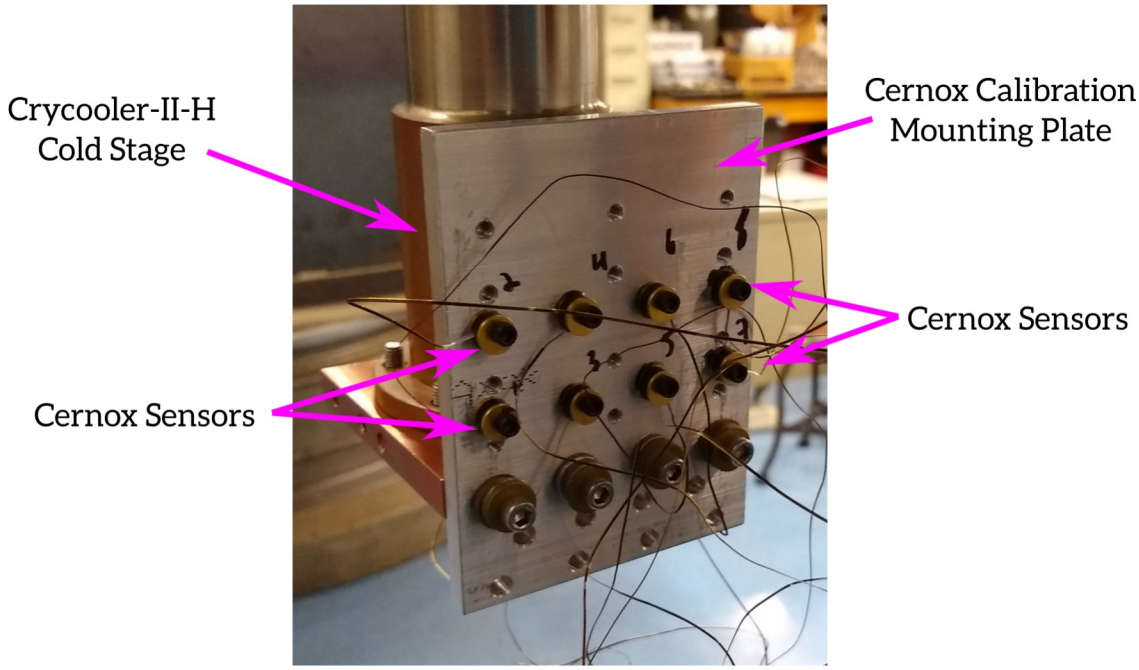

Figure 8.7. Annotated image of the Cernox sensor calibration setup.

The calibration setup features an aluminum mounting plate to hold the eight Cernox sensors, which in turn is secured to a Sumitomo RDK-415D cryocooler cold head. A resistance heater is attached to the bottom of the cold head (not visible in Figure 8.7) to allow control of the mounting plate temperature at temperatures less than about 8 K. At higher temperatures, the cooling power of the cryocooler exceeds the power output of the resistor and power supply. The entire calibration setup is actively shielded by the hot cryocooler stage (shield not shown in Figure 8.7) to prevent temperature gradients from developing in the mounting plate due to radiative loading.

The Cernox sensor signals are read by a Cryocon 18i temperature monitor via four wire connections.

At temperatures between about 3 K and 8 K, the temperature controller allows calibration samples to be obtained at temperatures constant in time. The lower temperature limit is constrained by the capacity of the cryocooler cold stage, while the upper limit is constrained by the maximum power output of the resistance heater and power supply, as mentioned previously. At temperatures above about 8 K, the calibration points are therefore obtained at temperatures unsteady in time, during system warm up after the cryocooler is deactivated. This likely leads to small inaccuracies due to the heat capacity of the calibration components and spatial separation of the sensors; however, this is unimportant because temperature measurements above about 8 K are not used for critical experiment performance calculations. Instead, temperatures in this range are used only for monitoring purposes during system startup and shutdown, during which high accuracy is not especially important. Table 8.5 and Table 8.6 contain the calibration data for each sensor.

Table 8.5. Cernox temperature sensor calibration data I.

$T_{HM-I-H-A}$		$T_{HM-I-H-B}$		$T_{HM-II-H-A}$		$T_{HM-II-H-B}$	
T / K	R / Ω	T / K	R / Ω	T / K	R / Ω	T / K	R / Ω
304.477	56.567	304.477	61.013	304.477	59.181	304.477	58.406
298.609	57.493	298.609	62.101	298.609	60.228	298.609	59.430
292.161	58.501	292.425	63.295	292.161	61.288	292.425	60.553
290.148	58.994	290.148	63.727	290.148	61.652	290.148	61.006
288.812	59.085	288.812	64.002	288.812	61.918	288.812	61.264
286.057	59.691	286.057	64.577	286.057	62.476	286.057	61.806
284.688	59.950	284.688	64.863	284.688	62.753	284.688	62.075
282.673	60.329	282.673	65.282	282.673	63.160	282.673	62.471
279.991	60.745	279.991	65.670	275.162	64.624	279.991	62.856
268.374	63.022	275.162	66.813	268.374	66.210	268.374	65.492

258.597	65.147	268.374	68.360	258.597	68.495	258.597	67.743
245.637	68.628	258.597	70.669	245.637	72.022	245.637	71.274
231.303	72.372	245.637	74.460	231.303	76.217	231.303	75.131
215.592	77.078	231.303	78.494	215.592	81.025	215.592	80.028
196.040	84.027	215.592	83.838	196.040	88.431	196.040	87.320
180.444	90.354	196.040	91.582	180.444	95.469	180.444	94.254
164.845	97.945	180.444	98.912	164.845	103.742	164.845	102.457
150.975	105.835	164.845	107.592	150.975	112.278	150.975	110.937
135.243	116.581	150.975	116.566	135.243	123.942	135.243	122.480
123.526	126.165	135.243	128.720	123.526	134.293	123.526	132.819
113.887	135.259	123.526	139.606	113.887	144.250	113.887	142.647
105.844	143.991	113.887	150.056	105.844	153.770	105.844	152.121
94.333	158.441	105.844	160.033	94.333	169.626	94.333	168.031
82.984	176.372	94.333	176.746	82.984	189.083	82.984	187.281
65.710	213.574	82.984	197.171	65.710	229.884	65.710	227.373
56.407	240.901	65.710	239.513	56.407	259.699	56.407	258.345
48.221	273.405	56.407	271.845	48.221	295.681	48.221	292.686
41.128	309.363	48.221	308.272	41.128	334.568	41.128	331.570
36.538	338.290	41.128	349.035	36.538	366.801	36.538	364.084
32.319	370.353	36.538	382.851	32.319	401.808	32.319	399.907
30.695	384.817	32.319	420.295	30.832	415.974	30.695	416.008
27.071	418.691	30.832	435.577	30.695	417.707	28.291	442.125
25.736	434.283	30.695	437.112	28.291	439.205	27.071	456.713
23.855	459.092	27.071	480.347	27.071	455.715	25.736	475.591
21.945	487.728	25.736	498.362	25.736	473.196	23.855	501.816
20.408	513.145	23.855	526.881	23.855	499.695	21.945	533.690
17.629	569.349	21.945	561.475	21.945	530.478	20.408	562.676
16.113	607.804	20.408	590.867	20.408	559.481	17.629	629.659
14.230	664.356	17.629	659.247	17.629	622.974	16.113	673.260
13.405	695.768	16.113	703.017	16.113	663.167	14.230	740.544
12.647	726.347	14.230	770.362	14.230	726.391	13.405	774.287
11.683	769.110	13.405	804.569	13.405	760.432	12.647	808.134
11.187	794.024	12.647	840.216	12.647	793.420	11.683	856.765
10.433	837.254	11.683	889.941	11.683	840.199	11.187	886.294
9.602	892.354	11.187	920.340	11.187	864.782	10.433	937.219
7.648	1067.210	10.433	971.116	10.433	914.307	9.602	999.808
7.646	1067.543	9.602	1036.540	9.602	974.996	7.648	1206.476
7.198	1122.897	7.648	1248.797	7.648	1171.335	7.646	1206.705
6.737	1188.892	7.646	1249.027	7.646	1171.571	7.198	1272.217
6.264	1265.694	7.198	1314.820	7.198	1233.157	6.737	1348.756
5.792	1359.080	6.737	1393.279	6.737	1305.055	6.264	1440.701
5.412	1447.469	6.264	1484.909	6.264	1391.315	5.792	1550.064

5.224	1497.074	5.792	1596.221	5.792	1494.352	5.607	1600.364
5.035	1550.602	5.607	1646.819	5.607	1541.622	5.412	1656.189
4.848	1610.078	5.412	1701.989	5.412	1592.798	5.224	1714.683
4.663	1674.596	5.224	1761.610	5.224	1646.748	5.035	1779.374
4.480	1745.059	5.035	1826.161	5.035	1707.636	4.848	1850.257
4.293	1819.696	4.848	1896.267	4.848	1772.951	4.663	1926.877
4.121	1899.269	4.663	1972.348	4.663	1842.757	4.480	2008.909
3.952	1989.408	4.480	2054.985	4.480	1920.600	4.293	2100.426
3.778	2089.570	4.293	2147.244	4.293	2005.670	4.121	2197.828
3.615	2192.638	4.121	2242.843	4.121	2094.962	3.952	2302.794
3.468	2300.827	3.952	2347.854	3.952	2194.193	3.778	2423.217
3.338	2403.129	3.778	2467.256	3.778	2305.985	3.615	2549.702
3.215	2509.517	3.615	2589.715	3.615	2422.383	3.468	2676.938
3.161	2559.750	3.468	2714.729	3.468	2539.748	3.338	2806.628
3.119	2604.934	3.338	2839.949	3.338	2655.207	3.215	2935.199
3.075	2649.713	3.215	2967.749	3.215	2774.146	3.161	2995.206
3.039	2688.740	3.161	3026.456	3.161	2834.741	3.119	3050.581
3.007	2724.107	3.119	3080.015	3.119	2885.909	3.075	3105.141
2.978	2756.457	3.075	3132.417	3.075	2936.433	3.039	3152.675
2.963	2774.115	3.039	3178.425	3.039	2980.635	3.007	3191.486
2.950	2789.171	3.007	3218.063	3.007	3014.490	2.978	3230.544
2.948	2791.231	2.978	3255.671	2.978	3050.777	2.963	3251.855
2.910	2833.158	2.963	3276.502	2.963	3070.889	2.950	3269.910
		2.950	3293.767	2.950	3088.326	2.948	3272.379
		2.948	3295.575	2.948	3091.472	2.910	3330.483
		2.910	3348.329	2.910	3138.148		

Table 8.6. Cernox temperature sensor calibration data II

$T_{PHP-I-H,COND}$		$T_{PHP-I-H,EVAP}$		$T_{PHP-II-H,COND}$		$T_{PHP-II-H,EVAP}$	
T / K	R / Ω	T / K	R / Ω	T / K	R / Ω	T / K	R / Ω
304.477	58.091	304.477	58.218	304.477	57.275	1.198	42246.342
298.609	59.123	298.609	59.236	298.609	58.274	1.309	33183.306
292.425	60.256	292.020	60.320	292.425	59.371	1.400	28006.146
290.148	60.610	290.148	60.648	290.148	59.729	1.597	20403.505
288.812	60.872	288.812	60.904	288.812	59.982	1.800	15693.825
286.057	61.423	286.057	61.441	286.057	60.514	2.001	12642.106
284.688	61.696	284.688	61.708	284.688	60.779	2.201	10527.642
282.673	62.098	282.673	62.100	282.673	61.166	2.397	9018.196
275.162	63.699	279.991	62.678	275.162	62.579	2.596	7856.865
268.374	65.165	275.162	63.687	268.374	63.993	2.800	6930.923

258.597	67.245	268.374	65.136	258.597	66.135	3.000	6212.727
245.637	70.704	258.597	67.198	245.637	69.606	3.202	5624.207
231.303	74.800	245.637	70.917	231.303	73.388	3.403	5142.684
215.592	79.734	231.303	74.833	215.592	78.237	3.603	4739.469
196.040	87.085	215.592	79.570	196.040	85.217	3.803	4396.782
180.444	94.059	196.040	86.847	180.444	91.914	4.003	4102.974
164.845	102.283	180.444	93.725	164.845	99.704	4.202	3847.662
150.975	110.789	164.845	101.831	150.975	107.838	4.601	3426.831
135.243	122.425	150.975	110.243	135.243	118.843	5.002	3094.033
123.526	132.788	135.243	121.714	123.526	128.688	5.500	2767.439
113.887	142.632	123.526	131.913	113.887	137.984	6.200	2419.675
105.844	152.191	113.887	141.593	105.844	147.053	7.005	2124.389
94.333	168.161	105.844	151.025	94.333	162.008	8.001	1854.807
82.984	187.703	94.333	166.661	82.984	180.151	9.004	1652.795
65.710	229.042	82.984	185.729	65.710	218.450	10.002	1496.730
56.407	259.451	65.710	225.416	56.407	246.091	11.001	1371.297
48.221	296.236	56.407	255.873	48.221	279.468	11.999	1268.070
41.128	336.589	48.221	289.811	41.128	316.061	12.998	1181.247
36.538	369.389	41.128	328.278	36.538	345.851	14.000	1106.978
32.319	406.216	36.538	359.268	32.319	378.539	14.998	1042.744
30.832	420.911	32.319	394.430	30.832	391.585	15.997	986.565
30.695	422.734	30.695	410.184	30.695	393.168	16.999	936.592
28.291	445.480	28.291	436.468	28.291	413.641	17.997	892.175
27.071	461.410	27.071	451.671	27.071	427.483	19.000	852.001
25.736	479.277	25.736	468.778	25.736	443.826	20.087	812.698
23.855	506.804	23.855	496.641	23.855	467.505	21.154	777.748
21.945	540.733	21.945	528.576	21.945	497.597	22.721	731.964
20.408	571.091	20.408	557.058	20.408	523.596	24.326	690.655
17.629	635.315	17.629	620.663	17.629	580.457	25.914	654.397
16.113	683.445	16.113	663.899	16.113	617.448	27.505	621.869
14.230	747.955	14.230	728.179	14.230	675.792	29.104	592.415
13.405	784.119	13.405	762.138	13.405	706.713	30.912	562.415
12.647	819.890	12.647	794.549	12.647	738.749	33.003	531.394
11.683	869.446	11.683	841.844	11.683	780.973	36.007	492.588
11.187	897.467	11.187	873.042	11.187	801.363	39.008	459.162
10.433	948.685	10.433	921.778	10.433	845.899	42.004	430.197
9.602	1014.424	9.602	984.300	9.602	900.678	44.995	404.747
7.648	1229.858	7.648	1182.888	7.648	1077.094	47.997	382.127
7.646	1230.128	7.646	1183.103	7.646	1077.302	49.992	368.414
7.198	1297.953	7.198	1246.760	7.198	1132.450	54.992	338.231
6.737	1377.373	6.737	1321.071	6.737	1196.583	59.983	312.709
6.264	1472.074	6.264	1409.314	6.264	1273.391	64.975	290.802

5.792	1587.135	5.792	1515.687	5.792	1364.523	69.960	271.825
5.607	1638.689	5.607	1563.884	5.607	1406.170	74.948	255.181
5.412	1695.627	5.412	1616.935	5.412	1451.580	79.944	240.437
5.224	1757.345	5.224	1675.317	5.224	1500.184	84.942	227.302
5.035	1826.485	5.035	1737.320	5.035	1552.743	89.937	215.517
4.848	1900.206	4.848	1805.228	4.848	1609.865	94.934	204.857
4.663	1979.065	4.663	1879.235	4.663	1672.241	99.929	195.242
4.480	2066.918	4.480	1960.236	4.480	1741.072	109.907	178.429
4.293	2164.681	4.293	2048.535	4.293	1815.651	119.914	164.215
4.121	2264.992	4.121	2141.646	4.121	1893.471	129.907	152.053
3.952	2379.880	3.952	2244.073	3.952	1978.559	139.891	141.549
3.778	2506.861	3.778	2361.011	3.778	2075.325	149.892	132.355
3.615	2643.915	3.615	2483.919	3.615	2175.239	159.892	124.261
3.468	2777.909	3.468	2605.056	3.468	2276.083	169.893	117.094
3.338	2915.487	3.338	2729.739	3.338	2376.509	179.884	110.706
3.215	3052.635	3.215	2853.278	3.215	2475.676	189.887	104.971
3.161	3121.073	3.161	2912.446	3.161	2525.424	199.888	99.801
3.119	3181.220	3.119	2965.885	3.119	2568.543	209.893	95.125
3.075	3240.649	3.075	3018.570	3.075	2610.783	219.894	90.882
3.039	3292.751	3.039	3064.867	3.039	2647.528	229.898	87.009
3.007	3340.746	3.007	3103.051	3.007	2680.190	239.900	83.469
2.978	3383.928	2.978	3140.993	2.978	2710.461	249.898	80.224
2.963	3407.821	2.963	3161.402	2.963	2726.433	259.908	77.238
2.950	3428.626	2.950	3179.185	2.950	2740.888	269.913	74.477
2.948	3432.474	2.948	3181.933	2.948	2743.114	279.912	71.934
2.910	3484.066	2.910	3231.884	2.910	2785.279	289.908	69.572
						299.913	67.375
						309.925	65.329
						314.952	64.357
						319.968	63.418
						325.962	62.339
						329.977	61.640

8.7 Nitrogen PHP thermal switch test data

Table 8.7. Nitrogen PHP thermal switch test results [Configuration = 2-circuit, Cryocooler-II-N Status = ON, $FR_{PHP-I-N}$= 0.520, $FR_{PHP-II-N}$ = 0.207]

$\dot{Q}_{CCP-N}$ [W]	$\dot{Q}_{PHP-I-N}$ [W]	$\dot{Q}_{PHP-II-N}$ [W]	$k_{PHP-I-N,EFF}$ [W/m-K]	$k_{PHP-II-N,EFF}$ [W/m-K]	$UA_{PHP-I-N,EFF}$ [W/K]	$UA_{PHP-II-N,EFF}$ [W/K]	$T_{PHP-I-N,COND}$ [K]	$T_{PHP-I-N,EVAP}$ [K]	$T_{PHP-II-N,COND}$ [K]	$T_{PHP-II-N,EVAP}$ [K]	$SR_{PHP-II-N}$
10.104	4.649	4.562	21000.030	42033.211	2.819	5.642	74.417	76.093	78.799	79.622	2410.234
12.037	5.870	5.448	24904.925	41986.956	3.343	5.635	75.295	77.072	79.747	80.723	2407.581
14.136	7.113	6.397	28074.112	44411.390	3.768	5.961	76.232	78.132	81.167	82.247	2546.601
16.208	8.365	7.428	32222.276	48647.640	4.325	6.529	77.215	79.155	82.886	84.029	2789.513

17.802	9.315	8.282	33811.794	51572.190	4.538	6.922	77.903	79.960	84.371	85.570	2957.210
10.108	4.372	4.678	16164.625	37986.029	2.170	5.098	69.381	71.450	74.127	75.106	2178.163
12.042	5.570	5.339	19992.161	38462.171	2.683	5.162	70.045	72.130	75.137	76.192	2205.466
14.232	6.912	6.417	20414.153	45177.343	2.740	6.064	71.028	73.559	76.897	77.984	2590.522
16.018	8.016	7.255	20845.376	42773.795	2.798	5.741	71.660	74.531	78.211	79.483	2452.700
18.010	9.163	8.181	20916.568	45815.354	2.807	6.149	72.491	75.758	79.654	80.989	2627.106

Table 8.8. Nitrogen PHP thermal switch test results [Configuration = 2-circuit, Cryocooler-II-N Status = ON, $FR_{PHP\text{-}I\text{-}N}$= 0.260, $FR_{PHP\text{-}II\text{-}N}$ = 0.259]

$\dot{Q}_{CCP-N}$ [W]	$\dot{Q}_{PHP-I-N}$ [W]	$\dot{Q}_{PHP-II-N}$ [W]	$k_{PHP-I-N,EFF}$ [W/m-K]	$k_{PHP-II-N,EFF}$ [W/m-K]	$UA_{PHP-I-N,EFF}$ [W/K]	$UA_{PHP-II-N,EFF}$ [W/K]	$T_{PHP-I-N,COND}$ [K]	$T_{PHP-I-N,EVAP}$ [K]	$T_{PHP-II-N,COND}$ [K]	$T_{PHP-II-N,EVAP}$ [K]	$SR_{PHP-II-N}$
9.970	6.500	2.716	32690.572	12179.931	4.388	1.635	75.617	77.207	75.559	78.047	698.411
11.890	8.049	3.161	41947.360	12066.578	5.630	1.620	76.889	78.326	76.358	79.801	691.912
14.159	9.668	4.048	46709.941	18178.879	6.269	2.440	78.095	79.639	77.793	80.699	1042.398
16.038	10.776	4.844	47545.892	24897.433	6.381	3.342	78.924	80.615	79.082	81.342	1427.648
17.828	11.887	6.133	48436.747	35342.702	6.501	4.744	79.753	81.585	81.293	82.655	2026.592
19.904	9.867	9.966	44360.399	52939.623	5.954	7.105	78.279	79.938	87.907	89.311	3035.620
11.879	5.128	5.723	28017.911	37191.399	3.760	4.992	69.519	70.907	76.613	77.799	2132.598
13.965	7.252	7.059	35876.048	40208.409	4.815	5.397	70.300	71.833	78.611	79.948	2305.597
16.024	7.342	7.954	33196.500	44088.174	4.456	5.917	71.138	72.819	80.450	81.812	2528.068
18.017	8.495	8.907	36004.425	46513.128	4.832	6.243	71.998	73.775	82.086	83.524	2667.117
19.891	9.615	9.730	39298.455	49257.208	5.275	6.611	72.839	74.668	83.441	84.921	2824.466
13.968	5.629	6.312	24738.462	36659.848	3.320	4.920	64.982	66.712	73.308	74.630	2102.119
15.834	6.653	7.290	27311.711	35917.438	3.666	4.821	65.666	67.502	75.110	76.562	2059.548
17.818	7.685	8.208	30553.180	38837.743	4.101	5.213	66.440	68.335	76.775	78.361	2227.002
19.699	8.688	9.036	33423.467	41193.090	4.486	5.529	67.169	69.124	78.288	79.940	2362.060

Table 8.9. Nitrogen PHP thermal switch test results [Configuration = 2-circuit, Cryocooler-II-N Status = ON, $FR_{PHP\text{-}I\text{-}N}$= 0.302, $FR_{PHP\text{-}II\text{-}N}$ = 0.303]

$\dot{Q}_{CCP-N}$ [W]	$\dot{Q}_{PHP-I-N}$ [W]	$\dot{Q}_{PHP-II-N}$ [W]	$k_{PHP-I-N,EFF}$ [W/m-K]	$k_{PHP-II-N,EFF}$ [W/m-K]	$UA_{PHP-I-N,EFF}$ [W/K]	$UA_{PHP-II-N,EFF}$ [W/K]	$T_{PHP-I-N,COND}$ [K]	$T_{PHP-I-N,EVAP}$ [K]	$T_{PHP-II-N,COND}$ [K]	$T_{PHP-II-N,EVAP}$ [K]	$SR_{PHP-II-N}$
6.074	2.571	2.115	17462.070	36755.134	2.344	4.933	72.875	74.114	74.587	75.064	2107.582
9.955	5.665	4.007	35742.445	45322.309	4.797	6.083	75.096	76.301	77.196	77.923	2598.834
12.043	6.779	4.498	37049.683	41808.075	4.973	5.611	75.956	77.342	77.907	78.803	2397.324
13.959	8.062	5.286	39771.003	44246.484	5.338	5.939	76.699	78.230	78.924	79.851	2537.145

Table 8.10. Nitrogen PHP thermal switch test results [Configuration = 2-circuit, Cryocooler-II-N Status = ON, $FR_{PHP\text{-}I\text{-}N}$= 0.415, $FR_{PHP\text{-}II\text{-}N}$ = 0.415]

$\dot{Q}_{CCP-N}$ [W]	$\dot{Q}_{PHP-I-N}$ [W]	$\dot{Q}_{PHP-II-N}$ [W]	$k_{PHP-I-N,EFF}$ [W/m-K]	$k_{PHP-II-N,EFF}$ [W/m-K]	$UA_{PHP-I-N,EFF}$ [W/K]	$UA_{PHP-II-N,EFF}$ [W/K]	$T_{PHP-I-N,COND}$ [K]	$T_{PHP-I-N,EVAP}$ [K]	$T_{PHP-II-N,COND}$ [K]	$T_{PHP-II-N,EVAP}$ [K]	$SR_{PHP-II-N}$
3.967	1.592	0.985	10727.640	9522.612	1.440	1.278	72.115	73.284	72.766	73.611	546.038
8.067	3.622	3.584	19842.382	27351.594	2.663	3.671	73.628	75.014	76.629	77.631	1568.372
9.953	4.725	4.235	23184.053	26691.079	3.112	3.582	74.415	75.972	77.692	79.095	1530.498
12.893	6.493	5.720	29494.696	35132.882	3.959	4.715	75.776	77.431	79.762	80.989	2014.561
14.141	8.235	5.343	34909.896	35890.712	4.686	4.817	77.037	78.810	79.062	80.184	2058.015
16.214	9.713	6.260	40078.313	43650.303	5.379	5.859	78.145	79.953	80.325	81.394	2502.960
18.214	9.896	8.097	40891.692	43543.015	5.488	5.844	78.325	80.130	82.984	84.371	2496.808

Table 8.11. Nitrogen PHP thermal switch test results [Configuration = 2-circuit, Cryocooler-II-N Status = ON, $FR_{PHP\text{-}I\text{-}N}$= 0.520, $FR_{PHP\text{-}II\text{-}N}$ = 0.520]

$\dot{Q}_{CCP-N}$ [W]	$\dot{Q}_{PHP-I-N}$ [W]	$\dot{Q}_{PHP-II-N}$ [W]	$k_{PHP-I-N,EFF}$ [W/m-K]	$k_{PHP-II-N,EFF}$ [W/m-K]	$UA_{PHP-I-N,EFF}$ [W/K]	$UA_{PHP-II-N,EFF}$ [W/K]	$T_{PHP-I-N,COND}$ [K]	$T_{PHP-I-N,EVAP}$ [K]	$T_{PHP-II-N,COND}$ [K]	$T_{PHP-II-N,EVAP}$ [K]	$SR_{PHP-II-N}$
10.030	5.833	3.914	24492.436	23872.011	3.287	3.204	75.166	76.956	77.951	79.363	1368.849
12.040	7.007	4.634	28263.161	30013.173	3.793	4.028	76.080	77.935	79.016	80.228	1720.991
14.140	8.560	5.506	32905.881	29702.742	4.417	3.987	77.259	79.204	80.301	81.686	1703.190
16.019	9.647	5.831	35252.631	31107.886	4.732	4.175	78.110	80.154	80.772	82.171	1783.763

18.006	9.694	8.090	36198.956	38281.913	4.859	5.138	78.205	80.203	84.515	86.091	2195.130
8.068	3.431	3.403	15953.997	23434.703	2.141	3.145	68.347	70.038	72.537	73.652	1343.773
10.108	4.594	4.414	13166.814	20267.430	1.767	2.720	68.992	72.153	74.148	75.909	1162.158
12.041	5.911	5.449	19317.825	30567.122	2.593	4.103	70.166	72.476	76.151	77.511	1752.755
13.959	6.931	6.202	19952.372	31122.008	2.678	4.177	70.781	73.375	77.146	78.650	1784.572
16.017	8.323	7.159	20834.043	30618.542	2.796	4.110	71.831	74.812	78.795	80.540	1755.703
18.011	9.666	8.080	29923.556	34361.157	4.016	4.612	72.882	75.299	80.315	82.071	1970.309
20.336	10.366	9.433	23812.163	36330.948	3.196	4.876	73.390	76.672	82.512	84.447	2083.259

Table 8.12. Nitrogen PHP thermal switch test results [Configuration = 2-circuit, Cryocooler-II-N Status = OFF, $FR_{PHP\text{-}I\text{-}N}$ = 0.520, $FR_{PHP\text{-}II\text{-}N}$ = 0.207]

$\dot{Q}_{CCP-N}$ [W]	$\dot{Q}_{PHP-I-N}$ [W]	$\dot{Q}_{PHP-II-N}$ [W]	$k_{PHP-I-N,EFF}$ [W/m-K]	$k_{PHP-II-N,EFF}$ [W/m-K]	$UA_{PHP-I-N,EFF}$ [W/K]	$UA_{PHP-II-N,EFF}$ [W/K]	$T_{PHP-I-N,COND}$ [K]	$T_{PHP-I-N,EVAP}$ [K]	$T_{PHP-II-N,COND}$ [K]	$T_{PHP-II-N,EVAP}$ [K]	$SR_{PHP-II-N}$
0.987	1.227	-0.239	9860.495	9.074	1.323	0.00122	71.880	73.571	281.721	84.293	
1.981	2.566	-0.585	16132.700	22.488	2.165	0.00302	72.841	74.099	283.304	89.405	
2.970	3.875	-0.905	19083.623	35.106	2.561	0.00471	73.845	75.398	284.805	92.654	
4.010	4.129	-0.119	20437.325	4.625	2.743	0.00062	73.901	75.442	286.323	93.643	
0.000	0.831	-0.831	5558.449	30.012	0.746	0.00403	66.561	68.675	287.190	79.634	N/A
1.036	2.528	-1.492	14497.989	55.397	1.946	0.00744	67.687	69.062	287.694	86.933	
1.981	3.216	-1.235	10295.998	46.240	1.382	0.00621	68.106	70.507	288.538	89.491	
2.970	3.658	-0.688	11994.711	25.878	1.610	0.00347	68.404	70.764	287.773	89.787	
4.012	4.341	-0.329	15584.337	12.414	2.092	0.00167	68.906	71.121	288.571	91.075	

Table 8.13. Nitrogen PHP thermal switch test results [Configuration = 2-circuit, Cryocooler-II-N Status = OFF, $FR_{PHP\text{-}I\text{-}N}$ = 0.260, $FR_{PHP\text{-}II\text{-}N}$ = 0.259]

$\dot{Q}_{CCP-N}$ [W]	$\dot{Q}_{PHP-I-N}$ [W]	$\dot{Q}_{PHP-II-N}$ [W]	$k_{PHP-I-N,EFF}$ [W/m-K]	$k_{PHP-II-N,EFF}$ [W/m-K]	$UA_{PHP-I-N,EFF}$ [W/K]	$UA_{PHP-II-N,EFF}$ [W/K]	$T_{PHP-I-N,COND}$ [K]	$T_{PHP-I-N,EVAP}$ [K]	$T_{PHP-II-N,COND}$ [K]	$T_{PHP-II-N,EVAP}$ [K]	$SR_{PHP-II-N}$
4.054	4.685	-0.203	36886.644	8.352	4.951	0.00112	74.527	75.601	288.379	107.339	
5.882	7.050	-0.200	44719.328	8.854	6.002	0.00119	76.256	77.471	288.412	120.100	
7.982	8.601	-0.246	48936.196	11.811	6.568	0.00159	77.478	78.792	277.330	122.390	
9.928	11.105	-0.292	52120.387	14.559	6.995	0.00195	79.391	80.981	284.625	135.105	N/A
12.007	13.440	-0.214	54293.115	11.153	7.287	0.00150	81.196	83.043	287.337	144.526	
14.102	15.705	-0.185	57757.370	10.180	7.752	0.00137	82.991	85.019	288.142	152.916	
15.979	17.633	-0.170	57337.757	9.886	7.696	0.00133	84.703	87.000	288.412	159.990	

Table 8.14. Nitrogen PHP thermal switch test results [Configuration = 2-circuit, Cryocooler-II-N Status = OFF, $FR_{PHP\text{-}I\text{-}N}$ = 0.302, $FR_{PHP\text{-}II\text{-}N}$ = 0.303]

$\dot{Q}_{CCP-N}$ [W]	$\dot{Q}_{PHP-I-N}$ [W]	$\dot{Q}_{PHP-II-N}$ [W]	$k_{PHP-I-N,EFF}$ [W/m-K]	$k_{PHP-II-N,EFF}$ [W/m-K]	$UA_{PHP-I-N,EFF}$ [W/K]	$UA_{PHP-II-N,EFF}$ [W/K]	$T_{PHP-I-N,COND}$ [K]	$T_{PHP-I-N,EVAP}$ [K]	$T_{PHP-II-N,COND}$ [K]	$T_{PHP-II-N,EVAP}$ [K]	$SR_{PHP-II-N}$
1.009	1.410	-0.769	17687.366	27.204	2.374	0.00365	72.107	72.717	291.385	80.871	
2.046	2.612	-0.267	20812.658	9.614	2.793	0.00129	72.980	74.131	291.786	84.712	N/A
3.051	3.556	-0.224	25080.334	8.201	3.366	0.00110	73.636	74.765	290.629	86.868	

Table 8.15. Nitrogen PHP thermal switch test results [Configuration = 2-circuit, Cryocooler-II-N Status = OFF, $FR_{PHP\text{-}I\text{-}N}$ = 0.415, $FR_{PHP\text{-}II\text{-}N}$ = 0.415]

$\dot{Q}_{CCP-N}$ [W]	$\dot{Q}_{PHP-I-N}$ [W]	$\dot{Q}_{PHP-II-N}$ [W]	$k_{PHP-I-N,EFF}$ [W/m-K]	$k_{PHP-II-N,EFF}$ [W/m-K]	$UA_{PHP-I-N,EFF}$ [W/K]	$UA_{PHP-II-N,EFF}$ [W/K]	$T_{PHP-I-N,COND}$ [K]	$T_{PHP-I-N,EVAP}$ [K]	$T_{PHP-II-N,COND}$ [K]	$T_{PHP-II-N,EVAP}$ [K]	$SR_{PHP-II-N}$
0.984	1.370	-0.451	12653.886	16.338	1.698	0.00219	72.096	73.190	289.405	83.558	
1.977	2.590	-0.413	20820.930	15.183	2.795	0.00204	73.000	74.086	290.122	87.478	
2.966	3.616	-0.357	25303.008	13.328	3.396	0.00179	73.759	74.870	290.468	90.830	N/A
1.978	3.105	-0.904	14719.145	33.962	1.976	0.00456	68.134	69.924	286.206	87.918	
2.966	3.876	-0.869	17194.842	32.669	2.308	0.00438	68.773	70.569	288.639	90.521	

Table 8.16. Nitrogen PHP thermal switch test results [Configuration = 2-circuit, Cryocooler-II-N Status = OFF, $FR_{PHP\text{-}I\text{-}N}$ = 0.520, $FR_{PHP\text{-}II\text{-}N}$ = 0.520]

$\dot{Q}_{CCP-N}$	$\dot{Q}_{PHP-I-N}$	$\dot{Q}_{PHP-II-N}$	$k_{PHP-I-N,EFF}$	$k_{PHP-II-N,EFF}$	$UA_{PHP-I-N,EFF}$	$UA_{PHP-II-N,EFF}$	$T_{PHP-I-N,COND}$	$T_{PHP-I-N,EVAP}$	$T_{PHP-II-N,COND}$	$T_{PHP-II-N,EVAP}$	$SR_{PHP-II-N}$

[W]	[W]	[W]	[W/m-K]	[W/m-K]	[W/K]	[W/K]	[K]	[K]	[K]	[K]	
0.985	1.671	-0.214	12835.904	7.754	1.723	0.00104	72.248	73.917	290.019	84.139	
1.977	2.759	-0.617	16407.274	22.316	2.202	0.00300	72.845	74.111	296.047	90.110	
4.053	4.944	-0.661	23747.912	25.173	3.187	0.00338	74.499	76.070	294.603	98.896	
6.001	6.728	-0.764	30805.897	30.541	4.135	0.00410	76.006	77.642	291.460	104.970	N/A
7.980	8.828	-0.202	24087.891	8.579	3.233	0.00115	72.280	75.043	289.743	114.462	
6.119	7.334	-0.199	20809.207	8.234	2.793	0.00111	71.154	73.789	289.587	109.370	
4.054	4.945	-0.210	19797.609	8.167	2.657	0.00110	69.327	71.316	289.445	97.930	

Table 8.17. Nitrogen PHP thermal switch test results [Configuration = 1-circuit, Cryocooler-II-N Status = ON, $FR_{PHP\text{-}I\text{-}N}$ = 0.507, $FR_{PHP\text{-}II\text{-}N}$ = 0.507]

$\dot{Q}_{CCP-N}$ [W]	$\dot{Q}_{PHP-I-N}$ [W]	$\dot{Q}_{PHP-II-N}$ [W]	$k_{PHP-I-N,EFF}$ [W/m-K]	$k_{PHP-II-N,EFF}$ [W/m-K]	$UA_{PHP-I-N,EFF}$ [W/K]	$UA_{PHP-II-N,EFF}$ [W/K]	$T_{PHP-I-N,COND}$ [K]	$T_{PHP-I-N,EVAP}$ [K]	$T_{PHP-II-N,COND}$ [K]	$T_{PHP-II-N,EVAP}$ [K]	$SR_{PHP-II-N}$
9.982	3.928	5.029	25405.654	24518.048	3.410	3.291	78.169	79.335	78.020	79.570	971.598
9.982	3.867	4.848	36658.985	9964.651	4.920	1.337	79.214	80.006	76.845	80.481	394.878
19.957	9.843	9.822	31594.623	38794.624	4.241	5.207	82.768	85.090	83.233	85.121	1537.348
19.959	10.426	9.476	14502.532	47121.993	1.946	6.325	78.803	84.161	82.738	84.237	1867.343
13.992	7.015	6.783	7165.993	49164.187	0.962	6.599	76.279	83.583	82.574	83.604	1948.271
13.992	6.471	6.863	12931.132	48505.494	1.736	6.510	80.219	83.952	82.733	83.789	1922.169
16.056	7.622	7.821	13109.477	49649.754	1.760	6.664	81.217	85.550	84.185	85.359	1967.513
16.057	7.696	8.062	18544.210	46742.550	2.489	6.274	81.220	84.314	82.810	84.098	1852.307
17.851	8.889	8.659	21816.471	46989.350	2.928	6.307	82.075	85.113	83.716	85.090	1862.087
9.982	3.830	4.850	36540.232	10052.006	4.904	1.349	79.204	79.991	76.844	80.453	398.339
19.957	9.849	9.794	31896.121	38678.717	4.281	5.191	82.779	85.080	83.224	85.111	1532.755
19.958	10.509	9.475	14880.692	47104.254	1.997	6.322	78.894	84.159	82.735	84.235	1866.640
19.958	10.106	9.560	20699.063	46133.003	2.778	6.192	80.851	84.490	82.856	84.400	1828.152
17.858	8.871	8.704	20929.639	45723.282	2.809	6.137	79.909	83.068	81.560	82.980	1811.916
16.063	7.384	7.890	40979.449	19036.568	5.500	2.555	80.839	82.184	79.412	82.507	754.378
9.983	4.066	4.676	38790.688	5516.712	5.206	0.740	78.314	79.096	73.984	80.306	218.615

Table 8.18. Nitrogen PHP thermal switch test results [Configuration = 1-circuit, Cryocooler-II-N Status = ON, $FR_{PHP\text{-}I\text{-}N}$ = 0.547, $FR_{PHP\text{-}II\text{-}N}$ = 0.547]

$\dot{Q}_{CCP-N}$ [W]	$\dot{Q}_{PHP-I-N}$ [W]	$\dot{Q}_{PHP-II-N}$ [W]	$k_{PHP-I-N,EFF}$ [W/m-K]	$k_{PHP-II-N,EFF}$ [W/m-K]	$UA_{PHP-I-N,EFF}$ [W/K]	$UA_{PHP-II-N,EFF}$ [W/K]	$T_{PHP-I-N,COND}$ [K]	$T_{PHP-I-N,EVAP}$ [K]	$T_{PHP-II-N,COND}$ [K]	$T_{PHP-II-N,EVAP}$ [K]	$SR_{PHP-II-N}$
12.091	5.394	5.841	9582.840	47355.152	1.286	6.356	75.119	79.321	78.290	79.217	1876.583
14.014	6.493	6.637	9406.732	36628.405	1.263	4.916	75.969	81.132	79.774	81.129	1451.505
16.081	7.924	7.557	10090.310	41769.154	1.354	5.606	77.177	83.033	81.706	83.057	1655.222
18.077	9.030	8.618	8536.717	48402.236	1.146	6.496	78.108	85.998	84.255	85.582	1918.077
17.878	8.777	7.934	16781.354	41650.521	2.252	5.590	77.757	81.657	79.929	81.351	1650.521
17.880	8.788	7.939	16819.571	42070.675	2.257	5.647	77.760	81.661	79.947	81.355	1667.171
16.085	7.667	7.199	19781.322	39057.138	2.655	5.242	76.935	79.843	78.308	79.686	1547.751
13.838	6.265	6.193	26071.657	26457.280	3.499	3.551	75.756	77.561	75.895	77.668	1048.445
14.018	6.241	6.193	35103.891	17318.363	4.712	2.324	75.763	77.098	74.887	77.674	686.290
12.095	5.154	5.361	36816.786	11865.578	4.941	1.593	74.921	75.979	73.174	76.664	470.207

Table 8.19. Nitrogen PHP thermal switch test results [Configuration = 1-circuit, Cryocooler-II-N Status = ON, $FR_{PHP\text{-}I\text{-}N}$ = 0.596, $FR_{PHP\text{-}II\text{-}N}$ = 0.596]

$\dot{Q}_{CCP-N}$ [W]	$\dot{Q}_{PHP-I-N}$ [W]	$\dot{Q}_{PHP-II-N}$ [W]	$k_{PHP-I-N,EFF}$ [W/m-K]	$k_{PHP-II-N,EFF}$ [W/m-K]	$UA_{PHP-I-N,EFF}$ [W/K]	$UA_{PHP-II-N,EFF}$ [W/K]	$T_{PHP-I-N,COND}$ [K]	$T_{PHP-I-N,EVAP}$ [K]	$T_{PHP-II-N,COND}$ [K]	$T_{PHP-II-N,EVAP}$ [K]	$SR_{PHP-II-N}$
10.141	4.042	5.565	4201.727	51590.866	0.564	6.924	74.007	81.179	79.881	80.730	2044.435
19.966	10.545	9.416	10624.092	41587.039	1.426	5.582	79.082	86.478	84.832	86.501	1648.005
19.962	10.583	9.538	7131.367	42056.851	0.957	5.645	79.137	90.195	88.532	90.241	1666.623
14.002	6.272	6.871	27433.732	22834.835	3.682	3.065	80.075	81.792	79.822	82.085	904.895
14.004	6.648	6.763	10077.368	40261.473	1.353	5.404	76.156	81.097	79.656	80.919	1595.476
14.000	6.748	6.731	6034.657	48755.868	0.810	6.544	76.198	84.543	83.314	84.370	1932.090
15.874	7.566	7.862	8318.419	46343.999	1.116	6.220	76.641	83.424	81.721	83.003	1836.513

18.068	9.212	8.589	10323.304	45808.019	1.386	6.148	78.092	84.743	83.147	84.559	1815.273
12.077	5.178	6.084	4440.253	44673.287	0.596	5.996	74.829	83.522	82.087	83.109	1770.306
12.080	5.115	5.937	26446.598	16538.849	3.550	2.220	79.144	80.527	78.330	81.014	655.399
12.078	5.332	6.033	9804.160	39875.384	1.316	5.352	79.315	83.373	82.072	83.231	1580.176
15.874	7.675	7.872	6507.147	44038.811	0.873	5.911	76.998	85.799	84.338	85.688	1745.164

Table 8.20. Nitrogen PHP thermal switch test results [Configuration = 1-circuit, Cryocooler-II-N Status = ON, $FR_{PHP\text{-}I\text{-}N}$= 0.705, $FR_{PHP\text{-}II\text{-}N}$ = 0.705]

$\dot{Q}_{CCP-N}$ [W]	$\dot{Q}_{PHP-I-N}$ [W]	$\dot{Q}_{PHP-II-N}$ [W]	$k_{PHP-I-N,EFF}$ [W/m-K]	$k_{PHP-II-N,EFF}$ [W/m-K]	$UA_{PHP-I-N,EFF}$ [W/K]	$UA_{PHP-II-N,EFF}$ [W/K]	$T_{PHP-I-N,COND}$ [K]	$T_{PHP-I-N,EVAP}$ [K]	$T_{PHP-II-N,COND}$ [K]	$T_{PHP-II-N,EVAP}$ [K]	$SR_{PHP-II-N}$
9.995	3.939	4.053	22902.423	3202.099	3.074	0.430	74.186	75.468	66.833	76.303	126.892
9.996	3.728	4.680	17932.819	7933.926	2.407	1.065	73.996	75.548	71.735	76.138	314.404
9.994	3.179	4.386	6592.030	21059.856	0.885	2.827	73.577	77.182	75.404	76.960	834.557
11.922	5.169	5.087	22619.815	4266.325	3.036	0.573	75.075	76.781	68.571	77.513	169.065
11.922	4.834	5.634	19814.741	11406.921	2.659	1.531	74.905	76.734	73.289	77.047	452.032
11.919	4.700	6.086	6460.177	25229.175	0.867	3.386	74.822	80.249	78.362	80.163	999.778
11.919	4.492	6.223	3014.268	28705.855	0.405	3.853	69.380	80.796	78.614	80.235	1137.551
11.923	4.769	5.810	5383.960	23936.373	0.723	3.213	69.472	76.108	73.780	75.598	948.547
14.012	6.451	5.638	23489.588	4453.876	3.153	0.598	76.163	78.211	69.760	79.215	176.498
14.013	6.382	6.249	22189.979	10313.343	2.978	1.384	76.074	78.221	74.612	79.133	408.696
14.010	6.119	7.109	7045.387	26109.691	0.946	3.504	75.849	82.398	80.265	82.311	1034.671
16.074	6.892	8.367	5509.763	27226.307	0.740	3.654	76.404	85.767	82.809	85.104	1078.920
16.083	7.323	6.749	24741.079	8148.545	3.321	1.094	76.819	79.027	72.919	79.117	322.909
16.080	7.397	7.833	12555.446	22469.697	1.685	3.016	76.798	81.208	78.453	81.057	890.426
18.080	8.402	7.561	23236.411	10184.293	3.119	1.367	77.703	80.399	74.740	80.279	403.582
18.078	8.470	8.334	14102.084	20195.276	1.893	2.711	77.646	82.128	79.284	82.364	800.295
18.074	8.292	9.041	6451.655	25660.062	0.866	3.444	77.404	86.997	84.304	86.932	1016.853
19.976	9.690	9.447	10081.632	24661.771	1.353	3.310	78.492	85.657	82.758	85.613	977.293

Table 8.21. Nitrogen PHP thermal switch test results [Configuration = 1-circuit, Cryocooler-II-N Status = OFF, $FR_{PHP\text{-}I\text{-}N}$= 0.507, $FR_{PHP\text{-}II\text{-}N}$ = 0.507]

$\dot{Q}_{CCP-N}$ [W]	$\dot{Q}_{PHP-I-N}$ [W]	$\dot{Q}_{PHP-II-N}$ [W]	$k_{PHP-I-N,EFF}$ [W/m-K]	$k_{PHP-II-N,EFF}$ [W/m-K]	$UA_{PHP-I-N,EFF}$ [W/K]	$UA_{PHP-II-N,EFF}$ [W/K]	$T_{PHP-I-N,COND}$ [K]	$T_{PHP-I-N,EVAP}$ [K]	$T_{PHP-II-N,COND}$ [K]	$T_{PHP-II-N,EVAP}$ [K]	$SR_{PHP-II-N}$
6.028	6.764	-0.378	14904.522	15.646	2.000	0.00210	76.146	79.537	269.790	89.820	N/A
7.018	7.985	-0.330	13377.166	13.535	1.795	0.00182	77.065	81.536	274.514	93.124	
9.065	11.271	-0.568	4257.184	26.269	0.571	0.00353	79.849	99.600	275.369	114.368	
4.072	5.074	-1.338	11697.773	51.053	1.570	0.00685	74.649	77.896	281.642	86.330	
5.110	5.883	-0.556	10681.251	21.304	1.434	0.00286	75.665	79.785	284.259	89.660	
2.895	3.613	-0.521	10542.849	19.329	1.415	0.00259	73.859	76.425	284.672	83.687	
1.986	2.352	-0.509	7772.680	18.618	1.043	0.00250	73.015	75.286	284.967	81.124	
1.140	1.423	-0.494	5726.772	17.823	0.769	0.00239	72.290	74.153	285.250	78.766	

Table 8.22. Nitrogen PHP thermal switch test results [Configuration = 1-circuit, Cryocooler-II-N Status = OFF, $FR_{PHP\text{-}I\text{-}N}$= 0.547, $FR_{PHP\text{-}II\text{-}N}$ = 0.547]

$\dot{Q}_{CCP-N}$ [W]	$\dot{Q}_{PHP-I-N}$ [W]	$\dot{Q}_{PHP-II-N}$ [W]	$k_{PHP-I-N,EFF}$ [W/m-K]	$k_{PHP-II-N,EFF}$ [W/m-K]	$UA_{PHP-I-N,EFF}$ [W/K]	$UA_{PHP-II-N,EFF}$ [W/K]	$T_{PHP-I-N,COND}$ [K]	$T_{PHP-I-N,EVAP}$ [K]	$T_{PHP-II-N,COND}$ [K]	$T_{PHP-II-N,EVAP}$ [K]	$SR_{PHP-II-N}$
1.987	2.596	-0.703	9767.273	25.831	1.311	0.00347	73.075	75.105	284.195	81.548	N/A
3.065	3.883	-0.722	13273.272	26.966	1.782	0.00362	74.070	76.272	283.952	84.454	
4.024	5.023	-0.767	15183.145	29.215	2.038	0.00392	75.040	77.520	282.667	87.148	
5.004	5.882	-0.745	14185.953	28.621	1.904	0.00384	75.757	78.865	283.557	89.493	
7.020	8.477	-0.777	13173.107	30.816	1.768	0.00414	77.631	82.501	283.848	95.904	

Table 8.23. Nitrogen PHP thermal switch test results [Configuration = 1-circuit, Cryocooler-II-N Status = OFF, $FR_{PHP\text{-}I\text{-}N}$= 0.596, $FR_{PHP\text{-}II\text{-}N}$ = 0.596]

$\dot{Q}_{CCP-N}$ [W]	$\dot{Q}_{PHP-I-N}$ [W]	$\dot{Q}_{PHP-II-N}$ [W]	$k_{PHP-I-N,EFF}$ [W/m-K]	$k_{PHP-II-N,EFF}$ [W/m-K]	$UA_{PHP-I-N,EFF}$ [W/K]	$UA_{PHP-II-N,EFF}$ [W/K]	$T_{PHP-I-N,COND}$ [K]	$T_{PHP-I-N,EVAP}$ [K]	$T_{PHP-II-N,COND}$ [K]	$T_{PHP-II-N,EVAP}$ [K]	$SR_{PHP-II-N}$

7.022	7.975	-0.690	11668.770	26.414	1.566	0.00355	72.193	77.304	285.020	90.501	N/A
7.952	8.220	-0.651	13885.442	24.758	1.864	0.00332	72.133	76.549	285.324	89.534	
6.021	6.740	-0.661	3407.690	29.559	0.457	0.00397	76.281	91.389	268.178	101.624	
3.066	4.150	-0.668	8147.362	24.518	1.094	0.00329	69.295	73.202	284.267	81.150	
5.006	5.400	-0.826	9434.058	31.875	1.266	0.00428	70.189	74.479	277.463	84.316	
3.064	3.734	-0.706	9682.911	26.439	1.300	0.00355	74.034	76.929	283.284	84.443	
5.001	5.784	-0.788	10112.988	30.720	1.357	0.00412	75.619	79.915	280.873	89.846	
7.010	8.569	-0.981	4696.829	42.132	0.630	0.00565	77.696	91.409	277.037	103.504	

Table 8.24. Nitrogen PHP thermal switch test results [Configuration = 1-circuit, Cryocooler-II-N Status = OFF, $FR_{PHP\text{-}I\text{-}N} = 0.705$, $FR_{PHP\text{-}II\text{-}N} = 0.705$]

$\dot{Q}_{CCP-N}$ [W]	$\dot{Q}_{PHP-I-N}$ [W]	$\dot{Q}_{PHP-II-N}$ [W]	$k_{PHP-I-N,EFF}$ [W/m-K]	$k_{PHP-II-N,EFF}$ [W/m-K]	$UA_{PHP-I-N,EFF}$ [W/K]	$UA_{PHP-II-N,EFF}$ [W/K]	$T_{PHP-I-N,COND}$ [K]	$T_{PHP-I-N,EVAP}$ [K]	$T_{PHP-II-N,COND}$ [K]	$T_{PHP-II-N,EVAP}$ [K]	$SR_{PHP-II-N}$
5.002	5.987	-0.204	11060.813	8.034	1.485	0.00108	75.880	79.944	280.517	91.801	N/A
4.073	4.884	-0.876	9885.860	33.741	1.327	0.00453	74.891	78.610	282.422	89.025	
1.987	2.533	-0.767	8555.965	28.085	1.148	0.00377	73.079	75.322	285.966	82.355	
1.090	1.536	-0.740	6350.866	26.598	0.852	0.00357	72.321	74.206	286.835	79.604	
5.973	6.900	-0.566	10564.338	22.120	1.418	0.00297	71.415	76.301	280.563	89.979	
5.007	5.732	-0.540	10982.846	20.629	1.474	0.00277	70.464	74.405	281.583	86.493	
4.025	4.703	-0.530	10061.312	19.917	1.350	0.00267	69.539	73.032	282.078	83.631	
1.988	2.291	-0.508	5579.013	18.494	0.749	0.00248	67.949	71.035	282.457	78.043	
1.040	1.266	-0.500	3376.764	17.989	0.453	0.00241	67.203	70.073	282.566	75.409	

8.8 Helium PHP thermal switch test data

Table 8.25. Helium PHP thermal switch test results [Configuration = 2-circuit, Cryocooler-II-H Status = ON, $FR_{PHP\text{-}I\text{-}H} = 0.203$, $FR_{PHP\text{-}II\text{-}H} = 0.187$]

$\dot{Q}_{CCP-H}$ [W]	$\dot{Q}_{PHP-I-H}$ [W]	$\dot{Q}_{PHP-II-H}$ [W]	$k_{PHP-I-H,EFF}$ [W/m-K]	$k_{PHP-II-H,EFF}$ [W/m-K]	$UA_{PHP-I-H,EFF}$ [W/K]	$UA_{PHP-II-H,EFF}$ [W/K]	$T_{PHP-I-H,COND}$ [K]	$T_{PHP-I-H,EVAP}$ [K]	$T_{PHP-II-H,COND}$ [K]	$T_{PHP-II-H,EVAP}$ [K]	$SR_{PHP-II-H}$
0.000	0.028	0.055	164580.400	93150.043	2.434	1.377	3.081	3.064	3.011	3.068	N/A
0.049	0.028	0.057	51850.581	63479.560	0.767	0.939	3.113	3.155	3.107	3.168	
0.098	0.102	0.071	68293.041	47711.899	1.010	0.706	3.156	3.256	3.175	3.276	
0.148	0.058	0.068	26100.578	32128.307	0.386	0.475	3.220	3.374	3.250	3.392	
0.197	0.121	0.106	36767.223	37765.487	0.544	0.558	3.272	3.494	3.333	3.523	
0.246	0.117	0.150	19637.047	38840.483	0.290	0.574	3.308	3.705	3.440	3.701	
0.295	0.110	0.183	15122.447	32539.476	0.224	0.481	3.367	3.868	3.506	3.890	
0.394	0.214	0.250	17212.551	26388.613	0.255	0.390	3.442	4.291	3.665	4.309	
0.444	0.204	0.264	13083.166	22199.858	0.193	0.328	3.496	4.558	3.750	4.565	
0.000	0.004	0.085	24808.574	533363.769	0.367	7.887	4.000	3.984	3.999	3.988	
0.098	-0.037	0.144	34679.069	108898.361	0.513	1.610	4.004	4.077	3.995	4.084	
0.197	0.034	0.154	12965.965	57176.863	0.192	0.845	4.007	4.179	4.003	4.186	
0.295	0.110	0.227	28121.180	55571.526	0.416	0.822	4.001	4.268	4.001	4.277	
0.394	0.168	0.293	29870.677	52663.709	0.442	0.779	3.995	4.375	4.003	4.379	
0.493	0.265	0.324	31358.729	38658.389	0.464	0.572	3.998	4.569	4.003	4.572	

Table 8.26. Helium PHP thermal switch test results [Configuration = 2-circuit, Cryocooler-II-H Status = ON, $FR_{PHP\text{-}I\text{-}H} = 0.287$, $FR_{PHP\text{-}II\text{-}H} = 0.302$]

$\dot{Q}_{CCP-H}$ [W]	$\dot{Q}_{PHP-I-H}$ [W]	$\dot{Q}_{PHP-II-H}$ [W]	$k_{PHP-I-H,EFF}$ [W/m-K]	$k_{PHP-II-H,EFF}$ [W/m-K]	$UA_{PHP-I-H,EFF}$ [W/K]	$UA_{PHP-II-H,EFF}$ [W/K]	$T_{PHP-I-H,COND}$ [K]	$T_{PHP-I-H,EVAP}$ [K]	$T_{PHP-II-H,COND}$ [K]	$T_{PHP-II-H,EVAP}$ [K]	$SR_{PHP-II-H}$
0.000	-0.004	0.052	72078.832	160474.212	1.066	2.373	3.052	3.087	3.068	3.090	N/A
0.049	0.060	0.055	70661.988	68531.956	1.045	1.013	3.114	3.171	3.135	3.190	
0.098	0.041	0.064	22753.906	43141.146	0.336	0.638	3.166	3.290	3.207	3.307	
0.148	0.049	0.072	18665.835	32228.136	0.276	0.477	3.231	3.413	3.287	3.439	
0.197	0.089	0.104	27019.791	38997.407	0.400	0.577	3.299	3.522	3.365	3.545	

0.246	0.162	0.143	38840.258	43791.607	0.574	0.648	3.346	3.628	3.432	3.653	
0.295	0.157	0.171	30748.959	44474.278	0.455	0.658	3.383	3.728	3.496	3.756	
0.345	0.180	0.181	31869.075	41042.423	0.471	0.607	3.448	3.832	3.567	3.865	
0.394	0.202	0.232	19679.578	28578.824	0.291	0.423	3.485	4.172	3.653	4.204	
0.444	0.228	0.259	20255.687	28465.377	0.300	0.421	3.533	4.297	3.713	4.328	
0.493	0.303	0.279	22819.629	25861.927	0.337	0.382	3.593	4.498	3.780	4.516	
0.542	0.323	0.327	20602.293	27289.887	0.305	0.404	3.614	4.680	3.866	4.676	
0.592	0.368	0.325	18879.476	19298.866	0.279	0.285	3.672	5.007	3.905	5.048	
0.641	0.318	0.355	9749.991	12797.973	0.144	0.189	3.680	5.885	4.000	5.875	
0.690	0.360	0.356	7886.069	8897.200	0.117	0.132	3.706	6.797	4.096	6.800	
0.000	-0.030	0.085	700330.395	38468912.090	10.356	568.842	3.603	3.595	3.601	3.603	
0.049	0.056	0.113	86488.407	153953.373	1.279	2.277	3.602	3.646	3.606	3.656	
0.123	0.035	0.123	36312.203	81805.171	0.537	1.210	3.608	3.699	3.605	3.707	
0.148	0.067	0.149	30384.223	67754.475	0.449	1.002	3.598	3.746	3.602	3.752	
0.197	0.105	0.175	35566.100	60808.089	0.526	0.899	3.594	3.796	3.604	3.799	
0.246	0.070	0.193	20020.023	52908.287	0.296	0.782	3.606	3.842	3.600	3.847	
0.295	0.148	0.201	35140.616	47093.800	0.520	0.696	3.597	3.885	3.602	3.891	
0.345	0.197	0.220	38161.451	41507.369	0.564	0.614	3.603	3.952	3.604	3.966	
0.394	0.250	0.260	29349.105	33007.237	0.434	0.488	3.599	4.176	3.668	4.203	
0.444	0.232	0.269	22900.281	32093.183	0.339	0.475	3.593	4.274	3.733	4.301	
0.493	0.293	0.270	22235.594	24360.605	0.329	0.360	3.615	4.508	3.782	4.533	
0.542	0.302	0.305	19323.959	23746.755	0.286	0.351	3.638	4.693	3.831	4.702	

Table 8.27. Helium PHP thermal switch test results [Configuration = 2-circuit, Cryocooler-II-H Status = ON, $FR_{PHP-I-H} = 0.432$, $FR_{PHP-II-H} = 0.406$]

$\dot{Q}_{CCP-H}$ [W]	$\dot{Q}_{PHP-I-H}$ [W]	$\dot{Q}_{PHP-II-H}$ [W]	$k_{PHP-I-H,EFF}$ [W/m-K]	$k_{PHP-II-H,EFF}$ [W/m-K]	$UA_{PHP-I-H,EFF}$ [W/K]	$UA_{PHP-II-H,EFF}$ [W/K]	$T_{PHP-I-H,COND}$ [K]	$T_{PHP-I-H,EVAP}$ [K]	$T_{PHP-II-H,COND}$ [K]	$T_{PHP-II-H,EVAP}$ [K]	$SR_{PHP-II-H}$
0.000	-0.057	0.047	5102748.908	117072.074	75.455	1.731	3.078	3.073	3.056	3.082	
0.098	0.056	0.073	29808.394	39808.377	0.441	0.589	3.195	3.322	3.215	3.340	
0.197	0.092	0.116	24819.791	36927.015	0.367	0.546	3.286	3.535	3.355	3.567	
0.295	0.117	0.174	22445.683	40289.294	0.332	0.596	3.405	3.758	3.494	3.787	
0.394	0.167	0.234	24381.480	42489.327	0.361	0.628	3.503	3.967	3.626	3.999	
0.493	0.276	0.245	34371.317	37455.811	0.508	0.554	3.621	4.164	3.759	4.201	
0.592	0.291	0.301	31096.058	39243.549	0.460	0.580	3.716	4.348	3.871	4.389	
0.690	0.401	0.350	37743.274	40981.732	0.558	0.606	3.804	4.523	3.983	4.560	
0.789	0.447	0.391	37966.881	41067.769	0.561	0.607	3.889	4.686	4.089	4.733	
0.888	0.532	0.443	42058.379	44128.567	0.622	0.653	3.965	4.822	4.190	4.869	
0.987	0.600	0.510	27128.681	29916.685	0.401	0.442	4.000	5.495	4.359	5.512	
1.061	0.574	0.604	21176.090	29872.936	0.313	0.442	4.011	5.851	4.494	5.861	
0.000	-0.061	0.112	392848.385	698332.494	5.809	10.326	4.000	4.005	4.003	4.014	
0.098	-0.004	0.155	35472.282	92841.959	0.525	1.373	4.001	4.108	4.001	4.114	N/A
0.197	0.044	0.185	18531.864	59763.871	0.274	0.884	4.010	4.205	4.002	4.211	
0.295	0.049	0.212	11175.400	46584.833	0.165	0.689	4.004	4.300	3.999	4.307	
0.419	0.138	0.260	23949.034	43546.744	0.354	0.644	4.010	4.401	3.998	4.401	
0.444	0.225	0.303	34157.413	46210.362	0.505	0.683	4.001	4.446	4.001	4.445	
0.493	0.165	0.290	23759.241	40699.178	0.351	0.602	4.016	4.486	4.001	4.483	
0.592	0.323	0.342	39307.878	41081.792	0.581	0.607	4.011	4.567	4.002	4.565	
0.690	0.364	0.374	37698.771	40627.329	0.557	0.601	4.011	4.663	4.051	4.674	
0.788	0.411	0.420	36984.190	43213.830	0.547	0.639	4.005	4.757	4.127	4.784	
0.838	0.447	0.418	38310.606	42326.461	0.567	0.626	4.008	4.798	4.166	4.834	
0.888	0.506	0.431	41213.051	42962.846	0.609	0.635	4.008	4.839	4.203	4.881	
0.937	0.609	0.452	47561.882	44058.593	0.703	0.651	4.017	4.882	4.239	4.932	
0.987	0.605	0.479	45775.170	45149.440	0.677	0.668	4.053	4.947	4.283	5.001	
1.085	0.487	0.621	18765.032	33174.584	0.277	0.491	4.040	5.805	4.526	5.794	

Table 8.28. Helium PHP thermal switch test results [Configuration = 2-circuit, Cryocooler-II-H Status = ON, $FR_{PHP-I-H} = 0.478$, $FR_{PHP-II-H} = 0.500$]

$\dot{Q}_{CCP-H}$ [W]	$\dot{Q}_{PHP-I-H}$ [W]	$\dot{Q}_{PHP-II-H}$ [W]	$k_{PHP-I-H,EFF}$ [W/m-K]	$k_{PHP-II-H,EFF}$ [W/m-K]	$UA_{PHP-I-H,EFF}$ [W/K]	$UA_{PHP-II-H,EFF}$ [W/K]	$T_{PHP-I-H,COND}$ [K]	$T_{PHP-I-H,EVAP}$ [K]	$T_{PHP-II-H,COND}$ [K]	$T_{PHP-II-H,EVAP}$ [K]	$SR_{PHP-II-H}$
0.000	0.000	0.045	70399.687	1205620.554	1.041	17.828	3.193	3.196	3.196	3.207	N/A
0.024	-0.030	0.043	90322.426	51202.315	1.336	0.757	3.197	3.237	3.196	3.252	
0.049	0.019	0.059	18841.281	44203.563	0.279	0.654	3.207	3.276	3.199	3.288	
0.074	0.023	0.066	14494.038	37294.274	0.214	0.551	3.206	3.315	3.205	3.325	
0.098	0.008	0.065	16791.635	29598.741	0.248	0.438	3.205	3.340	3.203	3.353	
0.148	0.047	0.077	15359.159	26358.452	0.227	0.390	3.236	3.436	3.259	3.457	
0.197	0.100	0.107	27158.772	30591.109	0.402	0.452	3.289	3.546	3.337	3.575	
0.246	0.081	0.131	17047.983	31099.178	0.252	0.460	3.347	3.668	3.413	3.697	
0.295	0.176	0.174	32367.512	36731.427	0.479	0.543	3.399	3.768	3.481	3.802	
0.345	0.149	0.179	24008.621	32243.222	0.355	0.477	3.450	3.869	3.541	3.917	
0.394	0.236	0.210	32715.908	34164.685	0.484	0.505	3.503	3.991	3.610	4.026	
0.444	0.252	0.243	32006.202	37395.947	0.473	0.553	3.564	4.097	3.688	4.128	
0.493	0.303	0.282	34619.316	39234.296	0.512	0.580	3.613	4.205	3.751	4.237	
0.542	0.337	0.316	35768.812	42001.324	0.529	0.621	3.667	4.303	3.828	4.336	
0.592	0.286	0.297	28044.868	35924.828	0.415	0.531	3.708	4.399	3.875	4.434	
0.641	0.396	0.347	36052.638	39795.258	0.533	0.588	3.750	4.492	3.936	4.526	
0.691	0.386	0.339	32977.911	36598.918	0.488	0.541	3.791	4.582	3.990	4.617	
0.739	0.411	0.378	34435.422	39103.911	0.509	0.578	3.850	4.657	4.042	4.696	
0.789	0.462	0.404	38164.578	40673.998	0.564	0.601	3.916	4.736	4.103	4.775	
0.838	0.466	0.402	37241.441	39708.005	0.551	0.587	3.948	4.795	4.150	4.834	
0.888	0.480	0.410	38161.843	39958.927	0.564	0.591	4.004	4.855	4.203	4.896	
0.938	0.501	0.430	38860.457	41328.952	0.575	0.611	4.042	4.915	4.253	4.957	
0.987	0.471	0.457	35911.409	43308.903	0.531	0.640	4.089	4.975	4.305	5.018	
1.036	0.674	0.533	50319.937	49650.073	0.744	0.734	4.132	5.038	4.362	5.088	
1.086	0.551	0.623	27926.098	47175.702	0.413	0.698	4.082	5.417	4.534	5.426	
1.134	0.584	0.628	24318.714	34643.799	0.360	0.512	4.130	5.755	4.547	5.773	
1.184	0.588	0.648	24192.887	37372.400	0.358	0.553	4.145	5.789	4.627	5.800	
1.233	0.594	0.676	23544.139	38754.321	0.348	0.573	4.168	5.875	4.698	5.878	
1.284	0.605	0.680	22178.889	35267.556	0.328	0.522	4.207	6.052	4.753	6.057	
1.331	0.612	0.696	20003.699	31649.407	0.296	0.468	4.240	6.308	4.819	6.305	
1.382	0.661	0.722	19522.052	28814.722	0.289	0.426	4.269	6.560	4.863	6.556	
0.000	-0.071	0.076	332435.355	199591.553	4.916	2.951	3.599	3.620	3.597	3.623	
0.049	-0.019	0.094	23490.896	78174.047	0.347	1.156	3.600	3.671	3.601	3.683	
0.098	0.028	0.132	23586.507	64516.333	0.349	0.954	3.601	3.724	3.599	3.736	
0.148	0.009	0.121	3237.187	41540.152	0.048	0.614	3.600	3.784	3.601	3.797	
0.197	0.040	0.140	11577.520	39636.852	0.171	0.586	3.596	3.834	3.602	3.841	
0.246	0.156	0.184	38257.574	42287.672	0.566	0.625	3.609	3.884	3.602	3.896	
0.295	0.114	0.196	23764.844	39327.956	0.351	0.582	3.609	3.932	3.604	3.941	
0.345	0.132	0.201	23469.729	35229.654	0.347	0.521	3.604	3.984	3.610	3.996	
0.394	0.194	0.223	28790.264	36113.817	0.426	0.534	3.598	4.051	3.655	4.073	
0.444	0.214	0.232	28060.382	35608.784	0.415	0.527	3.601	4.117	3.705	4.146	
0.493	0.282	0.265	33658.022	37280.769	0.498	0.551	3.642	4.209	3.764	4.245	
0.542	0.343	0.296	38969.675	38480.674	0.576	0.569	3.718	4.313	3.831	4.351	
0.592	0.372	0.316	37790.796	37973.757	0.559	0.562	3.734	4.400	3.876	4.440	
0.641	0.292	0.311	28132.643	35373.506	0.416	0.523	3.786	4.487	3.932	4.527	
0.690	0.368	0.334	32894.344	35624.869	0.486	0.527	3.816	4.572	3.981	4.614	
0.739	0.392	0.350	32990.081	35393.750	0.488	0.523	3.850	4.653	4.029	4.698	
0.789	0.464	0.366	37842.320	36126.835	0.560	0.534	3.893	4.723	4.083	4.769	
0.838	0.495	0.399	39886.454	38855.247	0.590	0.575	3.946	4.786	4.139	4.834	
0.888	0.558	0.428	43382.669	40714.209	0.642	0.602	3.975	4.845	4.185	4.896	
0.938	0.590	0.450	45357.327	42177.838	0.671	0.624	4.027	4.906	4.237	4.958	
0.987	0.610	0.469	45700.178	43461.564	0.676	0.643	4.061	4.964	4.287	5.017	

1.037	0.596	0.509	43113.729	46204.978	0.638	0.683	4.101	5.037	4.343	5.088	
1.086	0.569	0.585	31949.412	47981.844	0.472	0.710	4.096	5.301	4.499	5.324	
1.134	0.608	0.603	28174.769	35857.896	0.417	0.530	4.183	5.640	4.530	5.667	
1.184	0.581	0.646	26579.352	39024.289	0.393	0.577	4.210	5.690	4.597	5.717	
1.233	0.577	0.619	25084.994	36532.831	0.371	0.540	4.233	5.790	4.664	5.811	
1.284	0.689	0.687	25814.366	34966.055	0.382	0.517	4.231	6.037	4.723	6.051	
1.331	0.650	0.705	21625.288	31974.522	0.320	0.473	4.245	6.278	4.796	6.286	
1.382	0.627	0.714	19223.565	29787.934	0.284	0.440	4.261	6.465	4.850	6.470	
0.000	-0.002	0.128	30388.838	2714953.777	0.449	40.146	4.000	3.993	4.002	3.998	
0.049	0.037	0.149	37962.768	137049.192	0.561	2.027	3.995	4.061	3.997	4.071	
0.098	0.001	0.141	29168.643	71941.746	0.431	1.064	3.991	4.117	3.996	4.129	
0.148	0.094	0.189	35661.588	69026.363	0.527	1.021	3.999	4.177	4.004	4.189	
0.197	0.117	0.199	36993.725	58374.884	0.547	0.863	4.013	4.227	4.004	4.235	
0.246	0.089	0.207	21070.754	48890.639	0.312	0.723	3.989	4.275	3.996	4.283	
0.295	0.111	0.231	22892.667	46551.370	0.339	0.688	3.997	4.327	3.999	4.335	
0.345	0.196	0.263	35309.752	46081.843	0.522	0.681	4.002	4.378	3.997	4.384	
0.394	0.161	0.265	24905.448	40237.285	0.368	0.595	4.002	4.437	3.999	4.443	
0.444	0.180	0.283	24844.428	38673.383	0.367	0.572	3.998	4.486	3.996	4.491	
0.493	0.259	0.320	33655.805	41169.621	0.498	0.609	4.007	4.527	4.003	4.529	
0.542	0.250	0.332	29254.535	38961.185	0.433	0.576	3.992	4.571	3.997	4.573	
0.592	0.254	0.348	27626.081	38401.243	0.409	0.568	3.998	4.618	4.000	4.612	
0.641	0.352	0.381	35854.537	39837.311	0.530	0.589	3.998	4.663	4.015	4.662	
0.690	0.391	0.390	37579.423	39961.884	0.556	0.591	4.003	4.708	4.054	4.715	
0.764	0.389	0.399	34475.692	39682.314	0.510	0.587	4.004	4.767	4.103	4.783	
0.789	0.428	0.405	36300.886	40177.082	0.537	0.594	3.986	4.783	4.125	4.806	
0.838	0.460	0.404	37943.694	39434.422	0.561	0.583	4.002	4.821	4.165	4.858	
0.888	0.482	0.404	38211.107	39261.438	0.565	0.581	3.998	4.853	4.202	4.898	
0.987	0.514	0.446	38922.510	42021.277	0.576	0.621	4.071	4.963	4.298	5.016	

Table 8.29. Helium PHP thermal switch test results [Configuration = 2-circuit, Cryocooler-II-H Status = ON, $FR_{PHP-I-H} = 0.470$, $FR_{PHP-II-H} = 0.479$]

$\dot{Q}_{CCP-H}$ [W]	$\dot{Q}_{PHP-I-H}$ [W]	$\dot{Q}_{PHP-II-H}$ [W]	$k_{PHP-I-H,EFF}$ [W/m-K]	$k_{PHP-II-H,EFF}$ [W/m-K]	$UA_{PHP-I-H,EFF}$ [W/K]	$UA_{PHP-II-H,EFF}$ [W/K]	$T_{PHP-I-H,COND}$ [K]	$T_{PHP-I-H,EVAP}$ [K]	$T_{PHP-II-H,COND}$ [K]	$T_{PHP-II-H,EVAP}$ [K]	$SR_{PHP-II-H}$
0.000	0.010	0.035	1157705.966	19080.113	17.119	0.282	3.114	3.109	3.245	3.121	839.067
0.098	0.060	0.066	24444.527	45863.486	0.361	0.678	3.244	3.410	3.347	3.444	2016.893
0.197	0.132	0.122	32701.942	43683.227	0.484	0.646	3.369	3.642	3.489	3.678	1921.014
0.295	0.141	0.189	25148.236	45735.023	0.372	0.676	3.466	3.845	3.611	3.891	2011.243
0.394	0.196	0.216	27844.398	41684.679	0.412	0.616	3.559	4.037	3.734	4.085	1833.126
0.493	0.304	0.272	35586.914	44124.793	0.526	0.652	3.640	4.217	3.853	4.270	1940.432
0.592	0.364	0.299	36737.419	39931.478	0.543	0.590	3.742	4.413	3.962	4.468	1756.027
0.690	0.399	0.337	38409.852	38904.448	0.568	0.575	3.890	4.603	4.066	4.652	1710.862
0.739	0.486	0.344	41674.969	38198.500	0.616	0.565	3.887	4.675	4.120	4.729	1679.817
0.888	0.515	0.426	40792.729	43114.072	0.603	0.638	4.017	4.870	4.263	4.931	1895.985
0.888	0.448	0.431	34504.792	34923.671	0.510	0.516	4.189	5.064	4.257	5.093	1535.803
0.888	0.451	0.443	36032.172	36536.656	0.533	0.540	4.205	5.052	4.259	5.079	1606.736
0.888	0.460	0.420	39998.039	35887.951	0.591	0.531	4.197	4.976	4.226	5.018	1578.209
0.838	0.412	0.436	38877.732	43140.184	0.575	0.638	4.204	4.920	4.246	4.929	1897.133
0.789	0.413	0.429	41164.700	43211.251	0.609	0.639	4.209	4.886	4.214	4.885	1900.258
0.739	0.320	0.398	32692.236	41285.518	0.483	0.610	4.194	4.856	4.198	4.850	1815.572
0.690	0.284	0.380	30433.602	41322.826	0.450	0.611	4.197	4.828	4.198	4.820	1817.213
0.641	0.225	0.347	25107.334	39975.336	0.371	0.591	4.193	4.798	4.200	4.787	1757.955
0.592	0.231	0.364	27651.612	44393.167	0.409	0.656	4.202	4.767	4.200	4.754	1952.234
0.542	0.238	0.328	30231.904	42216.163	0.447	0.624	4.199	4.733	4.198	4.723	1856.498
0.492	0.206	0.278	27767.419	38796.197	0.411	0.574	4.188	4.691	4.196	4.681	1706.102
0.444	0.095	0.263	14304.466	40730.696	0.212	0.602	4.197	4.648	4.201	4.638	1791.173
0.394	0.143	0.281	23666.140	48328.599	0.350	0.715	4.193	4.602	4.199	4.592	2125.299

0.265	-0.007	0.173	1600.183	42840.219	0.024	0.633	4.195	4.478	4.202	4.475	1883.942
0.197	0.088	0.200	29138.236	64147.376	0.431	0.949	4.206	4.411	4.200	4.411	2820.945
0.098	0.052	0.158	34960.955	93331.079	0.517	1.380	4.209	4.309	4.200	4.315	4104.328
0.000	-0.006	0.051	4179398.095	489613.069	61.801	7.240	3.095	3.092	3.108	3.097	21531.226
0.049	0.022	0.057	16517.086	58238.826	0.244	0.861	3.138	3.227	3.181	3.248	2561.111
0.098	0.034	0.072	15642.817	42300.126	0.231	0.625	3.200	3.350	3.255	3.371	1860.190
0.148	0.093	0.096	30903.780	39899.311	0.457	0.590	3.255	3.461	3.327	3.490	1754.612
0.197	0.137	0.129	34592.937	41961.297	0.512	0.620	3.311	3.579	3.397	3.605	1845.290
0.246	0.131	0.152	28992.803	41859.438	0.429	0.619	3.385	3.691	3.473	3.718	1840.811
0.305	0.141	0.160	25128.545	37986.137	0.372	0.562	3.409	3.789	3.534	3.819	1670.478
0.345	0.191	0.194	31009.183	41850.405	0.459	0.619	3.476	3.892	3.605	3.919	1840.414
0.394	0.279	0.211	38644.104	39500.144	0.571	0.584	3.508	3.996	3.663	4.024	1737.058
0.444	0.300	0.258	38013.813	43688.288	0.562	0.646	3.566	4.100	3.729	4.128	1921.236
0.493	0.324	0.274	38331.628	42959.579	0.567	0.635	3.620	4.191	3.794	4.226	1889.191
0.542	0.312	0.288	32982.330	41455.845	0.488	0.613	3.647	4.287	3.852	4.321	1823.062
0.592	0.382	0.328	37395.282	43849.416	0.553	0.648	3.699	4.389	3.913	4.419	1928.322
0.690	0.415	0.373	36009.379	43717.210	0.532	0.646	3.785	4.564	4.021	4.597	1922.508
0.764	0.431	0.380	35384.608	41586.494	0.523	0.615	3.835	4.659	4.075	4.692	1828.808
0.813	0.476	0.415	38880.775	43968.783	0.575	0.650	3.911	4.738	4.136	4.775	1933.571
0.838	0.479	0.411	38314.689	42650.871	0.567	0.631	3.935	4.780	4.168	4.820	1875.615
0.888	0.479	0.437	30299.640	37441.970	0.448	0.554	3.963	5.033	4.276	5.065	1646.548
0.987	0.506	0.483	31811.364	33240.394	0.470	0.492	4.212	5.287	4.340	5.323	1461.780

Table 8.30. Helium PHP thermal switch test results [Configuration = 2-circuit, Cryocooler-II-H Status = ON, $FR_{PHP\text{-}I\text{-}H} = 0.589$, $FR_{PHP\text{-}II\text{-}H} = 0.577$]

$\dot{Q}_{CCP-H}$ [W]	$\dot{Q}_{PHP-I-H}$ [W]	$\dot{Q}_{PHP-II-H}$ [W]	$k_{PHP-I-H,EFF}$ [W/m-K]	$k_{PHP-II-H,EFF}$ [W/m-K]	$UA_{PHP-I-H,EFF}$ [W/K]	$UA_{PHP-II-H,EFF}$ [W/K]	$T_{PHP-I-H,COND}$ [K]	$T_{PHP-I-H,EVAP}$ [K]	$T_{PHP-II-H,COND}$ [K]	$T_{PHP-II-H,EVAP}$ [K]	$SR_{PHP-II-H}$
0.000	-0.009	0.044	2396950.784	119801.052	35.444	1.772	3.052	3.054	3.037	3.062	
0.098	0.003	0.071	4768.047	29794.138	0.071	0.441	3.155	3.332	3.186	3.347	
0.197	0.038	0.119	8472.990	31728.083	0.125	0.469	3.271	3.576	3.343	3.597	
0.295	0.148	0.170	24108.945	32842.429	0.357	0.486	3.383	3.801	3.482	3.834	
0.394	0.195	0.216	24705.053	33390.859	0.365	0.494	3.483	4.018	3.613	4.049	
0.493	0.222	0.263	23197.091	34522.721	0.343	0.510	3.587	4.233	3.747	4.262	
0.592	0.307	0.306	27696.529	34396.068	0.410	0.509	3.690	4.440	3.870	4.472	
0.690	0.445	0.369	35199.266	37127.614	0.520	0.549	3.766	4.621	3.981	4.654	
0.838	0.531	0.406	39904.873	38019.760	0.590	0.562	3.919	4.818	4.137	4.858	
0.888	0.461	0.424	34078.609	38872.964	0.504	0.575	3.964	4.880	4.186	4.923	
0.987	0.633	0.480	45700.666	43472.529	0.676	0.643	4.056	4.993	4.291	5.039	
1.086	0.603	0.543	42228.628	47847.356	0.624	0.708	4.141	5.105	4.389	5.156	
1.184	0.680	0.587	44858.547	47635.900	0.663	0.704	4.219	5.244	4.470	5.303	N/A
1.234	0.730	0.615	39931.656	40380.848	0.590	0.597	4.268	5.553	4.527	5.600	
1.382	0.685	0.658	27184.101	29662.344	0.402	0.439	4.383	6.086	4.645	6.145	
0.000	-0.100	0.091	1458269.549	307446.045	21.564	4.546	4.002	4.008	3.995	4.018	
0.098	-0.006	0.165	31395.102	78904.898	0.464	1.167	3.997	4.130	4.000	4.142	
0.197	0.060	0.209	16511.431	53708.399	0.244	0.794	3.992	4.249	4.000	4.263	
0.295	0.068	0.260	12349.841	46867.999	0.183	0.693	3.993	4.366	3.997	4.373	
0.394	0.167	0.239	23893.427	33884.814	0.353	0.501	4.009	4.481	4.004	4.480	
0.493	0.219	0.311	25250.917	35739.264	0.373	0.528	4.002	4.587	4.001	4.589	
0.592	0.324	0.356	32616.037	35922.405	0.482	0.531	4.006	4.678	4.006	4.676	
0.690	0.341	0.389	30435.054	36945.241	0.450	0.546	3.998	4.756	4.053	4.765	
0.789	0.409	0.421	33076.745	39301.692	0.489	0.581	3.997	4.834	4.131	4.854	
0.888	0.480	0.424	36055.646	39042.801	0.533	0.577	4.007	4.908	4.208	4.941	
0.987	0.505	0.477	35774.064	42884.432	0.529	0.634	4.044	4.999	4.292	5.044	

Table 8.31. Helium PHP thermal switch test results [Configuration = 2-circuit, Cryocooler-II-H Status = ON, $FR_{PHP-I-H} = 0.489$, $FR_{PHP-II-H} = 0.194$]

$\dot{Q}_{CCP-H}$ [W]	$\dot{Q}_{PHP-I-H}$ [W]	$\dot{Q}_{PHP-II-H}$ [W]	$k_{PHP-I-H,EFF}$ [W/m-K]	$k_{PHP-II-H,EFF}$ [W/m-K]	$UA_{PHP-I-H,EFF}$ [W/K]	$UA_{PHP-II-H,EFF}$ [W/K]	$T_{PHP-I-H,COND}$ [K]	$T_{PHP-I-H,EVAP}$ [K]	$T_{PHP-II-H,COND}$ [K]	$T_{PHP-II-H,EVAP}$ [K]	$SR_{PHP-II-H}$
0.000	0.032	0.033	906232.857	12698.300	13.401	0.188	3.112	3.114	3.326	3.123	558.420
0.113	0.052	0.076	21653.298	63831.541	0.320	0.944	3.271	3.430	3.381	3.461	2807.056
0.148	0.095	0.097	31660.524	55138.717	0.468	0.815	3.337	3.538	3.451	3.570	2424.780
0.197	0.146	0.124	37075.258	52177.073	0.548	0.772	3.383	3.650	3.517	3.677	2294.539
0.246	0.140	0.159	28493.498	54765.590	0.421	0.810	3.418	3.753	3.585	3.781	2408.372
0.295	0.141	0.188	25009.031	50602.458	0.370	0.748	3.482	3.863	3.642	3.893	2225.294
0.394	0.273	0.198	38018.589	38060.450	0.562	0.563	3.584	4.070	3.759	4.111	1673.746
0.493	0.365	0.242	40736.130	35172.057	0.602	0.520	3.684	4.292	3.870	4.340	1546.726
0.592	0.361	0.283	33323.386	28535.993	0.493	0.422	3.799	4.532	3.929	4.601	1254.899

Table 8.32. Helium PHP thermal switch test results [Configuration = 2-circuit, Cryocooler-II-H Status = OFF, $FR_{PHP-I-H} = 0.470$, $FR_{PHP-II-H} = 0.479$]

$\dot{Q}_{CCP-H}$ [W]	$\dot{Q}_{PHP-I-H}$ [W]	$\dot{Q}_{PHP-II-H}$ [W]	$k_{PHP-I-H,EFF}$ [W/m-K]	$k_{PHP-II-H,EFF}$ [W/m-K]	$UA_{PHP-I-H,EFF}$ [W/K]	$UA_{PHP-II-H,EFF}$ [W/K]	$T_{PHP-I-H,COND}$ [K]	$T_{PHP-I-H,EVAP}$ [K]	$T_{PHP-II-H,COND}$ [K]	$T_{PHP-II-H,EVAP}$ [K]	$SR_{PHP-II-H}$
0.000	0.075	-0.075	29138.326	18.024	0.431	0.00027	3.491	3.664	282.794	3.742	
0.020	0.165	-0.145	51116.674	34.898	0.756	0.00052	3.531	3.749	285.725	3.839	
0.039	0.182	-0.143	49302.915	34.414	0.729	0.00051	3.565	3.815	285.792	3.915	
0.059	0.164	-0.105	38378.643	25.222	0.568	0.00037	3.605	3.894	285.851	4.004	
0.078	0.228	-0.150	46370.312	35.967	0.686	0.00053	3.635	3.968	285.909	4.086	
0.098	0.196	-0.097	35337.850	23.375	0.523	0.00035	3.670	4.044	285.967	4.163	
0.118	0.209	-0.091	33337.522	21.856	0.493	0.00032	3.697	4.122	286.020	4.248	
0.128	0.177	-0.049	27608.600	11.812	0.408	0.00017	3.721	4.155	286.057	4.290	
0.157	0.252	-0.094	33726.559	22.663	0.499	0.00034	3.758	4.263	286.123	4.412	
0.177	0.254	-0.077	31746.180	18.383	0.469	0.00027	3.798	4.340	286.176	4.493	
0.197	0.333	-0.136	38000.359	32.636	0.562	0.00048	3.820	4.412	286.232	4.565	
0.216	0.350	-0.133	37840.533	32.014	0.560	0.00047	3.862	4.487	286.280	4.644	N/A
0.236	0.262	-0.025	26553.462	6.120	0.393	0.00009	3.896	4.562	286.334	4.725	
0.256	0.368	-0.113	36181.751	27.053	0.535	0.00040	3.934	4.623	286.393	4.790	
0.276	0.363	-0.088	34689.504	21.020	0.513	0.00031	3.964	4.672	286.451	4.849	
0.305	0.411	-0.106	37633.114	25.537	0.556	0.00038	3.992	4.731	286.513	4.915	
0.315	0.465	-0.150	42662.066	35.906	0.631	0.00053	4.020	4.757	286.553	4.944	
0.281	0.381	-0.100	36532.703	24.095	0.540	0.00036	3.966	4.673	286.613	4.849	
0.262	0.315	-0.053	31108.753	12.620	0.460	0.00019	3.943	4.627	286.668	4.797	
0.233	0.347	-0.113	36286.775	27.173	0.537	0.00040	3.902	4.549	286.719	4.712	
0.227	0.331	-0.105	35669.537	25.117	0.527	0.00037	3.881	4.508	286.753	4.670	
0.220	0.337	-0.117	37258.483	28.011	0.551	0.00041	3.880	4.490	286.789	4.651	
0.206	0.266	-0.060	30176.151	14.289	0.446	0.00021	3.845	4.442	286.820	4.600	

Table 8.33. Helium PHP thermal switch test results [Configuration = 2-circuit, Cryocooler-II-H Status = OFF,$FR_{PHP-I-H} = 0.489$, $FR_{PHP-II-H} = 0.194$]

$\dot{Q}_{CCP-H}$ [W]	$\dot{Q}_{PHP-I-H}$ [W]	$\dot{Q}_{PHP-II-H}$ [W]	$k_{PHP-I-H,EFF}$ [W/m-K]	$k_{PHP-II-H,EFF}$ [W/m-K]	$UA_{PHP-I-H,EFF}$ [W/K]	$UA_{PHP-II-H,EFF}$ [W/K]	$T_{PHP-I-H,COND}$ [K]	$T_{PHP-I-H,EVAP}$ [K]	$T_{PHP-II-H,COND}$ [K]	$T_{PHP-II-H,EVAP}$ [K]	$SR_{PHP-II-H}$
0.020	0.108	-0.088	35468.385	22.027	0.524	0.00033	3.466	3.672	275.426	3.762	N/A
0.039	0.098	-0.059	27394.351	14.789	0.405	0.00022	3.509	3.754	275.603	3.854	
0.059	0.129	-0.070	29585.282	17.455	0.437	0.00026	3.521	3.811	275.779	3.922	
0.078	0.185	-0.107	39062.247	26.515	0.578	0.00039	3.593	3.913	275.992	4.021	
0.098	0.226	-0.128	40977.996	31.827	0.606	0.00047	3.580	3.953	276.236	4.072	
0.118	0.189	-0.071	31831.124	17.617	0.471	0.00026	3.655	4.057	276.511	4.187	

0.138	0.256	-0.118	38376.520	29.295	0.567	0.00043	3.685	4.136	276.719	4.273	
0.157	0.177	-0.019	24844.749	26.069	0.367	0.00039	3.701	4.181	276.910	4.322	
0.177	0.221	-0.044	28069.677	10.926	0.415	0.00016	3.738	4.271	277.047	4.418	
0.197	0.250	-0.053	29487.786	13.131	0.436	0.00019	3.786	4.359	277.176	4.512	
0.216	0.263	-0.047	29622.958	11.666	0.438	0.00017	3.829	4.430	277.332	4.587	
0.000	0.088	-0.088	33186.489	21.466	0.491	0.00032	3.462	3.644	280.956	3.722	
0.024	0.112	-0.087	33085.686	21.232	0.489	0.00031	3.519	3.748	281.132	3.841	
0.049	0.139	-0.090	33699.222	22.029	0.498	0.00033	3.562	3.841	281.299	3.946	
0.074	0.188	-0.114	39557.963	27.883	0.585	0.00041	3.614	3.935	281.501	4.051	
0.098	0.203	-0.104	37073.456	25.429	0.548	0.00038	3.642	4.010	281.688	4.132	
0.123	0.225	-0.102	36103.447	24.919	0.534	0.00037	3.682	4.103	281.829	4.235	
0.148	0.255	-0.107	36895.348	26.121	0.546	0.00039	3.749	4.215	281.984	4.357	
0.172	0.250	-0.078	32687.191	19.067	0.483	0.00028	3.792	4.309	282.154	4.461	
0.197	0.293	-0.096	33644.952	23.387	0.498	0.00035	3.808	4.396	282.292	4.552	
0.222	0.312	-0.091	33154.522	22.060	0.490	0.00033	3.846	4.483	282.392	4.641	
0.246	0.243	0.003	24907.068	10.167	0.368	0.00015	3.901	4.561	283.082	4.723	

8.9 PHP thermal switch ON state model validation data

Table 8.34. PHP thermal switch ON state model validation data from various experiment sources

Fluid	Source	$N_{PHP,TUBES}$, $d_{PHP,i}$ [mm], $d_{PHP,o}$ [mm], $L_{PHP,ADIA}$ [mm], $L_{PHP,COND}$ [mm], $L_{PHP,EVAP}$ [mm]	FR	T_{COND} [K]	T_{EVAP} [K]	$\dot{Q}_{PHP,ON,EXPERIMENT}$ [W]	$\dot{Q}_{PHP,ON,MODEL}$ [W]	$UA_{PHP,ON,EXPERIMENT}$ [W/K]	$UA_{PHP,ON,MODEL}$ [W/K]	$\frac{\dot{Q}_{PHP,ON,RelativeError}}{UA_{PHP,ON,RelativeError}}$
Nitrogen	Present Work	20, 1.08, 1.47, 254, 102, 102	0.520	75.29	77.07	5.87	10.02	3.30	5.64	0.41
			0.520	72.49	75.76	9.16	13.18	2.80	4.03	-0.30
			0.260	81.20	83.04	13.44	12.45	7.28	6.74	0.08
			0.260	82.99	85.02	15.71	13.89	7.75	6.85	0.13
			0.260	84.70	87.00	17.63	16.64	7.68	7.25	0.06
			0.302	75.96	77.34	6.78	6.35	4.89	4.58	0.07
			0.302	76.70	78.23	8.06	6.96	5.27	4.55	0.16
			0.415	74.41	75.97	4.72	9.17	3.03	5.89	-0.48
			0.520	76.08	77.94	7.01	9.56	3.78	5.15	-0.27
			0.520	72.88	75.30	9.67	10.58	4.00	4.38	-0.09
			0.520	73.39	76.67	10.37	13.16	3.16	4.01	-0.21
			0.520	82.51	84.45	9.43	12.15	4.87	6.28	-0.22
			0.520	78.80	80.54	7.16	10.08	4.10	5.78	-0.29
			0.520	80.30	81.69	5.51	9.29	3.98	6.71	-0.41
			0.259	81.29	82.66	6.13	10.25	4.50	7.52	-0.40
			0.259	82.09	83.52	8.91	10.63	6.19	7.39	-0.16
			0.259	83.44	84.92	9.73	11.61	6.58	7.85	-0.16
			0.303	78.92	79.85	5.29	7.36	5.70	7.94	-0.28
	[39]	16, 1.65, 3.18, 100, 60, 40	0.480	80.15	85.65	22.50	20.37	4.09	3.70	0.10
			0.480	82.15	89.15	40.50	25.54	5.79	3.65	0.59
			0.480	79.15	91.15	68.80	41.78	5.73	3.48	0.65
			0.480	83.65	97.65	86.70	47.83	6.19	3.42	0.81
			0.480	81.65	100.65	125.70	62.50	6.62	3.29	1.01
Helium	Present Work	18, 0.51, 0.72, 501, 90, 90	0.203	4.00	4.57	0.27	0.28	0.46	0.49	-0.05
			0.187	4.00	4.57	0.32	0.29	0.57	0.5	0.13
			0.287	3.35	3.63	0.16	0.17	0.57	0.61	-0.06
			0.302	3.71	4.33	0.26	0.31	0.42	0.5	-0.16
			0.478	4.09	4.98	0.58	0.42	0.66	0.47	0.4
			0.589	3.69	4.44	0.31	0.3	0.41	0.4	0.03

			0.589	3.38	3.80	0.15	0.18	0.36	0.44	-0.19
			0.577	3.34	3.60	0.12	0.13	0.47	0.5	-0.06
			0.577	4.14	4.86	0.41	0.33	0.56	0.46	0.22
			0.470	3.56	4.04	0.20	0.22	0.41	0.47	-0.12
			0.470	3.89	4.60	0.40	0.35	0.56	0.49	0.14
			0.479	3.35	3.44	0.07	0.05	0.68	0.57	0.2
			0.479	3.96	4.47	0.30	0.24	0.59	0.48	0.23
			0.479	4.26	4.93	0.43	0.3	0.64	0.45	0.42
			0.432	3.35	3.53	0.09	0.11	0.51	0.62	-0.18
			0.432	3.76	4.16	0.28	0.22	0.68	0.54	0.25
			0.432	3.97	4.82	0.53	0.46	0.62	0.53	0.16
			0.406	3.49	3.79	0.17	0.18	0.60	0.62	-0.04
			0.406	4.09	4.73	0.39	0.31	0.61	0.48	0.27
	[40]	14, 0.50, 0.80, 300, 90, 30	0.700	3.33	3.60	0.05	0.08	0.19	0.31	-0.39
			0.700	3.75	4.10	0.10	0.11	0.29	0.31	-0.07
			0.700	4.00	4.60	0.15	0.31	0.25	0.52	-0.52
			0.700	4.20	4.80	0.18	0.34	0.29	0.56	-0.48
		14, 0.50, 0.80, 1000, 90, 30	0.580	3.60	3.90	0.08	0.11	0.25	0.35	-0.28
			0.580	3.75	4.10	0.10	0.11	0.29	0.33	-0.12
			0.580	4.00	4.60	0.15	0.16	0.25	0.27	-0.08
			0.580	4.20	4.80	0.18	0.12	0.29	0.20	0.47
Argon	[72]	40, 0.51, 0.72, 265, 50, 50	0.200	88.98	91.90	1.00	2.70	0.34	0.92	-0.63
			0.200	89.04	92.40	1.50	3.28	0.45	0.98	-0.54
			0.200	89.04	92.83	2.00	3.52	0.53	0.93	-0.43
			0.200	89.10	93.22	2.50	3.63	0.61	0.88	-0.31
			0.200	89.05	93.44	3.00	4.22	0.68	0.96	-0.29
			0.200	89.00	93.67	3.50	4.08	0.75	0.87	-0.14
			0.200	89.00	93.85	4.00	4.83	0.82	1.00	-0.17
			0.200	88.98	94.43	5.00	4.17	0.92	0.76	0.20
			0.200	89.09	101.77	6.00	12.45	0.47	0.98	-0.52
Hydrogen	[71]	4, 2.30, 3.30, 500, 55, 55	0.340	19.00	19.28	0.40	0.28	1.43	0.99	0.44
			0.340	19.00	20.80	3.00	1.28	1.67	0.71	1.34
			0.340	19.00	21.30	4.00	1.53	1.74	0.67	1.61
			0.340	19.00	21.80	5.00	1.82	1.79	0.65	1.75
			0.340	19.20	22.60	6.00	1.81	1.76	0.53	2.31
			0.340	23.20	27.80	8.00	3.05	1.74	0.66	1.63
		10, 2.30, 3.30, 500, 55, 55	0.340	19.00	19.25	0.40	0.58	1.60	2.34	-0.32
			0.340	19.00	19.80	3.00	2.08	3.75	2.60	0.44
			0.340	19.00	23.20	4.00	7.81	0.95	1.86	-0.49
			0.340	19.00	20.60	6.00	3.20	3.75	2.00	0.87
			0.340	21.30	23.20	8.00	4.48	4.21	2.36	0.78
			0.340	27.50	30.30	12.00	6.46	4.29	2.31	0.86
			0.340	19.00	20.25	5.00	2.38	4.00	1.91	1.10

8.10 Software packages

1. Python [75] – for data analysis and plots
2. Numpy [76] – for data analysis and plots
3. Matplotlib [77] – for data analysis and plots
4. Engineering Equation Solver (EES) [78] – for modeling and data analysis
5. Julia [68] - for modeling
6. DifferentialEquations.jl [69] - for modeling

9 References

1. Bugby D, Marland B, Stouffer C, et al. Advanced components and techniques for cryogenic integration. 31st International Conference on Environmental Systems, Orlando Florida USA, July 9-12 2001.
2. Goldsten J, Rhodes E, Boynton W, et al. The MESSENGER gamma-ray and neutron spectrometer. Space Science Reviews 131 (2007) 339-391. DOI: 10.1007/s11214-007-9262-7
3. Ross Jr R,. and Green K. AIRS Cryocooler System Design and Development. Proceedings of the 9th International Cryocooler Conference. Waterville Valley, Vermont, USA. June 1996. Plenum Publishing Corporation, New York.
4. Bugby D, Garzon J, Beres M, etal. Cryogenic diode heat pipe system for cryocooler redundancy. SPIE Conference on Optics and Photonics. San Diego, California, USA. August 2005. DOI: 10.1117/12.617242
5. Tate G. Linear-drive cryocoolers for the Department of Defense standard advanced dewar assembly (SADA). Defense and Security Conference, Orlando, Florida, USA. 2005. DOI: 10.1117/12.606441
6. Kirkconnell, C. Design of a 4K Hybrid Stirling/Pulse Tube Cooler for Tactical Applications. Proceedings of the 17th International Cryocooler Conference. Los Angeles, California, USA. 2017.
7. Nast T, Olson J, Champagne P, et al. Development of a 4.5 K pulse tube cryocooler for superconducting electronics. AIP Conference Proceedings 985, 881 (2008). DOI: 10.1063/1.2908684
8. Brake H, and Wigerinck G. Low-power cryocooler survey. Cryogenics 42 (2002) 705-718. DOI: 10.1016/S0011-2275(02)00143-1
9. Chen X, Xia M, Wang L, et al. The reliability development of miniature Stirling crycoolers. Proceedings of the 18th International Cryocooler Conference. Boulder, Colorado, USA. 2014.
10. Estrada R, Kuo D, and Phan Q. Reliability growth of Stirling-cycle coolers at L-3 CE. Proceedings of the 15th International Cryocooler Conference, Boulder, Colorado, USA. 2009.
11. Yasukawa Y, Ohshima K, Toyama K, et al. Design and test of a 70 K pulse tube cryocooler. Proceedings of the 12th International Cryocooler Conference, Cambridge, Massachusetts, USA. 2002.
12. DiPirro M, Shirron P, Kimball M, et al. Cryocooling technologies for the origins space telescope. Journal of Astronomical Telescopes, Instruments and Systems 7 1 011008 (2021). DOI: 10.1117/1.JATIS.7.1.011008
13. Radebaugh R. 2009. Cryocoolers: State of the art and recent developments. Journal of Physics-Condensed Matter. Online (Accessed June 6, 2021). https://tsapps.nist.gov/publication/get_pdf.cfm?pub_id=901013
14. Ross, R. Cryocooler reliability and redundancy considerations for long-life space missions. Proceedings of the 11th International Cryocooler Conference. Keystone, Colorado, USA. 2000.
15. Yang T, Kwon B, Weisensee P, et al. Millimeter-scale liquid metal droplet thermal switch. Applied Physical Letters 112 (2018) 063505. DOI:10.1063/1.5013623
16. Cho J, Richards C, Bahr D, et al. Evaluation of contacts for a MEMS thermal switch. Journal of Micromechanical Microengineering 18 (2009) 105012. DOI: 10.1088/0960-1317/18/10/105012
17. Dietrich M, Euler A, Thummes G. A compact thermal heat switch for cryogenic space applications operating near 100 K. Cryogenics 59 (2014) 70-75. DOI: 10.1016/

j.cryogenics.2013.11.004
18. Jahromi A, and Sullivan D. A piezoelectric cryogenic heat switch. Review of Scientific Instruments 85 (2014) 065118. DOI: 10.1063/1.4876483
19. Dietrich M, Euler A, and Thummes G. A lightweight thermal heat switch for redundant cryocooling on satellites. Cryogenics 83 (2017) 31–34. DOI: 10.1016/j.cryogenics.2017.02.003
20. DiPirro M, and Shirron P. Heat switches for ADRs. Cryogenics 62 (2014) 172-176. DOI: 10.1016/j.cryogenics.2014.03.017
21. Kimball M, Shirron P, Canavan E, et al. Passive gas-gap heat switches for use in low temperature cryogenic systems. Advances in Cryogenic Engineering: Proceedings of the Cryogenic Engineering Conference, Madison, Wisconsin, USA. 2017.
22. Shirron, P, Canavan E, DiPirro M, et al. Passive gas-gap heat switches for use in adiabatic demagnetization refrigerators. Proceedings of the Cryogenic Engineering Conference, Madison, Wisconsin, USA. 2001.
23. Shirron P, Canavan E, DiPirro M, et al. A compact, high-performance continuous magnetic refrigerator for space missions. Cryogenics 41 (11-12) (2001) 789-795. DOI: 10.1016/S0011-2275(01)00164-3
24. Catarino I, Afonso J, Martins D, Duband L, and Bonfait G. Gas gap thermal switches using neon or hydrogen and sorption pump. Vacuum 83 (2009) 1270-1273. DOI: 10.1016/j.vacuum.2009.03.021
25. Bugby D, Garzon J, Beres M, Stouffer C, Mehoke D, et al. Cryogenic diode heat pipe system for cryocooler redundancy. Proceedings of SPIE 58904, Cryogenic Optical Systems and Instruments XI, 59040Z. August 18 2005. DOI: 10.1117/12.617242.
26. Cepeda-Rizo J, Rodriquez J, and Bugby D. Methane cryogenic heat pipe for space use with a liquid trap for on-off switching. Advances in Cryogenic Engineering, AIP Conference Proceedings 1434 (2012) 293-300. DOI: 10.1063/1.4706932.
27. Engels J, Gorter F, Miedema A. Magnetoresistance of gallium – a practical heat switch at liquid helium temperatures. Cryogenics 12 (1972) 2 141-145. DOI: 10.1016/0011-2275(72)90016-1.
28. Tuttle J, Canava E, Delee C. Development of a space-flight ADR providing continuous cooling at 50 mK with heat rejection at 10 K. Advances in Cryogenic Engineering: Proceedings of the Cryogenic Engineering Conference, Madison, Wisconsin, USA. 2017.
29. Akachi H, Polasek F, and Stulc P. Pulsating heat pipes. Proceedings of the 5th International Heat Pipe Symposium, Melbourne Australia, 1996. 208-217.
30. Holley B, and Faghri A. Analysis of pulsating heat pipe with capillary wick and varying channel diameter. International Journal of Heat and Mass Transfer 48 (2005) 2635-2651.
31. Charoensawan P, Khandekar S, Groll M, and Terdtoon P. Closed loop pulsating heat pipes Part A: parametric experimental investigations. Applied Thermal Engineering 23 (2003) 2009-2020.
32. Khandekar S, Dollinger N, and Groll M. Understanding operational regimes of closed loop pulsating heat pipes: an experimental study, Applied Thermal Engineering 23 (2003) 707-719.
33. Khandekar S, Thermo-hydrodynamics of closed loop pulsating heat pipes. PhD dissertation, Institut für Kernenergetik und Energiesysteme der Universität Stuttgart, Stuttgart, Germany, 2004.
34. Kim J, Bui N, Kim J, Kim J, and Jung H. Flow visualization of oscillation characteristics of liquid and vapor flow in the oscillating capillary tube heat pipe. KSME International Journal 17 (2003) 1507-1519.

35. Fonseca L. Experimental characterization of cryogenic helium pulsating heat pipes. PhD Dissertation, University of Wisconsin – Madison, 2017.
36. White E, and Beardmore R. The velocity of rise of single cylindrical air bubbles through liquids contained in vertical tubes. Chemical Engineering Science 17 5 (1962) 351-361.
37. Touloukian Y, Powell R, Ho C, and Klemens P. Thermal Conductivity: Metallic Elements and Alloys. Springer, New York, 1970.
38. NIST Material Properties: OFHC Copper (UNS C10100/C10200). https://trc.nist.gov/cryogenics/materials/OFHC%20Copper/OFHC_Copper_rev1.htm. 7 Jun 2020.
39. Jiao A, Ma H, and Critser J. Experimental investigation of cryogenic oscillating heat pipes. International Journal of Heat and Mass Transfer 52 (2009) 3504-3509. DOI: 10.1016/j.ijheatmasstransfer.2009.03.013
40. Fonseca L, Miller F, and Pfotenhauer J. Experimental heat transfer analysis of a cryogenic nitrogen pulsating heat pipe at various liquid fill ratios. Applied Thermal Engineering 130 (2018) 343-353. DOI: 10.1016/j.applthermaleng.2017.11.029
41. Mito T, Natsume K, Yanagi N, Tamura H, Tamada T, Shikimachi K, Hirano N, and Nagaya S. Development of highly effective cooling technology for a superconducting magnet using cryogenic OHP. IEEE Transactions on Applied Superconductivity 20 3 (2010) 2023-2026. DOI: 10.1109/TASC.2010.2043724
42. Liang Q, Li Y, and Wang Q, Study on a neon cryogenic oscillating heat pipe with long heat transport distance. Heat and Mass Transfer 54 (6) (2018) 1721-1727. DOI: 10.1007/s00231-017-2269-z
43. Fonseca L, Miller F, and Pfotenhauer J. A helium based pulsating heat pipe for superconductive magnet. Advances in Cryogenic Engineering: Transactions of the Cryogenic Engineering Conference, Anchorage Alaska USA, 2013, 28-35.
44. Xu D, Li L, and Liu H, Experimental investigation on the thermal performance of helium based cryogenic pulsating heat pipe. Experimental Thermal and Fluid Science 70 (2016) 61-68. DOI: 10.1016/j.expthermflusci.2015.08.024
45. Fonseca L, Pfotenhauer J, and Miller F. Results of a three evaporator cryogenic helium pulsating heat pipe. International Journal of Heat and Mass Transfer 120 (2018) 1275-1286. DOI: 10.1016/j.ijheatmasstransfer.2017.12.108
46. Patel V, and Mehta H. Influence of gravity on the performance of closed loop pulsating heat pipe. World Academy of Science, Engineering and Technology International Journal of Mechanical and Mechatronics engineering 10 1 (2016) 219-223.
47. Okazaki S, Fuke H, Miyazaki Y, and Ogawa H. Development of Meter-Scale U-Shaped and O-Shaped Oscillating Heat Pipes for GAPS. Journal of Astronomical Instrumentation 3 2 (2014) 1440004. doi:10.1142/S2251171714400042
48. Gu J, Kawaji M, and Futamata R. Microgravity performance of micro pulsating heat pipes. Microgravity – Science and Technology 16 (2005) 181-185. DOI: 10.1007/BF02945972
49. Mameli M, Araneo L, Filippeschi S,et al. Thermal response of a closed loop pulsating heat pipe under a varying gravity force. International Journal of Thermal Sciences 80 (2014) 11-22. DOI: 10.1016/j.ijthermalsci.2014.01.023
50. Gu J, Kawaji M, and Futamata R. Effects of gravity on the performance of pulsating heat pipes. Journal of Thermophysics and Heat Transfer 18 (3) (2004) 370-378. DOI: 10.2514/1.3067
51. Harichian T, and Garimella S. A comprehensive flow regime map for microchannel flow boiling with quantitative transition criteria. International Journal of Heat and Mass Transfer 53 (2010) 694-702. DOI: 10.1016/j.ijheatmasstransfer.2010.02.039

52. Fonseca L, Pfotenhauer J, and Miller F. Short communications: thermal performance of a cryogenic helium pulsating heat pipe with three evaporator sections. International Journal of Heat and Mass Transfer 123 (2018) 655-656. DOI: 10.1016/j.ijheatmasstransfer.2018.03.013
53. Nellis G and Klein S. Heat Transfer. Cambridge University Press. 2012.
54. Lemmon E, and Jacobsen R. Viscosity and thermal conductivity equations for nitrogen, oxygen, argon, and air. International Journal of Thermophysics 25 1 (2004) 21-69.
55. Span R. A reference equation of state for the thermodynamic properties of nitrogen for temperatures from 63.151 to 1000 K and pressures to 2200 Mpa. Journal of Physical and Chemical Reference Data 29 (2000) 1361. DOI: 10.1063/1.1349047
56. NIST Material Properties: 304 Stainless (UNS S30400). https://trc.nist.gov/cryogenics/materials/304Stainless/304Stainless_rev.htm. Retrieved 7 Jun 2020.
57. Hands B and Arp V. A correlation of thermal conductivity data for helium. Cryogenics 21 (12) (1981) 697-703. DOI: 10.1016/0011-2275(81)90211-3
58. Vega D. A new wide range equation of state for helium-4. PhD Thesis, Texas A&M University. August 2013. http://oaktrust.library.tamu.edu/handle/1969.1/151301
59. Shaffii M, Faghri A, and Zhang Y. Analysis of heat transfer in unlooped and looped pulsating heat pipes. International Journal of Numerical Methods for Heat and Fluid Flow 12 (5) (2002) 585-609. DOI: 10.1108/09615530210434304
60. Ma H, Hanlon M, and Chen C. An investigation of oscillating motions in a miniature pulsating heat pipe. Microfluidics and Nanofluidics 2 (2006) 171-179. DOI: 10.1007/s10404-005-0061-8
61. Gürsel G, Frijns A, Homburg F, and van Steenhoven A. A mass-spring-damper model of a pulsating heat pipe with a non-uniform and asymmetric filling. Applied Thermal Engineering 91 (2015) 80-90. DOI:10.1016/j.applthermaleng.2015.06.014
62. Sun X, Li S, Wang B, Jiao B, et al. Numerical study of thermal performance of a hydrogen pulsating heat pipe. International Journal of Thermal Sciences 172 (A) (2022).DOI: 10.m/j.ijthermalsci.2021.107302
63. Gungor K and Winterton R. A general correlation for flow boiling in tubes and annuli. International Journal of Heat and Mass Transfer 29 (3) (1986) 351-358. DOI: 10.1016/0017-9310(86)90205-X
64. Nikolayev V. A dynamic film model of the pulsating heat pipe. Journal of Heat Transfer 133 (8) (2011). DOI: 10.1115/1.4003759
65. Aussillous P and Quéré D. Quick deposition of a fluid on the wall of a tube. Physics of FLuids 12 (2000). DOI: 10.1063/1.1289396
66. Göhl J, Mark A, Sasic S, and Edelvik F. An immersed boundary based dynamic contact angle framework for handling complex surfaces of mixed wettabilities. International Journal of Multiphase Flow 109 (2018) 164-177. DOI: 10.1016/j.ijmultiphaseflow.2018.08.001
67. Bell I, Wronski J, Quoilin S, and Lemort V. Pure and Pseudo-pure Fluid Thermophysical Property Evaluation and the Open-Source Thermophysical Property Library CoolProp. Industrial and Engineering Chemistry Research 53 (6) (2014) 2498-2508. DOI: 10.1021/ie4033999
68. The Julia Programming Language. Version 1.6.3. www.julialang.org
69. Rackauckas C and Qing N. Differentialequations.jl - a performant and feature-rich ecosystem for solving differential equations in julia. Journal of Open Research Software 5 (1) (2017). DOI: 10.5334/jors.151
70. Nlsolve.jl. https://github.com/JuliaNLSolvers/NLsolve.jl
71. Sun X, Li S, Jiao B, et al. Experimental study on hydrogen pulsating heat pipes under different number of turns. Cryogenics 111 (2020). DOI: 10.1016/j.cryogenics.2020.103174

72. Memje, Uzoma. Personal communication (2022).
73. Mameli M, Manno V, Filippeschi S, et al. Thermal instability of a closed loop pulsating heat pipe: combined effect of orientation and filling ratio, Experimental Thermal and Fluid Science 59 (2014) 222-229. DOI: 10.1016/j.expthermflusci.2014.04.009
74. LakeShore Cryotronics PT-100 series platinum RTD Specifications. https://www.lakeshore.-com/docs/default-source/product-downloads/lstc_platinum_l.pdf?sfvrsn=9157869c_5. Retrieved 7 JUN 2020.
75. Python Software Foundation. Version 3.9.5. www.python.org
76. Numpy. Version 1.20.0. www.numpy.org
77. Matplotlib. Version 3.4.2. www.matplotlib.org
78. Engineering Equation Solver. Www.fchartsoftware.com/ees/